Doctoral Dissertation
博士論文

Search for a heavy scalar resonance decaying into a pair of
photon-jets in *pp* collisions at $\sqrt{s}$ = 13 TeV
（重心系エネルギー13 TeVの陽子陽子衝突における
光子ジェット対に崩壊する重いスカラー粒子の探索）

A Dissertation Submitted for the Degree of Doctor of Philosophy
February 2019

平成31年2月博士（理学）申請
Department of Physics, Graduate School of Science,
The University of Tokyo
東京大学大学院理学系研究科物理学専攻
Yuya Kano
加納　勇也

Abstract

The Standard Model of particle physics is well established, but several unsolved problems remain, such as the hierarchy problem and the strong CP problem. They suggest the existence of physics beyond the Standard Model, but hints of new physics are not yet observed by past researches. At the energy-frontier pp collision experiments at the LHC, it is all the more important to search for new physics in a completely new final state. This thesis describes such a search in a novel final state called a "photon-jet" using pp collisions at $\sqrt{s}$ = 13 TeV. A photon-jet is a group of collimated photons that share close trajectories. Photon-jets can arise from a boson with a mass of $O(100)$ GeV decaying into lighter bosons with a mass of $O(1)$ GeV, that consecutively decays into photons. In such a case, the lighter boson is boosted, leading to collimated photons. The existence of photon-jets is well motivated by several beyond-the-Standard-Model scenarios that predict two or more new bosons, including the supersymmetry and the Peccei-Quinn mechanism. This research aims to look into a parameter space which conventional searches had limited sensitivity to, by employing an optimized event selection strategy based on shower shapes observed in the electromagnetic calorimeter.

The result of a search for a new heavy scalar resonance decaying into a pair of photon-jets using pp collisions at $\sqrt{s}$ = 13 TeV is presented. The dataset was collected with the ATLAS detector in 2015 and 2016, corresponding to an integrated luminosity of 36.7 fb^{-1}. Candidate events of a resonance decaying into a pair of photon-jets are selected from events with two high-momentum reconstructed photons, where each reconstructed photon corresponds to a photon-jet in the case of signal events. This search is performed in a largely model-independent way, so that the search is sensitive to beyond-the-Standard-Model scenarios leading to a pair of photon-jets in general. No significant excess of events from the Standard Model expectation is observed.

The result of a null observation is interpreted in the context of beyond-the-Standard-Model scenarios which assume a scalar resonance decaying into a final state with photons. One scenario assumes a scalar resonance X with a mass of $O(100)$ GeV, with a narrow width, and produced by the gluon–gluon fusion process; X decays into a pair of spin-0 particles a with a mass of $O(1)$ GeV that decays into a pair of photons, via $X \rightarrow aa \rightarrow 4\gamma$. Another scenario assumes the decay of the a particle into three neutral pions, via $X \rightarrow aa \rightarrow 6\pi^0 \rightarrow 12\gamma$. Upper limits on the product of the production cross section and the branching ratios are evaluated for the region 200 GeV $< m_X <$ 2 TeV and $m_a < 0.01 \times m_X$ using an asymptotic approximation. They are found to be as low as 0.2 fb for $m_X = 2$ TeV. Some scenarios predict photon-jets produced from a decay of a long-lived boson; the results are interpreted for such a case as well. The results are interpreted in the context of the Next-to-Minimal Supersymmetric Standard Model for the process $H \rightarrow aa \rightarrow 4\gamma$, where H is a new scalar Higgs boson with a mass larger than 200 GeV, and a is a pseudoscalar Higgs boson with a mass of $O(1)$ GeV.

This thesis presents the first result of a search for a heavy ($> 200\,\text{GeV}$) resonance decaying into photon-jets. The important feature of this research is the optimization of the search strategy utilizing the shower shape observed in the electromagnetic calorimeter. This research is a new frontier of direct searches using a novel final state. This result places constraints on the subset of the parameter space of the Next-to-Minimal Supersymmetric Standard Model that has not been looked into before.

Contents

1 Introduction

The Standard Model (SM) of particle physics describes the properties of elementary particles and their interactions. With the discovery of the Higgs boson in 2012, the SM is now well established. However, several unsolved problems remain, including the hierarchy problem [1, 2] and the strong CP problem [3, 4]. Several beyond-the-Standard-Model (BSM) scenarios are considered to solve these problems or realize the grand unification. These scenarios have been tested by past researches, for instance by the conventional direct searches conducted by the energy-frontier pp collision experiments at the Large Hadron Collider (LHC). However, hints of new physics are not yet observed, with a wide range of results at $\sqrt{s}$ = 7, 8, 13 TeV pp collisions at the LHC being consistent with the SM. The importance of a search for new physics with a completely new approach is increasing.

This thesis describes a search for new physics in a novel final state called a "photon-jet" using pp collisions at $\sqrt{s}$ = 13 TeV recorded with the ATLAS detector. A photon-jet is a group of collimated photons that share close trajectories (e.g. smaller than $O(0.01)$ radians in the lab frame) [5–7]. Photon-jets can arise from a boson X with a mass of $m_X = O(100)$ GeV decaying into lighter bosons a with a mass of $m_a = O(1)$ GeV that consecutively decays to photons, as shown in Figure 1. In such a case, the lighter boson a is boosted with a Lorentz factor of $\gamma_a = O(100)$, leading to collimated photons. At pp collisions of the ATLAS experiment, an interesting feature of a photon-jet is that the collimated photons enter a small area of the electromagnetic (EM) calorimeter (e.g. comparable to the Molière radius), typically leading to a single EM shower cluster. Conventional searches have limited sensitivity to such final states; in this research, the optimized event selection strategy, which utilizes the shower shapes in the EM calorimeter, allows to search for these signatures with the available ATLAS pp collision dataset.

For pp collision experiments at the LHC, final states with high-energetic photons have two advantages when searching for new physics. One is that requiring a final state containing high-energetic photons reduces the number of background SM events significantly. Another is that the good energy and angular resolutions of the EM calorimeters of the ATLAS and CMS detectors can be used to effectively separate signal photons and hadronic-jet backgrounds. A good example of these features is the search for SM Higgs boson with the decay channel $H \rightarrow \gamma\gamma$: Despite the small SM branching ratio (0.2%) of the decay $H \rightarrow \gamma\gamma$, this process was one of the main decay channel with which the Higgs boson was observed [8, 9]. Thus, a search for photon-jet final states is an advantageous method to search for new physics.

The existence of photon-jets is well motivated by several BSM scenarios that predict the presence of two or more new bosons [10–16]. The search is performed in a largely model-independent way, so that the search is sensitive to these BSM scenarios in general. The BSM scenarios are described briefly below:
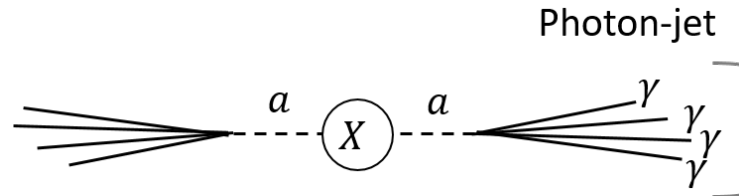

Figure 1: A schematic diagram of the process $X \rightarrow aa$ and a consecutively decaying into photons. X and a are hypothetical new bosons. When $m_X \gg m_a$, this process leads to a pair of photon-jets.

- Supersymmetry provides a solution to the hierarchy problem, provides scenarios realizing the grand unification, and provides candidates of dark matter [17]. One of the supersymmetric model, the Next-to-Minimal Supersymmetric Standard Model (NMSSM), introduces several new Higgs bosons [18]. This may result in the process $H \to aa \to 4\gamma$, where H is a new scalar Higgs boson with a mass of $m_H = O(100)$ GeV, and a is a new pseudoscalar Higgs boson with a mass of $m_a = O(1)$ GeV [10, 11]. This scenario is described in Section 2.3 in detail.

- The CP violation of strong interaction is experimentally not observed; this requires the CP-violating term to be small, leading to a fine tuning ("strong CP problem"). The Peccei-Quinn (PQ) mechanism solves this problem by introducing a spontaneously-broken global $U(1)$ symmetry, which leads to the existence of a new pseudoscalar particle ("axion") [3, 4]. One model that leads to photon-jets is the "visible heavy QCD axion model" [12]. This introduces a mirror copy of the SM, and a $\mathbb{Z}_2$ symmetry between the SM sector and the copy sector, leading to a heavy axion ($m_a > O(0.1)$ GeV). A complex scalar field is introduced to break the PQ symmetry spontaneously, resulting in a heavy scalar boson and its decay into a pair of axions. For axions that are not so heavy (i.e. $m_a \sim \Lambda_{\mathrm{QCD}}$, where Λ_{QCD} is the QCD scale), the axions decay via mixing with the η and η' mesons, thus having sizeable decay branching ratios into $a \to \gamma\gamma$ and $a \to 3\pi^0 \to 6\gamma$. A similar model is implemented with a model-independent effective field theory approach [13].

- A model incorporating a new gauge symmetry $U(1)'$ introduces a new vector boson Z' as a carrier. The new $U(1)'$ symmetry may arise from a larger gauge group in grand unified theories [19]. The boson Z' can decay into photons either by $Z' \to sa \to 4\gamma$, $Z' \to a\gamma \to 3\gamma$ [14], or by $Z' \to s\gamma \to 3\gamma$ [15], where a new scalar s and pseudoscalar a decay to pairs of photons, leading to photon-jets.

- The Randall-Sundrum model solves the hierarchy problem with the introduction of an additional dimension [20]. In this model, a Kaluza-Klein graviton may decay to a pair of radions [16]. In this case, the radion can have a sizeable decay to a pair of photons or a pair of neutral pions, leading to a photon-jet.

- A "hidden-valley-like model" [21] introduces two new real scalar fields, leading to the process $X \to YY \to 4\pi^0 \to 8\gamma$, where X and Y are new scalar bosons. When Y is considerably lighter than X, this process leads to a pair of photon-jets.

This research is closely related to a search for an "axion-like-particle (ALP)". Generally, a spontaneous breaking of a global $U(1)$ symmetry results in a massless Nambu-Goldstone boson. If the symmetry is explicitly broken, this boson becomes massive; such a boson is called a pseudo-Nambu-Goldstone boson, and also commonly as an ALP. Because of an approximate shift symmetry, ALPs can be naturally lighter than the electroweak scale (~ 247 GeV). ALPs exist in several well-motivated BSM scenarios, including the PQ mechanism discussed above. Experimental searches for ALPs have been performed by several past researches, and they are not found yet. Constraints on couplings of ALPs and photons are placed from these researches, as shown in Figure 2. Here, the effective coefficient $C_{\gamma\gamma}^{\mathrm{eff}}$ is defined as [22]

$$\Gamma(a \to \gamma\gamma) = \frac{4\pi\alpha^2 m_a^3}{\Lambda^2} \left| C_{\gamma\gamma}^{\mathrm{eff}} \right|^2 \tag{1}$$

where m_a is the mass of the ALP, and Λ is the new physics scale for the suppression of the dimension-5 operators. The parameter space of ALPs is strongly constrained from e.g. axion helioscopes, cosmological observations, and collider searches. However, the region $m_a \gtrsim 0.1$ GeV and $|\frac{C_{\gamma\gamma}^{\mathrm{eff}}}{\Lambda}| \lesssim 1$ TeV^{-1} is weakly
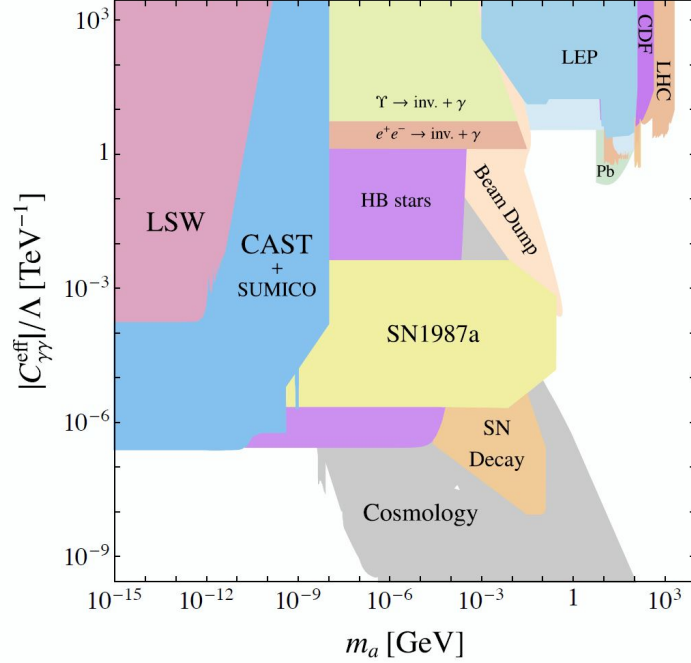
Figure 2: Existing constraints from past observations on the ALP-photon coupling. Several of these bounds are model dependent. [22]

constrained, as seen in Figure 2. This research can search for ALPs with smaller effective couplings, with the sensitivity of this search strongly dependent on the production cross section of the parent particle X in pp collisions, and the branching ratio of its decay to photons, e.g. $\mathcal{B}(X \to aa \to 4\gamma)$[1]. This research can search for ALPs with small effective couplings of as low as e.g. $|\frac{C_{\gamma\gamma}^{\text{eff}}}{\Lambda}| \gtrsim O(10^{-3})$ TeV^{-1}[2] for the case of $\gamma_a \sim 100$, $m_a \sim 1$ GeV, and $\mathcal{B}(a \to \gamma\gamma) \sim 1$; this lower bound is derived from the limitation that the ALPs need to decay before entering the ATLAS EM calorimeter, which has an inner radius of 1.5 m.

In the context of searches for a heavy ($> O(100)$ GeV) resonant boson decaying into a final state with at least three photons, e.g. $X \to aa \to 4\gamma$, there exist two related searches that have been performed in the past, as shown in Figure 3. One of these searches is a general search for new phenomena in events with at least three isolated photons, performed by the ATLAS experiment at Run 1 for pp collisions at $\sqrt{s} = 8$ TeV [23]. This search looked for a heavy boson decaying into a lighter bosons with a mass of $m_a = O(10)$ GeV, and was sensitive to the BSM signal scenario $X \to aa \to 4\gamma$ corresponding to the region $m_a/m_X \gtrsim 0.08$. Another search is a search for a scalar boson h decaying via $h \to aa \to 4\gamma$, performed by the ATLAS experiment at Run 1 for pp collisions at $\sqrt{s} = 7$ TeV [24]. This search was conducted before the discovery of the SM Higgs boson, assuming a SM Higgs-like boson with its mass of 110 GeV $< m_h <$ 150 GeV and its decay to pseudoscalars with a mass of 100 MeV $< m_a <$ 400 MeV. The search described in this thesis is sensitive to the region $m_X > 200$ GeV and $m_a/m_X < 0.01$, which is

---

[1]Obviously, this search has no sensivity to ALPs if a heavy (> 200 GeV) boson that is produced by pp collisions and that has a coupling to ALPs does not exist

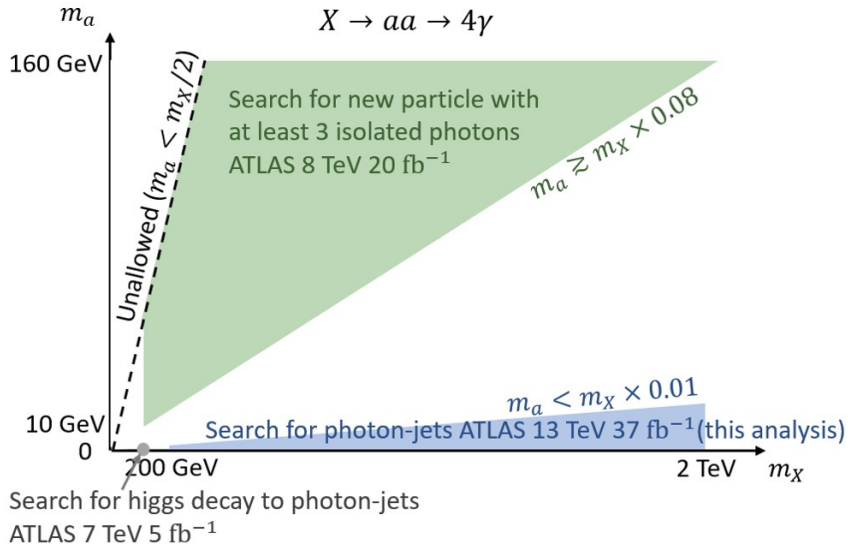[2]This lower bound is proportional to $\sqrt{\gamma_a \mathcal{B}(a \to \gamma\gamma)/m_a^3}$.

Figure 3: Approximate sensitivity of existing searches for multiphoton final states for the BSM process $X \to aa \to 4\gamma$. The lower blue region corresponds to the analysis described in this thesis. The upper green region corresponds to the search for new phenomena with at least three isolated photons performed by ATLAS at Run 1 [23]. The grey point corresponds to the search for a SM Higgs-like boson decaying into photon-jets performed by ATLAS at Run 1 [24].

a parameter region which has not been looked into before[3].

This research shares some features with the search for a heavy (> 200 GeV) resonant boson decaying into a pair of photons, performed by the ATLAS experiment at Run 2 for pp collisions at $\sqrt{s} = 13$ TeV [25]. This search looked for new physics in a final state leading to two high-energetic EM shower clusters in the EM calorimeter, with stringent photon identification selections applied to the EM clusters using information of shower shapes in the EM calorimeter. Because a photon-jet typically leads to a single EM cluster, this diphoton resonance search has some limited sensitivity to photon-jet signal models; an approximate sensitivity of this diphoton resonance search to the process $X \to aa \to 4\gamma$ is shown in Figure 4. This figure shows the case for a scalar boson X with a mass of $m_X = 800$ GeV, has a narrow width, and that is produced via the gluon–gluon fusion process (i.e. a coupling with a pair of gluons via a loop of quarks). As seen in the figure, this diphoton resonance search loses sensitivity (i.e. upper limit on the product of the signal cross section and branching ratios) for larger values of m_a, e.g. by an order of magnitude for $m_a/m_X > 0.003$. This is because a larger value of m_a leads to a smaller boost of a (i.e. smaller γ_a), leading to a wider EM shower in the EM calorimeter, thus being rejected by the stringent photon identification selection. It is important to look into the parameter region with large values of m_a in order to search for new physics.

This thesis describes the result of the search for a heavy (> 200 GeV) resonance decaying into a pair of photon-jets. It is performed using a dataset of pp collisions at $\sqrt{s} = 13$ TeV collected with the ATLAS detector at the LHC in 2015 and 2016, corresponding to an integrated luminosity of 36.7 fb^{-1}. A

---

[3]There exists an intermediate region, $0.01 < m_a/m_X \lesssim 0.08$, which is covered by neither the three-photon search at 8 TeV nor the search described in this thesis. The limitation here arises from the triggers for data collection. The search described in this thesis uses the dataset collected with the diphoton trigger, as described in Section 5.1.1. For the BSM scenario $X \to aa \to 4\gamma$ in the region $0.01 < m_a/m_X \lesssim 0.08$, the EM clusters of final-state photons will overlap and create wide EM clusters; these EM clusters are typically rejected by the trigger-level photon selections.
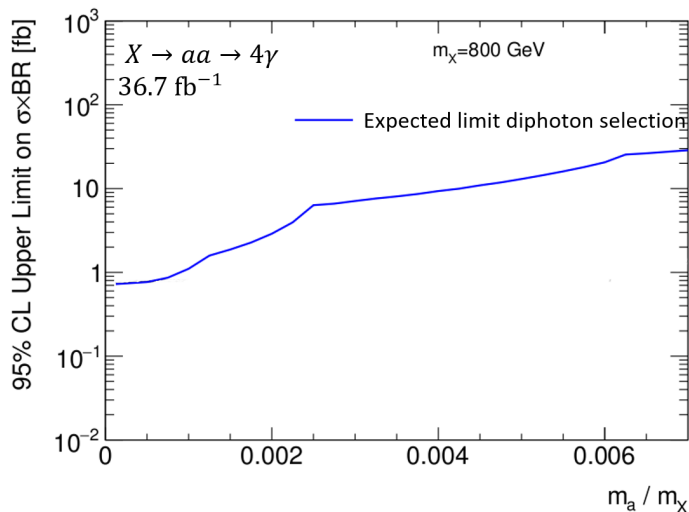
Figure 4: An approximate 95% expected limit on the signal production cross section times branching ratios of $X \to aa \to 4\gamma$, i.e. $\sigma_X \times \mathcal{B}(X \to aa) \times \mathcal{B}(a \to \gamma\gamma)^2$. The scalar boson X is assumed to have a mass of $m_X = 800$ GeV, have a narrow width, and that it is produced via the gluon–gluon fusion process (i.e. a coupling with a pair of gluons via a loop of quarks). The boson a is assumed to be spin-0. In principle, this approximation is performed based on the search result presented in the diphoton resonance search paper [25], with the selection efficiency of the signal process $X \to aa \to 4\gamma$ evaluated by a simulation. The details of the approximation method is described in Section 5.8.3. The zigzag structure of the limit is due to the interpolation method used for this approximation; the signal selection efficiency is linearly interpolated between the mass values (m_X, m_a) that the simulated signal samples are generated.

photon-jet typically leads to a single EM shower cluster in the EM calorimeter, and thus each photon-jet typically leads to one reconstructed photon. Candidate events of a heavy resonance decaying into a pair of photon-jets are selected from events with two high-momentum reconstructed photons, where each reconstructed photon corresponds to a photon-jet in the case of signal events. The event selection and the event categorization are optimized for the photon-jet events, utilizing the EM shower shape observed in the EM calorimeter. The search is performed in a largely model-independent way, by searching for a new resonance in an invariant mass spectrum of two reconstructed photons with a smoothly-falling background. To cover a wide range of values of m_X and m_a, several aspects of the search (e.g. reconstructed mass shape of X and signal selection efficiency) are parametrized as functions of m_X and m_a. The shape of the background component in the invariant mass of two reconstructed photons is evaluated with an analytic function. An excess of events is searched for by performing an unbinned maximum-likelihood fit, with the consideration of the signal and background components, to the invariant mass of two reconstructed photons. This research is a new frontier of direct searches using a novel final state.

A brief review of the SM, supersymmetry, and the NMSSM is given in Section 2. This section also describes the scenario of a new scalar Higgs boson decaying into a final state with photon-jets in the NMSSM. The LHC and the ATLAS detector are described in Section 3. The reconstruction and the identification of photons from pp collision data collected with the ATLAS detector are described in Section 4. The details and the result of the search for a resonance decaying into a pair of photon-jets are described in Section 5. The interpretation of the result in the context of the NMSSM for the process $H \to aa \to 4\gamma$ is described in Section 6.

The author's contribution includes the development of the analysis strategy and the computation of the

results as described in Section 5, and the interpretation of the result in the context of NMSSM as described in Section 6. The most important feature of this research is the development of the event selection strategy, which was optimized using simulations of signal processes, and with a focus on large values of m_a ($0.003 \lesssim m_a/m_X < 0.01$). The event selection strategy effectively utilizes the information of the shower shape in the EM calorimeter, as described in Section 5.3.

2 Theoretical overview

2.1 The Standard Model of particle physics

The SM is an established theory that describes the properties of elementary particles and their interactions. It describes three of the four fundamental forces of Nature (i.e. electromagnetic, weak, strong interactions and excluding gravitational force) within the framework of the gauge symmetry group $SU(3)_C \times SU(2)_L \times U(1)_Y$. The particle content of the SM is summarized in Tables 1 and 2. The gluon g, the weak bosons $W^\pm$ and Z, and the photon γ are the mediators of the strong, weak, and electromagnetic interactions. The Higgs field is introduced as a scalar complex $SU(2)$ doublet that causes the electroweak spontaneous symmetry breaking through the Brout-Englert-Higgs mechanism, introducing masses to weak bosons and massive fermions; this leads to the existence of a Higgs boson. With the discovery of the Higgs boson in 2012 [8, 9] by the ATLAS and CMS experiments at the LHC, all of the particles have been discovered.

It is understood that the theoretical prediction of the SM is consistent with most of the various experimental results and observations. Several unsolved problems that cannot be explained by the SM are known to exist, including the hierarchy problem (explained in Section 2.2.1), the existence of the dark matter (explained in Section 2.2.2), the strong CP problem, and the neutrino mass and its flavour oscillation.

2.2 Supersymmetry and the NMSSM

As described in Section 1, a resonance decaying into a pair of photon-jets can arise from the NMSSM. The NMSSM is a minimal extension of the Minimal Supersymmetric Standard Model (MSSM), and so the MSSM must be introduced first. Supersymmetry is introduced in Section 2.2.1; the MSSM in

Table 1: The fermions (i.e. quarks and leptons) of the Standard Model. Q is the electric charge, T and T^3 are the weak isospin and its third component, Y is the weak hyper charge, and N_C is the number of colour states.

	Generations			Q	T	T^3	Y	N_C
Quarks	$\begin{pmatrix} u \\ d \end{pmatrix}_L$	$\begin{pmatrix} c \\ s \end{pmatrix}_L$	$\begin{pmatrix} t \\ b \end{pmatrix}_L$	$\begin{pmatrix} 2/3 \\ -1/3 \end{pmatrix}$	$1/2$	$\begin{pmatrix} 1/2 \\ -1/2 \end{pmatrix}$	$1/3$	3
	u_R	c_R	t_R	$2/3$	0	0	$4/3$	3
	d_R	s_R	b_R	$-1/3$	0	0	$-2/3$	3
Leptons	$\begin{pmatrix} \nu_e \\ e^- \end{pmatrix}_L$	$\begin{pmatrix} \nu_\mu \\ \mu^- \end{pmatrix}_L$	$\begin{pmatrix} \nu_\tau \\ \tau^- \end{pmatrix}_L$	$\begin{pmatrix} 0 \\ -1 \end{pmatrix}$	$1/2$	$\begin{pmatrix} 1/2 \\ -1/2 \end{pmatrix}$	-1	0
	e_R	μ_R	τ_R	-1	0	0	-2	0

Table 2: The gauge bosons and the Higgs boson of the Standard Model. Q is the electric charge, T and T^3 are the weak isospin and its third component, Y is the weak hyper charge, and N_C is the number of colour states.

		Q	T	T^3	Y	N_C
Gauge bosons	g	0	0	0	0	8
	$W^\pm$	±1	1	±1	0	0
	Z	0	0	0	0	0
	γ	0	0	0	0	0
Higgs boson	h	0	$1/2$	$-1/2$	1	0

Section 2.2.2; the NMSSM in Section 2.2.3. Lastly,the scenario of a new scalar Higgs boson decaying into a final state with photon-jets in the NMSSM is described in Section 2.3.

2.2.1 Supersymmetry

"Supersymmetry" is defined as a symmetry relating fermions and bosons [17]. It is one of the BSM scenarios that is considered to solve problems of the SM, especially the hierarchy problem.

In the SM, the potential of the electrically neutral part of the Higgs field is given as

$$V = m_H^2 |H|^2 + \lambda |H|^4 \tag{2}$$

where H is a complex scalar field. The vacuum expectation value (VEV) is given by $\langle H \rangle = \sqrt{-m_H^2/2\lambda}$, which is known to be approximately 174 GeV from measurements of the weak interactions. The SM Higgs mass is given by $\sqrt{-2m_H^2}$ and it is measured to be around 125 GeV, implying $m_H^2 = -(92.9 \text{ GeV})^2$.

From a Dirac fermion f with mass m_f and coupling $-\lambda_f H \bar{f} f$, m_H^2 receives a loop correction

$$\Delta m_H^2 = -\frac{|\lambda_f|^2}{8\pi^2} \Lambda_{\text{UV}}^2 + ... \tag{3}$$

where Λ_{UV} is the ultraviolet momentum cutoff to regulate the loop integral. The "..." represents terms proportional to m_f^2, which grow at most logarithmically with Λ_{UV}.

From a hypothetical heavy complex scalar particle S with mass m_S and coupling $-\lambda_S |H|^2 |S|^2$, m_H^2 receives a loop correction

$$\Delta m_H^2 = \frac{\lambda_S}{16\pi^2} \left[\Lambda_{\text{UV}}^2 - 2m_S^2 \ln(\Lambda_{\text{UV}}/m_S) + ... \right] \tag{4}$$

These corrections, given in Eqs. (3) and (4), are sensitive to Λ_{UV}, which could be as high as the Planck scale. Also, both corrections are sensitive to a possible existence of a new heavy particle. These sensitivities lead to a possible unnatural large corrections to the Higgs potential, i.e. the hierarchy problem.

These corrections can be "neatly" cancelled by introducing supersymmetry. Because of the relative minus sign in Eqs. (3) and (4), the corrections cancel out when each fermion has a complex scalar partner with $\lambda_S = |\lambda_f|^2$.

The supersymmetry transformation operator Q is defined as

$$Q|\text{Boson}\rangle = |\text{Fermion}\rangle, \qquad Q|\text{Fermion}\rangle = |\text{Boson}\rangle \tag{5}$$

It follows anticommutation and commutation relations

$$\{Q_\alpha, Q_\beta^\dagger\} = -2\sigma_{\alpha\beta}^\mu P_\mu \tag{6}$$

$$\{Q_\alpha, Q_\beta\} = 0 \tag{7}$$

$$\{Q_\alpha^\dagger, Q_\beta^\dagger\} = 0 \tag{8}$$

$$[Q_\alpha, P^\mu] = 0 \tag{9}$$

$$[Q_\alpha^\dagger, P^\mu] = 0 \tag{10}$$

where P^μ is the four-momentum generator of spacetime translations, and α, β are the spinor indices.

The irreducible representations of the supersymmetry algebra is called "supermultiplets". A supermultiplet is composed of fermion and boson states; these states are defined as "superpartners" of each other. A "chiral supermultiplet" is defined as a combination of a two-component Weyl fermion and a complex scalar field. The "gauge supermultiplet" is defined as a combination of a spin-1 gauge boson and a gaugino (two-component spin-1/2 Weyl fermion with same gauge transformation properties as its partner).

In a supersymmetric model, "sparticles" (i.e. superpartners of SM particles and Higgs boson(s)) are introduced. Considering that the sparticles are not experimentally found yet, their masses are assumed to be heavier than their superpartners. This leads to the assumption of a "soft" supersymmetry breaking. Here, "soft" means that the relationship $\lambda_S = |\lambda_f|^2$ of the superpartners are maintained after the supersymmetry breaking, to avoid the hierarchy problem. The soft supersymmetry breaking is triggered by an additional term $\mathcal{L}_{\text{soft}}$ to the Lagrangian

$$\mathcal{L} = \mathcal{L}_{\text{SUSY}} + \mathcal{L}_{\text{soft}} \tag{11}$$

where $\mathcal{L}_{\text{SUSY}}$ contains all gauge and Yukawa interactions in a way that preserves the supersymmetry invariance. It can be broken down as

$$\mathcal{L}_{\text{SUSY}} = \mathcal{L}_{\text{chiral}} + \mathcal{L}_{\text{gauge}} + \mathcal{L}_{\text{residual}} \tag{12}$$

where $\mathcal{L}_{\text{chiral}}$ is the chiral supermultiplet Lagrangian, $\mathcal{L}_{\text{gauge}}$ is the gauge supermultiplet Lagrangian, and $\mathcal{L}_{\text{residual}}$ is the residual terms.

The chiral supermultiplet Lagrangian $\mathcal{L}_{\text{chiral}}$ is given as

$$\mathcal{L}_{\text{chiral}} = -\nabla^\mu \phi^{*i} \nabla_\mu \phi_i + i\psi^{\dagger i} \bar{\sigma}^\mu \nabla_\mu \psi_i - \frac{1}{2}\left(W^{ij}\psi_i\psi_j + W^*_{ij}\psi^{\dagger i}\psi^{\dagger j}\right) - W^i W^*_i \tag{13}$$

$$W^{ij} = \frac{\partial^2}{\partial\phi_i \partial\phi_j}W \tag{14}$$

$$W^i = \frac{\partial W}{\partial\phi_i} \tag{15}$$

where ϕ_i is a complex scalar field, and ψ_i is a left-handed two-component Weyl fermion. i runs over all gauge (i.e. colour and weak isospin) and flavour degrees of freedom of chiral supermultiplets. ∇_μ is the covariant derivative. W is the superpotential, defined as

$$W = L^i \phi_i + \frac{1}{2}M^{ij}\phi_i\phi_j + \frac{1}{6}y^{ijk}\phi_i\phi_j\phi_k \tag{16}$$

where M^{ij} is the symmetric mass matrix with a dimension of [mass], and y^{ijk} is the dimension-less Yukawa coupling that is symmetric under the interchange of i, j, k. L^i are parameters with dimensions of [mass]^2 which are allowed only if ϕ_i is a gauge singlet.

Denoting the largest mass scale of the soft terms $\mathcal{L}_{\text{soft}}$ by m_{soft}, the correction to the Higgs scalar squared mass will be of the form

$$\Delta m_H^2 = m_{\text{soft}}^2 \left[\frac{\lambda'}{16\pi^2}\ln(\Lambda_{\text{UV}}/m_{\text{soft}}) + ...\right] \tag{17}$$

where λ' is a schematic variable for various dimensionless couplings, and the "..." stands for terms independent of Λ_{UV} and higher loop corrections. Because the Higgs scalar squared mass should not be unnaturally larger than the electroweak breaking scale, a condition that m_{soft} is not much larger than the TeV scale is derived.

Table 3: Chiral supermultiplets of the MSSM. The spin-0 fields are complex scalars, and the spin-1/2 fields are left-handed two-component Weyl fermions. [17]

Names		spin 0	spin 1/2	$SU(3)_C, SU(2)_L, U(1)_Y$
squarks, quarks	Q	$(\tilde{u}_L \quad \tilde{d}_L)$	$(u_L \quad d_L)$	$\left(\mathbf{3}, \mathbf{2}, \frac{1}{6}\right)$
($\times 3$ families)	$\bar{u}$	$\tilde{u}_R^*$	$u_R^\dagger$	$\left(\bar{\mathbf{3}}, \mathbf{1}, -\frac{2}{3}\right)$
	$\bar{d}$	$\tilde{d}_R^*$	$d_R^\dagger$	$\left(\bar{\mathbf{3}}, \mathbf{1}, \frac{1}{3}\right)$
sleptons, leptons	L	$(\tilde{\nu} \quad \tilde{e}_L)$	$(\nu \quad e_L)$	$\left(\mathbf{1}, \mathbf{2}, -\frac{1}{2}\right)$
($\times 3$ families)	$\bar{e}$	$\tilde{e}_R^*$	$e_R^\dagger$	$(\mathbf{1}, \mathbf{1}, 1)$
Higgs, higgsinos	H_u	$(H_u^+ \quad H_u^0)$	$(\tilde{H}_u^+ \quad \tilde{H}_u^0)$	$\left(\mathbf{1}, \mathbf{2}, +\frac{1}{2}\right)$
	H_d	$(H_d^0 \quad H_d^-)$	$(\tilde{H}_d^0 \quad \tilde{H}_d^-)$	$\left(\mathbf{1}, \mathbf{2}, -\frac{1}{2}\right)$

Table 4: Gauge supermultiplets of the MSSM. [17]

Names	spin 1/2	spin 1	$SU(3)_C, SU(2)_L, U(1)_Y$
gluino, gluon	$\tilde{g}$	g	$(\mathbf{8}, \mathbf{1}, 0)$
winos, W bosons	$\tilde{W}^\pm \quad \tilde{W}^0$	$W^\pm \quad W^0$	$(\mathbf{1}, \mathbf{3}, 0)$
bino, B boson	$\tilde{B}^0$	B^0	$(\mathbf{1}, \mathbf{1}, 0)$

2.2.2 MSSM

The MSSM [17] is the minimal construction of the supersymmetric model. The chiral supermultiplets of the MSSM are given in Table 3. The gauge supermultiplets of the MSSM are given in Table 4. Contrary to the SM, two Higgs doublets (and thus two Higgs chiral supermultiplets) are introduced, with weak hypercharge $Y = 1/2$ and $Y = -1/2$, in order to avoid gauge anomalies. The chiral supermultiplet H_u has the Yukawa couplings to up-type quarks, and H_d has the Yukawa couplings to down-type quarks and charged leptons[4]. The details of MSSM are given in Section 2.2.2.

In the MSSM, the superpotential is given as (with the gauge (i.e. colour and weak isospin) and flavour indices suppressed)

$$W_{\text{MSSM}} = \bar{u}\mathbf{y_u}QH_u - \bar{d}\mathbf{y_d}QH_d - \bar{e}\mathbf{y_e}LH_d + \mu H_u H_d \tag{18}$$

where only the scalar components of the objects $H_u, H_d, Q, L, \bar{u}, \bar{d}, \bar{e}$ are considered. Here, $\mathbf{y_u}, \mathbf{y_d}, \mathbf{y_e}$ are the dimensionless Yukawa couplings in 3×3 matrix in family space. μ is the "μ term" with a dimension of [mass].

The soft supersymmetry breaking terms in the MSSM is given as (with the gauge and flavour indices

---

[4]This can be seen in Eq. (18) for the MSSM. This association of two Higgs doublets to quarks and leptons is necessary because of two reasons: (1) The superpotential, defined in Eq. (16), has to be gauge invariant. (2) The superpotential has to be holomorphic in the complex fields ϕ_i by construction.

suppressed)

$$\mathcal{L}_{\text{soft}}^{\text{MSSM}} = -\frac{1}{2}\left(M_3\tilde{g}\tilde{g} + M_2\tilde{W}\tilde{W} + M_1\tilde{B}\tilde{B} + \text{c.c.}\right)$$
$$- \left(\tilde{\bar{u}}\mathbf{a_u}\tilde{Q}H_u - \tilde{\bar{d}}\mathbf{a_d}\tilde{Q}H_d - \tilde{\bar{e}}\mathbf{a_e}\tilde{L}H_d + \text{c.c.}\right)$$
$$- \tilde{Q}^\dagger\mathbf{m}_Q^2\tilde{Q} - \tilde{L}^\dagger\mathbf{m_L^2}\tilde{L} - \tilde{\bar{u}}\mathbf{m_{\bar{u}}^2}\tilde{\bar{u}}^\dagger - \tilde{\bar{d}}\mathbf{m_{\bar{d}}^2}\tilde{\bar{d}}^\dagger - \tilde{\bar{e}}\mathbf{m_{\bar{e}}^2}\tilde{\bar{e}}^\dagger$$
$$- m_{H_u}^2 H_u^* H_u - m_{H_d}^2 H_d^* H_d - (bH_uH_d + \text{c.c.})$$

$$(19)$$

Here, M_3, M_2, M_1 are the gaugino masses; $m_{H_u}^2$ and $m_{H_d}^2$ are the Higgs squared masses; $\mathbf{m}_Q^2, \mathbf{m_{\bar{u}}^2}, \mathbf{m_{\bar{d}}^2}, \mathbf{m^2_L}, \mathbf{m_{\bar{e}}^2}$ are the squark and slepton masses in 3×3 matrix in family space; $\mathbf{a_u}, \mathbf{a_d}, \mathbf{a_e}$ are the trilinear couplings in complex 3×3 matrix in family space, with dimensions of [mass]; b is the scalar squared-mass parameter.

To suppress flavour-changing and CP-violating effects, the following limit is assumed ("soft supersymmetry-breaking universality hypothesis") at a very high energy scale Q_0 ("input scale"):

$$\mathbf{m_Q^2} = m_Q^2\mathbf{1}, \quad \mathbf{m_{\bar{u}}^2} = m_{\bar{u}}^2\mathbf{1}, \quad \mathbf{m_{\bar{d}}^2} = m_{\bar{d}}^2\mathbf{1}, \quad \mathbf{m_L^2} = m_L^2\mathbf{1}, \quad \mathbf{m_{\bar{e}}^2} = m_{\bar{e}}^2\mathbf{1} \tag{20}$$

$$\mathbf{a_u} = A_t\mathbf{y_u}, \quad \mathbf{a_d} = A_b\mathbf{y_d}, \quad \mathbf{a_e} = A_\tau\mathbf{y_e} \tag{21}$$

$$\text{Im}(M_1), \text{Im}(M_2), \text{Im}(M_3), \text{Im}(A_t), \text{Im}(A_b), \text{Im}(A_\tau) = 0 \tag{22}$$

To suppress baryon number and lepton number violating effects, the conservation of the following symmetry is assumed ("R-parity"):

$$P_R = (-1)^{3(\text{B}-\text{L})+2s} \tag{23}$$

where B is the baryon number, L is the lepton number, and s is the spin. B $= +1/3$ is assigned to the chiral supermultiplets Q_i ($i = 1, 2, 3$), and B $= -1/3$ to $\bar{u}_i$ and $\bar{d}_i$. L $= +1$ is assigned to L_i, and L $= -1$ to $\bar{e}_i$. This definition results in $P_R = +1$ for SM particles and the Higgs bosons, and $P_R = -1$ for sparticles.

When R-parity is exactly conserved, particles and sparticles have no mixing. Every interaction vertex contains an even number of sparticles, and sparticles will be produced in even numbers. The lightest sparticle ("LSP") will be stable; each sparticle will eventually decay into a final state with odd number of LSPs.

The VEV of neutral Higgs fields is defined as

$$v_u = \langle H_u^0 \rangle, \qquad v_d = \langle H_d^0 \rangle \tag{24}$$

Variables v and $\tan\beta$ are defined as

$$v^2 = v_u^2 + v_d^2 \simeq (174 \text{ GeV})^2 \tag{25}$$
$$\tan\beta = v_u/v_d \tag{26}$$

Implications of MSSM

Supersymmetry is knwon to provide scenarios realizing the grand unification, and to provide candidates of dark matter. They are described in this section in the context of the MSSM.

In the MSSM, from the calculation of the two-loop renormalization group equations, the quantities $\alpha = g^2/4\pi$ (where g is the gauge coupling) can unify at a scale $M_U \sim 1.5 \times 10^{16}$ GeV, as seen in Figure 5. This is a strong hint to the grand unified theory at a scale below Planck scale.
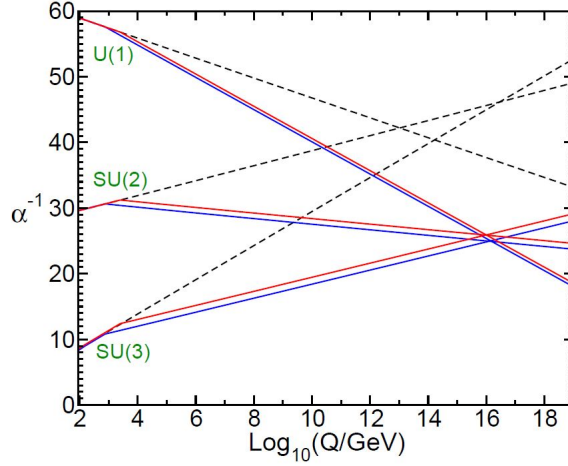
15

Figure 5: Two-loop renormalization group evolution of the inverse gauge couplings, in the SM (dashed line) and the MSSM (solid line) [17]. The normalization for the gauge coupling of $U(1)$ is chosen to agree with the canonical covariant derivative for grand unification in $SU(5)$ or $SU(10)$. Here, Q is the renormalization group scale.

An electrically neutral LSP is an attractive candidate for non-baryonic dark matter. The neutralino (mixed state of neutral higgsino, neutral wino, and bino) interacts only weakly with ordinary matter. The cold dark matter density from cosmological observations is measured as [26]

$$\Omega_{\text{DM}} h^2 \simeq 0.120 \tag{27}$$

Here, $\Omega_{\text{DM}} = \rho_{\text{DM}}/\rho_{\text{crit}}$, where ρ_{DM} is the average mass density of dark matter, and ρ_{crit} is the critical density leading to flat Universe. $h \simeq 0.674$ [26] is the Hubble constant in units of 100 km sec^{-1} Mpc^{-1}. The LSP dark matter may explain the dark matter density $\Omega_{\text{DM}} h^2 \simeq 0.120$ [27, 28].

2.2.3 NMSSM

One of the problems of the MSSM is the "μ problem". In the MSSM, the Z boson mass is given as

$$m_Z^2 = \frac{\left| m_{H_d}^2 - m_{H_u}^2 \right|}{\sqrt{1 - \sin^2 2\beta}} - m_{H_u}^2 - m_{H_d}^2 - 2|\mu|^2 \tag{28}$$

$$\sin 2\beta = \frac{2b}{m_{H_u}^2 + m_{H_d}^2 + 2|\mu|^2} \tag{29}$$

The parameters $b, m_{H_u}^2$, and $m_{H_d}^2$ appear in the soft supersymmetry breaking Lagrangian, and so they are expected to be around or below the order of m_{soft}. As shown in Eq. (17), these terms should not be much larger than the TeV scale. In contrast, μ appears in the supersymmetry invariant Lagrangian, and it does not have a constraint on its mass scale so far. Assuming that unnatural cancellations do not occur between the terms in Eq. (28), a condition that μ should not be much larger than the TeV scale is derived. However, this condition that μ should be many orders of magnitude smaller than the Planck scale is "unnatural". A condition that the conceptually unrelated parameters, μ and m_{soft}, should be roughly of the same order is "unnatural" as well. This μ problem necessitates a mechanism that relates μ to the soft supersymmetry breaking.

16

The NMSSM [18] is one of the solutions to this μ problem. In the NMSSM, a new gauge-singlet chiral supermultiplet is added to the MSSM, where S stands for both the new chiral supermultiplet and its complex scalar component. In the simplest form of the NMSSM ("$\mathbb{Z}_3$-invariant NMSSM"), the superpotential is extended as

$$W_{\text{NMSSM}} = W_{\text{MSSM}} + \lambda S H_u H_d + \frac{1}{3} \kappa S^3 \tag{30}$$

with $\mu = 0$ in W_{MSSM}. Here, λ and κ are dimensionless Yukawa couplings. The soft supersymmetry-breaking Langrangian is extended as

$$\mathcal{L}_{\text{soft}}^{\text{NMSSM}} = \mathcal{L}_{\text{soft}}^{\text{MSSM}} - \left(\lambda A_\lambda S H_u H_d - \frac{1}{3} \kappa A_\kappa S^3 + \text{c.c.} \right) \tag{31}$$

with $b = 0$ in $\mathcal{L}_{\text{soft}}^{\text{MSSM}}$. Here, A_λ and A_κ are the trilinear couplings with dimensions of [mass].

An effective μ term is given as

$$\mu_{\text{eff}} = \lambda v_s \tag{32}$$

where $v_s = \langle S \rangle$ is the VEV of S. The value of μ_{eff} is determined by v_s, which is constrained by the other dimensionless couplings and soft terms (see Eq. (34)). This mechanism relates μ to the soft supersymmetry breaking, thus solving the μ problem in the NMSSM.

The Higgs potential is given as

$$\begin{aligned}
V_{\text{Higgs}} = {} & \left| \lambda \left(H_u^+ H_d^- - H_u^0 H_d^0 \right) + \kappa S^2 \right|^2 + \left(m_{H_u}^2 + |\lambda S|^2 \right) \left(|H_u^0|^2 + |H_u^+|^2 \right) \\
& + \left(m_{H_d}^2 + |\lambda S|^2 \right) \left(|H_d^0|^2 + |H_d^-|^2 \right) + \frac{g_1^2 + g_2^2}{8} \left(|H_u^0|^2 + |H_u^+|^2 - |H_d^0|^2 - |H_d^-|^2 \right)^2 \\
& + \frac{g_2^2}{2} \left| H_u^+ H_d^{0*} + H_u^0 H_d^{-*} \right|^2 + m_S^2 |S|^2 + \left[\lambda A_\lambda \left(H_u^+ H_d^- - H_u^0 H_d^0 \right) S + \frac{1}{3} \kappa A_\kappa S^3 + \text{c.c.} \right]
\end{aligned} \tag{33}$$

where g_1 and g_2 are the $U(1)_Y$ and $SU(2)$ gauge couplings, respectively. From the minimisation conditions, the following conditions for the VEVs are obtained.

$$\begin{aligned}
& v_u \left[m_{H_u}^2 + \mu_{\text{eff}}^2 + \lambda^2 v_d^2 + \frac{g_1^2 + g_2^2}{4} \left(v_u^2 - v_d^2 \right) \right] - v_d \mu_{\text{eff}} (A_\lambda + \kappa v_s) = 0 \\
& v_d \left[m_{H_d}^2 + \mu_{\text{eff}}^2 + \lambda^2 v_u^2 + \frac{g_1^2 + g_2^2}{4} \left(v_d^2 - v_u^2 \right) \right] - v_u \mu_{\text{eff}} (A_\lambda + \kappa v_s) = 0 \\
& v_s \left[m_S^2 + \kappa A_\kappa v_s + 2\kappa^2 v_s^2 + \lambda^2 \left(v_u^2 + v_d^2 \right) - 2\lambda \kappa v_u v_d \right] - \lambda v_u v_d A_\lambda = 0
\end{aligned} \tag{34}$$

Hereafter, μ_{eff} is denoted by μ for simplicity.

NMSSM Higgs sector

Given $m_Z^2 = \frac{1}{2}(g_1^2 + g_2^2)(v_u^2 + v_d^2)$, the NMSSM Higgs sector has six independent parameters. In this thesis, they are chosen to be

$$\lambda, \kappa, A_\lambda, A_\kappa, \tan\beta, \mu \tag{35}$$

The MSSM has three electrically neutral Higgs bosons: two scalar and one pseudoscalar. In contrast, the introduction of a new gauge-singlet complex scalar field in the NMSSM leads to five neutral Higgs

bosons: three scalar and two pseudoscalar. Below, the mass matrices of the neutral Higgs bosons and higgsinos are given, because they are necessary for the discussions in Section 2.3.

The mass matrix of neutral scalar Higgs bosons is given below. Here, the basis is chosen as ($H_{\text{SM}} = \cos\beta H_{dR} + \sin\beta H_{uR}, H_D = -\sin\beta H_{dR} + \cos\beta H_{uR}, H_S = S_R$); the basis of the doublet sector is rotated by an angle β because the upper left 2×2 submatrix will be approximately diagonal (i.e. the lightest scalar will be dominantly H_{SM} and SM-like) in the case of $M_{H_D} \gg v$.

$$M_S^2 = \begin{pmatrix} m_Z^2 \cos^2\beta + \lambda^2 v^2 \sin^2 2\beta & (\lambda^2 v^2 - m_Z^2)\sin 2\beta \cos 2\beta & 2\lambda\mu v \left[1 - \left(\frac{M_A \sin 2\beta}{2\mu}\right)^2\right] \\ (\lambda^2 v^2 - m_Z^2)\sin 2\beta \cos 2\beta & M_{H_D}^2 & -\frac{\lambda v}{2\mu} M_A^2 \sin 2\beta \cos 2\beta \\ 2\lambda\mu v \left[1 - \left(\frac{M_A \sin 2\beta}{2\mu}\right)^2\right] & -\frac{\lambda v}{2\mu} M_A^2 \sin 2\beta \cos 2\beta & M_{H_S}^2 \end{pmatrix} \tag{36}$$

$$M_{H_D}^2 = M_A^2 + (m_Z^2 - \lambda^2 v^2)\sin^2 2\beta \tag{37}$$

$$M_{H_S}^2 = \left(\frac{2\kappa}{\lambda}\mu\right)^2 \left(1 + \frac{\lambda A_\kappa}{4\kappa\mu}\right) - \frac{\kappa\lambda}{2} v^2 \sin 2\beta \left(1 - \frac{\lambda M_A^2}{\kappa\mu^2}\right) \tag{38}$$

$$M_A^2 = \frac{2\mu\left(A_\lambda + \frac{\kappa}{\lambda}\mu\right)}{\sin 2\beta} \tag{39}$$

The mass matrix of pseudoscalar Higgs bosons is given below. Here, the basis is chosen as ($A_D = \cos\beta H_{uI} + \sin\beta H_{dI}, A_S = S_I$); the doublet sector is rotated by an angle β to neglect the massless Goldstone mode.

$$M_P^2 = \begin{pmatrix} M_A^2 & \lambda\left(A_\lambda - \frac{2\kappa}{\lambda}\mu\right)v \\ \lambda\left(A_\lambda - \frac{2\kappa}{\lambda}\mu\right)v & M_{A_S}^2 \end{pmatrix} \tag{40}$$

$$M_{A_S}^2 = \lambda^2\left(A_\lambda + \frac{4\kappa}{\lambda}\mu\right)\frac{v^2 \sin 2\beta}{2\mu} - \frac{3\kappa}{\lambda} A_\kappa \mu \tag{41}$$

These mass matrices lead to five neutral Higgs bosons, namely

$$H_1, H_2, H_3, a, A \tag{42}$$

where H_i ($i = 1, 2, 3$) are the scalar bosons in the order of their masses, and a, A are the pseudoscalar bosons in the order of their masses.

The mass matrix of scalar Higgs bosons M_S^2 in the basis $H_i^{\text{weak}} = (H_{dR}, H_{uR}, S_R)$ is diagonalized by an orthogonal 3×3 matrix S_{ij} which rotates H_i^{weak}, namely

$$H_i = S_{ij} H_j^{\text{weak}} \tag{43}$$

The mass eigenstates of pseudoscalar Higgs bosons are given by a 2×3 matrix P_{ij} in the basis (H_{dI}, H_{uI}, S_I) as

$$\begin{pmatrix} a \\ A \end{pmatrix} = \begin{pmatrix} P_{11} & P_{12} & P_{13} \\ P_{21} & P_{22} & P_{23} \end{pmatrix} \begin{pmatrix} H_{dI} \\ H_{uI} \\ S_I \end{pmatrix} \tag{44}$$

The neutralino mass matrix in the basis $(-i\lambda_1, -i\lambda_2^3, \psi_d^0, \psi_u^0, \psi_S)$ is given as

$$\mathcal{M}_0 = \begin{pmatrix} M_1 & 0 & -\frac{g_1 v_d}{\sqrt{2}} & \frac{g_1 v_u}{\sqrt{2}} & 0 \\ & M_2 & \frac{g_2 v_d}{\sqrt{2}} & -\frac{g_2 v_u}{\sqrt{2}} & 0 \\ & & 0 & \mu & -\lambda v_u \\ & & & 0 & -\lambda v_d \\ & & & & \frac{2\kappa}{\lambda}\mu \end{pmatrix} \tag{45}$$

where λ_1 is the $U(1)_Y$ gaugino, λ_2^i $(i = 1, 2, 3)$ are the $SU(2)$ gauginos, and $\psi_d^0, \psi_u^0, \psi_S$ are the neutral higgsinos.

The charged $SU(2)$ gauginos are $\lambda^- = \frac{1}{\sqrt{2}}(\lambda_2^1 + i\lambda_2^2)$ and $\lambda^+ = \frac{1}{\sqrt{2}}(\lambda_2^1 - i\lambda_2^2)$, and the charged higgsinos are ψ_u^+ and ψ_d^-. Defining $\psi^+ = (-i\lambda^+, \psi_u^+)$ and $\psi^- = (-i\lambda^-, \psi_d^-)$, the mass terms in the Lagrangian is given as

$$\mathcal{L} = -\frac{1}{2}\left(\psi^+, \psi^-\right)\begin{pmatrix} 0 & X^T \\ X & 0 \end{pmatrix}\begin{pmatrix} \psi^+ \\ \psi^- \end{pmatrix} + \text{c.c.}$$

$$X = \begin{pmatrix} M_2 & g_2 v_u \\ g_2 v_d & \mu \end{pmatrix} \tag{46}$$

The 2×2 diagonalization matrices U and V into the mass eigenstates χ^-, χ^+ are given as

$$\chi_i^- = U_{ij}\psi_j^-, \quad \chi_i^+ = V_{ij}\psi_j^+ \tag{47}$$

Considering renormalisation group equations, theoretical constraints on the values of $\tan\beta$ are obtained, that are applicable both to the MSSM and the NMSSM. The relationships between the Yukawa couplings and the quark masses are given as

$$y_t = \frac{m_t}{v \sin\beta}, \quad y_b = \frac{m_b}{v \cos\beta} \tag{48}$$

where y_t, y_b are the Yukawa couplings, and m_t, m_b are the masses of the top and bottom quarks. If $\tan\beta$ is large, y_t may become too large $(\gtrsim \sqrt{4\pi})$ at the grand unification scale, resulting in a Landau singularity; this imposes an approximate lower bound of $\tan\beta \gtrsim 1$. Similarly, considering y_b, an upper bound of $\tan\beta \lesssim 80$ is obtained.

The Higgs sector of the NMSSM is constrained by direct searches for new Higgs bosons, as well as the measurements of the 125 GeV Higgs boson, that are performed by the ATLAS and CMS experiments. The summary of the constraints, interpreted in the hMSSM scenario [29], is shown in Figure 6. The hMSSM scenario is a MSSM scenario in which the lightest scalar Higgs boson is constrained to 125 GeV, thus constraining the dominant radiative corrections of the Higgs sector and approximately reducing the number of free parameters. The constraints in Figure 6 can be naively applied to the NMSSM, leading to an approximate constraint of $M_A \gtrsim 500$ GeV and $\tan\beta \lesssim 10$–80. However, it must be noted that the constraints in the hMSSM scenario are not directly applicable to the NMSSM. This is because, due to the introduction of an additional gauge-singlet field S that lead to two new mass eigenstates, the Higgs sector of the NMSSM is more complicated compared to the MSSM. It is necessary for the constraints from the past researches to be considered quantitatively by numerical calculations.
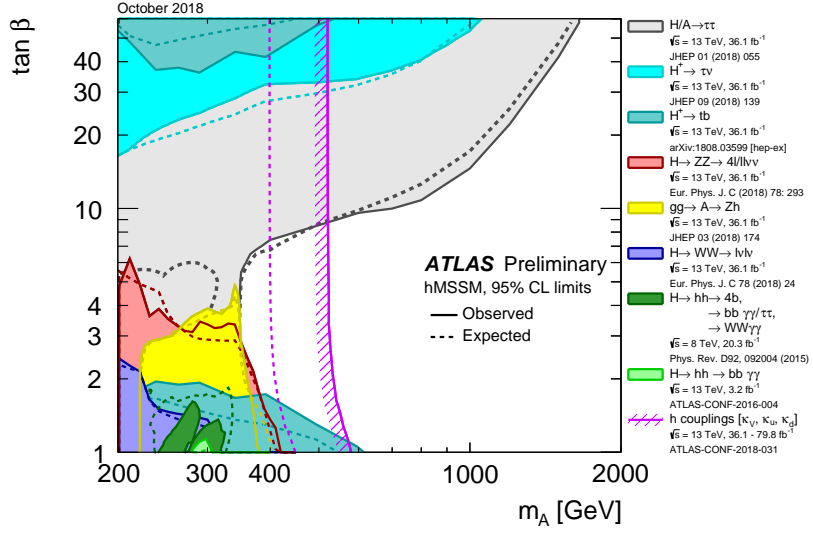
Figure 6: Regions of the (M_A, $\tan\beta$) plane in the hMSSM model that are excluded by direct searches for BSM Higgs and the measurements of SM Higgs cross section, at 95% CL. [30]
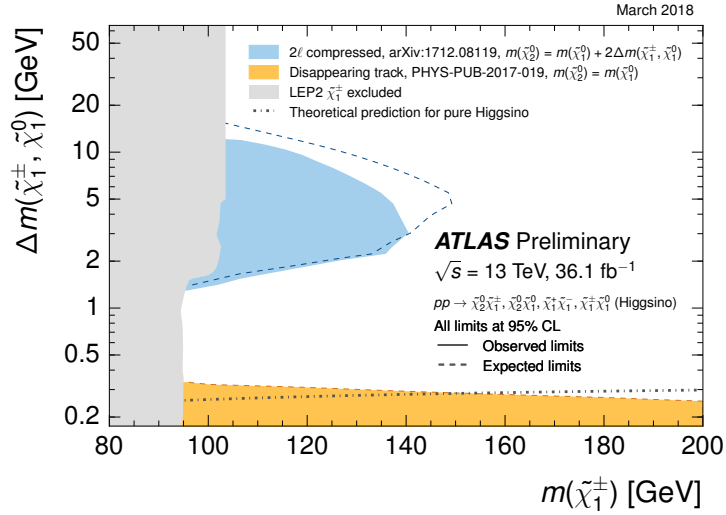

Figure 7: Exclusion of the $\tilde{\chi}_1^0$ and $\tilde{\chi}_1^\pm$ masses at 95% CL for the higgsino pair production with SM-boson-mediated decays. [31]

The value of μ is constrained from searches for higgsino pair production by collider experiments (ATLAS and LEP), as shown in Figure 7. An approximate limit of $\mu \gtrsim 100$ GeV is obtained, because the chargino mass has a strong dependence on μ as seen in Eq. (46).

Other four parameters of the NMSSM Higgs sector, i.e. the dimensionless coupling constants λ, κ and the trilinear coupling constants A_λ, A_κ, are weakly constrained from past researches. A subset of the region of these four parameters can be probed by the search described in this thesis, as described in the next section.

2.3 Photon-jets from NMSSM

In the NMSSM, the decay of a heavy scalar Higgs boson (either H_2 or H_3, collectively denoted by H) decaying into aa pair can result in a pair of photon-jets [10, 11]. The process of H produced by gluon–gluon fusion process ($gg \rightarrow H$) and decaying via $H \rightarrow aa \rightarrow 4\gamma$ is schematically shown in Figure 8. This section describes the parameter space of the NMSSM in which a heavy scalar Higgs boson may decay into a pair of photon-jets.

2.3.1 Light state a

When the state a is mostly singlet-like (i.e. $a \simeq S_I$), this state can be light ($m_a = O(1)$ GeV). From Eq. (41), $m_a = O(1)$ GeV corresponds to $A_\kappa \lesssim O(1)$ GeV.

A light ($m_a \lesssim O(1)$ GeV) a naturally arise in the "R-symmetry limit" $\lambda A_\lambda, \kappa A_\kappa \rightarrow 0$ [32]. The R-symmetry is a global $U(1)_R$ symmetry that exists in several well-motivated supersymmetry breaking models called the O'Raifeartaigh models [33]. The R-symmetry is spontaneously broken by the VEVs v_u, v_d, v_s and explicitly broken by the gaugino mass terms, leading to the existence of an ALP ("R-axion"). In the R-symmetry limit $\lambda A_\lambda, \kappa A_\kappa \rightarrow 0$, the pseudoscalar Higgs boson a becomes the R-axion.

The pseudoscalar singlet field does not have couplings to SM fermions in the Lagrangian. The pseudoscalar a has couplings to SM fermions from its doublet component ($A_D = \cos\beta H_{uI} + \sin\beta H_{dI}$). Naively thinking,
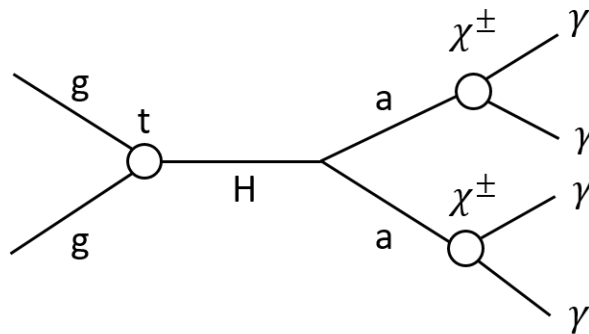

Figure 8: A schematic diagram of a heavy Higgs boson decaying via $H \rightarrow aa \rightarrow 4\gamma$. H is produced via the gluon–gluon fusion process, i.e. via a loop of quarks (mainly top quark). a decays into a pair of photons via a loop of charged higgsinos.
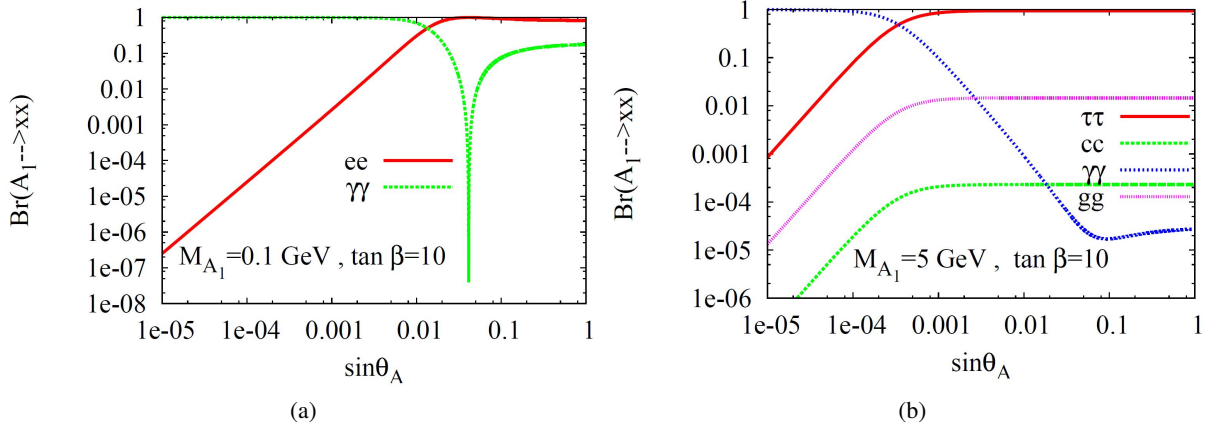
Figure 9: The branching ratios of the light pseudoscalar Higgs boson a as a function of the mixing angle θ_A. The parameters assumed here are $\tan\beta = 10$, $\lambda = 1$, $\mu = 150$ GeV, and $M_2 = 500$ GeV. They are presented for the cases (a) $m_a = 0.1$ GeV and (b) $m_a = 5$ GeV. [34]

a decays dominantly to a pair of SM fermions or gluons. There are two possibilities for the pseudoscalar a to have a sizeable $\mathcal{B}(a \to \gamma\gamma)$ (e.g. more than 30%), as explained below.

Case 1: Decoupling limit

$\mathcal{B}(a \to \gamma\gamma)$ can be large when a is a nearly pure singlet state ("decoupling limit"). In such a case, the branching ratio of a into a pair of SM fermions or gluons will be considerably small; a decays dominantly into $\gamma\gamma$ via a loop of charged higgsinos [34]. The mixing angle θ_A is defined by

$$\begin{pmatrix} a \\ A \end{pmatrix} = \begin{pmatrix} \cos\theta_A & -\sin\theta_A \\ \sin\theta_A & \cos\theta_A \end{pmatrix} \begin{pmatrix} S_I \\ \cos\beta \cdot H_{uI} + \sin\beta \cdot H_{dI} \end{pmatrix} \tag{49}$$

Figure 9 shows the typical case of the relationship between the mixing angle θ_A and the branching ratios of a. The mass matrix of pseudoscalar Higgs bosons is given in Eq. (40). At tree level, the decoupling limit of the pseudoscalar Higgs bosons is achieved with the following condition:

$$\tan 2\theta_A = \frac{2\lambda \left(A_\lambda - \frac{2\kappa}{\lambda}\mu \right) v}{M_A^2 - M_{A_S}^2} \ll 1 \tag{50}$$

In the decoupling limit, it is possible for a to be "long lived", i.e. decaying outside of the beam pipe at the ATLAS detector, because of its small decay width. The partial decay width is given as [35]

$$\Gamma(a \to \gamma\gamma) = \frac{G_F \alpha_{em}^2 m_a^3}{32\sqrt{2}\pi^3} \left| \sum_f N_c e_f^2 g_f^a A_f(\tau_f) + \sum_{\tilde{\chi}_i^\pm} g_{\tilde{\chi}_i^\pm}^a A_{\tilde{\chi}_i^\pm} \left(\tau_{\tilde{\chi}_i^\pm} \right) \right|^2 \tag{51}$$

$$A_x(\tau_x) = \tau_x \left(\sin^{-1} \frac{1}{\sqrt{\tau_x}} \right)^2 \tag{52}$$

$$\tau_x = \frac{4m_x^2}{m_a^2} \qquad (x = f, \tilde{\chi}_i^\pm) \tag{53}$$

Here, N_c is the QCD color factor, e_f is the electric charge of the fermions, and g_x^a is the couplings of a with the fermions. The coupling constant is given as

$$g_{\tilde{\chi}_i^\dagger \tilde{\chi}_j^\mp A_1} = \frac{i}{\sqrt{2}} \left[\lambda P_{13} U_{i2} V_{j2} - g_2 \left(P_{12} U_{i1} V_{j2} + P_{11} U_{i2} V_{j1} \right) \right] \tag{54}$$

In the decoupling limit, $g_f^a = 0$, $P_{13} = 1$, and $P_{12} = P_{11} = 0$. Thus, the partial decay width is typically $\Gamma(a \to \gamma\gamma) \sim O(1)$ meV for $\lambda = O(0.01)$, $m_a = O(1)$ GeV, $m_{\tilde{\chi}_i^\pm} = O(100)$ GeV. In the decoupling limit, the decay width of a is approximately equal to the partial decay width to photons, i.e. $\Gamma_a \simeq \Gamma(a \to \gamma\gamma)$. For $m_H = O(100)$ GeV and $m_a = O(1)$ GeV, the Lorentz factor of a is $\gamma_a = O(100)$. This leads to an average decay length at the lab frame of $l = \gamma_a \beta_a c / \Gamma_a \simeq \gamma_a \beta_a c / \Gamma(a \to \gamma\gamma) \simeq O(1)$ cm. Here, β_a is the ratio of the velocity of the a and the speed of light. Thus, in the decoupling limit, it is possible for a to be long lived.

An upper limit on the BSM decay branching ratio of 125 GeV Higgs is $\sim 20\%$ at 95% confidence level (CL), evaluated by performing global fits to experimental results from Tevatron and LHC Run 1 [36]. With this taken into consideration, a limit of roughly $\theta_A \lesssim 1\%$ is placed when $m_a < \frac{125}{2}$ GeV (i.e. the decay $h \to aa$ is kinematically allowed) [37]. This experimental limit can be mitigated when taking the decoupling limit, i.e. $\theta_A \to 0$. However, in the decoupling limit $P_{13} = 1$ and $P_{11} = P_{12} = 0$, the triple Higgs coupling for H_1 and a is given as

$$g_{H_1 aa} \simeq \frac{\lambda^2}{\sqrt{2}} (v_d S_{11} + v_u S_{12}) + \frac{\lambda \kappa}{\sqrt{2}} (v_d S_{12} + v_u S_{11}) + \left(\frac{\sqrt{2} \kappa^2}{\lambda} \mu - \frac{\kappa A_\kappa}{\sqrt{2}} \right) S_{13} \tag{55}$$

This places a limit of $\lambda \lesssim O(0.1)$ [37].

Experimental constraints on ALPs need to be considered. The constraints from past observations on the ALP-photon coupling is shown in Figure 2. For the case of the decoupling limit in Case 1, the value of the effective coeffcient is typically $|C_{\gamma\gamma}^{\text{eff}}|/\Lambda = O(0.01)\,\text{TeV}^{-1}$ for $\Gamma(a \to \gamma\gamma) = O(1)$ meV and $m_a = O(1)\,\text{GeV}$. This is smaller by two orders of magnitude than the upper limit, i.e. $|C_{\gamma\gamma}^{\text{eff}}|/\Lambda < O(1)\,\text{TeV}^{-1}$, for $m_a = O(1)$ GeV. Thus, in the decoupling limit mentioned above, the limit from ALPs searches are mitigated.

Case 2: Mixing with pseudoscalar meson, or dimuon loop

$\mathcal{B}(a \to \gamma\gamma)$ can be large when m_a is within a limited region, namely near the masses of either a neutral pion, two muons, or an eta meson [10, 11, 38]. The branching ratios of a for a typical case is shown in Figure 10. When m_a is close to a mass of a neutral pion, it can have a large mixing with a neutral pion and then decay via $a \to \gamma\gamma$. When m_a is close to a mass of an eta meson, it can have a large mixing with an eta meson and then decay via $a \to \gamma\gamma$ and $a \to 3\pi^0 \to 6\gamma$. When m_a is right below the dimuon threshold, a decays via $a \to \gamma\gamma$ by a muon loop. As seen in Figure 10, the value of m_a has to be in close proximity to these values for large $\mathcal{B}(a \to \gamma\gamma)$, e.g. within $O(100)$ MeV for $\mathcal{B}(a \to \gamma\gamma) > 30\%$. This scenario is out of scope of this thesis, and it is not discussed further in this thesis.

2.3.2 Heavy state H

For the process $gg \to H \to aa$ to have a sizeable (e.g. around the order of $O(1$ fb)) cross section in $\sqrt{s} = 13$ TeV pp collisions, the state H has to be a mixed state of both the doublet ($H_D = -\sin\beta H_{dR} + \cos\beta H_{uR}$) and singlet ($H_S = S_R$) components. This is explained by the following reasons. The scalar singlet field
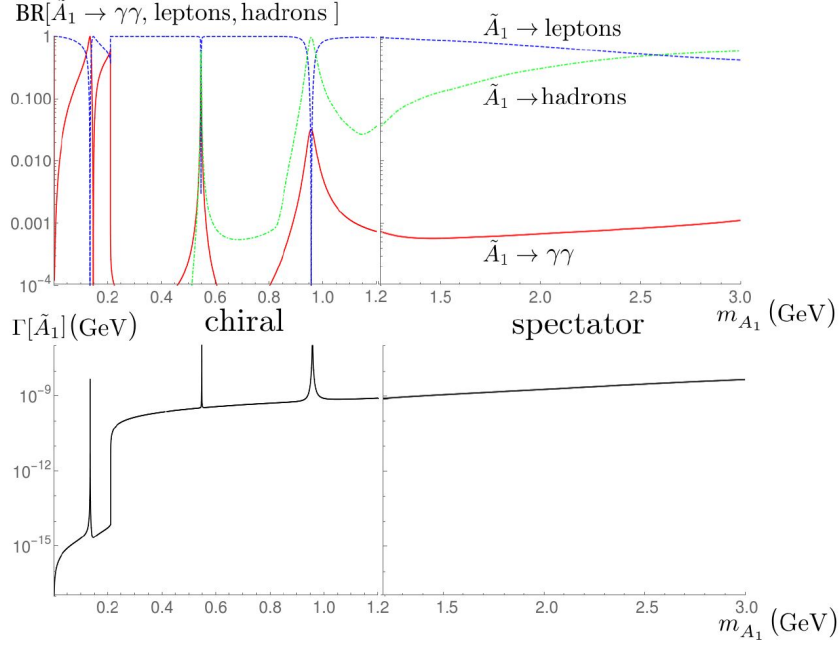
Figure 10: The decay branching ratios of a (denoted by A_1) in the NMSSM for $\sin\theta_A = 0.03$ and $\tan\beta = 10$. [38]

does not have couplings to SM fermions in the Lagrangian. Thus, the state H has to have a large contribution of the doublet component in order to have a sizeable coupling to the top quark. However, a doublet-like H decays dominantly into SM fermions. This is because of its weak coupling to a, i.e. $\Gamma(H_D \to t\bar{t}, b\bar{b}) \gg \Gamma(H_D \to aa)$. In contrast, the coupling of a singlet-like H to aa can be large, i.e. $\Gamma(H_S \to aa) \sim \Gamma(H_D \to t\bar{t}, b\bar{b})$. Thus, $gg \to H \to aa$ has a sizeable cross section when H is a mixed state of both the singlet and doublet components.

A large mixture of singlet and doublet components for H is realized when $M_{H_D} \sim M_{H_S}$, as shown in Eq. (36). From Eqs. (37) and (38), this leads to $M_A \sim \frac{2\kappa}{\lambda}\mu$, with an assumption that A_κ is small ($A_\kappa < O(1)$ GeV) and $\tan\beta = O(1)$. Considering the definition of M_A as given in Eq. (39), these assumptions lead to:

$$A_\lambda + \frac{\kappa}{\lambda}\mu \sim \frac{2\kappa^2 \sin 2\beta}{\lambda^2}\mu \qquad (56)$$

In conclusion, the search described in this thesis can probe the parameter space of the NMSSM Higgs sector, i.e. $(\tan\beta, \mu, \lambda, \kappa, A_\lambda, A_\kappa)$, that satisfy the relationships in Eqs. (50) and (56).

24

3 ATLAS detector at the LHC

3.1 Large Hadron Collider

The LHC [39] is an energy-frontier experiment that enables direct searches for new physics at the TeV scale. It is a hadron collider with superconducting magnets installed in two parallel beamlines. It is placed in a tunnel with 27 km circumference and a depth of down to 175 m. Its design is to collide proton beams at $\sqrt{s}$ = 14 TeV and an instantaneous luminosity of 10^{34} cm^{-2}s^{-1}, and also to collide heavy ions (e.g. Pb). It is designed to accelerate 2808 beam bunches with 10^{11} protons per bunch. 1232 dipole magnets are installed that operate with 8 T magnetic field. Seven detectors are installed at four crossing points, including the two general-purpose ATLAS [40] and CMS [41] detectors.

During the operation from 2009 to early 2013 ("Run 1"), the LHC performed pp collisions at $\sqrt{s}$ = 7, 8 TeV; the dataset that the ATLAS detector recorded corresponds to 5 fb^{-1} for $\sqrt{s}$ = 7 TeV and 20 fb^{-1} for $\sqrt{s}$ = 8 TeV after applying data-quality requirements. During the operation from 2015 to 2018 ("Run 2"), the LHC performed pp collisions at $\sqrt{s}$ = 13 TeV; the dataset that the ATLAS detector recorded corresponds to 140 fb^{-1} after applying data-quality requirements.

Before being injected to the LHC, the proton beams are accelerated with a series of accelerators, as shown in Figure 11. The initial proton beam at 50 MeV is generated with the LINAC 2; it is accelerated to 1.4 GeV with the Proton Synchrotron Booster; it is accelerated to 26 GeV with the Proton Synchrotron; it is accelerated to 450 GeV with the Super Proton Synchrotron, then injected into the LHC main ring.
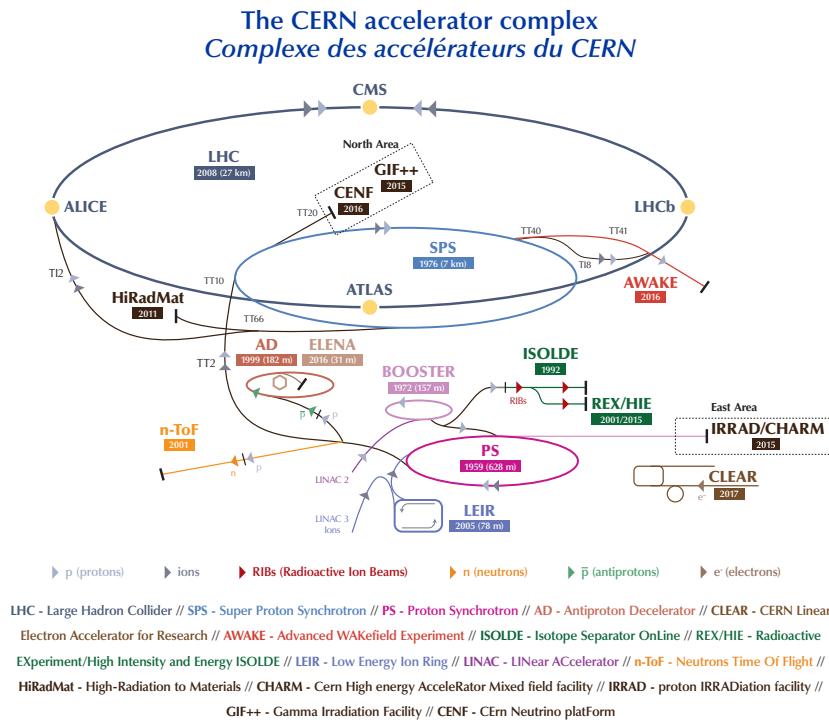

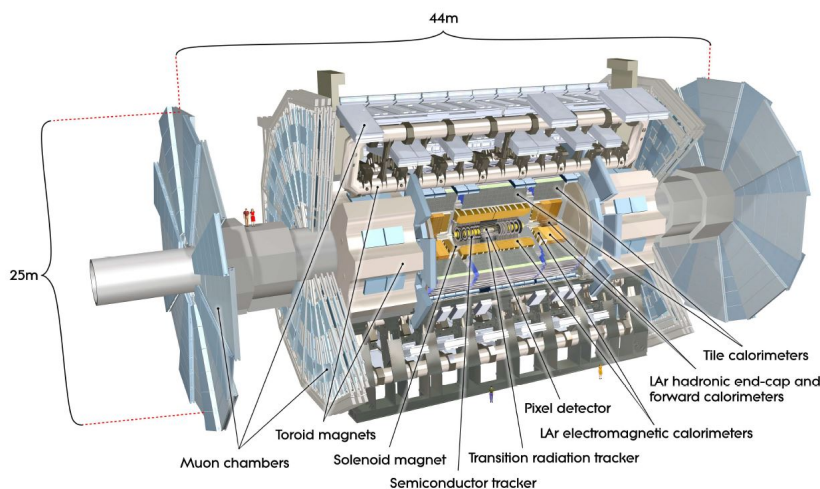Figure 11: A schematic diagram of the accelerator complex at CERN including the LHC. [42]

Figure 12: Schematic diagram of the ATLAS detector. [40]

3.2 ATLAS detector

The ATLAS (A Toroidal LHC ApparatuS) detector[40] is a general-purpose detector with a forward–backward symmetric cylindrical geometry, as shown in Figure 12. The detector covers nearly the entire solid angle around the collision point. The detector is 25 m in height and 44 m in length, and has an overall weight of approximately 7000 tones. The inner tracking detector is surrounded by a 2 T thin superconducting solenoid magnet. The calorimeter system comprises EM and hadronic calorimeters, and it is placed outside of the solenoid magnet. The muon spectrometer is covered by the three large air-core superconducting toroid magnets (one barrel and two end-caps).

ATLAS uses a right-handed coordinate system with its origin at the nominal interaction point in the centre of the detector. The z axis is defined as the beam direction. The x axis is defined as pointing from the interaction point to the centre of the LHC ring. The y axis is defined as pointing upwards. The azimuthal angle ϕ is defined around the beam axis. The polar angle θ is defined as the angle with respect to the beam axis. These angles are defined in radians. The pseudorapidity η is defined as $\eta = -\ln\tan(\theta/2)$. Angular distance is measured in units of $\Delta R = \sqrt{(\Delta\eta)^2 + (\Delta\phi)^2}$[5]. The transverse momentum p_T and the transverse energy E_T are defined in the x–y plane[6].

3.2.1 Inner Detector

The inner tracking system (Inner Detector) is composed of the Pixel detector, the Semiconductor Tracker (SCT), and the Transition Radiation Tracker (TRT), as shown in Figure 13. The system is immersed in a 2 T axial magnetic field generated by the central solenoid magnet. The system provides charged-particle tracking in the range $|\eta| < 2.5$.

The Pixel detector and the SCT cover the region $|\eta| < 2.5$. The Pixel detector uses pixel-shaped oxygen-enriched n-in-n silicon semiconductor as its sensors. They are located on concentric cylinders around the

---

[5]Note that by this definition, ΔR is Lorentz invariant for a massless particle.

[6]The use of transverse momentum is convenient for hadron collider experiments, because those of the final state particles arising from a parton–parton collision add up to zero, whereas the longitudinal components will not.
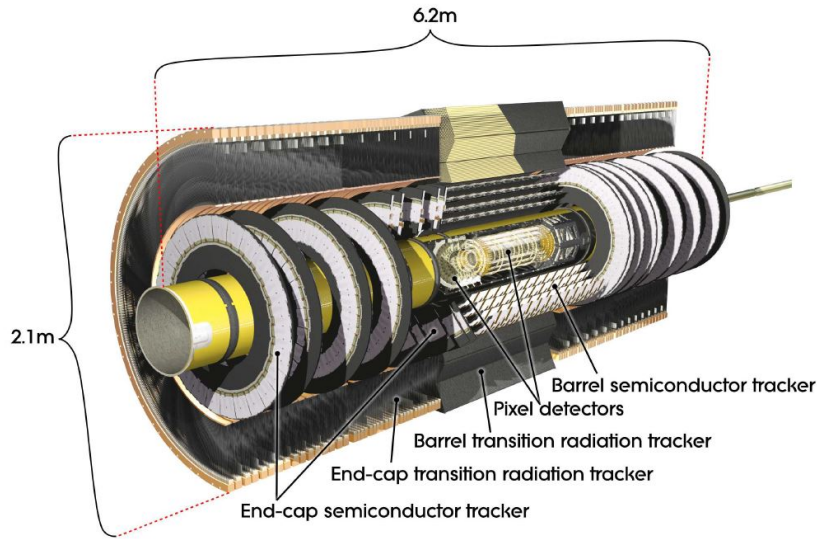
26

Figure 13: Schematic diagram of the inner detector. [40]

beam axis in the barrel region, and on disks perpendicular to the beam axis in the end-cap regions. The innermost barrel layer of the Pixel detector, the insertable B-layer (IBL) [43], was installed between Run 1 and Run 2. The Pixel detector has four cylinder layers in the barrel at a radius of 31–123 mm, and three disk layers in the end-cap. The Pixel detector typically provides four measurements per track. The size of the pixel sensors is $50 \times 250 \ \mu m^2$ in the IBL and $50 \times 400 \ \mu m^2$ minimum in the other layers. The intrinsic accuracy in the barrel (end-cap) region is 4 μm in the $R - \phi$ direction and 115 μm in the z (R) direction.

The SCT uses microstrip-shaped single-sided p-on-n silicon semiconductor as its sensors. The SCT typically provides four two-dimensional measurement points per track using eight strip layers. The strips have 40 mrad stereo angle and a pitch of 80 μm. The intrinsic accuracy per module in the barrel (end-cap) region is 17 μm in the $R - \phi$ direction and 580 μm in the z (R) direction.

The TRT is a gaseous detector composed of 4 mm-diameter straw tubes confined with xenon-based active gas. A gold-plated tungsten wire of 31 μm diameter is placed in the centre of each tube and acts as the anode to collect ionized secondary electrons. The spaces between the straws are filled with polypropylene fibres in the barrel region, and polypropylene foils in the end-cap region, to create transition radiation. The transition radiation is useful for particle identification, especially the separation of electrons and charged pions, because the energy of the transition radiation is proportional to the Lorentz factor $\gamma = E/m$ of the particle. The TRT provides radially extended track reconstruction up to $|\eta| = 2.0$. It provides $R - \phi$ information with an intrinsic accuracy of 130 μm per straw tubes. It also provides electron identification information based on the fraction of hits (typically 30 in total) above a higher energy-deposit threshold corresponding to transition radiation.

The cumulative amount of material in the Inner Detector is shown in Figure 14. Here, X_0 is the radiation length.
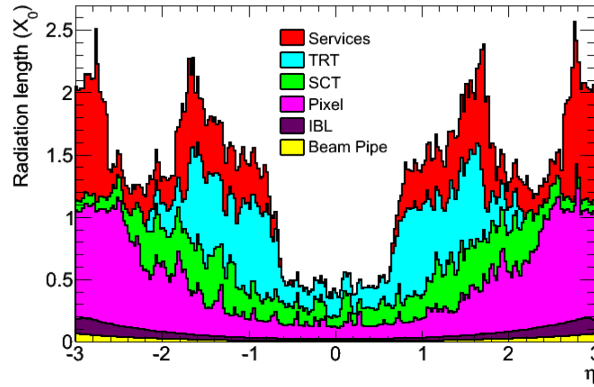
Figure 14: The cumulative amount of material in the Inner Detector, including the services and thermal enclosures, in units of X_0 and as a function of $|\eta|$. [43]
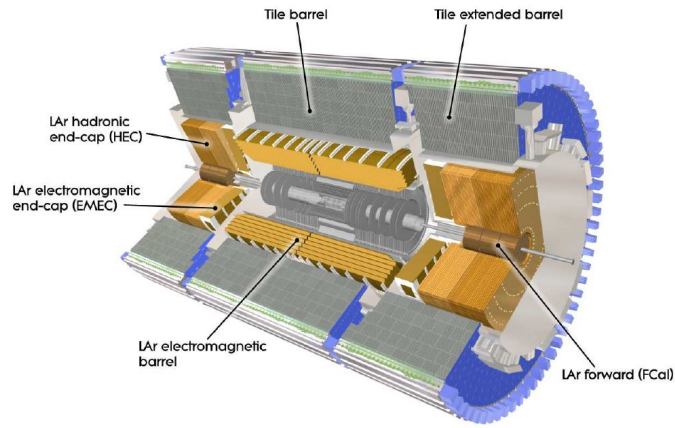

Figure 15: Schematic diagram of the calorimeter system. [40]

3.2.2 Calorimeter

The calorimeter system is composed of the EM calorimeter and the hadronic calorimeters that use different technologies, as shown in Figure 15. The calorimeter system covers the range $|\eta| < 4.9$.

EM calorimeter

The EM calorimeter is described in detail below, because it is the most important component for the search described in this thesis.

The EM calorimeter is a sampling calorimeter with lead absorbers and liquid argon (LAr) active medium. It has kapton electrodes with accordion shape, which provides complete ϕ symmetry without cracks. The Molière radius of the EM calorimeter is approximately 1.6 cm. The EM calorimeter is divided into the barrel section covering $|\eta| < 1.475$ and the two end-cap sections covering $1.375 < |\eta| < 3.2$. The end-cap is further divided into the outer wheel region $1.375 < |\eta| < 2.5$ and the inner wheel region $2.5 < |\eta| < 3.2$.
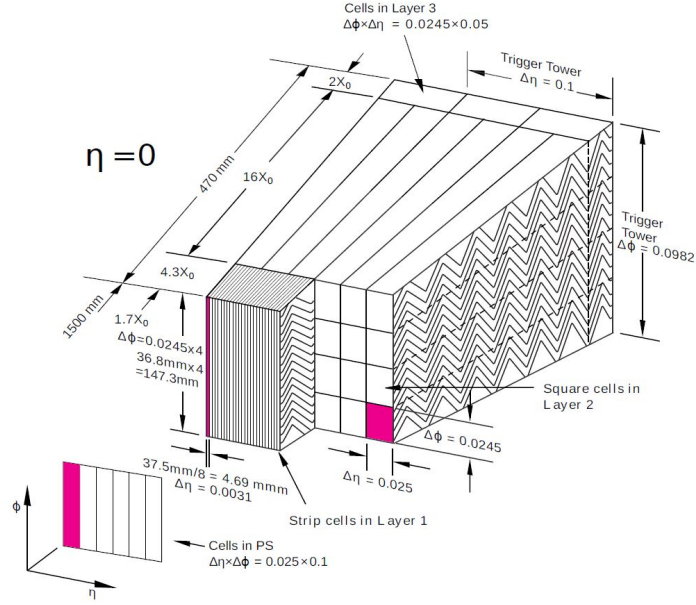
Figure 16: Schematic diagram of the EM calorimeter at $\eta = 0$. [44]

For $|\eta| < 2.5$ (i.e. the barrel and outer wheel regions), the EM calorimeter is composed of three sampling layers in the longitudinal direction of shower depth, as shown in Figure 16. The thicknesses of the first, second, and third layers at $\eta = 0$ are 4.3 X_0, 16 X_0, and 2 X_0, respectively. The thicknesses vary with the $|\eta|$ range, as shown in Figure 17. The first layer is segmented into high-granularity strips in the η direction, with a typical cell size of $\Delta\eta \times \Delta\phi = 0.003 \times 0.1$ for the ranges $|\eta| < 1.4$ and $1.5 < |\eta| < 2.4$, and a coarser cell size of $\Delta\eta \times \Delta\phi = 0.025 \times 0.1$ for other regions. The second layer has a cell size of $\Delta\eta \times \Delta\phi = 0.025 \times 0.025$. This layer collects most of the energy deposited in the calorimeter by photon and electron showers. The third layer is used to correct for energy leakage beyond the EM calorimeter from high-energy showers. Placed in front of these layers, an additional thin LAr presampler layer covering $|\eta| < 1.8$ is used to correct for energy loss in material upstream of the calorimeters. As described above, the first sampling layer has a fine granularity in η; this allows the identification of events with two overlapping showers originating from the decays of neutral hadrons in hadronic jets, mostly $\pi^0 \rightarrow \gamma\gamma$ decays. This is shown in Figure 18.

For $2.5 < |\eta| < 3.2$ (i.e. the end-cap inner wheel region), the EM calorimeter is segmented in two sections in the longitudinal direction, and has a coarser lateral granularity.

The design goal of the energy resolution is $\sigma_E/E = 10\%/\sqrt{E} \oplus 0.7\%$ (where E is in units of GeV), with similar results obtained from measurements using electron test beams and pp collisions.

Hadronic calorimeters

Hadronic calorimeter system is composed of the Tile calorimeter, the Hadronic End-cap Calorimeter, (HEC) and the Forward Calorimeter (FCal).

The Tile calorimeter is a sampling calorimeter with steel absorbers and plastic scintillating tiles as the sampling medium. The scintillating tiles are read out through wavelength shifting fibres and photomultiplier tubes. It is composed of the barrel region covering $|\eta| < 1.0$ and the extended barrel region
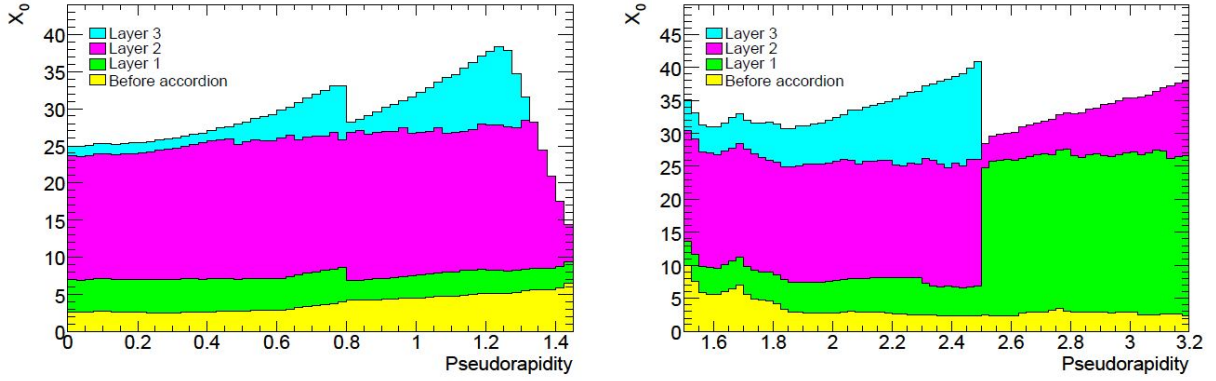
Figure 17: The cumulative amount of material in the EM calorimeter, and also in front of the first layer, in units of X_0 as a function of $|\eta|$. [40]
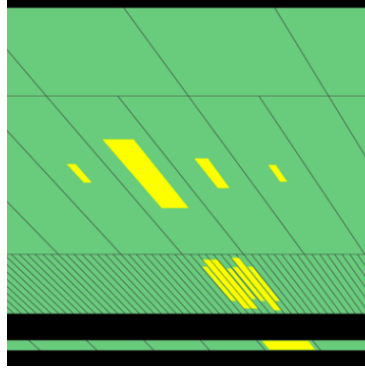

Figure 18: An event display of a candidate event of a neutral pion decaying into two photons. It is shown in the $R - z$ plane, with the yellow boxes indicating the size of the recorded energy in each cell. The four layers each correspond to the presampler, first, second, and third layers of the EM calorimeter, from bottom to top. [45]

$0.8 < |\eta| < 1.7$. They are segmented in depth into three layers, with the thicknesses of approximately 1.5 interaction lengths (λ), 4.1 λ, and 1.8 λ respectively for the barrel region. The thicknesses are 1.5 λ, 2.6 λ, and 3.3 λ respectively for the extended barrel region.

The HEC is a sampling calorimeter with copper absorbers and LAr active medium. It covers the region $1.5 < |\eta| < 3.2$. It is composed of four layers.

The FCal is divided into three modules in depth. The first module is a sampling calorimeter with copper absorbers and LAr active medium that is optimized for EM measurements. The second and third modules are sampling calorimeters with tungsten absorbers and LAr active medium that are optimized for hadronic measurements. The total depth of the modules is approximately 10 λ.

3.2.3 Muon spectrometer

The magnetic bending is provided by the barrel toroid in the range $|\eta| < 1.4$, and by the two end-cap toroids in the range $1.6 < |\eta| < 2.7$. In the transition region $1.4 < |\eta| < 1.6$, the magnetic bending is provided by the combination of the barrel and end-cap toroids. The three toroids are each consisted
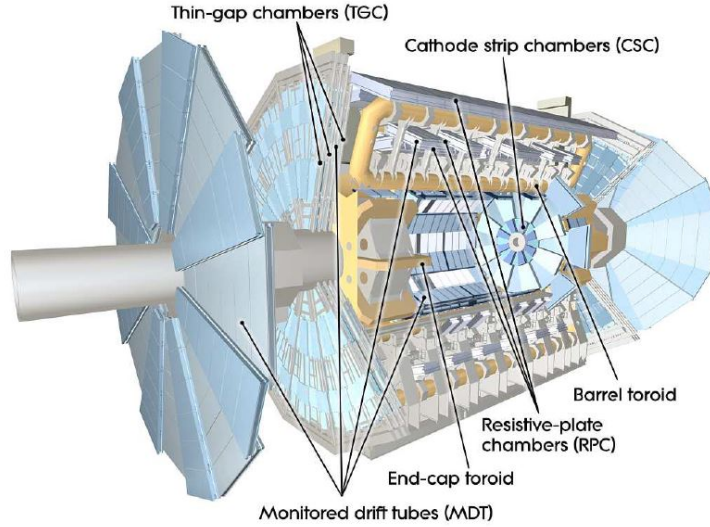
Figure 19: Schematic diagram of the muon spectrometer. [40]

of eight coils, assembled radially and symmetrically around the beam axis, to provide a magnetic field in the azimuthal direction. The field integral of the magnetic field perpendicular to the trajectory of an infinite-momentum muon (i.e. straight trajectory) is in the range 1.5–5.5 Tm for $|\eta| < 1.4$, and in the range 1–7.5 Tm for $1.6 < |\eta| < 2.7$.

The muon spectrometer is composed of four different detectors, as shown in Figure 19. The Monitored Drift Tube (MDT) is a gaseous drift chamber filled with a mixed gas of Ar (93%) and CO_2 (7%), and provides a precise measurement of the muon track coordinates in the bending direction. The relative position and deformations of the MDT chambers are monitored by precise alignment sensors based on optical monitoring. The Cathode Strip Chamber (CSC) is a multiwire proportional chamber filled with a mixed gas of Ar (80%) and CO_2 (20%) and uses strip-shaped cathodes. It is installed in the region $2 < |\eta| < 2.7$ to withstand the high rate. The trigger chambers consist of the Resistive Plate Chamber (RPC) in the barrel region and the Thin Gap Chamber (TGC) in the end-cap region. The RPC is a gaseous detector filled with a mixed gas (mainly $C_2H_2F_4$). The TGC is a multi-wire proportional chamber filled with a mixed gas of CO_2 and n-pentan, and has small distances between the anode wires and the read-out cathode strips of 1.4 mm. These trigger chambers provide the bunch-crossing identification and muon track coordinates orthogonal to those of the MDT and CSC.

3.2.4 Luminosity detector

LUCID-2 (Luminosity Cherenkov Integrating Detector) [46] measures the luminosity delivered to the ATLAS detector. It is placed in the forward region at ±17 m from the interaction point, and it measures the inelastic pp scattering. It uses quartz as the Cherenkov radiation medium, and measures the radiated light with photomultiplier tubes. It was installed between Run 1 and Run 2 to replace the previous LUCID, to cope with the increase in energy of the proton beams and the higher luminosity.

The measurement of the instantaneous luminosity relies on the detection of the pp inelastic scattering. The measurement is performed with several methods, and the "hit-counting" method using LUCID-2 is

described below. The "visible number of interactions" μ^{vis} is defined as the product of the efficiency of the measurement method, detector acceptance, and the number of interactions μ. Using the 8 PMTs (4 on $+z$ side and 4 on $-z$ side), μ^{vis} is evaluated from a logarithmic formula based on $N_{\mathrm{HIT}}/N_{\mathrm{PMT}}$, where N_{HIT} is the number of hits per bunch crossing, and N_{PMT} is the number of PMTs. The logarithmic formula is based on an assumption that the number of interactions follow a Poissonian distribution (e.g. assuming that the probability to observe no hit in a PMT is $e^{-\mu \varepsilon_{\mathrm{PMT}}}$, where $\varepsilon_{\mathrm{PMT}}$ is the efficiency times acceptance to observe a hit in a PMT). The number of hits N_{HIT} is averaged over a time of roughly one minute, and it is measured separately for each of the 3564 bunch slots in the LHC orbit. This "hit-counting" method was used in 2016, since it can measure a high number of interactions of up to $\mu < 172$ [46].

The calibration of the luminosity scale was performed in August 2015 and May 2016, using x–y beam-separation scans ("van der Meer scans"). It is performed using the following equation:

$$\mathcal{L} = \frac{f_{\mathrm{LHC}} n_1 n_2}{2\pi \Sigma_x \Sigma_y}$$

where $\mathcal{L}$ is the instantaneous luminosity, f_{LHC} is the LHC revolution frequency, Σ_x and Σ_y are the convoluted beam sizes obtained from the scan width of the van der Meer scans. n_1 and n_2 are the beam bunch populations obtained from the measurement of the beam bunch current. Additionally, the response of the LUCID-2 has a slight dependence on the number of beam bunches in a train, due to e.g. reflection of signal pulses in the read-out chain that affect neighbouring bunches. This dependence is corrected by a comparison with the number of reconstructed tracks in the Inner Detector; this correction is called the "calibration transfer".

The uncertainty of the combined 2015+2016 integrated luminosity is evaluated as 2.1%. This is derived following a method similar to that detailed in Ref. [47]. The main contribution ($\sim 1.6\%$) is due to the evaluation uncertainty of the calibration transfer. This uncertainty is estimated by reevaluating the calibration transfer using the Tile calorimeter response instead of the number of Inner Detector tracks.

3.2.5 Trigger and data acquisition

The trigger and data acquisition system is composed of several subsystems, as shown in Figure 20. The pp beam bunch crossing rate is roughly 40 MHz, and the trigger system is used to reduce the event rate for data storage. The trigger system is composed of two levels, namely the first-level trigger (L1) and the High Level Trigger (HLT) [48]. L1 is hardware based and uses a subset of the information from the detectors; information of the L1 calorimeter trigger (L1Calo), L1 muon trigger (L1Muon), and other subsystems are processed with the central trigger processor (CTP) to implement trigger menus made from combinations of trigger selections. L1 event rate is about 100 kHz. When the L1 trigger is accepted, the detector data read from Readout Drivers (ROD) are buffered in the Read-Out System. HLT is software-based and receives the region-of-interest (i.e. η and ϕ coordinates) information from the L1, which is used for regional reconstruction of the detector data. HLT event rate is about 1 kHz. The events accepted by the HLT are transferred to the data storage and CERN's computing centre.

The L1Calo algorithm looks for high-p_{T} electrons, photons, τ decaying into hadrons, hadronic jets, large missing transverse energy, and large total transverse energy. It uses information from calorimeters with reduced granularity (typically 0.1×0.1 in $\Delta\eta \times \Delta\phi$). For the electron, photon, and τ, a region-of-interest with the size of 2×2 (in units of $\Delta\eta \times \Delta\phi = 0.1 \times 0.1$) is looked for that has high sum of E_{T} in the EM calorimeter. A requirement can be placed that the sum of E_{T} in the corresponding 2×2 region in the
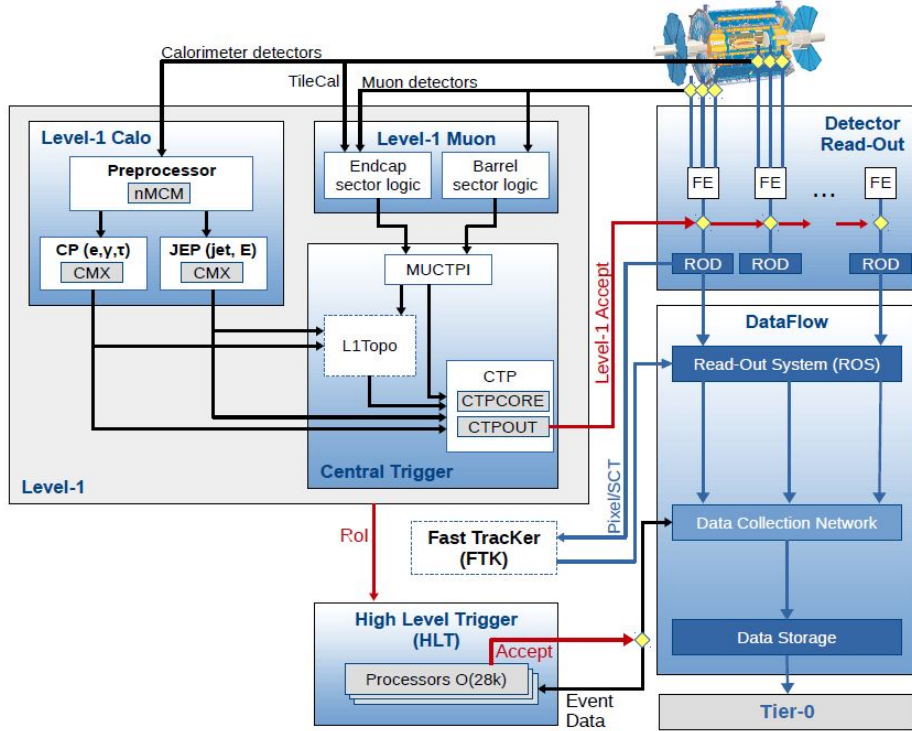
Figure 20: Schematic diagram of the trigger and data acquisition system.[48] L1Topo and FTK were being commissioned during 2015 and 2016.

hadronic calorimeter is smaller than a threshold ("hadronic veto"). For hadronic jets, a region-of-interest with the size of 4×4 or 8×8 is looked for, that has a 2×2 core and a high sum of E_T in the EM and hadronic calorimeters.

The L1Muon algorithm looks for high-p_T muons using information from muon trigger chambers (i.e. RPC and TGC). It searches for hits consistent with a muon originating from the interaction region.

The HLT algorithm uses Inner Detector tracks, finer-granularity calorimeter information, and precision measurements from the muon spectrometer. For the electron and photon reconstruction, a similar method as that for the offline reconstruction (see Section 4.1) is used; the sliding window algorithm is used to look for EM cluster with high E_T in the EM calorimeter, within the region-of-interest provided by L1; a regression algorithm based on Boosted Decision Trees is used for energy correction. For photon identification, the Loose and Tight selections (see Section 4.2) are defined using the shower shape in the EM calorimeter.

3.3 ATLAS Run 2 operation

The Run 2 operation of the ATLAS experiment was performed from 2015 to 2018 at $\sqrt{s} = 13$ TeV for pp collisions. The peak instantaneous luminosity was as high as 1.4×10^{34} cm^{-2} s^{-1} during stable beam conditions in 2016. The distribution of the mean number of interactions per bunch crossing (i.e. pile-up), recorded during the stable beam conditions in Run 2, is shown in Figure 21. The value of pile-up is calculated as $\mu = L_{bunch}\sigma_{inel}/f_{LHC}$, where L_{bunch} is the per bunch instantaneous luminosity, σ_{inel} is the pp
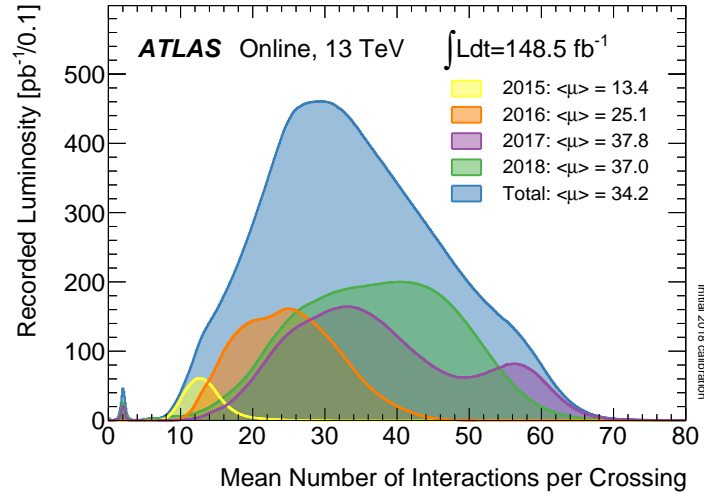
Figure 21: The mean number of interactions per bunch crossing. The data recorded by the ATLAS detector during stable beam conditions are shown. The distribution is weighted by the luminosity. [49]

inelastic cross section taken to be 80 mb, and f_{LHC} is the LHC revolution frequency. The dataset used in the analysis presented in this thesis was recorded during 2015 and 2016, with a pile-up of as high as 40. The details of this dataset is described in Section 5.1.1.

4 Photon reconstruction and identification

4.1 Reconstruction

The reconstruction of electrons and photons proceeds in parallel [44, 50]. Electrons and photons in the region $|\eta| < 2.47$ are reconstructed from clusters of energy deposited in the EM calorimeter cells. A seed cluster is determined with a sliding window algorithm [51], using a window size of 3×5 in units of $\Delta\eta \times \Delta\phi = 0.025 \times 0.025$ (corresponding to the typical cell size of the EM calorimeter second sampling layer). The window size is set wider in the ϕ direction compared to the η direction, considering the solenoid magnetic field that is parallel to the beam axis; the trajectories of electrons (those originating from the beam interaction region or e^+e^- pairs originating from conversions of photons) are bent in the ϕ direction. The seed cluster is required to have a total transverse energy of larger than 2.5 GeV. Duplicate seed clusters are removed; if two seed clusters are within 2×2 in units of $\Delta\eta \times \Delta\phi = 0.025 \times 0.025$, the one with lower energy is removed. From MC simulations, the efficiency of seed cluster reconstruction is estimated to be larger than 99% for photons with $E_T > 20$ GeV.

Track pattern recognition in the Inner Detector is first performed using the connected component analysis and a neutral network classifier [52, 53] to create a track seed (i.e. a track with three hits in the silicon detectors). The track seed is extrapolated to the TRT hits using a Kalman filter formalism [54], with the charged pion hypothesis that assumes energy loss of a minimum-ionizing particle interacting with the detector material. When this initial track pattern recognition fails, a second track extrapolation is performed using an electron hypothesis which allows for larger energy loss of up to 30%. The second track extrapolation is performed only if the track seed has a transverse momentum of larger than 1 GeV and it is within the region-of-interest[7] of an EM seed cluster. The track seeds are fit with the global χ^2 fitter [55]. The tracks obtained from the track fitting is loosely matched to EM seed clusters; the tracks are extrapolated to the EM calorimeter second sampling layer, and the η and ϕ coordinates are compared with the barycentre of the EM seed clusters. A track fit using Gaussian-sum filter fitter [56] is performed for tracks with silicon detector hits to improve the precision of the obtained track.

The reconstructed tracks are used for the reconstruction of conversion vertices of $\gamma \rightarrow e^+e^-$. A two-track conversion vertex is reconstructed from two tracks with opposite charges, and it is required to be consistent with that of a massless particle. A single-track conversion vertex is reconstructed, to reconstruct vertices with asymmetric tracks where one of the track has a low momentum $p_T < 5$ GeV and is not reconstructed, or vertices with two tracks that are close to each other and cannot be separately reconstructed. A single-track conversion vertex is reconstructed from a track with no hits in the innermost silicon layers. The tracks of the conversion vertex is required to have a high likelihood to be electrons based on TRT hits, with tighter requirements for single-track conversion vertex and conversion vertex with no hits in the silicon sensors. When there are two or more conversion vertices associated to a seed cluster, a vertex is chosen with the priority in the following order; a vertex with two tracks with silicon sensor hits, a vertex with two tracks, and a vertex with single track.

An EM seed cluster with a matching track consistent with electrons originating from the beam interaction region is classified as an electron, as shown in Figure 22. A seed cluster with one or two matching tracks consistent with the photon conversion hypothesis in the Inner Detector is classified as a "converted photon", i.e. a photon converted into a e^+e^- pair before leaving the Inner Detector. A seed cluster with no matching

---

[7]The region-of-interest is defined as $\Delta R < 0.3$ with respect to the barycentre of the seed cluster that satisfies a loose shower shape requirement ($R_\eta > 0.65$ and $R_{had} < 0.1$, where the two variables are those defined in Table 5).
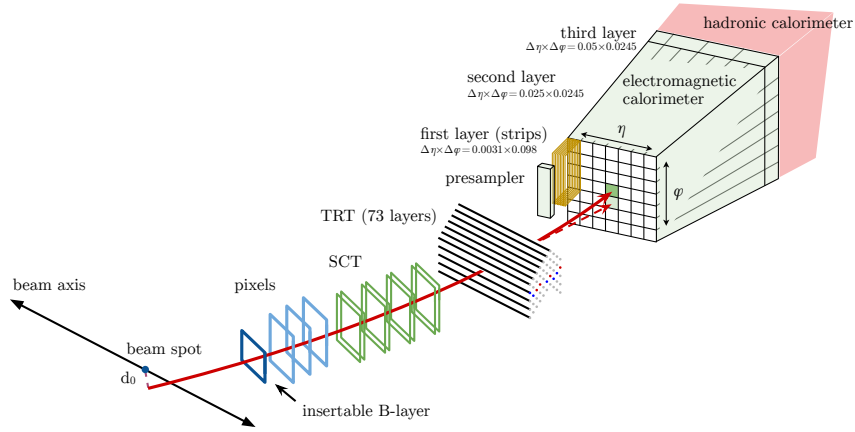
Figure 22: A schematic diagram illustrating the reconstruction of an electron.[50]

tracks is classified as an "unconverted photon", i.e. a photon traversing outside the Inner Detector without e^+e^- conversion. To increase the photon reconstruction efficiency, a further classification is performed to determine an EM seed cluster as an electron or a photon by using the track p_T and E/p (where E is the cluster energy and p is the track momentum). From simulation, the efficiency to reconstruct a true converted photon (i.e. a photon converted to a e^+e^- pair within a radius of 80 cm from the Interaction Point) as a converted photon is evaluated to be larger than 65% for a pile-up of 60 for $E_T > 20$ GeV. The fake rate to reconstruct a true unconverted photon as a converted photon is evaluated to be below 9% for a pileup of 60. Overall, approximately 70% of photons are classified as unconverted photons, and the remaining 30% are classified as converted photons.

From simulations, the overall efficiency to reconstruct a "prompt photon" (i.e. a photon not originating from decays of hadrons) as a photon (i.e. either a converted or an unconverted photon) is estimated to be 96% for $E_T > 25$ GeV. The other 4% is erroneously classified as an electron. For higher E_T, the two tracks from a photon conversion becomes difficult to separate; this leads to a decrease in the efficiency of the photon reconstruction to approximately 90% for $E_T \simeq 1$ TeV.

The energy of the photon is estimated using a clustering algorithm [51] that forms clusters around the EM seed cluster. A window size of 3×7 in units of $\Delta\eta \times \Delta\phi = 0.025 \times 0.025$ is used in the barrel region, and a window size of 5×5 in the end-cap region. The procedure for energy calibration is performed in several steps [57]. A regression algorithm based on Boosted Decision Trees is used to correct for the energy lost in the material upstream of the EM calorimeter, the energy deposited in the cells outside of the η and ϕ clusters, and the energy lost beyond the EM calorimeter. The algorithm is trained separately for electrons, converted photons, and unconverted photons, using simulated data. It is performed in intervals of E_T and $|\eta|$. The relative calibration between the different layers of the EM calorimeter is derived using $Z \to \mu\mu$ and $Z \to ee$ events and comparing collision data and simulated data. $Z \to \mu\mu$ events are used here because muons energy deposits are insensitive to the amount of material in front of the EM calorimeter. The energy is corrected further for geometric effects at the boundaries of calorimeter modules and HV settings in the regions of the calorimeter.

The overall calibration for the energy scale and energy resolution is performed by comparing $Z \to ee$ events in collision data and simulation, with the same results applied to electrons and photons [57]. The
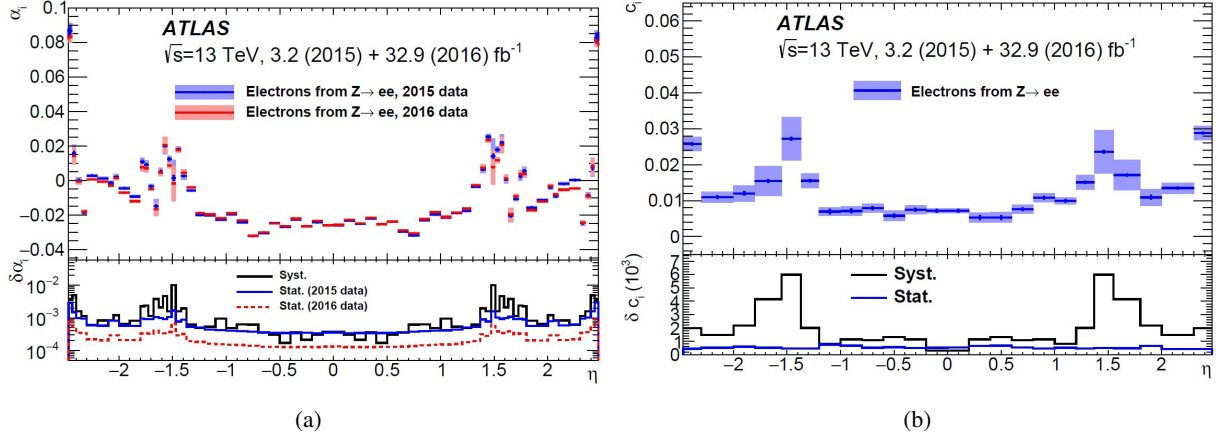
Figure 23: The corrections to energy scale and energy resolution evaluated by comparing $Z \to ee$ events in the collision data and simulated data. [57]
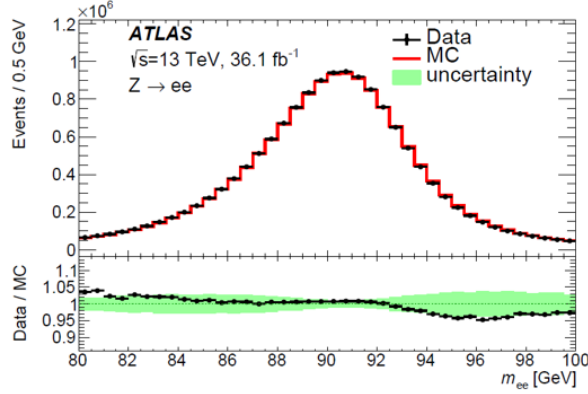

Figure 24: The comparison of the $Z \to ee$ invariant mass distribution obtained from collision data and that from simulation, with the energy scale and energy resolution corrections applied for the simulation. The distribution from the simulation is normalized to that of the collision data. [57]

corrections, α_i for energy scale and c_i for energy resolution, is defined by

$$E^{\text{data}} = E^{\text{MC}}(1 + \alpha_i), \qquad \left(\frac{\sigma_E}{E}\right)^{\text{data}} = \left(\frac{\sigma_E}{E}\right)^{\text{MC}} \oplus c_i \tag{57}$$

where i corresponds to different regions in η. The dielectron mass distribution is compared for collision data and simulated data, and the corrections are determined by minimizing the χ^2 of the two distributions. The resulting corrections are shown in Figure 23. Several sources of systematic uncertainties are evaluated, and the total fractional systematic uncertainty of energy scale is estimated to be at the level of $O(0.1)\%$. The total fractional systematic uncertainty of energy resolution is estimated to be 5–10% for 30–60 GeV, and 20–50% for higher energy. Figure 24 shows the $Z \to ee$ invariant mass distribution obtained from collision data and that from simulation, with the energy scale and energy resolution corrections applied for the simulation. The derived energy scale and resolution are cross checked that they are applicable to photons, using $Z \to ee\gamma$ and $Z \to \mu\mu\gamma$ events in collision data and simulated data.

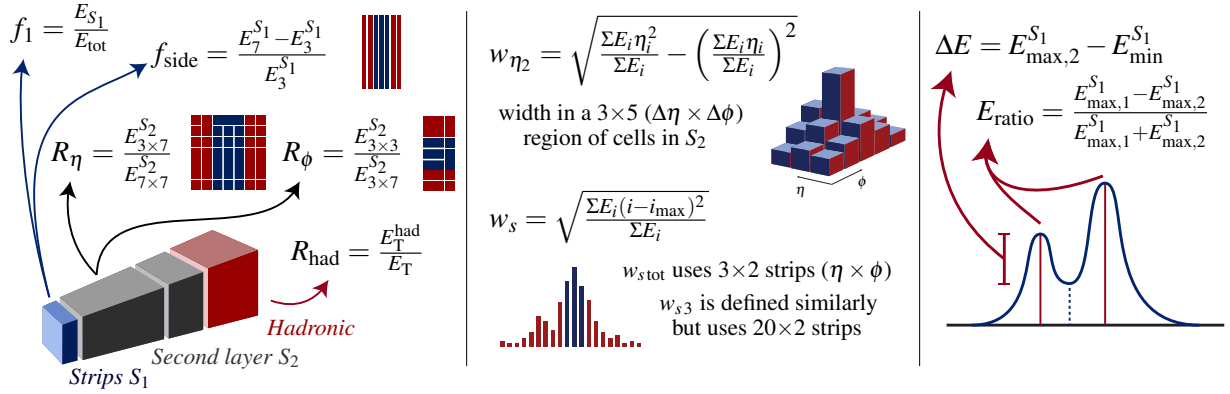Reconstructed photons are required to match photons reconstructed at the trigger level, within the separa-

Figure 25: Schematic diagrams showing the definition of the shower shape variables. [58]

tion of $\Delta R < 0.07$.

4.2 Identification

Photon identification (ID) is based on a set of requirements placed on several discriminating variables which characterize the EM shower development in the calorimeter ("shower shapes") [44]. They are defined to efficiently select prompt photons and reject backgrounds (i.e. hadronic jets erroneously reconstructed as photons, and photons originating from decays of hadrons). The discriminating variables ("shower shape variables") are defined in Table 5. A schematic representation of the shower shape variables is shown in Figure 25. Two variables quantify the shower leakage fraction in the hadronic calorimeter. Three variables quantify the lateral shower development in the EM calorimeter second sampling layer. One variable quantifies the fraction of energy in the EM calorimeter first sampling layer. Five variables quantify the lateral shower development in the finely-segmented strip cells of the EM calorimeter first sampling layer. The two of the five variables are utilized to find photon candidates with two separate local energy maxima in the strips cells; such shower shape is characteristic of neutral hadron decays, e.g. $\pi^0 \rightarrow \gamma\gamma$, as shown in Figure 18. The distributions of the shower shape variables are shown in Appendix B as Figures 88 and 89.

Several photon ID selections are defined [44]. The "Loose" selection is defined using shower shape variables in the EM calorimeter second sampling layer and the shower leakage fraction in the hadronic calorimeter, as shown in Table 5. It is used for photon ID selections at the trigger level. The "Tight" selection is based on all variables, as shown in Table 5. It is the standard photon ID selection used for the ATLAS experiment, but it is not used in the search presented in this thesis. Variations of the "Loose′" selections are defined, as shown in Table 6. They are defined by removing selection requirements on several variables with respect to the Tight selection. The number represents the number of selection requirements removed with respect to the Tight selection, e.g. Loose′5 represents that requirements on five variables are removed.

The thresholds for the requirements on shower shape variables are defined differently for several intervals of the $|\eta|$ of the photon candidate, namely 0–0.6, 0.6–0.8, 0.8–1.15, 1.15–1.37, 1.52–1.81, 1.81–2.01, 2.01–2.37. The binning is defined to consider the difference in the EM calorimeter geometry and the difference in the material upstream of the EM calorimeter. Also, the thresholds are defined differently for an unconverted photon and a converted photon. These thresholds are optimized so that the rejection of

Table 5: Shower shape variables used for photon ID [44]. A slight modification is made from the original table. "Loose′5" is shown as one example of the variations of the Loose′ selections.

Category	Description	Name	Loose	Tight	Loose′5
Hadronic leakage	Ratio of E_T in the first sampling layer of the hadronic calorimeter to E_T of the EM cluster (used over the ranges $\lvert\eta\rvert < 0.8$ or $\lvert\eta\rvert > 1.52$)	R_{had1}	✓	✓	✓
	Ratio of E_T in the hadronic calorimeter to E_T of the EM cluster (used over the range $0.8 < \lvert\eta\rvert < 1.37$)	R_{had}	✓	✓	✓
EM middle layer	Ratio of the energy in 3×7 $\eta \times \phi$ cells over the energy in 7×7 cells centred around the photon cluster position	R_η	✓	✓	✓
	Lateral shower width, $\sqrt{\left(\Sigma E_i \eta_i^2\right)/(\Sigma E_i) - \left((\Sigma E_i \eta_i)/(\Sigma E_i)\right)^2}$, where E_i is the energy and η_i is the pseudorapidity of cell i and the sum is calculated within a window of 3×5 cells	$w_{\eta 2}$	✓	✓	✓
	Ratio of the energy in 3×3 $\eta \times \phi$ cells over the energy of 3×7 cells centred around the photon cluster position	R_ϕ		✓	✓
EM strip layer	Lateral shower width, $\sqrt{\left(\sum E_i\,(i - i_{max})^2\right)/(\sum E_i)}$, where i runs over all strips in a window of 3×2 $\eta \times \phi$ strips, and i_{max} is the index of the highest-energy strip calculated from three strips around the strip with maximum energy deposit	w_{s3}		✓	
	Total lateral shower width, $\sqrt{\left(\sum E_i\,(i - i_{max})^2\right)/(\sum E_i)}$, where i runs over all strips in a window of 20×2 $\eta \times \phi$ strips, and i_{max} is the index of the highest-energy strip measured in the strip layer	w_{stot}		✓	
	Energy outside the core of the three central strips but within seven strips divided by energy within the three central strips	f_{side}		✓	
	Difference between the energy associated with the second maximum in the strip layer and the energy reconstructed in the strip with the minimum value found between the first and the second maxima	ΔE		✓	
	Ratio of the energy difference between the maximum energy deposit and the energy deposit in the secondary maximum in the cluster to the sum of these energies	E_{ratio}		✓	
	Ratio of the energy in the first layer to the total energy of the EM cluster	f_1		✓	✓

Table 6: Definition of the variations of the Loose′ selections.

Name	Requirements not applied with respect to Tight selection
Tight	-
Loose′2	f_{side}, w_{s3}
Loose′3	$f_{\text{side}}, w_{s3}, \Delta E$
Loose′4	$f_{\text{side}}, w_{s3}, \Delta E, E_{\text{ratio}}$
Loose′5	$f_{\text{side}}, w_{s3}, \Delta E, E_{\text{ratio}}, w_{\text{stot}}$
Loose′6	$f_{\text{side}}, w_{s3}, \Delta E, E_{\text{ratio}}, w_{\text{stot}}, w_{\eta 2}$
Loose′7	$f_{\text{side}}, w_{s3}, \Delta E, E_{\text{ratio}}, w_{\text{stot}}, w_{\eta 2}, R_\phi$

backgrounds is maximized while retaining the identification efficiency of prompt photons, using simulated events of hadronic jets and prompt photons. The thresholds used for the shower shape variables are the same for the Tight selection and the various Loose′ selections, and they are looser for the Loose selection.

Data-driven corrections are applied to the shower shape variables [44]. The EM shower shape obtained from MC simulations do not perfectly agree with that observed in the collision data due to the mismodelling, especially the lateral shower development, due to e.g. imperfections of EM shower simulation in the detector. This results in the deviations of the central values of the shower shape variable distributions; these deviations are typically 10% of the standard deviation of the distributions. The corrections are applied as a constant shift to the value of the shower shape variable. The value of the shift is defined as a function of the E_{T} and $|\eta|$ of the photon candidate, with bin boundaries of 8, 15, 20, 25, 30, 40, 50, 60, 80, 100, 250, and 1000 GeV in E_{T}, and a binning of 0–0.6, 0.6–0.8, 0.8–1.15, 1.15–1.37, 1.52–1.81, 1.81–2.01, and 2.01–2.37 in $|\eta|$. They are separately defined for unconverted and converted photons. The shifts are determined by minimizing the χ^2 between the distributions of the MC simulations and the collision data, as shown in Figure 26[8]. For $E_{\text{T}} < 50$ GeV, photon candidates from $Z \rightarrow ee\gamma$ and $Z \rightarrow \mu\mu\gamma$ events are used from the collision data and simulated data. For $E_{\text{T}} > 50$ GeV, high-E_{T} photon candidates obtained from collision data collected using single-photon triggers, which use Loose ID selection and have large prescaling, are used. The resulting shifts are typically 10% of the standard deviation of the distribution; their values are, at most for $E_{\text{T}} > 60$ GeV, 0.001 ± 0.0007 for R_{had}, 0.008 ± 0.002 for R_η, 0.008 ± 0.001 for R_ϕ, 0.0005 ± 0.0001 for $w_{\eta 2}$, 0.20 ± 0.02 for w_{stot}, 0.05 ± 0.01 for F_{side}, and 0.044 ± 0.004 for w_{s3}. The shifts are not defined for ΔE and E_{ratio}, because their shifts are small (e.g. for $E_{\text{T}} > 60$ GeV, 10 MeV at most for ΔE, and 0.005 at most for E_{ratio}), and also well below their associated uncertainties.

The photon ID efficiency to select prompt photons with the Tight selection is measured using collision data [44], and it is shown in Figure 27. It is measured using three different events, to cover a wide range of E_{T}; photon candidates from $Z \rightarrow ee\gamma$ and $Z \rightarrow \mu\mu\gamma$ events; electron candidates from $Z \rightarrow ee$ events; and high-E_{T} photon candidates from events collected using single-photon triggers. Figure 27 shows the measurement with the $Z \rightarrow ee$ events and single-photon events. For $Z \rightarrow ee$ events, a correction is applied to the distributions of the shower shape variables, to reproduce those of photons; this correction is derived from the differences in the distributions of the shower shape variables observed in simulations of photons and electrons. For single-photon trigger events, contamination of backgrounds (i.e. hadronic jets erroneously reconstructed as photons, and photons originating from decays of hadrons) are subtracted.

---

[8]For instance, for w_{stot} for 60 GeV $< E_{\text{T}} <$ 80 GeV and $|\eta| < 0.6$ for converted photons, the resulting reduced χ^2 calculated over 500 bins is approximately 1.2.
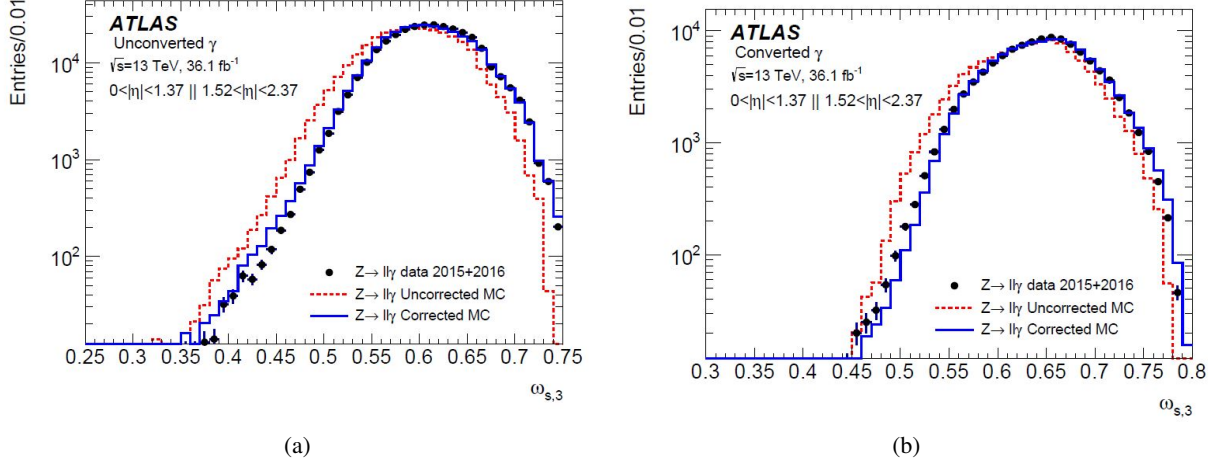
Figure 26: Comparison of the w_{s3} distributions of $Z \to ll\gamma$ events from collision data and simulated data with and without data-driven corrections. Photon candidates with 10 GeV < E_T < 50 GeV and $|\eta|$ < 2.37 (excluding 1.37 < $|\eta|$ < 1.52) are used. They are shown for (a) unconverted photons and (b) converted photons. Here, w_{s3} is denoted by $\omega_{s,3}$. [44]

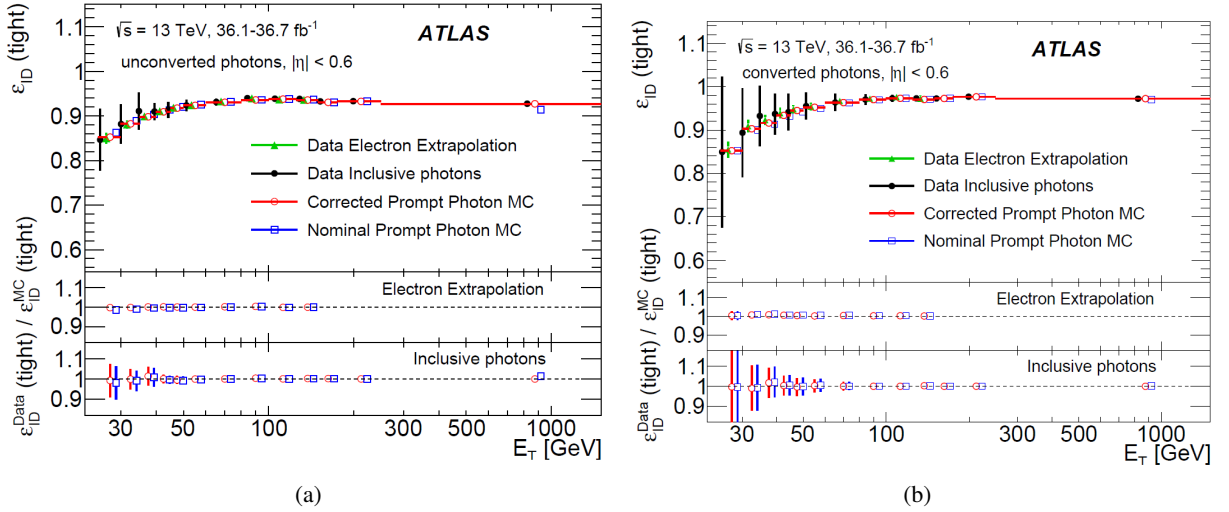

Figure 27: The photon ID efficiency to select prompt photons with the Tight selection requirement. It is shown for $|\eta|$ < 0.6 for (a) unconverted photons and (b) converted photons. For the simulated events, the efficiencies calculated with and without the data-driven corrections to the shower shape variables are shown. The panels below show the efficiency scale factors. [44]

The "efficiency scale factors" (i.e. corrections applied to Tight selection efficiency in simulations) are derived; they are consistent with 1 within the statistical uncertainty, and are at the level of 1% or less.

The rejection factor (i.e. the inverse of the selection efficiency) of backgrounds is estimated to be $O(10^3)$ for E_T > 25 GeV; this is estimated from simulations of SM background events consisting of one photon and one hadronic jet from the hard process.
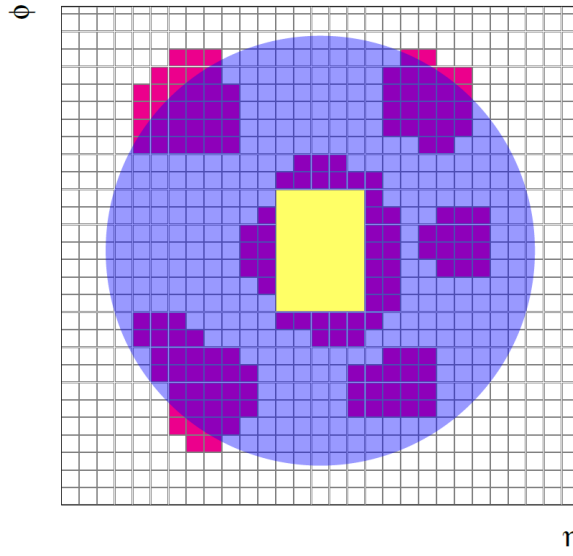
Figure 28: Schematic illustration of the definition of the calorimeter cone energy E_T^{cone}. The grid represents the cells of the EM calorimeter second layer. The shaded circle represents the cone ΔR around the barycentre of the EM cluster. The yellow filled box represent the subtracted cells corresponding to the photon EM cluster. The red filled squares represent the energy deposits in the calorimeter. [50]

4.3 Isolation

To further reject backgrounds (i.e. hadronic jets erroneously reconstructed as photons, and photons originating from decays of hadrons), the reconstructed photons are required to be isolated from other calorimeter energy deposits and from nearby tracks not associated with the reconstructed photon ("isolation requirement") [44].

The cone energy E_T^{cone} is defined as the sum of energy deposits in the calorimeters (i.e. EM and hadronic calorimeters) in a cone of size $\Delta R = 0.4$ around the barycentre of the photon EM cluster, subtracting the energy associated with the photon EM cluster, as shown in Figure 28. E_T^{cone} is corrected for the leakage of the photon energy from the photon EM cluster and for the effects of pile-up [59]. The calorimeter isolation variable of a reconstructed photon is defined as $E_T^{iso} = E_T^{cone} - 0.022 \times E_T$. It is required to satisfy $E_T^{iso} < 2.45$ GeV.

To account for the small differences observed between collision data and simulation, data-driven corrections are applied to the values of E_T^{cone}. The corrections are derived using single-photon events, where the events of collision data are selected using single-photon triggers with Loose ID selection. From the events in collision data, the contributions of hadronic jets are subtracted; here, the shape of E_T^{cone} of hadronic jet contribution is taken from a control sample defined by inverting the photon ID selection. The data-driven correction to the simulation is performed by a shift in the E_T^{cone} distribution; this shift is defined as the difference in the peak position of the E_T^{cone} distributions of the collision data and simulated data. The shifts are determined in bins of E_T and η. The values of the shifts are 2 GeV at most.

The track isolation variable p_T^{iso} is defined as the scalar sum of the transverse momenta of tracks not associated with the reconstructed photon in a cone of size $\Delta R = 0.2$ around the barycentre of the photon EM cluster. It is required to satisfy $p_T^{iso} < 0.05 \times E_T$.

To account for the small differences observed between collision data and simulation, data-driven corrections are applied to the track isolation efficiency. The efficiency corrections are derived using single-photon events, where the events of collision data are selected using single-photon triggers with Loose ID selection. From the events in collision data, the contributions of hadronic jets are subtracted; here, the shape of the track isolation variable p_T^{iso} of hadronic jet contribution is taken from a control sample defined by inverting photon ID selection. The track isolation efficiency correction is defined as the difference in the track isolation efficiency between the collision data and simulated data. The efficiency corrections are determined in bins of E_T and η. The values of the corrections are 2% at most.

5 Search for a resonance decaying into a pair of photon-jets

A search for a new scalar resonance decaying into a pair of photon-jets is performed. Two benchmark signal scenarios are introduced. They assume a heavy scalar boson X with a narrow width, that is produced via gluon–gluon fusion process, and decays into a pair of spin-0 particles a. One benchmark signal scenario assumes the decay of a into a pair of photons, i.e. $X \rightarrow aa \rightarrow 4\gamma$, as shown in Figure 29(a). Another benchmark signal scenario assumes the decay of a into a set of three neutral pions and their subsequent decay into photons, i.e. $X \rightarrow aa \rightarrow 6\pi^0 \rightarrow 12\gamma$, as shown in Figure 29(b). For $m_X > 200$ GeV and $m_a \sim O(1$ GeV), the photons from the decay of a will be highly collimated and will form a photon-jet. The two benchmark signal scenarios are introduced to interpret the search result in scenarios consisting photon-jets with both a low multiplicity and high multiplicity of photons. Here, the decay of a is considered to be "prompt", i.e. having a negligible lifetime.

An overview of the analysis strategy is described below. A photon-jet can lead to a single EM cluster in the EM calorimeter, as depicted in Figure 30; in such a case, each photon-jet typically leads to one reconstructed photon. Thus, this analysis selects events containing at least two high-E_T reconstructed photons to search for a resonance decaying into a pair of photon-jets, as shown in Figure 31; note that in the case of a photon-jet signal event, one reconstructed photon corresponds to one photon-jet. Hereafter, a reconstructed photon is denoted by γ_R. The signal region is defined with event selection strategy optimized to increase the sensitivity to photon-jet signal events. The reconstructed diphoton mass $m_{\gamma_R \gamma_R}$ is defined as the invariant mass of the two reconstructed photons, and it corresponds to the value of m_X in the case of signal events. As shown in Figure 32, the $m_{\gamma_R \gamma_R}$ distribution of SM background events forms a smoothly falling shape, with the rate of events decreasing logarithmically with respect to the value of $m_{\gamma_R \gamma_R}$. In contrast, the $m_{\gamma_R \gamma_R}$ distribution of signal events form a peaklike shape, with a width of the shape corresponding to the detector resolution if the X boson has a narrow decay width (well below 1 GeV). With these contrasting features of the background and signal events in mind, a "bump-hunting" technique is employed; an excess of events from the SM background expectation is searched for by performing an unbinned maximum-likelihood fit to the $m_{\gamma_R \gamma_R}$ distributions with the consideration of the background and signal components.

The SM backgrounds that enter the signal region consist of mainly three components:

- Events containing two high-E_T prompt photons ($\gamma\gamma$)

- Events containing one high-E_T prompt photon and one high-E_T hadronic jet (γj or $j\gamma$)

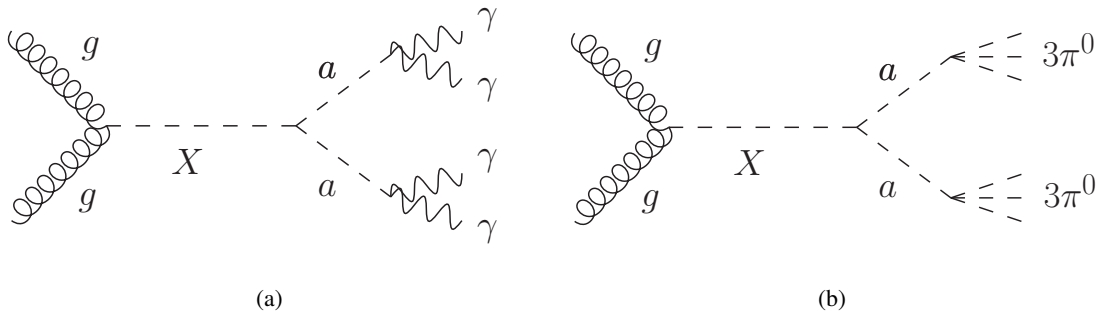<center>(a)   (b)</center>

Figure 29: Diagrams of benchmark signal scenarios of a new scalar resonance decaying into a pair of photon-jets, for the processes (a) $X \rightarrow aa \rightarrow 4\gamma$ and (b) $X \rightarrow aa \rightarrow 6\pi^0$.
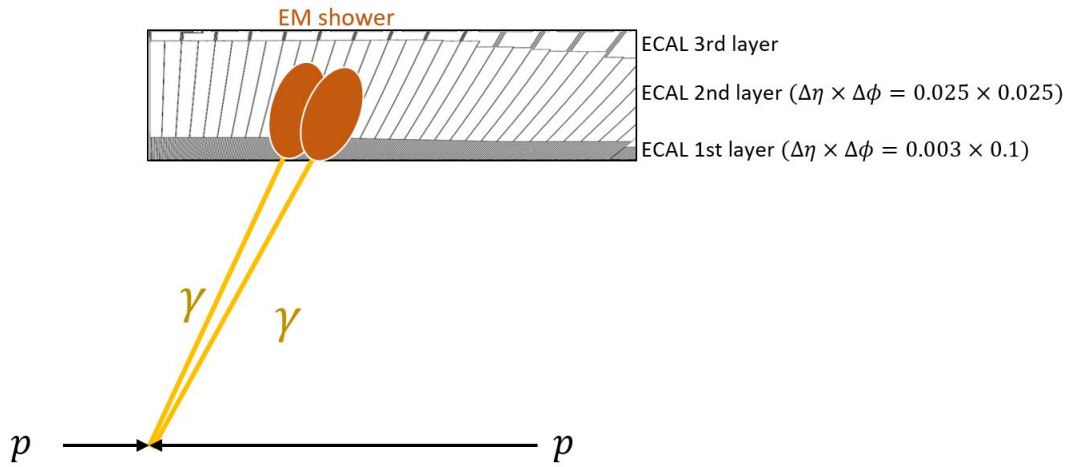
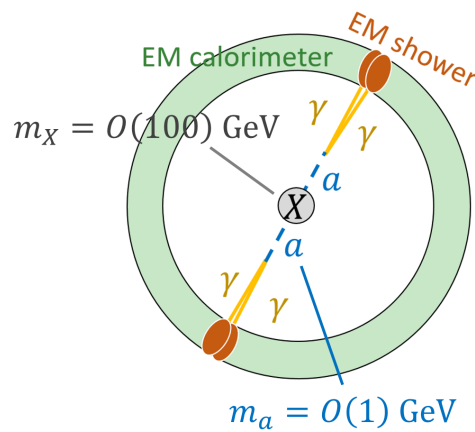Figure 30: Schematic diagram of a photon-jet $a \to \gamma\gamma$ entering the EM calorimeter.

Figure 31: A schematic diagram illustrating the decay of the benchmark signal scenario $X \to aa \to 4\gamma$ in the ATLAS detector. The cross section in the x–y plane is shown. The boson X is produced by a pp collision. It decays to a pair of a bosons, and each a boson decays to a pair of photons. Because the a boson is highly boosted, the two photons form a photon-jet, which creates a single EM cluster in the EM calorimeter.
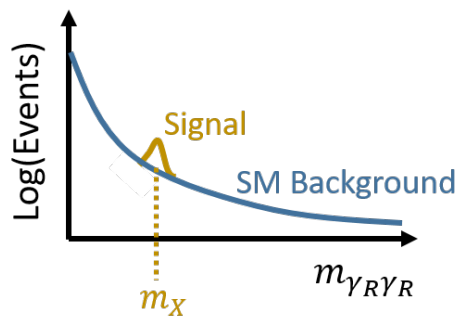
Figure 32: A schematic diagram illustrating the concept of a resonance search.

45

- Events containing two high-E_T hadronic jets (jj)

A hadronic jet can be erroneously reconstructed as a photon. γj ($j\gamma$) denotes events with the prompt photon having a larger (smaller) E_T than the hadronic jet.

The structure of this section (Section 5) is described briefly below. The descriptions of the collision dataset and the simulated samples of signal and background events are given in Section 5.1. The experimental characteristics of photon-jet signal events are described in Section 5.2. The event selection requirements are optimized to increase sensitivity to photon-jet signal events, as described in Section 5.3.1. The signal region is divided into two orthogonal event categories to increase sensitivity to photon-jet signal events, as described in Section 5.3.2. An unbinned likelihood fit to the $m_{\gamma_R \gamma_R}$ distributions is performed, simultaneously in the two event categories, and considering probability density functions of both the signal and background components. As an input to the unbinned likelihood fit, the probability density functions of the signal component and the background component are described in Sections 5.4 and 5.5, respectively. The systematic uncertainties affecting the unbinned likelihood fit is described in Section 5.6. The statistical method of the unbinned likelihood fit is described in Section 5.7. The search result and its interpretation are presented in Section 5.8. A long-lived a arises in BSM models, for instance in NMSSM when the decay width of a is small (e.g. $\Gamma_a \sim O(1 \text{ meV})$), as discussed in Section 2.3.1[9]. The interpretation of the results for the case of a long-lived a in $X \rightarrow aa \rightarrow 4\gamma$ is described in Section 5.9.

5.1 Event samples

5.1.1 Collision data

The dataset used for this search was collected under normal data-taking conditions for pp collisions at a center-of-mass energy of $\sqrt{s}$ = 13 TeV during 2015 and 2016. It corresponds to an integrated luminosity of 36.7 fb^{-1} after applying data-quality requirements.

The data were collected using an unprescaled diphoton trigger implemented in the HLT. This trigger selects events with two EM clusters with E_T > 35 GeV and E_T > 25 GeV and satisfying the Loose photon ID selection[10]. This trigger is seeded with a L1 trigger that requires two EM clusters with E_T > 15 GeV and satisfying hadronic veto[11].

5.1.2 Simulated samples

Samples of the benchmark signal scenarios $X \rightarrow aa \rightarrow 4\gamma$ and $X \rightarrow aa \rightarrow 6\pi^0$ were simulated with the following set up. For the production of the X via gluon–gluon fusion, MadGraph5_aMC@NLO [60] Version 2.3.3 at next-to-leading order (NLO) in quantum chromodynamics (QCD) was used with the NNPDF30NLO parton distribution function (PDF) set [61]. For the subsequent decay of the X into aa and into photons, and also the parton-shower and hadronization simulation of initial state radiation jets, Pythia8 [62] Version 8.210 with the A14 tune [63] was used. The samples were produced using a narrow-width approximation (NWA) approach with the resonance widths of the X and a set to 4 MeV

---

[9]The case of a long-lived a in the scenario $X \rightarrow aa \rightarrow 6\pi^0$ is not considered. This is because such case arise in the NMSSM only when m_a is within some value, as described in Section 2.3.1 as Case 2. Such case is out of scope of this thesis, and is not considered.

[10]This HLT trigger is named "HLT_g35_loose_g25_loose" in the ATLAS trigger paper [48].

[11]This L1 trigger is named "L1_2EM15VH" in the ATLAS trigger paper [48].

and 1 MeV, respectively. Samples for $X \rightarrow aa \rightarrow 4\gamma$ ($X \rightarrow aa \rightarrow 6\pi^0$) were simulated for mass ranges of 200 GeV $< m_X <$ 2000 GeV and 0.1 GeV $< m_a <$ 10 GeV (0.5 GeV $< m_a <$ 10 GeV). For the signal scenario $X \rightarrow aa \rightarrow 4\gamma$, samples for a that decays promptly as well as those for long-lived a were simulated, ranging from $c\tau = 0$ to $c\tau = 25$ mm, where c is the speed of light and τ is the average lifetime of the particle a at rest.

Samples of the SM background events consisting of two photons from the hard process were simulated with SHERPA 2.1.1 [64]. Matrix elements were calculated at leading order (LO) in QCD with up to two additional partons. It is then merged with the SHERPA parton-shower simulation [65] using the ME+PS@LO prescription [66]. The CT10 PDF set [67] was used in conjunction with a dedicated parton-shower tune of SHERPA.

Samples of the SM background events consisting of one photon and one hadronic jet from the hard process were also simulated with SHERPA 2.1.1. Matrix elements were calculated at LO in QCD with up to four additional partons. The same merging prescription, PDF set, and parton-shower tune as for the diphoton sample were used.

Additional interactions in the pile-up were simulated and overlayed on the simulated signal and SM background events. These events were simulated using Pythia 8.186 [62] using the A2 tune [68] and the MSTW2008LO PDF set [69] .

All simulated event samples were produced using the ATLAS simulation infrastructure [70], using the full GEANT 4 [71] simulation of the ATLAS detector. The simulated events were passed through the digitisation process that simulates the detector responses, then they were reconstructed with the same software as that used for the reconstruction of the collision data.

5.2 Photon-jet signal characteristics

Photon-jets can arise from the decays of boosted particles into photons. These boosted particles arise when the particles are decay products of a higher-mass resonance.

For the benchmark signal scenarios, the angular separation of photons in a photon-jet depends on the ratio of the masses m_a/m_X, when particle X is produced nearly at rest. For instance, for $X \rightarrow aa \rightarrow 4\gamma$, the distribution of $\Delta R_{\gamma\gamma}$ is shown in Figure 33. Here, $\Delta R_{\gamma\gamma} = \sqrt{(\Delta\eta)^2 + (\Delta\phi)^2}$ is the angular separation of photons in the decay $a \rightarrow \gamma\gamma$. From the kinematics of boosted particles, the distribution of $\Delta R_{\gamma\gamma}$ has a peak at $\Delta R_{\gamma\gamma} = 2/\gamma_a$, where $\gamma_a = E_a/m_a$ is the Lorentz factor of the a particle. Considering that the energy of the a particle has a median value of $E_a \sim m_X/2$, the distribution of $\Delta R_{\gamma\gamma}$ has a peak at $\Delta R_{\gamma\gamma} \sim 4 \times m_a/m_X$. The proportionality of the angular separation of photons within a photon-jet to m_a/m_X holds for photon-jets in general, including $X \rightarrow aa \rightarrow 6\pi^0$. Because the two scenarios $X \rightarrow aa \rightarrow 4\gamma$ and $X \rightarrow aa \rightarrow 6\pi^0$ are similar, some parts of the descriptions in the following sections are only mentioned for $X \rightarrow aa \rightarrow 4\gamma$, but they apply to $X \rightarrow aa \rightarrow 6\pi^0$ as well.

For small values of the ratio $m_a/m_X < 0.01$, the boost of the a can lead to small angular separations of the final-state photons ($\Delta R \lesssim 0.04$); Thus the collimated photons may enter a small area of the EM calorimeter that is comparable to the Molière radius. In this case, the decay of the a into photons will lead to a single EM cluster, and hence to one reconstructed photon, as depicted in Figure 30. Thus, events with two high-E_T reconstructed photons can be used as a starting point for a search for a resonance decaying to a pair of photon-jets. This analysis presents a search for a scalar resonance X decaying to a pair of photon-jets for the range $m_X > 200$ GeV. Based on the estimations using simulated signal samples, it

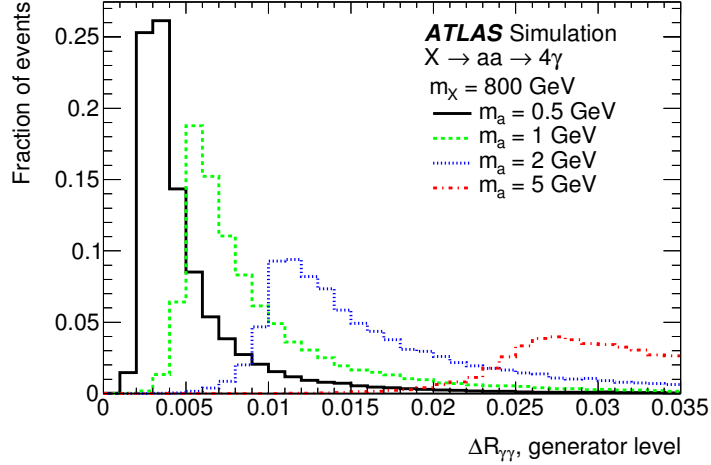Figure 33: The distribution of $\Delta R_{\gamma\gamma}$ for $X \to aa \to 4\gamma$ using simulated signal samples at the generator level. [72]

is found that the analysis is sensitive to the parameter region $m_a/m_X < 0.01$, which is defined as the parameter region of interest of this analysis.

For large values of the ratio $m_a/m_X \gtrsim 0.08$, the final-state photons can be isolated and lead to separate EM clusters when their angular separations are larger than roughly 0.3. As already described in Section 1, a general search for new phenomena in events with at least three isolated photons was performed by ATLAS at Run 1 for pp collisions at $\sqrt{s}$ = 8 TeV [23]. This search was sensitive to the BSM signal scenario $X \to aa \to 4\gamma$ corresponding to the region $m_a/m_X \gtrsim 0.08$, as shown in Figure 3.

5.3 Event selection

5.3.1 Definition of the signal region

Events containing at least two reconstructed photons are selected. The reconstructed photons with the highest and the second highest E_T are defined as the "leading" and the "subleading" reconstructed photons, respectively. The two leading reconstructed photons are required to be within the fiducial calorimeter region of $|\eta| < 2.37$, excluding the transition region at $1.37 < |\eta| < 1.52$ between the barrel and end-cap sections of the EM calorimeter. The two leading reconstructed photons are required to satisfy $E_T > 25$ GeV and the Loose photon ID selection. These requirements are defined as the "preselection".

As described in Section 4.3, the two leading reconstructed photons are required to be isolated from other calorimeter energy deposits and from nearby tracks not associated with the reconstructed photons. The calorimeter and track isolation variables of the reconstructed photons are required to satisfy $E_T^{iso} < 2.45$ GeV and $p_T^{iso} < 0.05 \times E_T$. The distributions of the calorimeter and track isolation variables are shown in Figure 34.

The requirement $E_T > 0.4 \times m_{\gamma_R\gamma_R}$ is applied to the leading reconstructed photon, and $E_T > 0.3 \times m_{\gamma_R\gamma_R}$ to the subleading reconstructed photon. This requirement increases the sensitivity to a scalar resonance decaying into a pair of photon-jets, because such events contain reconstructed photons with
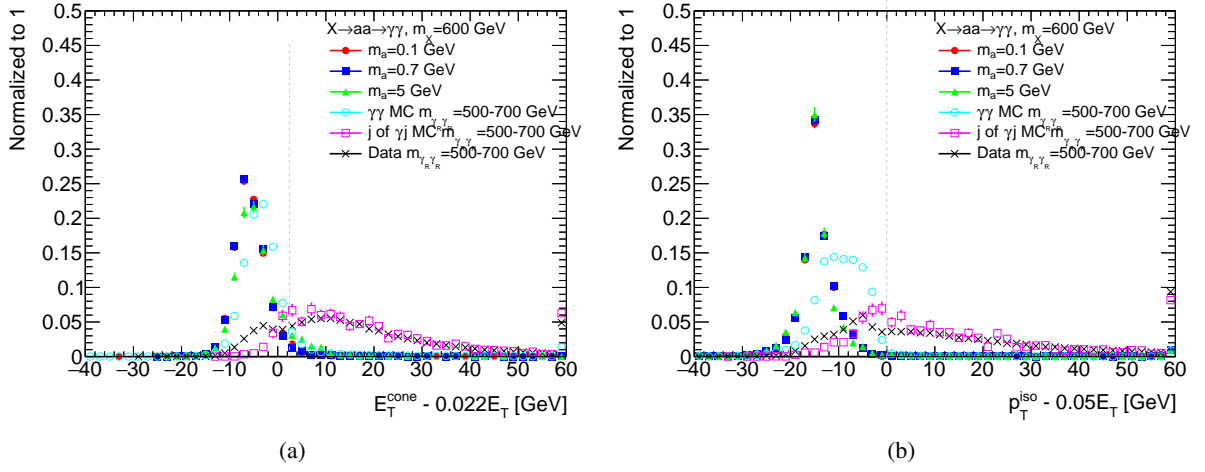
48

Figure 34: The distributions of (a) the calorimeter isolation variable $E_\mathrm{T}^\mathrm{cone} - 0.022 \times E_\mathrm{T}$ and (b) the track isolation variable $p_\mathrm{T}^\mathrm{iso} - 0.05 \times E_\mathrm{T}$. The histograms are plotted as the sum of leading and subleading reconstructed photons. The events which satisfy the preselection requirements are plotted. The filled markers represent the distributions obtained from simulated signal samples of the process $X \to aa \to 4\gamma$ for $m_X = 600$ GeV. The empty markers represent the distributions obtained from simulated samples of SM processes $\gamma\gamma$ and γj in the region 500 GeV $< m_{\gamma_R\gamma_R} <$ 700 GeV. For the square markers, reconstructed photons originating from hadronic jets are exclusively chosen. The "X" markers represent the distributions obtained from collision dataset in the region 500 GeV $< m_{\gamma_R\gamma_R} <$ 700 GeV. The vertical dotted line represents the threshold used for the requirement placed on the variable.

larger $E_\mathrm{T}/m_{\gamma_R\gamma_R}$ ratios compared to those from background events dominated by t-channel processes [25]. The distributions of $E_\mathrm{T}/m_{\gamma_R\gamma_R}$ are shown in Figure 35.

The two leading reconstructed photons are required to satisfy the Loose′5 photon ID selection, defined in Section 4.2. The Loose′5 selection is a looser requirement by definition compared to the Tight selection, which is the standard photon ID selection used for the ATLAS experiment. Based on the sensitivity estimation using simulated samples of signal and SM background processes, this Loose′5 selection is found to provide better sensitivity to photon-jet signals, compared to the Tight selection[12]. This is because photon-jet signal events with large values of m_a/m_X (e.g. $m_a/m_X \gtrsim 0.003$) may lead to wider EM shower in the EM calorimeter, and such events can be rejected by the Tight selection. The distributions of the shower shape variables of photon-jet signal events are shown in Appendix B. Thus, the selection efficiency of signal events increases with the use of the Loose′5 selection. For instance, for $X \to aa \to 4\gamma$ with mass values in the region $0.003 < m_a/m_X < 0.006$ and $m_X > 200$ GeV, the selection efficiency is less than 5% when the Tight selection is used, and this increases to 20%–50% with the Loose′5 selection (i.e. an increase of approximately a factor 4–10). Also, an increase in the number of background events is moderate ($\sim 30\%$) with the Loose′5 selection compared to that with the Tight selection. Thus, the sensitivity to photon-jet signals is increased with the use of the Loose′5 selection.

Additionally, an important point is that a "control region" (i.e. a region similar and orthogonal to the signal region) can be defined with the use of the Loose′5 selection. This is because the Loose′5 selection is a tighter selection compared to the Loose photon ID selection. As described in Section 5.1.1, the collision dataset is collected with the diphoton trigger, which requires two EM clusters to satisfy the trigger-level Loose photon ID selection. Reconstructed photons in the dataset that do not satisfy the Loose′5 selection

---

[12]The details of the sensitivity estimation using simulated samples are described in Appendix C.
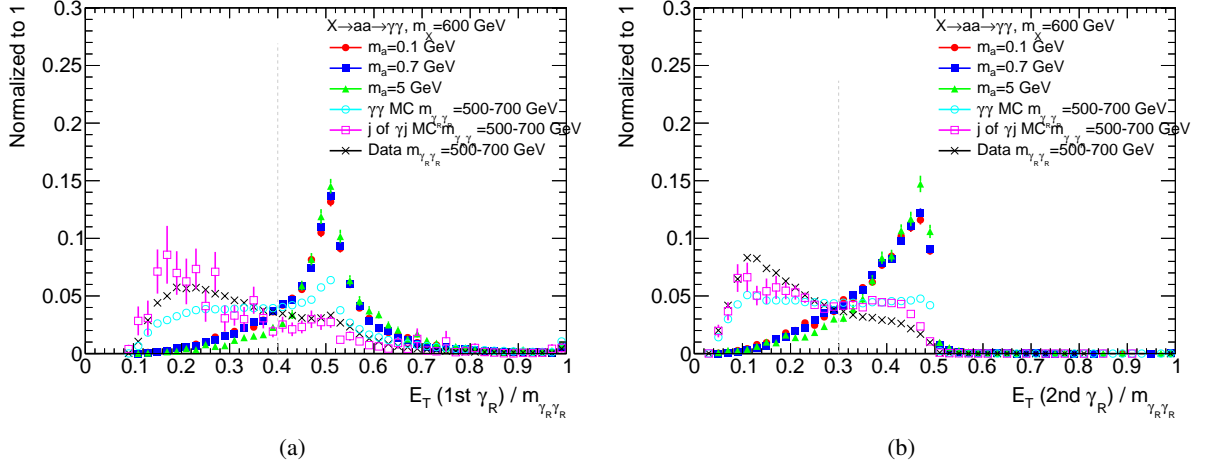
Figure 35: The distributions of $E_T/m_{\gamma_R\gamma_R}$ for (a) leading reconstructed photons and (b) subleading reconstructed photons. The events which satisfy the preselection requirements are plotted. The filled markers represent the distributions obtained from simulated signal samples of the process $X \to aa \to 4\gamma$ for $m_X = 600$ GeV. The empty markers represent the distributions obtained from simulated samples of SM processes $\gamma\gamma$ and γj in the region 500 GeV $< m_{\gamma_R\gamma_R} <$ 700 GeV. For the square markers, reconstructed photons originating from hadronic jets are exclusively chosen. The "X" markers represent the distributions obtained from collision dataset in the region 500 GeV $< m_{\gamma_R\gamma_R} <$ 700 GeV. The vertical dotted line represents the threshold used for the requirement placed on the variable.

is used for the estimation of the rate of hadronic jets satisfying the calorimeter isolation requirement, as described in Section 5.5.1.

Hereafter, Loose′5 is denoted by Loose′ for simplicity.

Events are required to satisfy $m_{\gamma_R\gamma_R} > 175$ GeV.

The signal selection efficiency ε is defined as the efficiency to select signal events including kinematic acceptance, namely

$$\varepsilon = \frac{\text{Number of events that satisfy event selection requirements}}{\text{Number of all generated events}} \tag{58}$$

The signal selection efficiency evaluated using simulated samples are shown in Figure 36. The selection efficiency increases for larger m_X because of the E_T, η, and isolation requirements. It also decreases for larger m_a/m_X, because a larger m_a/m_X leads to a wider EM shower; such events are rejected by mainly the trigger-level Loose ID selection and additionally the isolation requirement. For the parameter region $m_a/m_X > 0.01$, the value of ε is smaller than 0.04.

The comparison of the signal selection efficiencies with the use of different photon ID selections is shown in Figure 37.
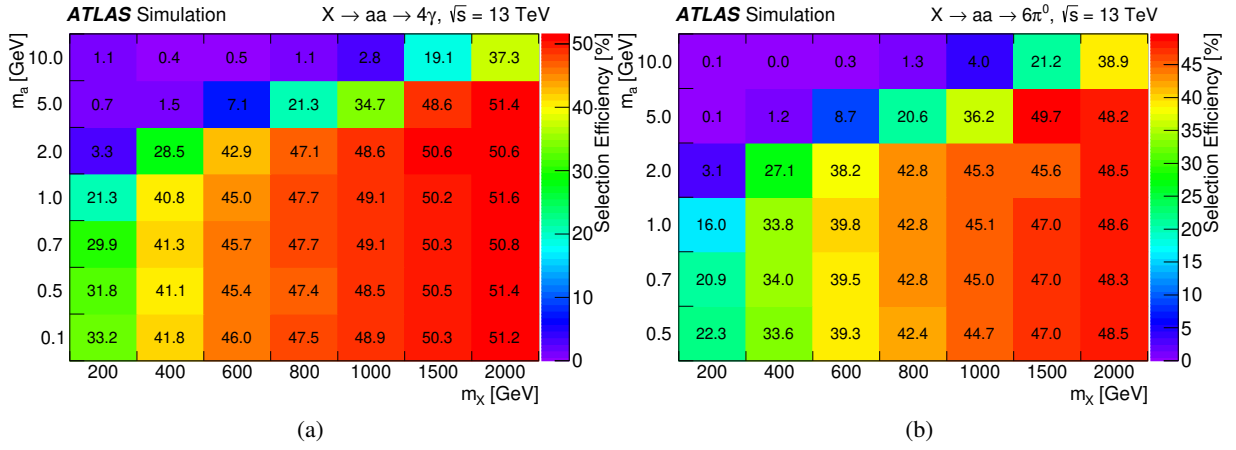
Figure 36: The signal selection efficiency ε as a function of m_X and m_a, for (a) $X \rightarrow aa \rightarrow 4\gamma$ and (b) $X \rightarrow aa \rightarrow 6\pi^0$. [72]
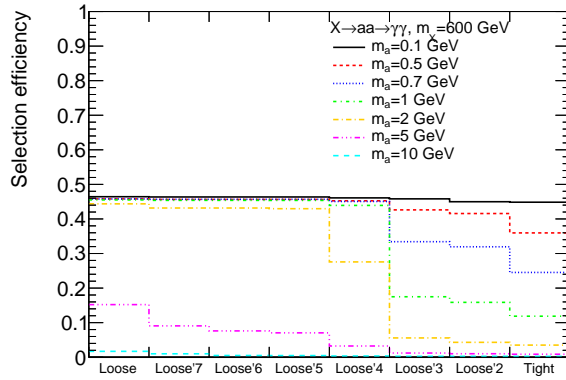

Figure 37: The comparison of the signal selection efficiencies with the use of different photon ID selections. They are shown for $X \rightarrow aa \rightarrow 4\gamma$ for $m_X = 600$ GeV and different values of m_a.

5.3.2 Categorization of events by the shower shape variable ΔE

The signal region is divided into two orthogonal event categories based on the value of the shower shape variable ΔE of the reconstructed photons. As described in Table 5, ΔE quantifies the relative size of the second maximum of an EM cluster in the EM calorimeter first sampling layer. It is defined as

$$\Delta E = E_{\text{max},2}^{S1} - E_{\text{min}}^{S1}$$

where $E_{\text{max},2}^{S1}$ is the energy of the strip cell with the second largest energy, and E_{min}^{S1} is the energy of the strip cell with the lowest energy located between the strips with the largest and the second largest energy. This is depicted in Figure 38. If the strip cells with the largest and the second largest energy are located next to each other, then $\Delta E = 0$. When a photon-jet from decays $a \to \gamma\gamma$ and $a \to 3\pi^0 \to 6\gamma$ have separation of photons in η larger than the segmentation of strip cells, it can lead to large values of ΔE, as depicted in Figure 30. Thus, when m_a/m_X is larger, ΔE becomes larger, as shown in Figure 39[13]. In contrast, a single photon entering the EM calorimeter typically has smaller values of ΔE, as seen in the figure[14]. Figure 40 shows the comparison of the ΔE distributions obtained from the collision dataset and that from simulated samples. This figure shows the level of agreement between the two.
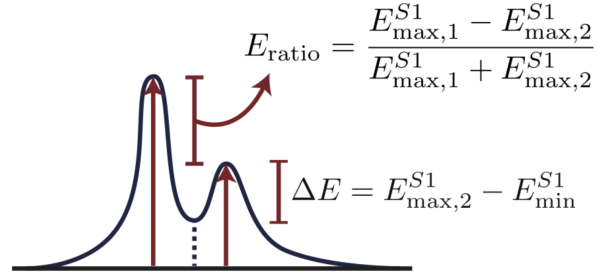

$$E_{\text{ratio}} = \frac{E_{\text{max},1}^{S1} - E_{\text{max},2}^{S1}}{E_{\text{max},1}^{S1} + E_{\text{max},2}^{S1}}$$

$$\Delta E = E_{\text{max},2}^{S1} - E_{\text{min}}^{S1}$$

Figure 38: A schematic diagram illustrating the definition of the shower shape variable ΔE. The energy deposit of the EM shower in a strip cell in the first layer of the EM calorimeter is displayed as a function of η. The variable $E_{\text{max},1}^{S1}$ is the energy of the strip cell with the largest energy. [72]

The two orthogonal event categories are defined as the following:

- **Low-ΔE category:** The two leading reconstructed photons have values of ΔE below the threshold. This typically corresponds to a shower shape in the first layer of the EM calorimeter with a single peak.

- **High-ΔE category:** At least one of the two leading reconstructed photons has a value of ΔE above the threshold. This typically corresponds to a shower shape in the first layer of the EM calorimeter with more than one peak.

The thresholds of the value of ΔE used for the definition of categories are the same as those used in the standard Tight photon ID selection, which is tuned to select standard single photons and reject hadronic jets (including $\pi^0 \to \gamma\gamma$ events). They range in 100–250 MeV for $|\eta| < 1.81$, and in 400–500 MeV for $1.81 < |\eta| < 2.37$, as shown in Table 7.

---

[13]The values of ΔE have wider distribution in the end-cap sector, compared to the barrel sector. This is because of several reasons, including the fact that the width of the EM calorimeter first layer cells becomes narrower for fixed $\Delta\eta$ in the end-cap sector, and the fact that the $\Delta\eta$ segmentation is larger for larger η (e.g. $\Delta\eta = 0.006$ for $2.0 < |\eta| < 2.4$)

[14]Note that the ΔE distribution of standard photons may have non-zero values, as seen in Figure 39. This is because the cells of EM calorimeter first layer have a noise of $O(10)$ MeV that originate from several sources, e.g. pile-up.
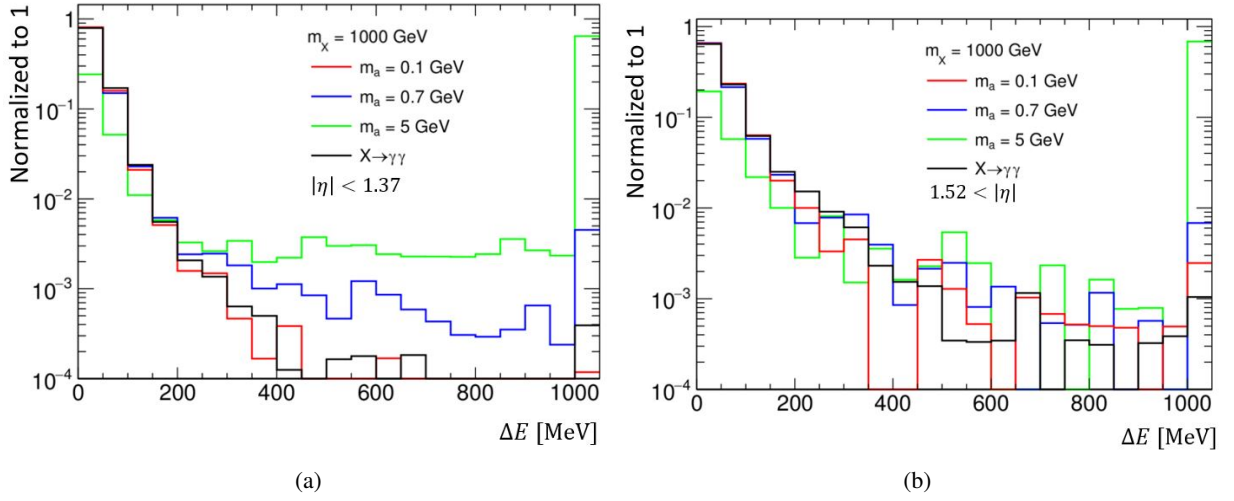
Figure 39: The distributions of ΔE of reconstructed photons in the signal region. They are displayed for $X \rightarrow aa \rightarrow 4\gamma$ for $m_X = 1$ TeV and $m_a = 0.1, 0.7, 5$ GeV obtained from simulated samples. The black lines show the distributions for reconstructed photons originating from a scalar resonance with a mass of 1 TeV produced by gluon–gluon fusion process and decaying into two photons. The last bin of the histogram shows the overflow, i.e. the sum of events with the value of ΔE larger than 1 GeV. The distributions are displayed for reconstructed photons entering (a) the barrel section and (b) the end-cap section of the EM calorimeter.

Table 7: Thresholds for the values of ΔE that are used for the definition of the two event categories.

$\lvert\eta\rvert$	Threshold of ΔE [MeV]					
	$0 - 0.6$	$0.6 - 0.8$	$0.8 - 1.37$	$1.52 - 1.81$	$1.81 - 2.01$	$2.01 - 2.37$
Unconverted	200	111	140	250	400	400
Converted	188	175	150	176	400	493

The category fraction f is defined as the fraction of signal events that appear in the low-ΔE category, namely

$$f = \frac{\text{Number of events in the low-}\Delta E \text{ category}}{\text{Number of events that satisfy event selection requirements}} \tag{59}$$

The values of f evaluated using simulated signal samples are presented in Figure 41. The value of f decreases for larger m_a/m_X, because a larger m_a/m_X leads to larger ΔE, as described above.

Additionally, the value of f increases when m_a/m_X is larger than 0.01, as seen in Figure 41. This is because such signal events, i.e. events from the parameter region $m_a/m_X > 0.01$ and satisfying the event selection requirements of the signal region, are heavily biased events in which the photons consisting a photon-jet have an asymmetric distribution of the momentum. A large fraction of the momentum of the parent a particle is transferred to only one photon in the photon-jet, thus leading to a shower shape similar to that of a prompt photon. Such events satisfy the event selection requirement and are likely to be included in the low-ΔE category. However, this feature does not affect the search, because the parameter region of interest is set to $m_a/m_X < 0.01$.

As seen in Figure 41, the values of f for $X \rightarrow aa \rightarrow 4\gamma$ and $X \rightarrow aa \rightarrow 6\pi^0$ are similar. The main distinction is the threshold of m_a/m_X for f to transition from $f > 0.5$ to $f < 0.5$. This threshold is
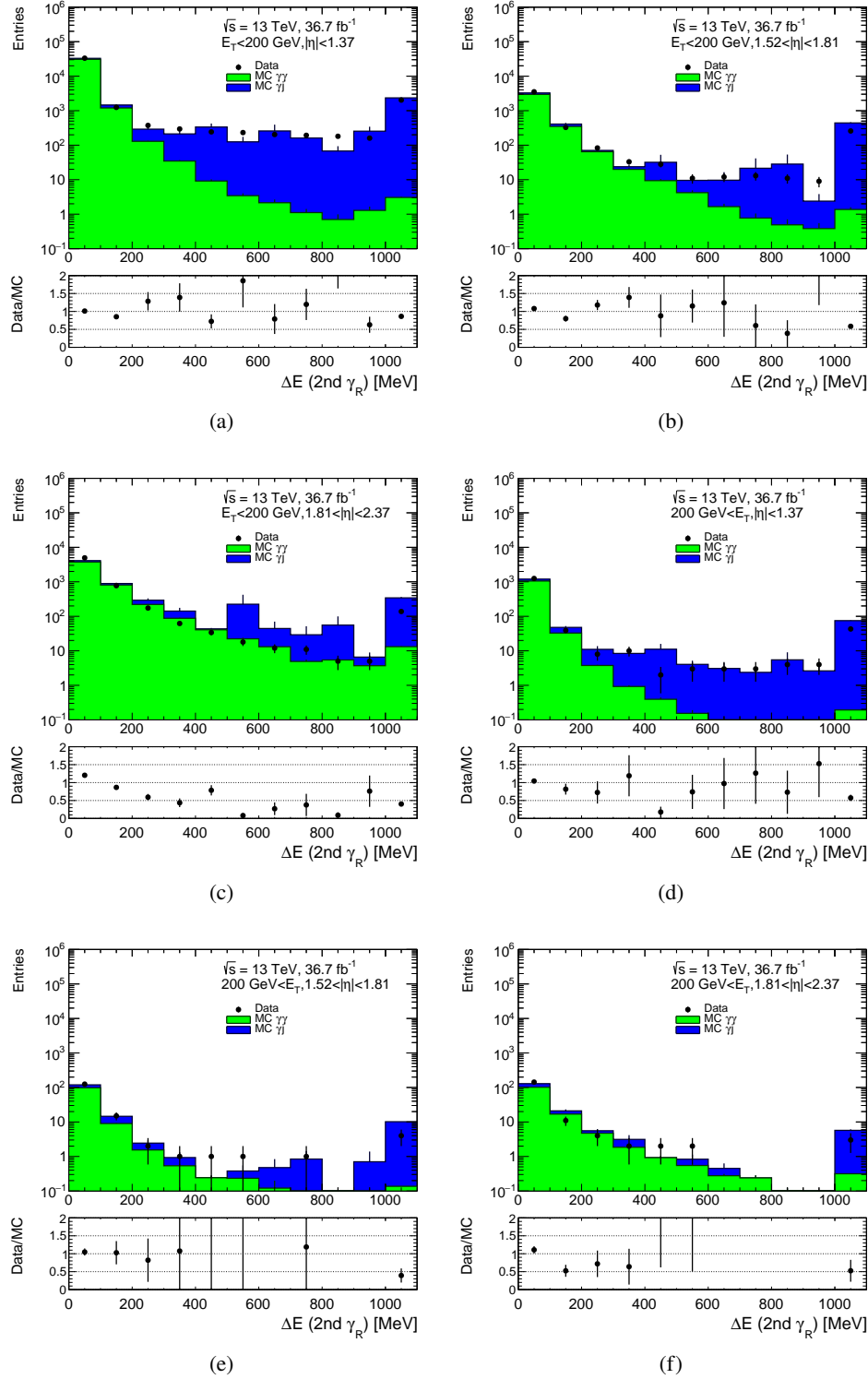
Figure 40: Comparison of the distributions of ΔE obtained from the collision dataset and that from the simulated samples. The distributions are shown for subleading reconstructed photons in the signal region, with additionally Tight photon ID selection applied to the leading reconstructed photon; this is to ensure that the subleading reconstructed photon of the γj simulated sample is originating dominantly from hadronic jets. The ratio of the normalizations of the two simulated samples, $\gamma\gamma$ (green) and γj (blue), is evaluated from their production cross sections. A scaling is applied to the histograms of simulated samples, so that the event yields of the histograms from the collision dataset and that from simulated samples are equal. The comparison is shown for different kinematic regions of the subleading reconstructed photon, namely: (a) $E_{\mathrm{T}} < 200$ GeV, $|\eta| < 1.37$, (b) $E_{\mathrm{T}} < 200$ GeV, $1.52 < |\eta| < 1.81$, (c) $E_{\mathrm{T}} < 200$ GeV, $1.81 < |\eta| < 2.37$, (d) 200 GeV $< E_{\mathrm{T}}, |\eta| < 1.37$, (e) 200 GeV $< E_{\mathrm{T}}, 1.52 < |\eta| < 1.81$, (f) 200 GeV $< E_{\mathrm{T}}, 1.81 < |\eta| < 2.37$.
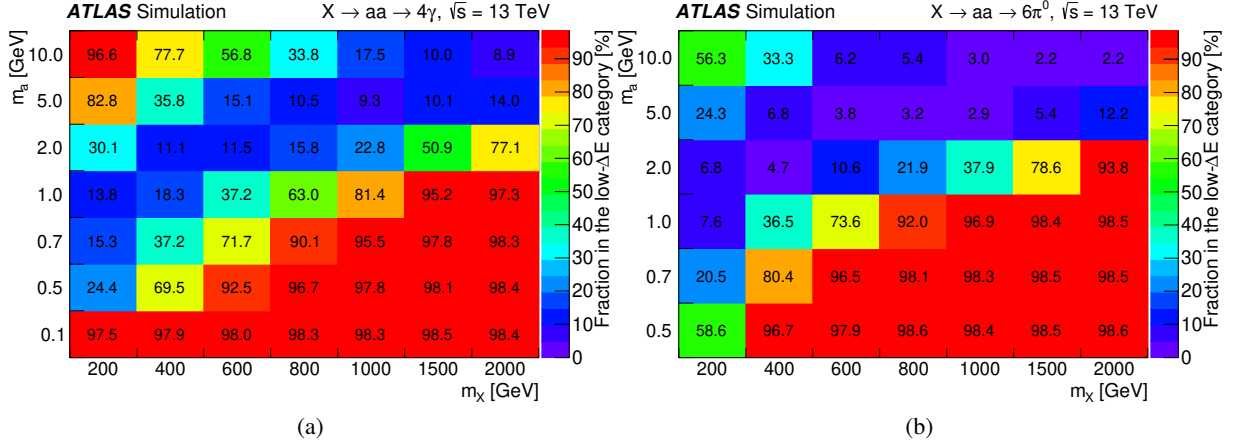
54

Figure 41: The category fraction f as a function of m_X and m_a, for (a) $X \to aa \to 4\gamma$ and (b) $X \to aa \to 6\pi^0$. [72]

Table 8: Number of events in the collision dataset that satisfy the successive selection requirements. Also, the selection efficiency of signal events that satisfy the successive selection requirements, for $X \to aa \to 4\gamma$ calculated using the simulated samples.

		Selection efficiency $X \to aa \to 4\gamma$, $m_X = 600$ GeV	
	Events in collision data	$m_a = 0.1$ GeV	$m_a = 2$ GeV
All triggered events	6.4×10^9	0.86	0.78
Preselection	3.1×10^7	0.73	0.66
Loose$'$ photon selection	1.7×10^7	0.72	0.62
Isolation	2.2×10^6	0.62	0.53
E_T selection	1.7×10^6	0.46	0.43
$m_{\gamma_R \gamma_R} > 175$ GeV	6.7×10^4	0.46	0.43
Low-ΔE category	5.6×10^4	0.46	0.05
High-ΔE category	1.0×10^4	0.01	0.39

$m_a/m_X \simeq 0.0015$ for $X \to aa \to 4\gamma$ and $m_a/m_X \simeq 0.0020$ for $X \to aa \to 6\pi^0$.

The high-ΔE category is found to have a significantly smaller number of background events compared to the low-ΔE category, as seen in Table 8. This is because the events of the main source of the SM background, $\gamma\gamma$, are mostly contained in the low-ΔE category. Hadronic jets from SM processes containing $\pi^0 \to \gamma\gamma$ decays mostly lead to reconstructed photons with large ΔE, but their contribution in the high-ΔE category is small due to the isolation requirements. Thus, the introduction of this categorization increases the sensitivity to photon-jet signals, especially in the region $0.002 < m_a/m_X < 0.01$ by a factor two[15].

As seen in Figure 40, a deviation of ΔE distribution from simulation and that from collision data is observed; this is treated as a source of systematic uncertainty of the category fraction f, as described in Section 5.6.2.

---

[15]The details of the sensitivity estimation using simulated samples are described in Appendix C.

5.4 Signal modelling

As described in Section 5.3 and in detail in Section 5.7, a search for an excess of events from the SM background expectation in the $m_{\gamma_R \gamma_R}$ distributions is performed by a simultaneous fit to the distributions in the two event categories. To perform this, the parametrizations of the probability density function of $m_{\gamma_R \gamma_R}$ of the signal component ("signal mass shape"), signal selection efficiency ε, and category fraction f are necessary. This is because the simulated signal samples are generated only for a few chosen points of (m_X, m_a); it is necessary to evaluate the signal mass shape, ε, and f for any (m_X, m_a) in the parameter region of interest of this search, $m_X > 200$ GeV and $m_a/m_X < 0.01$.

5.4.1 Signal mass shape

As the probability density function of $m_{\gamma_R \gamma_R}$ of the signal component, the double-sided Crystal-Ball (DSCB) function is used. The DSCB function has a Gaussian core surrounded by asymmetric exponential low- and high-mass tails. It is an empirical function that is known to describe a reconstructed invariant mass of a resonance with tails arising from e.g. bremsstrahlung. It is defined as

$$
f_{\mathrm{CB}}\left(m_{\gamma_R \gamma_R}; \mu_{\mathrm{CB}}, \sigma_{\mathrm{CB}}, \alpha_{\mathrm{low}}, \alpha_{\mathrm{high}}, n_{\mathrm{low}}, n_{\mathrm{high}}\right) = N \cdot
\begin{cases}
e^{-v^2/2} & (-\alpha_{\mathrm{low}} \le v \le \alpha_{\mathrm{high}}) \\[2ex]
\dfrac{e^{-\alpha_{\mathrm{low}}^2/2}}{\left[\dfrac{\alpha_{\mathrm{low}}}{n_{\mathrm{low}}}\left(\dfrac{n_{\mathrm{low}}}{\alpha_{\mathrm{low}}} - \alpha_{\mathrm{low}} - v\right)\right]^{n_{\mathrm{low}}}} & (v < -\alpha_{\mathrm{low}}) \\[3ex]
\dfrac{e^{-\alpha_{\mathrm{high}}^2/2}}{\left[\dfrac{\alpha_{\mathrm{high}}}{n_{\mathrm{high}}}\left(\dfrac{n_{\mathrm{high}}}{\alpha_{\mathrm{high}}} - \alpha_{\mathrm{high}} + v\right)\right]^{n_{\mathrm{high}}}} & (\alpha_{\mathrm{high}} < v)
\end{cases}
$$

(60)

where v is defined as $v = (m_{\gamma_R \gamma_R} - \mu_{\mathrm{CB}})/\sigma_{\mathrm{CB}}$, and N is the normalization factor. For signal events, each reconstructed photon corresponds to a photon-jet, and so the reconstructed $m_{\gamma_R \gamma_R}$ corresponds to the mass of the parent particle m_X.

Figure 42 shows examples of a fit of the DSCB function to the $m_{\gamma_R \gamma_R}$ distributions of the simulated signal samples. The width σ_{CB} is determined by the detector resolution. For small values of m_a/m_X ($m_a/m_X \lesssim 0.005$), σ_{CB} increases linearly with m_X from $\sigma_{\mathrm{CB}} = 2$ GeV for $m_X = 200$ GeV to $\sigma_{\mathrm{CB}} = 14$ GeV for $m_X = 2$ TeV. For larger values of m_a/m_X ($m_a/m_X \gtrsim 0.005$), the width σ_{CB} increases further, and also the peak position μ_{CB} decreases. This is because of the wider angular separation of the photons inside a photon-jet; it leads to a greater fraction of the energy of the EM shower leaking out of the window defined by the cells of the EM calorimeter to collect energy for the reconstruction of photons.

The parameters of the DSCB function are parametrized as functions of m_X and m_a using simulated signal samples, so that the $m_{\gamma_R \gamma_R}$ shape for any (m_X, m_a) values can be estimated. The results are presented in Tables 9 and 10 for $X \to aa \to 4\gamma$ and $X \to aa \to 6\pi^0$, respectively. Here, Δm_X is defined as $\Delta m_X = \mu_{\mathrm{CB}} - m_X$, i.e. the shift of the peak position with respect to m_X. Variables t and u are defined as $t = m_X/(100 \text{ GeV})$ and $u = 100 \times m_a/m_X$. The values of n_{low} and n_{high} are fixed to reasonable values prior to the parametrization, and they are chosen to be $n_{\mathrm{low}} = 15$ and $n_{\mathrm{high}} = 5$. The parametrization of the other DSCB parameters are performed by a fit to the best-fit values of each parameter, obtained by performing DSCB function fits to the simulated signal samples.
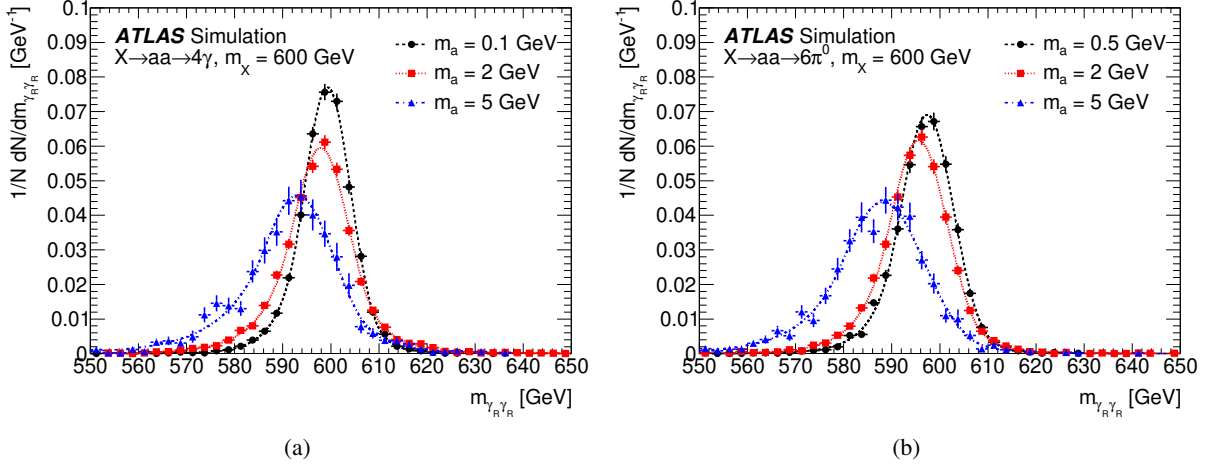
Figure 42: Examples of a fit of the DSCB function to the $m_{\gamma_R\gamma_R}$ distribution of simulated signal samples. They are shown for $m_X = 600$ GeV and different values of m_a, for (a) $X \to aa \to 4\gamma$ and (b) $X \to aa \to 6\pi^0$. They are presented for the signal region, i.e. the combination of the low-ΔE and high-ΔE categories. [72]

Table 9: The result of the parametrization of the signal mass shape for $X \to aa \to 4\gamma$.

Parameter	Parametrization function	A	B	C	D	E
Δm_X [GeV]	$A \times (1 + Bt) \times (1 + Cu + Du^2 + Eu^3)$	-0.0684	1.2	-5.54	50.4	-30.7
σ_{CB} [GeV]	$A \times (1 + Bt) \times (1 + Cu + Du^2 + Eu^3)$	0.991	0.68	0.265	1.81	-1.55
α_{low}	$A + Bu$	1.36	-0.491			
α_{high}	$(A + u)^B + Cu$	0.583	-1.4	1.28		
n_{low}	A	15				
n_{high}	A	5				

As seen in Table 9, the parametrization functions for Δm_X and σ_{CB} are chosen to be a product of two polynomial functions; one function of m_X and one function of m_a/m_X. The former function parametrizes the dependence of Δm_X and σ_{CB} on m_X, especially the linear increase of σ_{CB} with respect to m_X. The latter function parametrizes the dependence of Δm_X and σ_{CB} on m_a/m_X, which is caused by the leakage of the energy of the EM shower from the photon reconstruction window, as described above.

Figures 43, 44, and 45 show the visualization of the parametrization result for $X \to aa \to 4\gamma$. Those for $X \to aa \to 6\pi^0$ are qualitatively the same.

The same mass shape modelling results are used for both the low-ΔE and high-ΔE categories. This is because only a small change in the $m_{\gamma_R\gamma_R}$ distributions due to the categorization is observed. The comparison of the signal mass shape modelling result and the $m_{\gamma_R\gamma_R}$ distribution of each event category is presented in Figure 46.

Table 10: The result of the parametrization of the signal mass shape for $X \to aa \to 6\pi^0$.

Parameter	Parametrization function	A	B	C	D	E
Δm_X [GeV]	$A \times (1 + Bt) \times (1 + Cu + Du^2 + Eu^3)$	-0.807	0.115	3.93	10.9	-5.57
σ_{CB} [GeV]	$A \times (1 + Bt) \times (1 + Cu + Du^2 + Eu^3)$	1.65	0.394	-0.234	2.35	-1.49
α_{low}	$A + Bu$	1.36	-0.276			
α_{high}	$(A + u)^B + Cu$	0.411	-0.913	1.34		
n_{low}	A	15				
n_{high}	A	5				
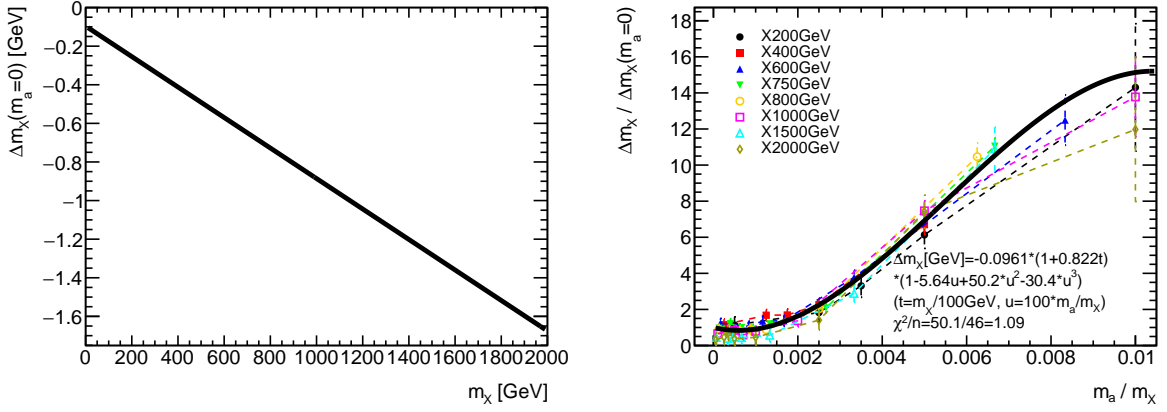
Figure 43: The parametrization of Δm_X for $X \to aa \to 4\gamma$. The lines represent the result of the parametrization that is shown in Table 9. (Left) The first two factors of the parametrization function, $A \times (1 + Bt)$. (Right) The third factor of the parametrization function, $(1 + Cu + Du^2 + Eu^3)$. The markers represent the best-fit values of Δm_X obtained from the fit of the DSCB function to the simulated signal samples, divided by $A \times (1 + Bt)$. The bars represent the statistical uncertainty arising from the DSCB function fit.
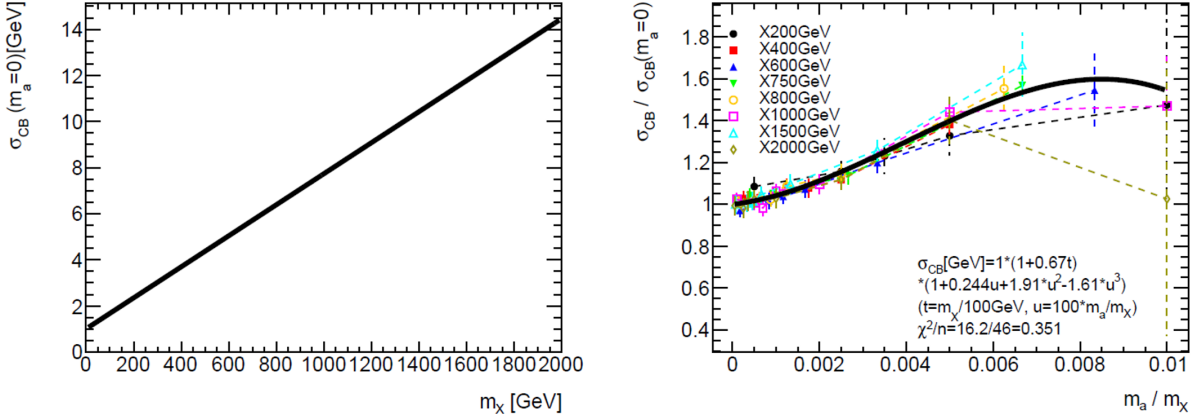
Figure 44: The parametrization of σ_{CB} for $X \to aa \to 4\gamma$. The lines represent the result of the parametrization that is shown in Table 9. (Left) The first two factors of the parametrization function, $A \times (1 + Bt)$. (Right) The third factor of the parametrization function, $(1 + Cu + Du^2 + Eu^3)$. The markers represent the best-fit values of σ_{CB} obtained from the fit of the DSCB function to the simulated signal samples, divided by $A \times (1 + Bt)$. The bars represent the statistical uncertainty arising from the DSCB function fit.
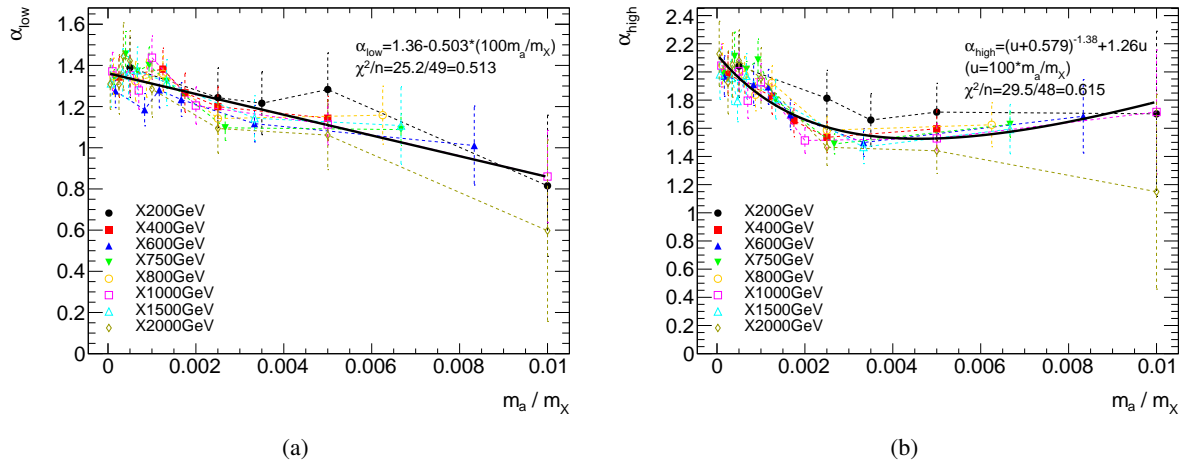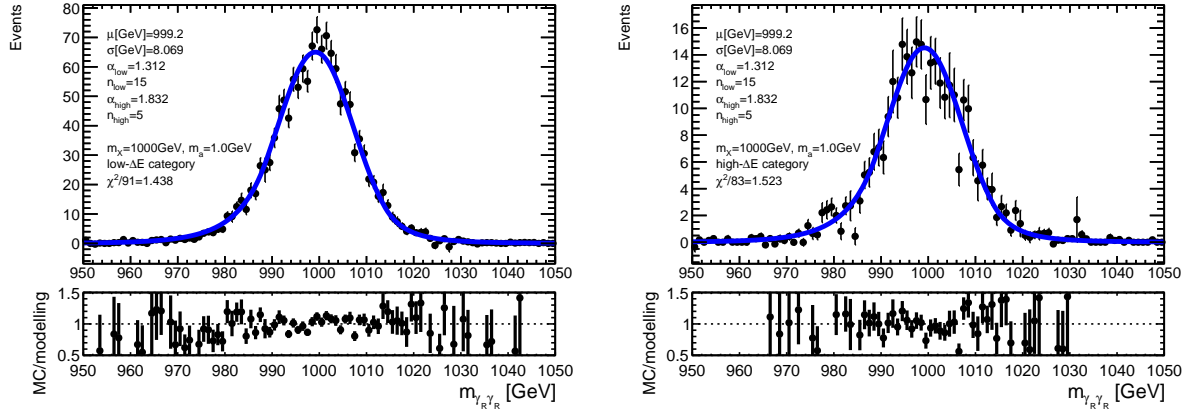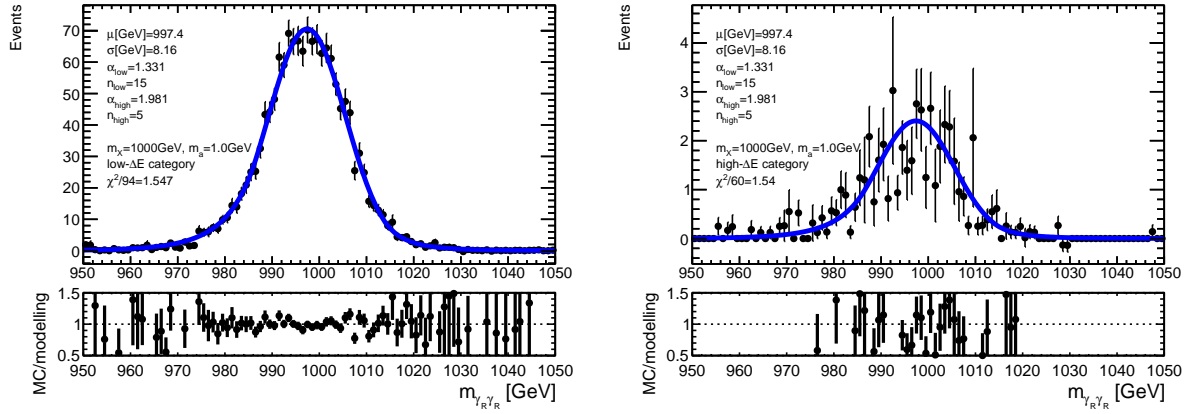
Figure 45: The parametrization of (a) α_{low} and (b) α_{high} for $X \rightarrow aa \rightarrow 4\gamma$. The lines represent the result of the parametrization that is shown in Table 9. The markers represent the best-fit values of each variable obtained from the fit of the DSCB function to the simulated signal samples. The bars represent the statistical uncertainty arising from the DSCB function fit.

(a)

(b)

Figure 46: Comparison of the signal mass shape modelling result and the $m_{\gamma_R\gamma_R}$ distribution of the simulated signal samples. This is presented for $m_X = 1000$ GeV, $m_a = 1$ GeV for (a) $X \to aa \to 4\gamma$ and (b) $X \to aa \to 6\pi^0$. The diagrams on the left are for the low-ΔE category, and those on the right are for the high-ΔE category.

5.4.2 Signal selection efficiency

The signal selection efficiency ε is parametrized as a function of m_X and m_a using simulated signal samples, so that its value can be estimated for any (m_X, m_a). ε is defined by Eq. (58). As described in Section 5.3.1, the value of ε increases for larger m_X because of the E_T, $|\eta|$, and isolation requirements. It also decreases for larger m_a/m_X, because a larger m_a/m_X leads to wider EM shower, and such events are rejected by the trigger-level Loose ID selection and additionally the isolation requirement. The parametrization of ε is used for the calculation of the cross section times branching ratios from observed number of events for the benchmark signal scenarios.

The parametrization of ε is performed with 2 different methods: (1) a function of m_X for separate values of m_a, and (2) a function of m_X and m_a. The first method uses the following parametrization:

$$\varepsilon(m_X) = \frac{A}{1 + B \exp\left(\frac{C}{m_X}\right)} + D \tag{61}$$

The second method uses the following parametrization:

$$\varepsilon(m_X, m_a) = A \cdot [1 - B \exp(-C m_X)] \cdot \left[\frac{1}{1 + D \exp\left(E \frac{m_a}{m_X}\right)} + F \right] + G \tag{62}$$

The first method is used for the evaluation of upper limits on the production cross section times branching ratios of the benchmark signal scenario as a function of m_X for different values of m_a, as shown in Figure 64(a) in Section 5.8.2. The second method is used for the evaluation of the upper limits as a function of m_a/m_X, as shown in Figure 64(b) in the same section. These two different methods are used because the first method gives smaller systematic uncertainties compared to the second method, and so the first method is optimal for the evaluation of upper limits as a function of m_X.

The result of the first method is shown in Figure 47 for $X \to aa \to 4\gamma$. That for $X \to aa \to 6\pi^0$ is qualitatively the same, because the two benchmark signal scenarios share similar characteristics, as described in Section 5.2. The ratio of the value of ε obtained from simulated samples and that from the parametrization is also presented in the figure. An envelope to cover these ratios, as shown in the lower panels of Figure 47, is taken as a source of systematic uncertainty in the parametrization of ε.

The result of the second method is shown in Figure 48. The ratio of the value of ε obtained from simulated samples and that from the parametrization is also shown. An envelope to cover these ratios is taken as a source of systematic uncertainty in the parametrization. The evaluation of the second method is limited to $\frac{m_a}{m_X} \leq 0.007$, because this parametrization gives large deviation from the values of ε from simulated samples ($\sim 80\%$) for larger values of m_a/m_X. This is because the assumption that ε can be parametrized by Eq. (62) breaks down in this region.
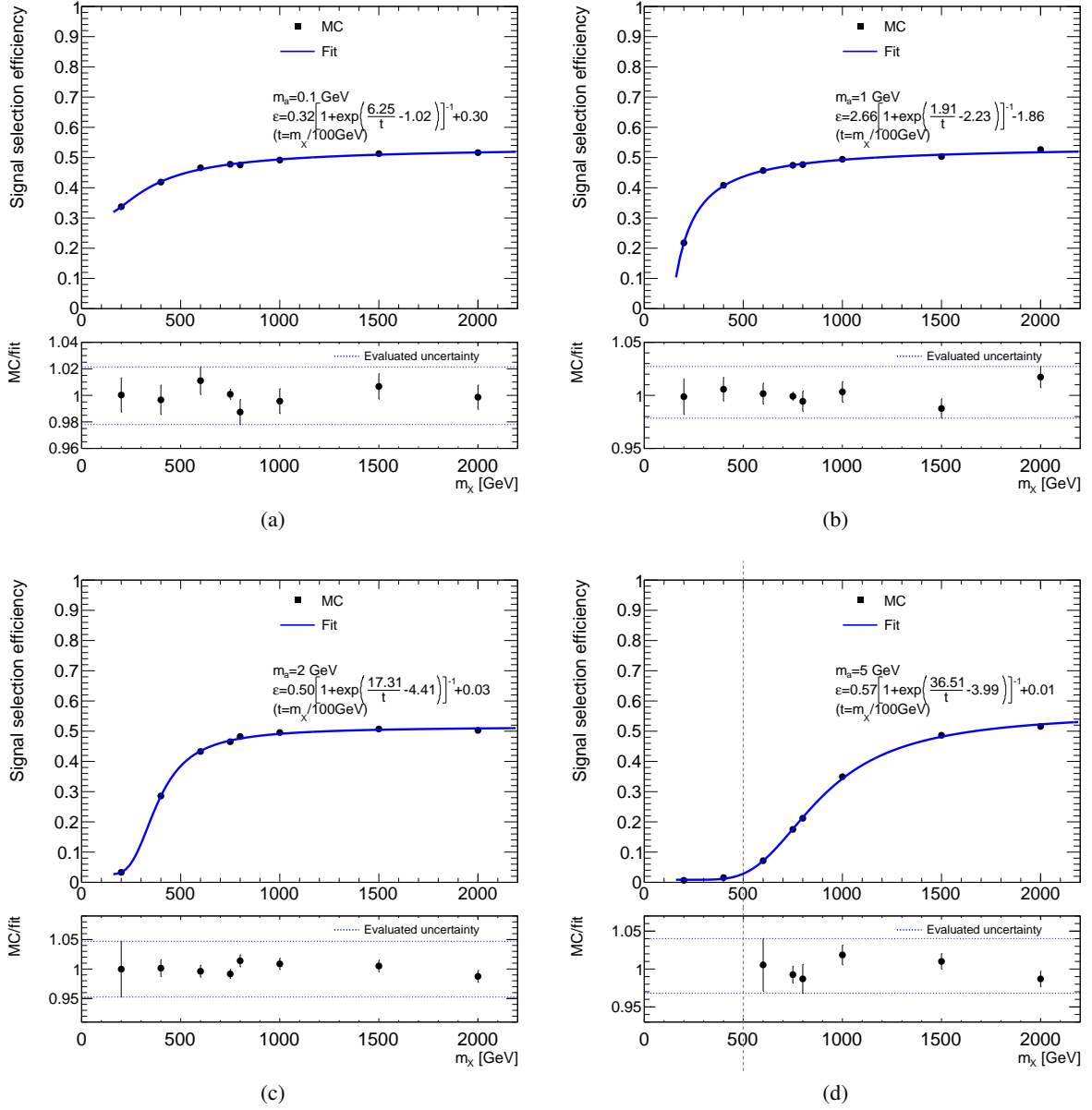
Figure 47: Parametrization of ε as a function of m_X for $X \to aa \to 4\gamma$, for (a) $m_a = 0.1$ GeV, (b) $m_a = 1$ GeV, (c) $m_a = 2$ GeV, and (d) $m_a = 5$ GeV. The lower panels show the ratio of the value of ε obtained from simulated signal samples and that from the parametrization. The systematic uncertainty of this parametrization is evaluated by an envelope to cover the deviations, as shown with horizontal blue dotted lines in the lower panels. For (d), the parametrization is limited to $m_X > 500$ GeV because the parameter region of interest is limited to $m_a < 0.01 \times m_X$.
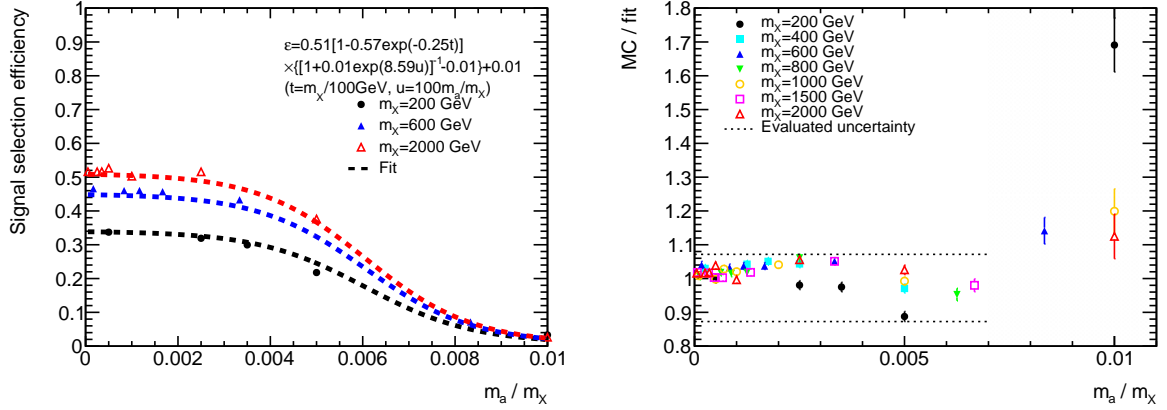
Figure 48: Parametrization of ε as a function of m_X and m_a for $X \rightarrow aa \rightarrow 4\gamma$. (Left) The comparison of the parametrization with the values of ε obtained from simulated signal samples, for the cases $m_X = 200$ GeV, 600 GeV, and 2000 GeV. (Right) The ratio of the value of ε obtained from simulated signal samples and that from the parametrization. The systematic uncertainty of this parametrization is evaluated by defining an envelope to cover the deviations, as shown with horizontal dotted lines.

5.4.3 Category fraction

The category fraction f is parametrized as a function of m_X and m_a using simulated signal samples, so that its value can be estimated for any (m_X, m_a). f is defined by Eq. (59). As described in Section 5.3.2, the value of f decreases for larger m_a/m_X, because a larger m_a/m_X leads to larger ΔE of reconstructed photons. The value of f serves as an input to the simultaneous fit to the $m_{\gamma_R\gamma_R}$ distributions, as described in Section 5.7.

The values of f are taken from simulated samples and a third-order spline interpolation is performed as a function of m_a/m_X[16]. For $X \rightarrow aa \rightarrow 4\gamma$, f is parametrized as a function of the ratio m_a/m_X. For $X \rightarrow aa \rightarrow 6\pi^0$, it is parametrized as a function of $\frac{m_a}{m_X} \cdot \frac{1}{\sqrt{1+(3m_{\pi^0}/m_a)^2}}$, where m_{π^0} is the mass of π^0. These variables are chosen because they are roughly proportional to the angular separation of photons consisting a photon-jet. The results of these interpolations are presented in Figures 49 and 50. An envelope to cover the deviations of the values of f from simulation and the interpolation is taken as a source of systematic uncertainty in the parametrization of f, and this is also presented in Figures 49 and 50. The envelope is defined with a function of the form $A\sqrt{f(1-f)}$, which is similar to a function commonly used to estimate the uncertainty of the mean of a binomial distribution. The result of the modelling of f is mostly the same for the two benchmark signal scenarios, $X \rightarrow aa \rightarrow 4\gamma$ and $X \rightarrow aa \rightarrow 6\pi^0$. The main distinction is in the different trend in f with respect to m_X and m_a, especially the threshold of m_a/m_X for f to transition from $f > 0.5$ to $f < 0.5$. This threshold is $m_a/m_X \simeq 0.0015$ for the decay $X \rightarrow aa \rightarrow 4\gamma$, and $m_a/m_X \simeq 0.0020$ for $X \rightarrow aa \rightarrow 6\pi^0$.

---

[16]The simulated signal samples for $m_X = 750$ GeV is used for the interpolation, because these samples have the most statistics of generated events compared to other simulated samples.
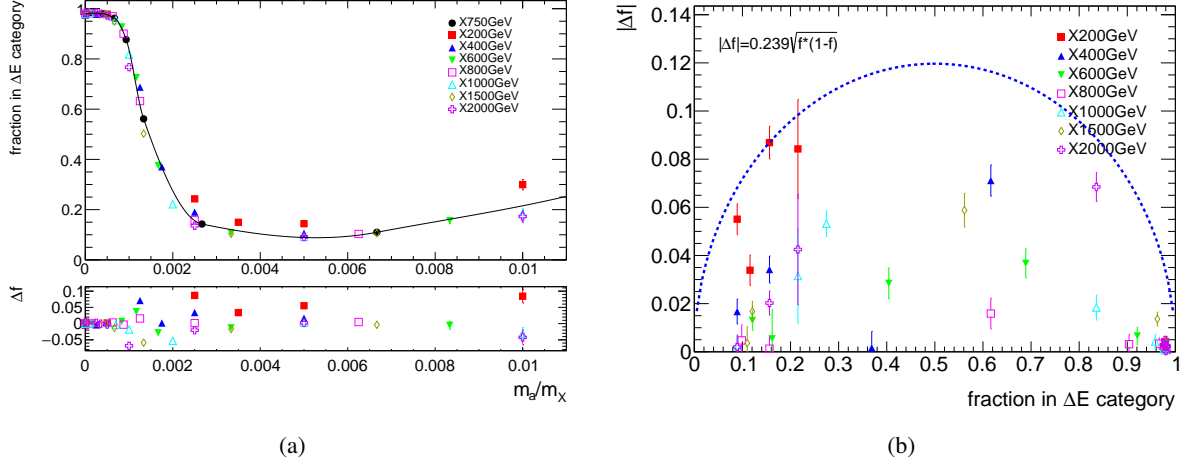
Figure 49: (a) Parametrization of f as a function of m_X and m_a for $X \rightarrow aa \rightarrow 4\gamma$. (b) The deviation of the values of f obtained from simulated samples and those from the parametrization, Δf. It is plotted with respect to the value of f obtained from the parametrization (i.e. the black line in Figure (a)). An envelope to cover the values of Δf is presented with a blue dotted line.
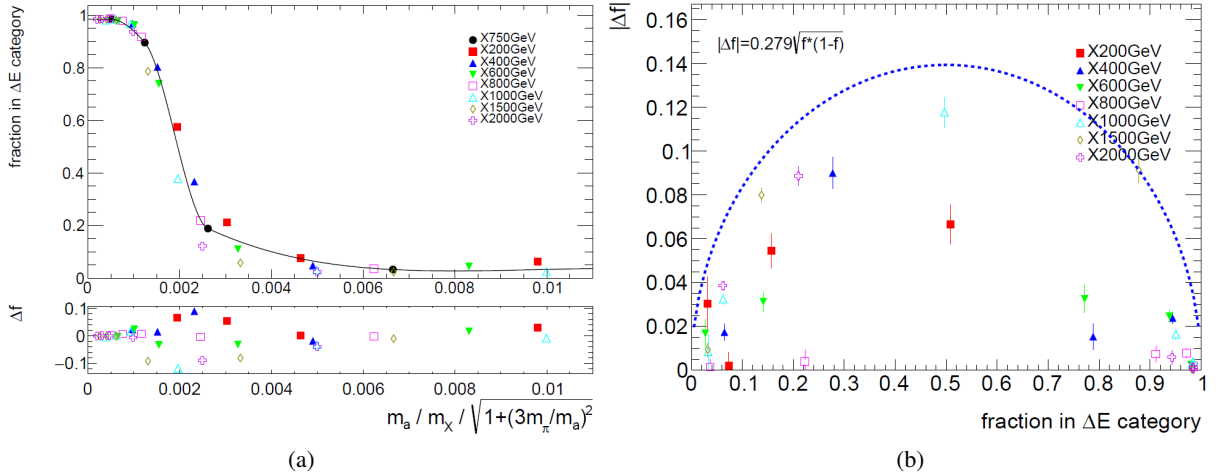

Figure 50: (a) Parametrization of f as a function of m_X and m_a for $X \rightarrow aa \rightarrow 6\pi^0$. (b) The deviation of the values of f obtained from simulated samples and those from the parametrization, Δf. It is plotted with respect to the value of f obtained from the parametrization (i.e. the black line in Figure (a)). An envelope to cover the values of Δf is presented with a blue dotted line.

5.5 Background modelling

The SM backgrounds in this search consist of mainly three components, $\gamma\gamma$, γj or $j\gamma$, and jj, as described in the beginning of Section 5. The $m_{\gamma_R\gamma_R}$ distribution of the sum of these components is evaluated by an analytic function, separately for each of the two ΔE categories. The parameters of these two analytic functions are determined from a fit to the $m_{\gamma_R\gamma_R}$ distributions of each event category of the collision data in the region $m_{\gamma_R\gamma_R} > 175$ GeV.

The analytic function to be used in the analysis is chosen from a family of functions [17] adapted from those used by searches for new physics signatures in dijet final states [73]:

$$g_k\left(x; a, \{b_j\}_{j=0,k}\right) = N \left(1 - x^{\frac{1}{2}}\right)^a x^{\sum_{j=0}^{k} b_j (\log x)^j} \tag{63}$$

The variable x is defined as $x = m_{\gamma_R\gamma_R}/\sqrt{s}$. The parameters a and b_j are free parameters and N is the normalization factor. The value of k is chosen so that the analytic function evaluates the $m_{\gamma_R\gamma_R}$ distribution of the background component well, i.e. the associated systematic uncertainty is minimal. This choice is made by performing the "Spurious Signal test", which evaluates the systematic uncertainty arising from the choice of the analytic function, as described in Section 5.5.3. The test uses a dataset that reproduces the $m_{\gamma_R\gamma_R}$ distributions of the two event categories of the collision dataset (the "background template"), as described in Section 5.5.2. Prior to the derivation of the background template, the measurement of the composition of the background component is performed, as described in Section 5.5.1.

5.5.1 Background composition measurement

The background composition is measured using the matrix method [74], which uses the difference in the calorimeter isolation energy of photons and hadronic jets, to decompose the event yields into four components, $\gamma\gamma, \gamma j, j\gamma$, and jj. The method is described in detail below.

For each of the two event categories, a region is defined where the calorimeter isolation requirement is removed and all the other requirements are identical to the signal region. The events in this region of the collision dataset are divided into four subsets by whether both, only the leading, only the subleading, or neither of the two leading reconstructed photons satisfy the calorimeter isolation requirement, as shown in Figure 51. The number of events in each subset is denoted by $F^{\text{Pass, Pass}}$, $F^{\text{Pass, Fail}}$, $F^{\text{Fail,Pass}}$, and $F^{\text{Fail, Fail}}$, respectively. The number of events of each background component in the region, $F_{\gamma\gamma}, F_{\gamma j}, F_{j\gamma}$, and F_{jj}, can be determined by solving the following equation:

$$\begin{pmatrix} F^{\text{Pass, Pass}} \\ F^{\text{Pass, Fail}} \\ F^{\text{Fail, Pass}} \\ F^{\text{Fail, Fail}} \end{pmatrix} = \begin{pmatrix} \varepsilon_1\varepsilon_2 & \varepsilon_1 f_2 & f_1\varepsilon_2 & f_1 f_2 \\ \varepsilon_1(1-\varepsilon_2) & \varepsilon_1(1-f_2) & f_1(1-\varepsilon_2) & f_1(1-f_2) \\ (1-\varepsilon_1)\varepsilon_2 & (1-\varepsilon_1)f_2 & (1-f_1)\varepsilon_2 & (1-f_1)f_2 \\ (1-\varepsilon_1)(1-\varepsilon_2) & (1-\varepsilon_1)(1-f_2) & (1-f_1)(1-\varepsilon_2) & (1-f_1)(1-f_2) \end{pmatrix} \begin{pmatrix} F_{\gamma\gamma} \\ F_{\gamma j} \\ F_{j\gamma} \\ F_{jj} \end{pmatrix} \tag{64}$$

Here, ε_1 and ε_2 denote the rate at which a prompt photon satisfies the calorimeter isolation requirement ("isolation efficiency") for the leading and the subleading reconstructed photon, respectively. Similarly,

---

[17]These functions are motivated by the similarity to the PDF parametrization functions, and have been known empirically to be applicable to background probability density functions of resonance searches.
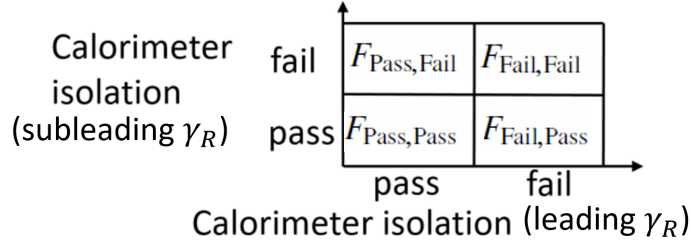
Figure 51: Schematic diagram illustrating the background composition measurement using the matrix method. Note that the region in the bottom left (corresponding to $F^{\text{Pass, Pass}}$) corresponds to the signal region.

f_1 and f_2 denote the rate at which a hadronic jet satisfies the calorimeter isolation requirement ("isolation fake rate"). The values of ε_1, ε_2, f_1 and f_2 are given as inputs to the matrix method.

The isolation efficiencies ε_1 and ε_2 are estimated using simulated samples of prompt photons. As described in Section 4.3, the calorimeter isolation variable of reconstructed photons in simulated samples are adjusted by applying data-driven correction factors. A systematic uncertainty for the estimation of the isolation efficiency is evaluated by comparing the nominal value with that derived without these correction factors applied.

The isolation fake rates f_1 and f_2 are estimated using subsets of collision data that are similar and orthogonal to the signal region ("control regions"), with the procedures described below:

- **Central values:** The central values of the isolation fake rates f_1 and f_2 are estimated using subsets of collision data in the control region. The control regions are defined by requiring the reconstructed photon to fail the baseline Loose′5 photon selection and satisfy the Loose′7 photon selection (defined in Table 6). The Loose′7 photon selection is a looser photon selection requirement compared to the Loose′5.

- **Systematic uncertainty arising from the definition of the control region:** The systematic uncertainty of the fake rate arising from the definition of the control region is evaluated as the change in the value obtained by alternatively using the Loose′6 (defined in Table 6) instead of the Loose′7.

- **Systematic uncertainty arising from the difference in the $E_{\text{T}}^{\text{iso}}$ distributions:** A shift of approximately 1 GeV is observed for the distribution of the calorimeter isolation energy $E_{\text{T}}^{\text{iso}}$ between the signal and control regions using simulated samples of hadronic jets. The effect of this shift in the result is accounted for by shifting the threshold of the isolation requirement by ± 1 GeV, determining the resulting change in the fake rates, and assigning this change as a systematic uncertainty.

Table 11 summarizes the obtained values of the isolation efficiency and fake rate, together with their associated uncertainties.

Finally, the composition of the background components in each of the two event categories is obtained by the following equation:

$$
\begin{aligned}
F_{\gamma\gamma}^{\text{Pass,Pass}} &= \varepsilon_1 \varepsilon_2 F_{\gamma\gamma} \\
F_{\gamma j}^{\text{Pass,Pass}} &= \varepsilon_1 f_2 F_{\gamma j} \\
F_{j\gamma}^{\text{Pass,Pass}} &= f_1 \varepsilon_2 F_{j\gamma} \\
F_{jj}^{\text{Pass,Pass}} &= f_1 f_2 F_{jj}
\end{aligned}
\tag{65}
$$

Table 11: Estimated calorimeter isolation efficiency and fake rate for events in the region where the calorimeter isolation requirement is removed and all the other requirements are identical to the corresponding event category. The associated statistical uncertainty is derived from the dataset used for the evaluation, and the systematic uncertainty is derived with the procedures described in the text.

	Low-ΔE category	High-ΔE category
ε_1	$0.927 \pm 0.006(\text{stat}) \pm 0.003(\text{syst})$	$0.874 \pm 0.007(\text{stat}) \pm 0.006(\text{syst})$
ε_2	$0.862 \pm 0.007(\text{stat}) \pm 0.004(\text{syst})$	$0.793 \pm 0.009(\text{stat}) \pm 0.006(\text{syst})$
f_1	$0.220 \pm 0.017(\text{stat}) \pm 0.079(\text{syst})$	$0.206 \pm 0.005(\text{stat}) \pm 0.058(\text{syst})$
f_2	$0.209 \pm 0.011(\text{stat}) \pm 0.068(\text{syst})$	$0.171 \pm 0.004(\text{stat}) \pm 0.051(\text{syst})$

Table 12: The measured background compositions for the two event categories. [72] Note that they add up to 1 for each event category.

	Low-ΔE category	High-ΔE category
$\gamma\gamma$	$0.930^{+0.027}_{-0.031}$	0.48 ± 0.16
γj	$0.051^{+0.021}_{-0.018}$	$0.32^{+0.08}_{-0.09}$
$j\gamma$	$0.014^{+0.004}_{-0.005}$	$0.108^{+0.001}_{-0.016}$
jj	$0.005^{+0.006}_{-0.003}$	$0.09^{+0.09}_{-0.05}$

The resulting background composition is shown in Table 12.

Figure 52 presents the validation of the result of the background composition measurement. This figure compares the distribution of the calorimeter isolation energy E_T^iso obtained from the collision dataset and that obtained as a result of the background composition measurement. Both distributions agree within their associated uncertainties.
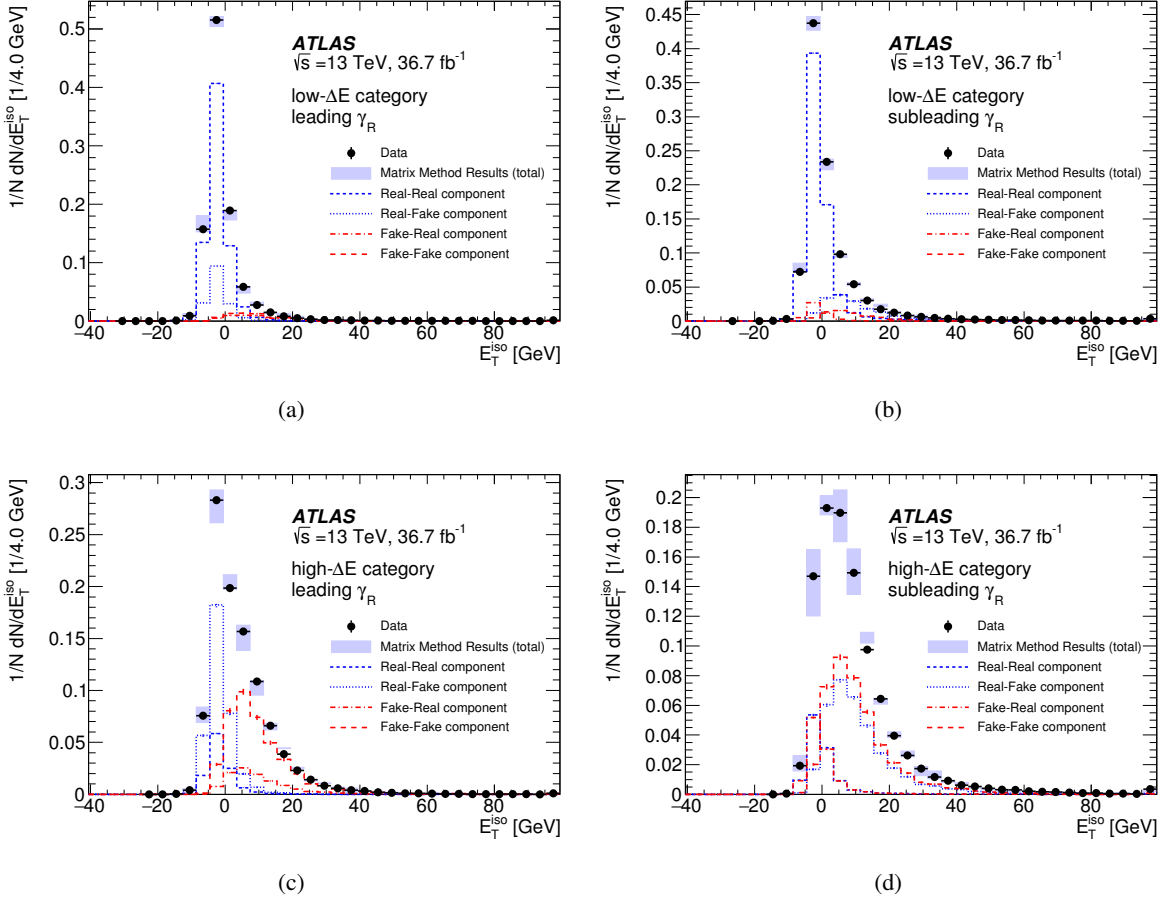
(a)

(b)

(c)

(d)

Figure 52: Comparison of the calorimeter isolation energy E_T^{iso} distribution of the collision dataset and the expected distribution based on the background composition measurement results. The distributions of the $\gamma\gamma$ component (dashed) obtained from simulated samples of prompt photons, and the γj (dotted), $j\gamma$ (dot-dashed), and jj (long-dashed) components obtained from the control region of the collision dataset, are added using the background composition measured with the matrix method. The results are compared for each of the two event categories where they are shown for (a) the leading reconstructed photon in the low-ΔE category, (b) the subleading reconstructed photon in the low-ΔE category, (c) the leading reconstructed photon in the high-ΔE category, and (d) the subleading reconstructed photon in the high-ΔE category. These plots present the validation of the background composition measurement result, as described in the text. [72]

5.5.2 Background template

The background templates are determined using both the simulation and collision data, separately for each of the two event categories.

For the background $\gamma\gamma$ component, a simulated sample of prompt diphoton events is used.

For the background γj, $j\gamma$, and jj components, the subsets of collision data that are similar but orthogonal to the signal region are used. For γj, a subset with the subleading reconstructed photon failing the default isolation requirement and satisfying a looser one is used. Similarly, for $j\gamma$, a subset with the leading reconstructed photon failing the default isolation requirement and satisfying a looser one is used. For jj, a subset with both leading reconstructed photons failing the default isolation requirement and satisfying a looser one is used. The looser requirement mentioned above is defined by loosening the threshold for the calorimeter isolation variable to $E_{\mathrm{T}}^{\mathrm{iso}} < 7$ GeV. The choice of this selection for the γj, $j\gamma$, and jj components is validated using simulated samples of SM γj and jj events; the shape of the $m_{\gamma_R\gamma_R}$ distribution for events satisfying this requirement is identical to that for events contained in the signal region, within the statistical uncertainty.

The resulting samples of $\gamma\gamma$, γj, $j\gamma$, and jj are summed to derive the background templates, scaled with the background composition results given in Table 12. The resulting background template is presented in Figure 53. Figure 54 shows the comparison of the background template and the $m_{\gamma_R\gamma_R}$ distribution obtained from the collision dataset. This figure shows the level of agreement between the two.
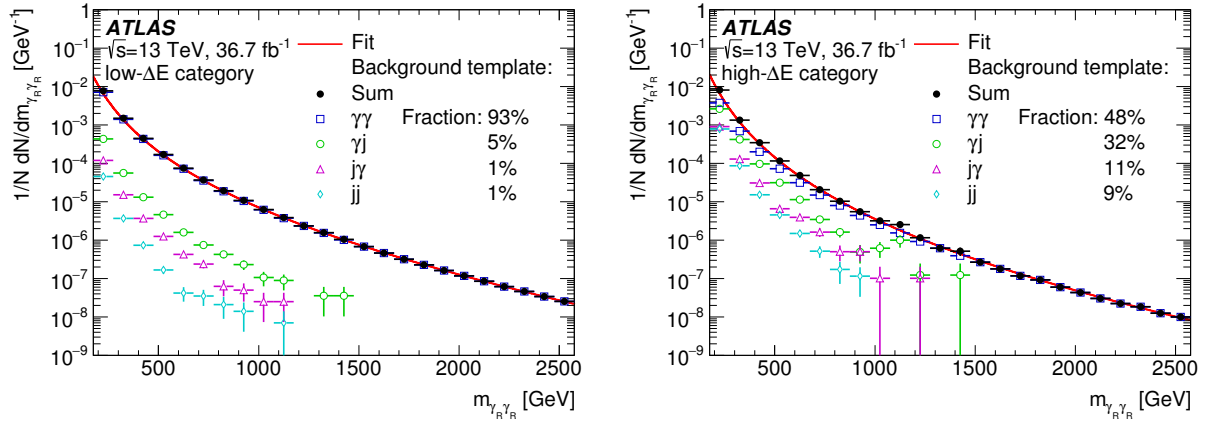

Figure 53: Background templates obtained from the sum of the background components for each of the two event categories. The breakdown into components ($\gamma\gamma$, γj, $j\gamma$, and jj) is also shown. The unbinned likelihood fit with an analytic function (Eq. (63) with $k = 1$) is superimposed. [72]
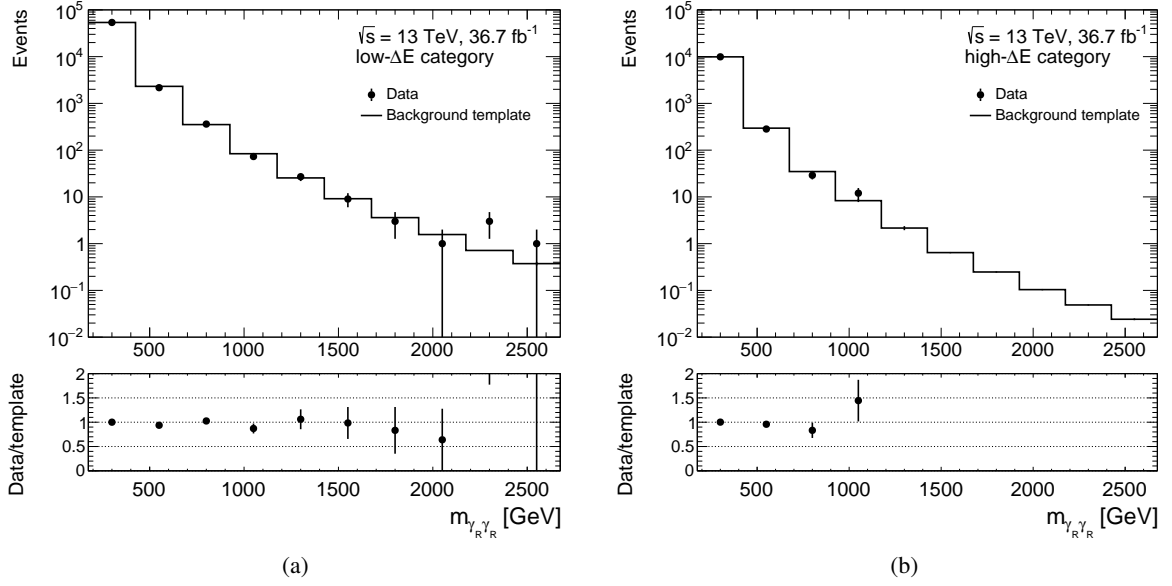
Figure 54: Comparison of the background template (shown in Figure 53) and the $m_{\gamma_R\gamma_R}$ distribution obtained from the collision dataset. The bin width is set to be large (250 GeV) with the purpose of blinding; because the signal mass shape width σ_{CB} is 30 GeV at most for the parameter region of interest of this search, an excess of events due to a possible existence of signal events is not visible in this figure. A scaling is applied to the background template, so that the event yields of the background template and the distribution of the collision dataset are equal. The comparison is shown for (a) low-ΔE category and (b) high-ΔE category.

5.5.3 Spurious signal test

The Spurious Signal test is performed to evaluate the size of the systematic uncertainty associated to the analytic function fit, and to decide the analytic function to be used as the background probability density function. The functions defined in Eq. (63) are tested. The "Spurious Signal" is defined as the potential bias toward the identification of signal events when none is present, i.e. the systematic uncertainty associated to the choice of the background probability density function. The size of the Spurious Signal, S, is estimated by performing an unbinned maximum-likelihood fit to the background template of each event category, using the sum of the signal and background probability density functions; the normalization of the signal probability density function is taken as the value of S. For the signal probability density function, the signal mass shape modelling described in Section 5.4.1 is used. The background templates are normalized to the number of events observed in each event category of the collision dataset. The Spurious Signal is allowed to be negative as well as positive.

The result of the Spurious Signal test is shown in Figures 55 and 56, with the signal mass shape for $X \rightarrow aa \rightarrow 4\gamma$. For this result, Eq. (63) with $k = 1$ is tested as the analytic function. Additionally in Figure 56, the estimated statistical uncertainty of the 37 fb^{-1} dataset associated to the signal yield is shown[18]. It is found that this analytic function has associated Spurious Signals that are considerably small, i.e. smaller than 30% of the estimated statistical uncertainty for most of the range of m_X. Thus, this analytic function (Eq. (63) with $k = 1$) is chosen as the background probability density function, because

---

[18]This estimation of the statistical uncertainty is performed by calculating the uncertainty associated to S arising from the fit, without the consideration of the weights of the background template.

the associated systematic uncertainty is evaluated to be sufficiently small. Figure 53 shows the level of agreement between this analytic function and the background templates.

The size of the Spurious Signal is taken as the source of systematic uncertainty associated to the background modelling. In order to have a continuous parametrization of the Spurious Signal as a function of m_X, the parametrization of Spurious Signal is performed with the function defined as

$$\sigma_{\text{Spurious}}(m_X) = \left[1 - \left(\frac{m_X}{\sqrt{s}} \right) \right]^a \left(\frac{m_X}{\sqrt{s}} \right)^{b + c \log \frac{m_X}{\sqrt{s}}} \tag{66}$$

This function is chosen considering a similarity with Eq. (63). The result of the parametrization of the Spurious Signal is presented in Figures 55 and 56.

The same parametrized result of the Spurious Signal is used as the systematic uncertainty of the background modelling when combined with the signal mass shape for $X \rightarrow aa \rightarrow 6\pi^0$ as well. It is checked that the result of the Spurious Signal test performed with the signal mass shape modelling of $X \rightarrow aa \rightarrow 4\gamma$ and that of $X \rightarrow aa \rightarrow 6\pi^0$ are in agreement, within the statistical uncertainty associated to the values of the Spurious Signal.

The test result is validated by checking that similar results are obtained when the Spurious Signal test is performed using variations of the background templates, for which the background compositions are shifted within the uncertainties presented in Table 12. When the fraction of the $\gamma\gamma$ component is shifted up and those for other components are shifted down, or vice versa, the size of the resulting Spurious Signals are consistent within the statistical uncertainty of the background templates.
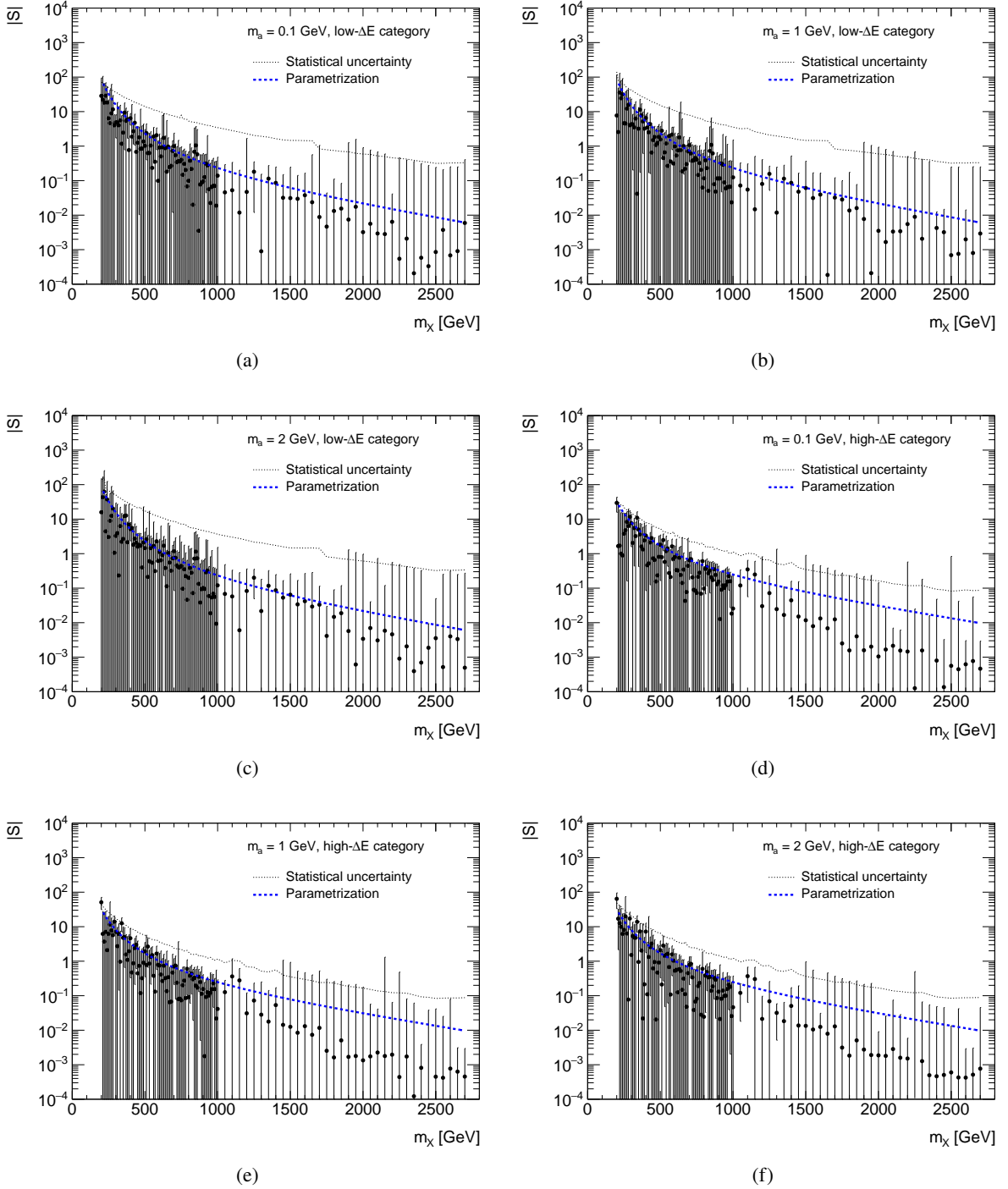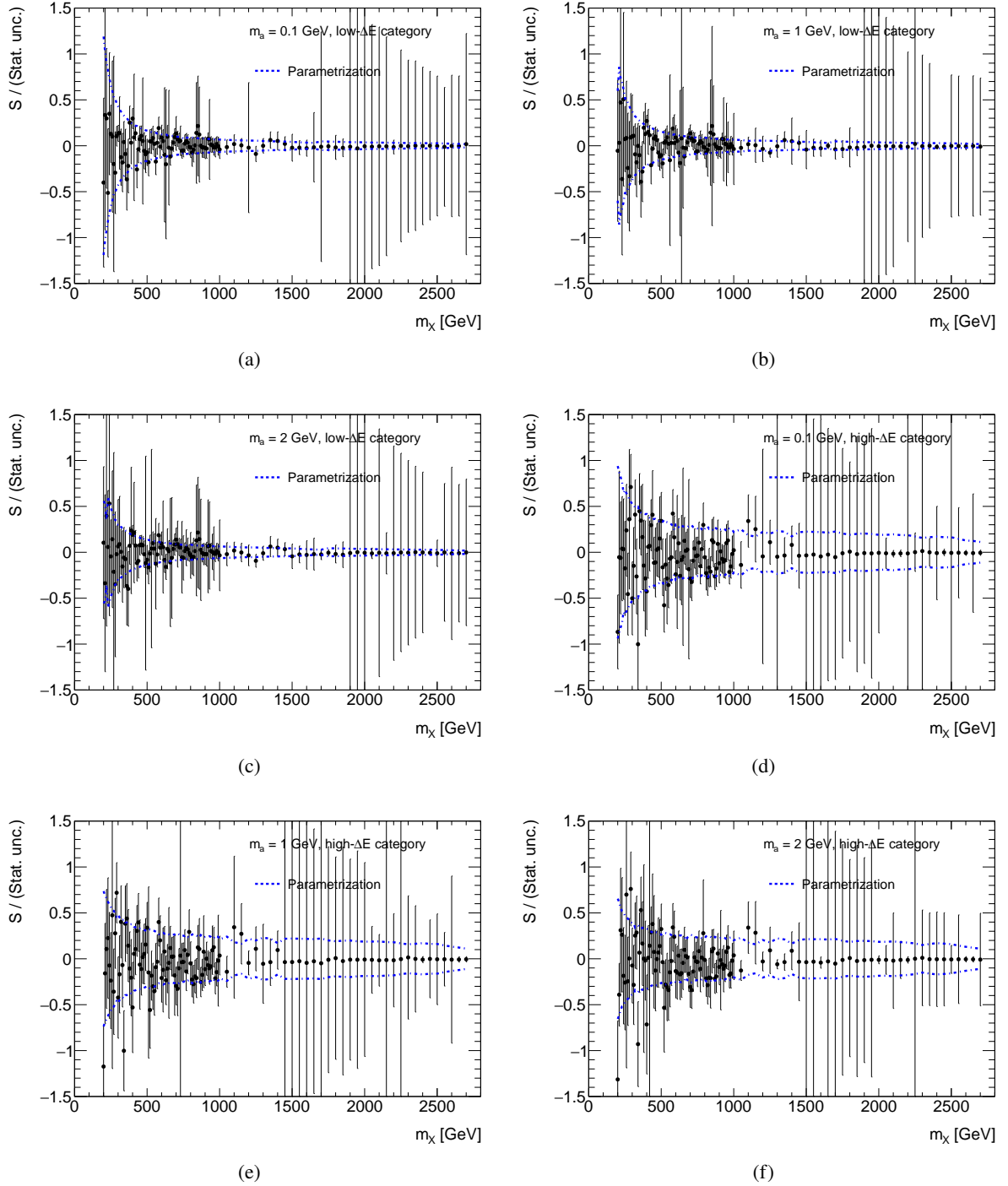
Figure 55: Result of the Spurious Signal test performed with the signal mass shape modelling result for $X \rightarrow aa \rightarrow 4\gamma$. The size of the Spurious Signal is displayed as a function of m_X. The bars represent the uncertainty of the Spurious Signal, evaluated with the consideration of the weights of the background template. The black dotted line represents the estimated statistical uncertainty of the 37 fb^{-1} dataset associated to the signal yield. The blue dashed line represents the parametrization of the Spurious Signal as a function of m_X. (a), (b), and (c) are for the low-ΔE category and different values of m_a. (d), (e), and (f) are for the high-ΔE category and different values of m_a.

Figure 56: Result of the Spurious Signal test performed with the signal mass shape modelling result for $X \rightarrow aa \rightarrow 4\gamma$. The vertical axis represents the ratio $S/\delta S$, where S is the size of the Spurious Signal, and δS is the estimated statistical uncertainty of the 37 fb^{-1} dataset associated to the signal yield. The bars represent the uncertainty of the Spurious Signal, evaluated with the consideration of the weights of the background template, divided by δS. The blue dashed line represents the parametrization of the Spurious Signal as a function of m_X, divided by δS (Note that this blue dashed line appears to be zigzag; this is because of the limited precision for the evaluation of the denominator, δS). (a), (b), and (c) are for the low-ΔE category and different values of m_a. (d), (e), and (f) are for the high-ΔE category and different values of m_a.

5.6 Systematic uncertainties

Several sources of systematic uncertainties that affect the analysis are taken into account. In most cases, systematic uncertainties are found to be smaller than the statistical uncertainty, as described in Sec. 5.8.2.

5.6.1 Signal mass shape modelling

The parametrization of the signal mass shape is described in Section 5.4.1. An "injection test" is performed to validate the signal mass shape parametrization result, with the following procedures:

1. A pseudo-dataset is generated with the same number of background events as that in the collision dataset and with a fixed number of signal events. The background events are generated from the background probability density function (Eq. (63) defined in Section 5.5, with $k = 1$) with its parameters determined from a fit to the observed $m_{\gamma_R\gamma_R}$ distributions in the collision dataset. The signal events are generated from the DSCB function with its parameters determined from a fit to the $m_{\gamma_R\gamma_R}$ distribution of the simulated signal sample.

2. A fit is performed to the $m_{\gamma_R\gamma_R}$ distribution of the pseudo-dataset considering both the signal and background components. Eq. (63) with $k = 1$ is used for the background probability density function, and the signal mass shape parametrization result (Table 9 or 10) is used for the signal probability density function[19].

3. Steps 1 and 2 are repeated 1000 times. This procedure is performed separately for the low-ΔE and high-ΔE categories, and for each signal hypothesis. Examples are shown in Figure 57.

4. Step 3 is repeated several times for different numbers of generated signal events, as shown for example in Figure 58. The average of the number of signal events obtained from these injection tests and the number of signal events in the pseudo-dataset should be identical in an ideal case. As shown in Figure 58, a linear function fit to the relationship of the two numbers is performed. In an ideal case, the slope of this linear function fit should equal unity. The deviation of the value of the slope from 1 is taken as a systematic uncertainty in the extracted signal yield due to the signal mass shape parametrization.

The values of the systematic uncertainty, evaluated as a function of m_X and m_a, are presented in Figure 59. This systematic uncertainty is found to be less than 5% for most of the cases[20].

The impact of the systematic uncertainty of photon energy resolution on the parametrization of the signal mass shape width σ_{CB} is evaluated. The description of the photon energy resolution estimation is given in Section 4.1. Variations of the simulated samples of the benchmark signal models are produced with the photon energy resolution adjusted by one standard deviation from the nominal value in both positive and negative directions. Using these variations of the simulated samples, the parametrization of σ_{CB} as a function of (m_X, m_a) is repeated with the same procedure as described in Section 5.4.1. The relative

---

[19]Note that the signal probability density functions that are used in Steps 1 and 2 are different, as described in the text.

[20]This evaluated systematic uncertainty is larger than 5% for large values of m_a for the low-ΔE category and small values of m_a for the high-ΔE category. This is because the numbers are overestimated due to the limited statistics of the simulated signal samples for these cases. The impact of this overestimated systematic uncertainty on the analysis is negligible, because most of the signal events are expected to be in the other event category for these cases (i.e. high-ΔE category for large values of m_a, and low-ΔE category for small values of m_a).
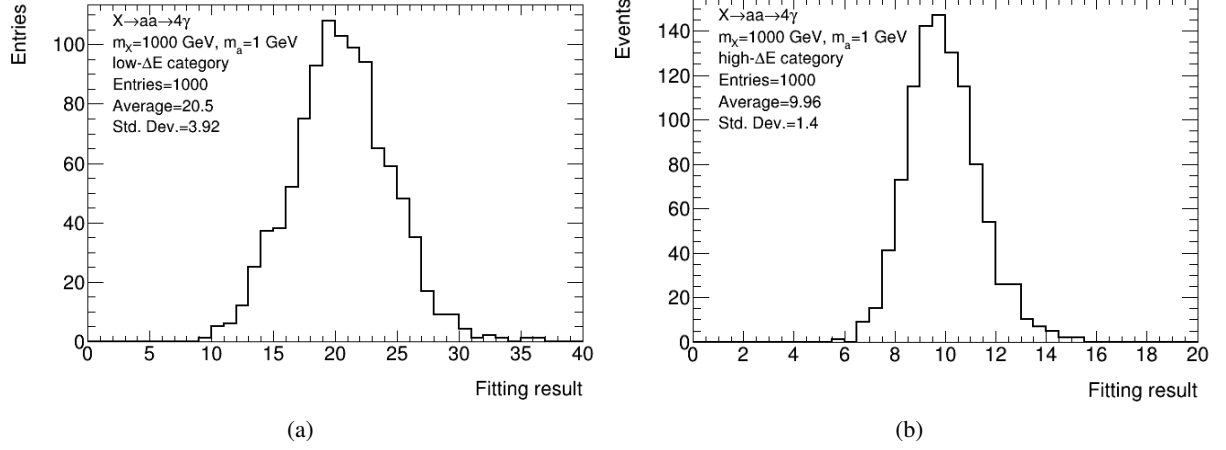
(a)

(b)

Figure 57: Examples of the injection tests performed for the validation of the signal mass shape parametrization results. The distribution of the extracted signal yield obtained from the fit to pseudo-datasets is shown. They are shown for $X \rightarrow aa \rightarrow 4\gamma$ for $m_X = 1$ TeV, $m_a = 1$ GeV, and for (a) the low-ΔE category and (b) the high-ΔE category. For (a), the number of generated signal events is 20. For (b), the number of generated signal events is 10.
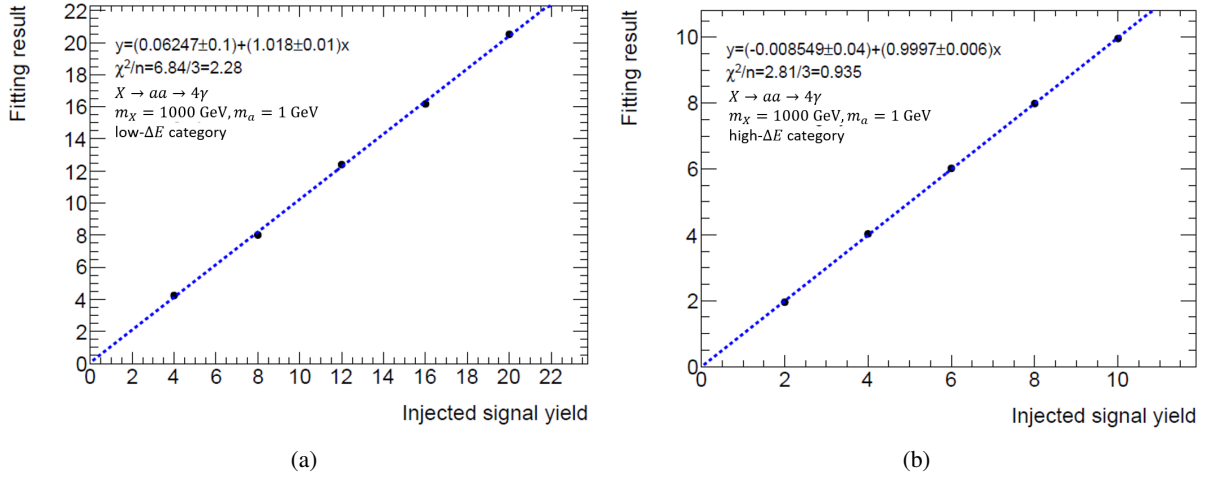

(a)

(b)

Figure 58: Examples of the injection tests performed for the validation of the signal mass shape parametrization results. The markers represent the extracted signal yield obtained from the fit to pseudo-datasets, averaged over 1000 trials. The error bars show the standard deviation of the 1000 trials divided by $\sqrt{1000}$, and they are not visible in the plots because they are small. The blue line represents the result of a linear function fit. They are shown for $X \rightarrow aa \rightarrow 4\gamma$ for $m_X = 1$ TeV, $m_a = 1$ GeV, and for (a) the low-ΔE category and (b) the high-ΔE category.

75
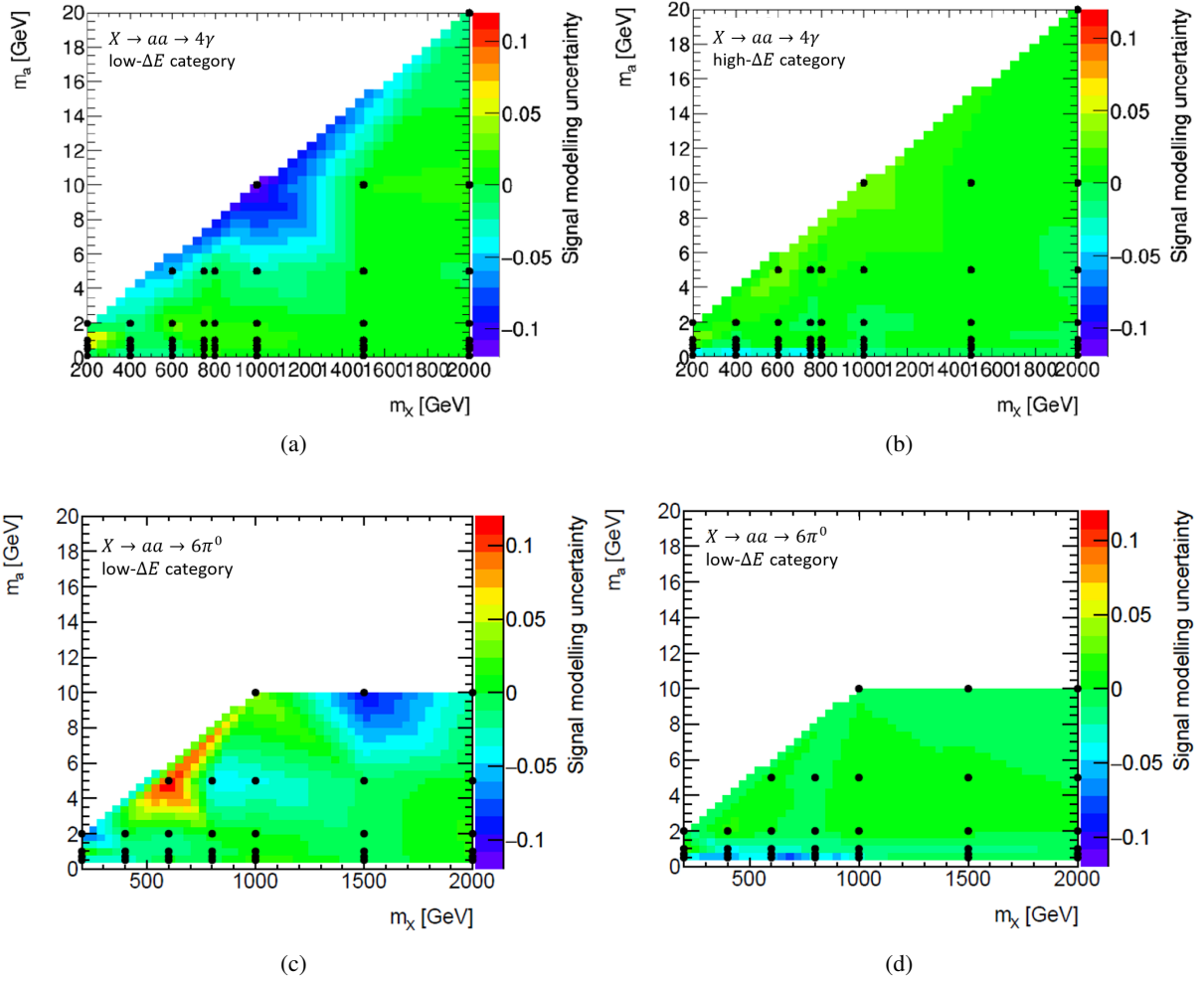
Figure 59: The results of the injection tests. The black markers represent the values of (m_X, m_a) for which the injection tests are performed. The coloured bands show the values evaluated by linear interpolation between the black markers. They are shown for $X \to aa \to 4\gamma$ for the (a) low-ΔE category, (b) high-ΔE category, and for $X \to aa \to 6\pi^0$ for the (c) low-ΔE category, (d) high-ΔE category
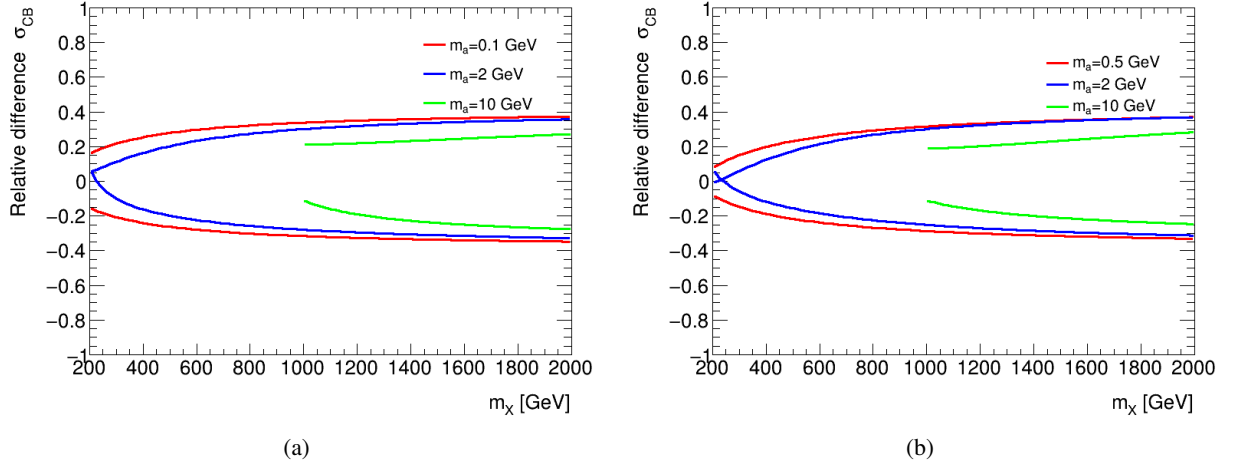
Figure 60: Impact of the systematic uncertainty of photon energy resolution on the signal mass shape width σ_{CB}. The relative difference in the value of σ_{CB} is presented as a function of m_X. The relative difference is defined as the difference between the parametrized value of σ_{CB} using a variation of the simulated signal samples and that from the nominal signal mass shape modelling result, divided by the nominal result. The lines above 0 represent the relative differences when the photon energy resolution is adjusted by one standard deviation from the nominal value in the positive direction. The lines below 0 represent those when the photon energy resolution is adjusted in the negative direction[21]. Those for a few values of m_a are displayed as examples, for (a) $X \to aa \to 4\gamma$ and (b) $X \to aa \to 6\pi^0$.

difference with respect to the nominal parametrization of σ_{CB} is shown in Figure 60. The difference ranges from a few percent to as large as 40%, increasing with larger m_X and dependent slightly on m_a.

5.6.2 Signal selection efficiency and category fraction

Uncertainties in the parametrization of the signal selection efficiency ε are evaluated by an envelope to cover the deviations of the values of ε from simulation and the parametrization, as described in Sec. 5.4.2. It is found to be less than 12%.

Uncertainties in the modelling of the category fraction f are evaluated by an envelope to cover the deviations of the values of f from simulation and the parametrization. The absolute value of the change in f varies as a function of m_a/m_X, from 0.03 at $m_a/m_X = 0$, increasing to 0.12–0.14 at around $m_a/m_X = 0.002$, and decreasing to 0.06–0.10 at $0.002 < m_a/m_X < 0.01$.

Uncertainties in the values of ε and f from experimental uncertainty sources are evaluated. This is performed by comparisons between nominal and variations of the simulated signal samples with each of the sources adjusted by its associated systematic uncertainty. It is performed for the following sources of uncertainties:

- Photon energy scale: The description of the photon energy scale estimation is given in Section 4.1.

---

[21]For $m_a = 2$ GeV (blue line) and low m_X values ($m_X \sim 200$ GeV), the relative difference in σ_{CB} when the photon energy resolution is adjusted in the negative direction appears to be larger than 0. For these cases, the relative difference is considered to be sufficiently small and thus is ignored.

- EM shower shape modelling: The description of the data-driven correction to shower shape variables is given in Section 4.2. The effect of the shower shape modelling uncertainty on the values of ε is evaluated by shifting the shower shape variables by their data-driven corrections. As described in Section 4.2, the data-driven corrections are not defined for the shower shape variable ΔE. Here, the effect of the modelling uncertainty of ΔE on the values of f are evaluated by shifting the values of ΔE by a few MeV[22]; the resulting uncertainty is 0.008 at most.

- Calorimeter isolation requirement: This is evaluated by simulated signal samples produced without the data-driven corrections to the calorimeter isolation variable E_T^{iso}. The details of the corrections are given in Section 4.3.

- Track isolation requirement: This is evaluated by using simulated signal samples produced without the track isolation efficiency corrections. The details of the corrections are given in Section 4.3.

- Pile-up: A weight ("pile-up weight") is defined at the event-level of the simulated samples to correct the distribution of the number of pile-up to match that of the collision data. The difference in the number of vertices between the collision data and simulated data is propagated as an uncertainty in the pile-up weight. The uncertainty due to the pile-up is evaluated by shifting this weight by $\pm 1\sigma$.

These uncertainties are less than 1% of ε or f in almost all cases, rising to 4% for some isolation and shower shape uncertainties for larger values of m_a/m_X at the edge of the analysis sensitivity.

The impact on ε due to the kinematic acceptance arising from the uncertainty of the PDF used for the simulation is evaluated. This is evaluated by variations of the PDF set used for the simulation of the signal samples. It is less than 1% in most cases, rising to 4% for large m_X around $m_X \sim 2$ TeV.

5.6.3 Other sources

The systematic uncertainty of the background modelling is determined from the Spurious Signal method as described in Section 5.5. This parametrization is performed in a way that can slightly overestimate the size of Spurious Signals, especially at the lower end of the m_X range, $m_X = 200$ GeV. The size of the parametrized Spurious Signal decreases for larger m_X, and depends slightly on the m_a value. It ranges from 6×10^{-3} to 85 for the low-ΔE category, and from 1×10^{-2} events to 32 for the high-ΔE category.

The uncertainty in the combined 2015+2016 integrated luminosity is 2.1%. The LUCID-2 detector is used for luminosity measurements, as described in Section 3.2.4. The systematic uncertainty of the measurement is derived following a methodology similar to that detailed in Ref. [47].

5.7 Statistical analysis

5.7.1 Definition of the likelihood function

For a given hypothesis, a fit to the reconstructed diphoton mass $m_{\gamma_R \gamma_R}$ distributions is performed for the range $m_{\gamma_R \gamma_R} > 175$ GeV using an unbinned maximum-likelihood approach, and simultaneously for the two event categories (low-ΔE and high-ΔE). Both the signal and background components are considered. The ratio of the two signal normalization factors for the two event categories is fixed to $f : (1 - f)$.

---

[22]These values correspond to the data-driven corrections that were used by the ATLAS experiment for the pp collision dataset collected in 2011–2012 at $\sqrt{s} = 8$ TeV.

Systematic uncertainties are treated with nuisance parameters in the likelihood function, where each is a floating parameter constrained by a Gaussian function.

A per-event likelihood $\mathcal{L}_i$ is defined for the two event categories, where $i = 1$ is for the low-ΔE category and $i = 2$ is for the high-ΔE category. It is defined as

$$\mathcal{L}_i(x_j; \mu, m_X, m_a, N_{B,i}, \boldsymbol{k}_i, \boldsymbol{\theta}) = \left[N_{S,i}(\mu, m_X, m_a, \boldsymbol{\theta}_S) + \sigma_{\text{Spurious},i} \theta_{\text{Spurious},i} \right] \cdot f_S \left(x_j; m_X, m_a, \theta_{\text{resolution}} \right) \tag{67}$$

$$+ N_{B,i} f_B(x_j; \boldsymbol{k}_i)$$

where each variable is defined as the following:

- $x_j = m_{\gamma_R \gamma_R, j} / \sqrt{s}$ is the observed value of $m_{\gamma_R \gamma_R}$ divided by $\sqrt{s}$ for the j-th event in the i-th event category

- $\mu = \sigma_X \times \mathcal{B}$ is the parameter of interest, which is defined as the product of the signal production cross section and the branching ratios

- $\boldsymbol{k}_i$ is the shape parameters of the background probability density function for the i-th category

- $\boldsymbol{\theta}$ collectively designates the nuisance parameters used to describe the systematic uncertainties

- $N_{S,i}$ is the normalization of the signal probability density function for the i-th category

- $\boldsymbol{\theta}_S$ is the subset of the nuisance parameters affecting $N_{S,i}$

- $\sigma_{\text{Spurious},i}$ and $\theta_{\text{Spurious},i}$ are the value of the background modelling uncertainty (i.e. Spurious Signal) and its associated nuisance parameter for the i-th event category

- f_S is the signal probability density function

- $\theta_{\text{resolution}}$ is the nuisance parameter associated to the systematic uncertainty of the photon energy resolution

- $N_{B,i}$ is the normalization of the background probability density function for the i-th event category

- f_B is the background probability density function

The normalization of the signal probability density function $N_{S,i}$ is defined as

$$N_{S,i}(\mu, m_X, m_a, \boldsymbol{\theta}_S) = \mathcal{L}_{\text{luminosity}} \cdot \mu \cdot \varepsilon(m_X, m_a) \cdot f_i(m_X, m_a, \boldsymbol{\theta}_{\text{migration}}) \cdot \prod_l (1 + \sigma_{\text{normalization},l})^{\theta_{\text{normalization},l}} \tag{68}$$

where each variable is defined as the following:

- $\mathcal{L}_{\text{luminosity}}$ is the integrated luminosity of the collision data

- ε is the signal selection efficiency described in Sec. 5.4.2

- f_i are the fraction of signal events in the i-th category

- $\boldsymbol{\theta}_{\text{migration}}$ is the subset of $\boldsymbol{\theta}_S$ for the systematic uncertainty sources that affect the category fraction, as described in Section 5.6.2 (i.e. category fraction parametrization, photon energy scale, EM shower shape modelling, calorimeter isolation, track isolation, and pile-up)

- $\boldsymbol{\theta}_{\text{normalization}}$ is the subset of $\boldsymbol{\theta}_S$ for the systematic uncertainty sources that affect the normalization of the signal probability density function, as described in Sections 5.6.1, 5.6.2, and 5.6.3 (i.e. signal mass shape modelling, selection efficiency parametrization, photon energy scale, EM shower shape modelling, calorimeter isolation, track isolation, pile-up, PDF, and luminosity)

- $\sigma_{\text{normalization},l}$ is the size of the systematic uncertainties affecting the signal normalization

The fraction of events f_i is defined as

$$f_1(m_X, m_a, \boldsymbol{\theta}_{\text{migration}}) = f(m_X, m_a) + \sum_m \sigma_{\text{migration},m} \theta_{\text{migration},m} \tag{69}$$

$$f_2(m_X, m_a, \boldsymbol{\theta}_{\text{migration}}) = 1 - f_1(m_X, m_a, \boldsymbol{\theta}_{\text{migration}}) \tag{70}$$

where each variable is defined as the following:

- f is the nominal value of the category fraction, described in Section 5.4.2

- $\sigma_{\text{migration},m}$ are the values of the systematic uncertainties affecting the category fraction

The signal probability density function f_S is defined as

$$f_S\left(x_j; m_X, m_a, \theta_{\text{resolution}}\right) = f_{\text{CB}}\left(m_{\gamma_R \gamma_R, j}; \boldsymbol{p}_{\text{CB}}(m_X, m_a, \theta_{\text{resolution}})\right) \tag{71}$$

where f_{CB} is a double-sided Crystal Ball function defined in Eq. (60). Its parameters $\boldsymbol{p}_{\text{CB}} = \{\mu_{\text{CB}}, \sigma'_{\text{CB}}, \alpha_{\text{low}}, \alpha_{\text{high}}, n_{\text{low}}, n_{\text{high}}\}$ are the DSCB parameters described in Section 5.4.1 σ'_{CB} is defined as $\sigma'_{\text{CB}} = \sigma_{\text{CB}} \cdot (1 + \sigma_{\text{resolution}})^{\theta_{\text{resolution}}}$, where σ_{CB} is the nominal width and $\sigma_{\text{resolution}}$ is the value of the systematic uncertainty affecting the signal mass shape width due to the photon resolution uncertainty.

The background probability density function f_B is defined as

$$f_B(x_j; a_i, b_i, c_i) = N_i \left(1 - x_j^{\frac{1}{2}}\right)^{a_i} \cdot x_j^{b_i + c_i \log x_j} \tag{72}$$

where N_i is the normalization factor, and $\boldsymbol{k}_i = \{a_i, b_i, c_i\}$ are the free parameters of the probability density function.

The overall likelihood, including extended and constraint terms, are

$$\mathcal{L}(\mu, m_X, m_a, N_{B,1}, N_{B,2}, \boldsymbol{k}_1, \boldsymbol{k}_2, \boldsymbol{\theta}) = \tag{73}$$

$$\frac{e^{-(N_{S,1}+N_{S,2}+N_{B,1}+N_{B,2})}}{(n_1+n_2)!} \left\{ \prod_{i=1}^{2} \left[\prod_{j=1}^{n_i} \mathcal{L}_i(x_j; \mu, m_X, m_a, N_{B,i}, \boldsymbol{k}_i, \boldsymbol{\theta}) \right] \right\} \left[\prod_l \exp\left(-\frac{\theta_l^2}{2}\right) \right]$$

where n_i is the number of events in the i-th category in the dataset. The last factor, $\left[\prod_l \exp\left(-\frac{\theta_l^2}{2}\right) \right]$, is the Gaussian function to constrain the nuisance parameters associated to the systematic uncertainties.

The "visible cross-section" is defined as the product of the production cross-section, the branching ratios, and the signal selection efficiency. Additionally to the calculation of limits on the product of the production cross-section and the branching ratios, the calculation of the upper limits on the visible cross-section is

performed. In this case, the parameter of interest μ is defined as $\mu = \sigma_X \times \mathcal{B} \times \varepsilon(m_X, m_a)$, and the normalization factor of the signal probability density function $N_{S,i}$, defined in Eq. (68), is redefined as

$$N_{S,i}(\mu, m_X, m_a, \boldsymbol{\theta}_S) = \mathcal{L}_{\text{luminosity}} \cdot \mu \cdot f_i(m_X, m_a, \boldsymbol{\theta}_{\text{migration}}) \cdot \prod_l (1 + \sigma_{\text{normalization},l})^{\theta_{\text{normalization},l}} \qquad (74)$$

where $\boldsymbol{\theta}_{\text{normalization}}$ is defined as the subset of $\boldsymbol{\theta}_S$ which affects the normalization of the signal probability density function but excluding those associated to the signal selection efficiency (i.e. signal mass shape modelling uncertainty and the integrated luminosity uncertainty).

5.7.2 Hypothesis testing

The *p*-values are calculated with the profile likelihood ratio as the basis for the test statistic and utilizing an asymptotic approximation [75]. The details of the test statistic and the asymptotic approximation are given in Appendix D.

The calculation of *p*-values for the background-only hypothesis (p_0) is performed from $m_X = 200$ GeV to $m_X = 2.7$ TeV with a scan step of 1 GeV, for the benchmark signal scenario involving a scalar particle X with a narrow width decaying via $X \to aa \to 4\gamma$. Since the samples for the benchmark signal scenario were simulated for the m_X values in the range 200 GeV $< m_X < 2$ TeV, the results of the parametrizations of the signal mass shape, category fraction f, and systematic uncertainties are extrapolated for the m_X values in the range 2 TeV $< m_X < 2.7$ TeV.

The upper limits at the 95% CL on the production cross-section times the product of branching ratios are calculated following the CL$_{\text{s}}$ modified frequentist method [76]. The "observed upper limit" and the "expected upper limit" are evaluated separately, where the observed limit is defined as a limit evaluated using the events in the signal region of the collision dataset, and the expected limit is defined as the median of the limit assuming a background-only hypothesis. Upper limits are determined separately for the two benchmark signal models, $X \to aa \to 4\gamma$ and $X \to aa \to 6\pi^0$, as a function of the values of (m_X, m_a). The assumptions inherent in the use of the asymptotic approximation are validated by sampling distributions of the test-statistic using pseudo-experiments. This comparison is performed for a few signal mass points. The expected upper limits obtained from the asymptotic approximation are within 5% of those calculated with the pseudo-experiments sampling for most of the values of m_X and m_a tested. Due to the small number of events in collision data in the region $m_{\gamma_R \gamma_R} > 1$ TeV in the high-ΔE category, larger deviations are observed for $m_X > 1$ TeV and large m_a. The deviation is smaller than 5% at $(m_X, m_a) = (1$ TeV, 10 GeV$)$, and increases to 20% for $(m_X, m_a) = (1.5$ TeV, 10 GeV$)$ and 30% for $(m_X, m_a) = (2$ TeV, 10 GeV$)$, with the asymptotic approximation giving stronger limits. The details of the CL$_{\text{s}}$ method are given in Appendix D.

The evaluation of the upper limit at the 95% CL on the visible cross-section is performed as a function of the values of (m_X, f). For the probability density function of the signal component, the signal mass shape modelling result for the decay $X \to aa \to 4\gamma$ is used.
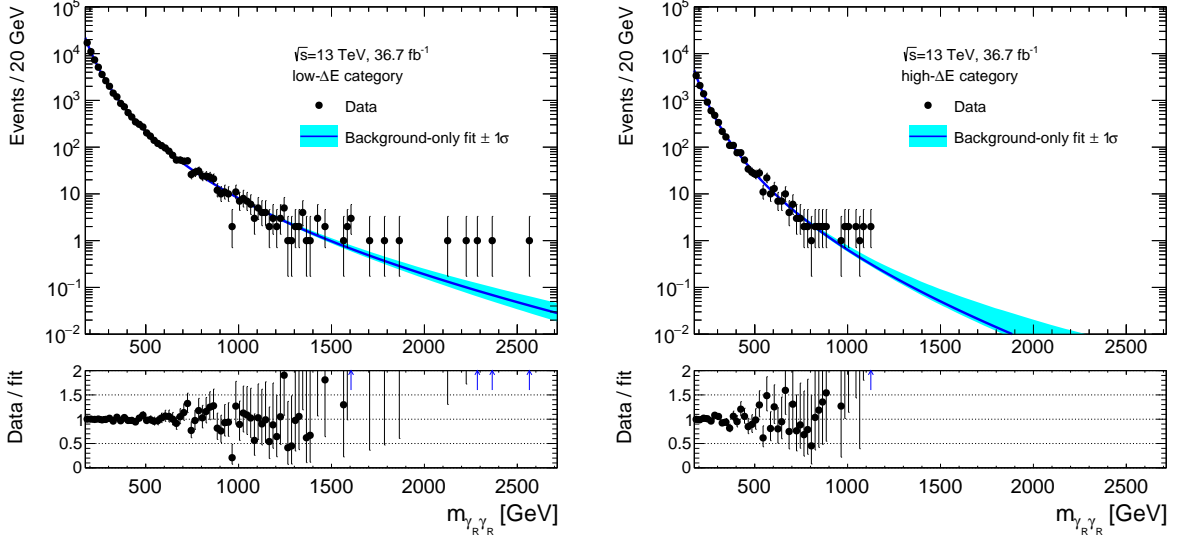
Figure 61: The observed $m_{\gamma_R \gamma_R}$ distributions in the two event categories of the signal region. The result of a background-only fit assuming $\mu = 0$ is superimposed. The $\pm 1\sigma$ uncertainty of the fit result, due to the uncertainties in the fit function parameter values, is shown as a shaded band. In the lower panels, the ratios of the observed event yield and the expectation from the fit result are presented. The blue arrows represent the bins with this ratio larger than two, i.e. out of the range of the plot.

5.8 Results

5.8.1 Results of the null hypothesis test

The observed $m_{\gamma_R \gamma_R}$ distributions in the signal region is shown in Figure 61. The result of a background-only fit assuming $\mu = 0$ is superimposed in the figure.

The result of the p_0 values, expressed in local significance (i.e. the number of standard deviations away from the mean of a normal distribution) is presented in Figure 62. Two different regions can be observed in this plot, above and below the threshold at $m_a \sim 0.0015 \times m_X$. These are a result of the categorization of events based on the shower shape variable ΔE. For $m_a \lesssim 0.0015 \times m_X$, a larger fraction of signal events is expected in the low-ΔE category, and for $m_a \gtrsim 0.0015 \times m_X$, a larger fraction of signal events is expected in the high-ΔE category.

The largest local deviation from the background-only hypothesis is found to be 2.7σ, corresponding to m_X = 729 GeV and $m_a = 0.1$ GeV for $X \rightarrow aa \rightarrow 4\gamma$. The width of the signal mass shape for $m_X = 729$ GeV and $m_a = 0.1$ GeV is $\sigma_{CB} = 6$ GeV, and thus this deviation appears as a small area in Figure 62. A small excess of events is also observed centred around $m_X = 1.1$ TeV and $m_a = 7$ GeV, which corresponds to a local deviation of 2.2σ.
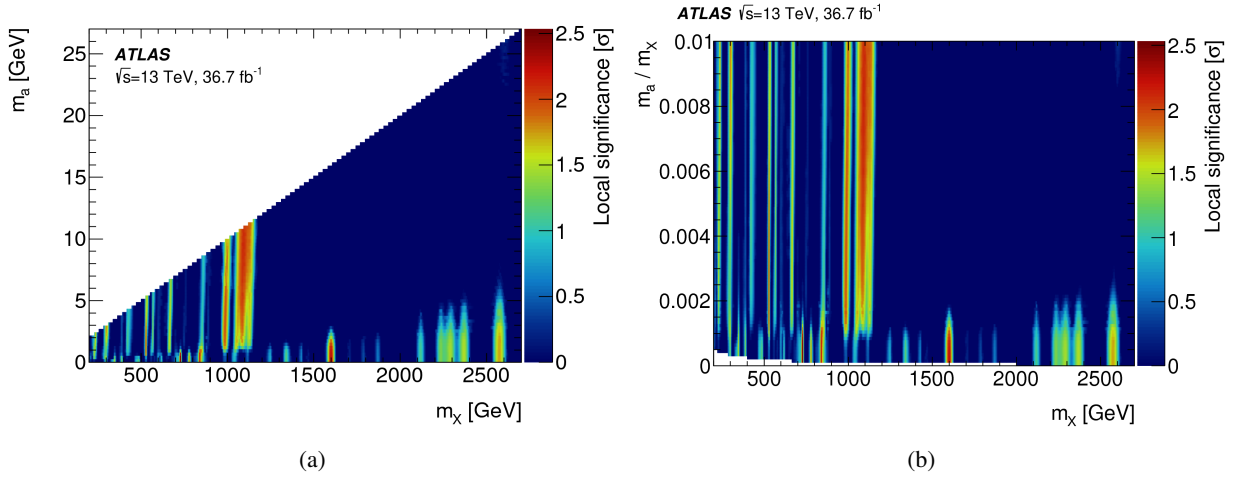
Figure 62: Results of the search for deviations from the background-only hypothesis in the observed distributions of the $m_{\gamma_R \gamma_R}$, expressed in significance. They are presented as a function of m_X and m_a for the benchmark signal scenario involving a scalar particle X with narrow width decaying via $X \to aa \to 4\gamma$. Only the values of local significance that are positive are shown. The vertical axis represents m_a for (a), and m_a/m_X for (b). [72]

To quantify the statistical significance of obtaining the observed maximum local deviation (i.e. the "global significance"), a test with pseudo-experiments is performed. Using the probability density function obtained from the background-only fit (as presented in Figure 61), 40 sets of pseudo-datasets with the same number of events as the collision dataset are generated. From these pseudo-datasets, the distribution of the maximum local significance is obtained by calculating the maximum local significance in the search region defined as m_X values from 200 GeV to 2.7 TeV and m_a values from 0.1 GeV to $0.01 \times m_X$. The result is presented in Figure 63. It is found that the observed maximum local deviation, 2.7σ, is less significant than the median of the largest local deviation obtained in pseudo-experiments[23]. Thus, it is found that the $m_{\gamma_R \gamma_R}$ distributions are consistent with the background-only hypothesis.

---

[23]Because the number of pseudo-datasets is 40, the uncertainty in the evaluation of the median is not small (~ 0.07). However, the important conclusion is that the observed maximum local deviation is not significant, and that the $m_{\gamma_R \gamma_R}$ distributions are consistent with the background-only hypothesis.
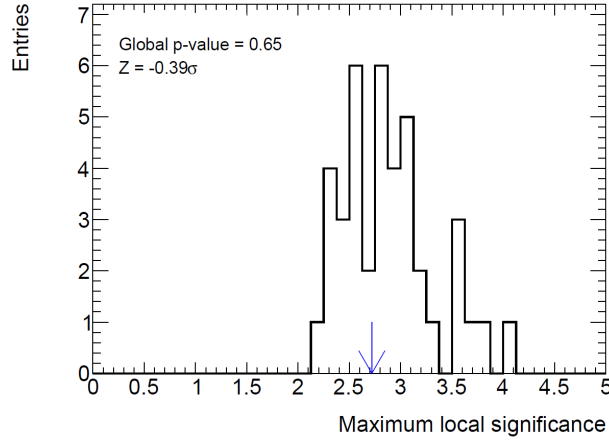
Figure 63: The distribution of the maximum local significance, calculated from pseudo-experiments. The observed maximum local significance, which is 2.7σ, is indicated by an arrow. The corresponding global p-value is 0.65, which corresponds to a negative global significance.

5.8.2 Upper limits on signal cross-section times branching ratios

Since it is found that the $m_{\gamma_R\gamma_R}$ distribution of the collision dataset is consistent with the background-only hypothesis, the 95% CL observed and expected upper limits on the product of the production cross-section and the branching ratios are evaluated. They are presented in Figures 64 and 65.

Figure 64 shows the limits for the cross-section of the production via gluon–gluon fusion of a high-mass scalar particle X with a narrow width, times the branching ratios into a pair of a particles and the subsequent decay of each a into a pair of photons, $\sigma_X \times \mathcal{B}(X \to aa) \times \mathcal{B}(a \to \gamma\gamma)^2$. Figure 64(b) illustrates the two features of this search. First, when the ratio m_a/m_X is larger than a threshold of roughly 0.0015, more signal events are expected in the high-ΔE category, which has a significantly better signal-to-background ratio compared to the low-ΔE category, thus leading to stronger upper limits. Second, for larger values of m_a/m_X, the decrease in the signal selection efficiency leads to weaker upper limits.

Figure 65 shows the limits for the cross-section times product of branching ratios for the decay of the a into three neutral pions, $\sigma_X \times \mathcal{B}(X \to aa) \times \mathcal{B}(a \to 3\pi^0)^2$. This result shows features similar to that shown in Figure 64, with slight differences arising mainly from the different trend of the category fraction f with respect to the values of m_X and m_a.

Figures 66 and 67 show the same results as Figures 64 and 65, together with the bands representing the statistical uncertainty associated to the expected limits.
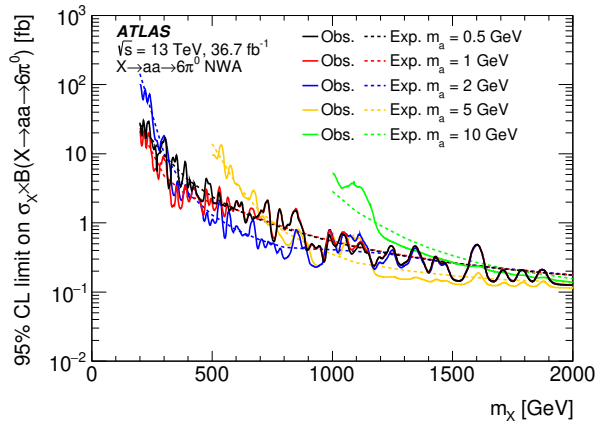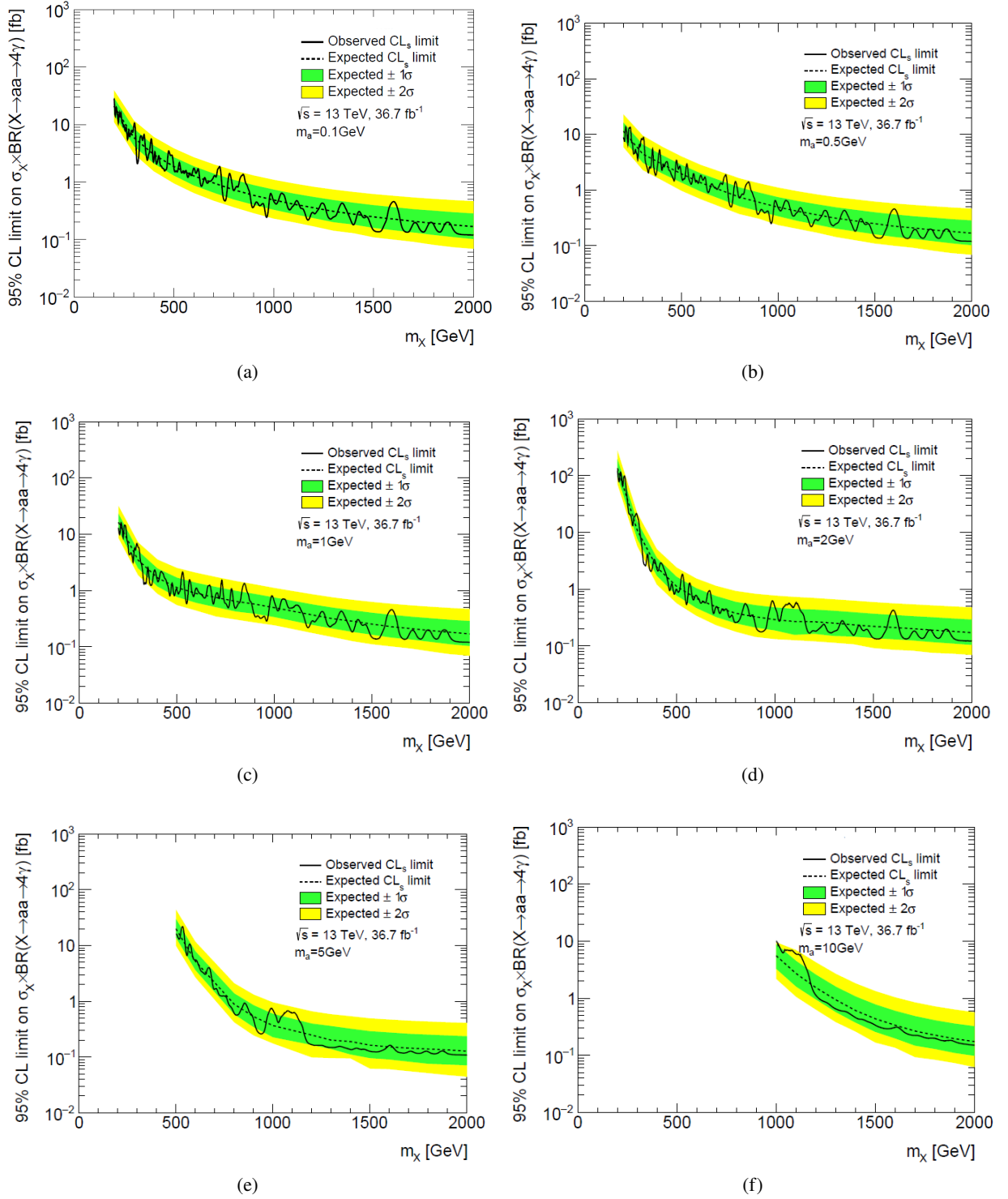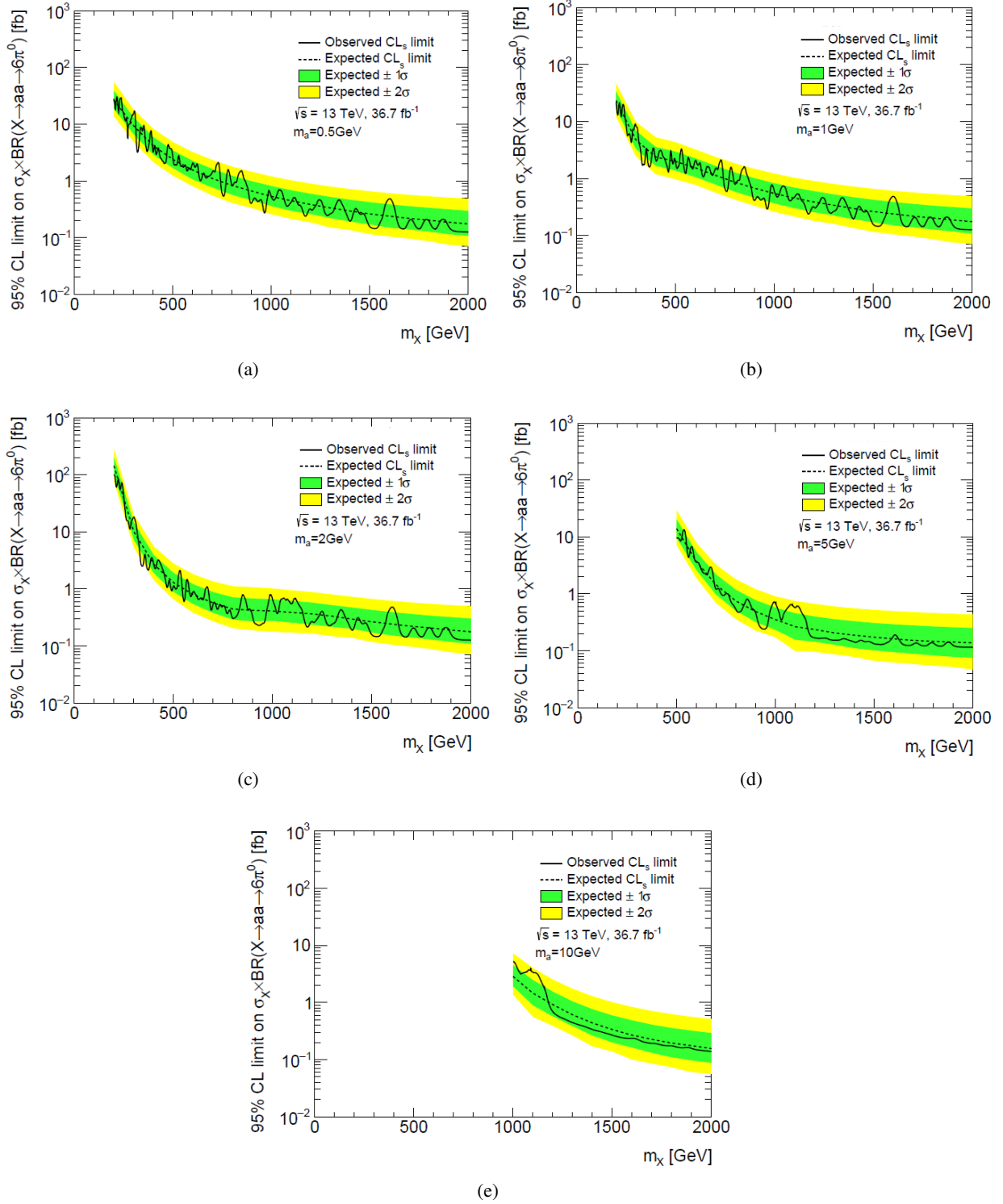
(a)

(b)
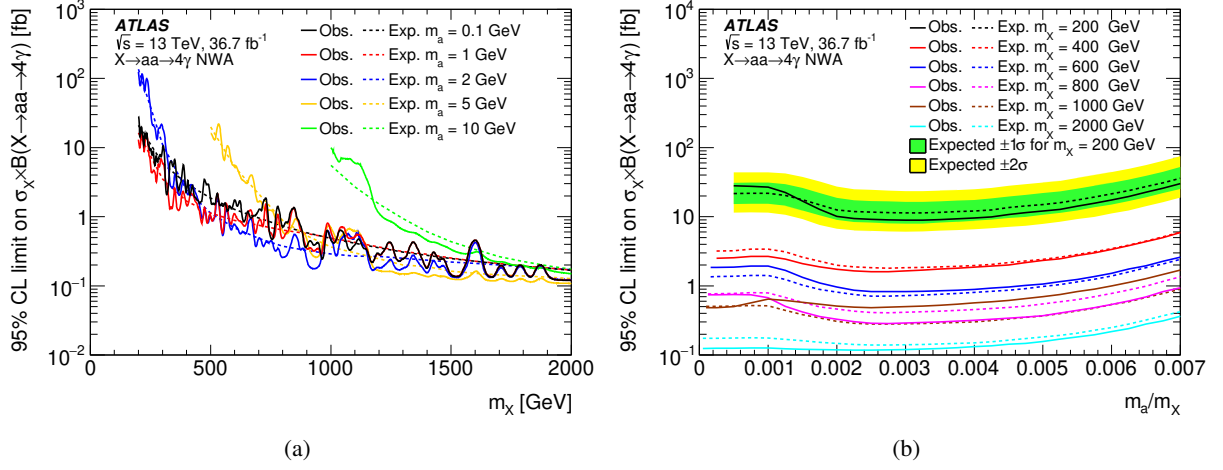
Figure 64: The observed and expected upper limits on the production cross-section times the product of branching ratios for the benchmark signal scenario involving a scalar particle X with a narrow width decaying via $X \rightarrow aa \rightarrow 4\gamma$, $\sigma_X \times \mathcal{B}(X \rightarrow aa) \times \mathcal{B}(a \rightarrow \gamma\gamma)^2$. (a) The limits presented as a function of m_X. The limits for $m_a = 5$ GeV and 10 GeV do not cover as large a range as the other mass points, since the region of interest is limited to $m_a < 0.01 \times m_X$. (b) The limits presented as a function of m_a/m_X. The statistical uncertainty bands for $m_X = 200$ GeV are shown as an example. [72]

Figure 65: The observed and expected upper limits on the production cross-section times the product of branching ratios for the benchmark signal scenario involving a scalar particle X with narrow width decaying via $X \rightarrow aa \rightarrow 6\pi^0$, $\sigma_X \times \mathcal{B}(X \rightarrow aa) \times \mathcal{B}(a \rightarrow 3\pi^0)^2$. The limits for $m_a = 5$ GeV and 10 GeV do not cover as large a range as the other mass points, since the region of interest is limited to $m_a < 0.01 \times m_X$. [72]

Figure 66: The observed and expected upper limits on the production cross-section times the product of branching ratios for the benchmark signal scenario involving a scalar particle X with a narrow width decaying via $X \to aa \to 4\gamma$, $\sigma_X \times \mathcal{B}(X \to aa) \times \mathcal{B}(a \to \gamma\gamma)^2$. They are shown for different values of m_a: (a) $m_a = 0.1$ GeV, (b) $m_a = 0.5$ GeV, (c) $m_a = 1$ GeV, (d) $m_a = 2$ GeV, (e) $m_a = 5$ GeV, and (f) $m_a = 10$ GeV.

Figure 67: The observed and expected upper limits on the production cross-section times the product of branching ratios for the benchmark signal scenario involving a scalar particle X with narrow width decaying via $X \rightarrow aa \rightarrow 6\pi^0$, $\sigma_X \times \mathcal{B}(X \rightarrow aa) \times \mathcal{B}(a \rightarrow 3\pi^0)^2$. They are shown for different values of m_a: (a) $m_a = 0.5$ GeV, (b) $m_a = 1$ GeV, (c) $m_a = 2$ GeV, (d) $m_a = 5$ GeV, and (e) $m_a = 10$ GeV.

5.8.3 Comparison of upper limit with that from diphoton resonance search

As discussed in Section 1, this research shares some features with the search for a heavy (> 200 GeV) resonant boson decaying into a pair of photons, performed by the ATLAS experiment at Run 2 for pp collisions at $\sqrt{s}$ = 13 TeV [25]. This search looked for new resonances leading to a final state with two photonlike EM clusters in the calorimeter. The notable difference, compared to the search described in this thesis, is the event selection strategy; the diphoton search uses the standard Tight photon ID selection (the "diphoton selection"), and does not introduce an event categorization.

A comparison of the expected upper limit on signal cross section times branching ratios, $\sigma_X \times \mathcal{B}(X \rightarrow aa) \times \mathcal{B}(a \rightarrow \gamma\gamma)^2$, of the search described in this thesis, and that derived for the diphoton selection, is shown in Figure 68. The expected upper limit for the diphoton selection is evaluated with the following prodedures. The signal selection efficiency is evaluated using simulated signal samples, and a linear interpolation is performed to evaluate that for the (m_X, m_a) values for which the simulated signal samples are not produced. The parametrizations of the signal mass shape and the evaluation of the systematic uncertainties are substituted with those used for the low-ΔE category. The expected limits are calculated by performing a fit to the $m_{\gamma_R \gamma_R}$ distribution of the events in the collision dataset that satisfy the diphoton selection. There is a difference of approximately as much as a factor 20 between the two expected limits. In conclusion, this research is able to search for photon-jet signal events with large m_a (e.g. $0.001 \lesssim m_a < 0.01$ for $X \rightarrow aa \rightarrow 4\gamma$) with a sensitivity that was never achieved before.
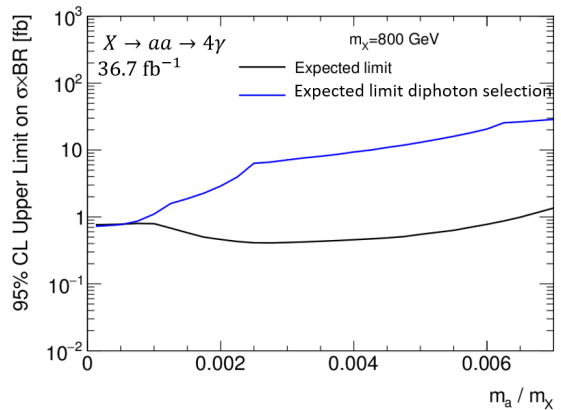
Figure 68: Comparison of the expected upper limit on signal cross section times branching ratios, $\sigma_X \times \mathcal{B}(X \rightarrow aa) \times \mathcal{B}(a \rightarrow \gamma\gamma)^2$, of the search described in this thesis, and that derived for the conventional diphoton selection. For details, see text.

88

5.8.4 Impact of systematic uncertainties

The impact of systematic uncertainties on the analysis results are shown in Figures 69 and 70.

Figure 69 shows the impact of systematic uncertainties on the unconditional fit to the collision data, where the parameter of interest $\mu = \sigma_X \times BR$ is treated as a free parameter, for $X \rightarrow aa \rightarrow 4\gamma$. The markers represent the "pull". The pull is defined as the value of the nuisance parameters θ obtained from an unconditional fit. The bars of the markers represent the $\pm 1\sigma$ uncertainty of the nuisance parameters arising from the fit. The bar charts represent the ratio of the "impact" $\Delta\mu$ and the total uncertainty σ_{tot}. The impact $\Delta\mu$ is defined as the deviation of the value of μ with respect to the nominal result, when an unconditional fit is repeated with one of the nuisance parameters shifted by 1σ of its error and treated as a fixed parameter. The variable σ_{tot} is the total uncertainty of μ from the nominal unconditional fit. In principle, the ratio $\Delta\mu/\sigma_{\text{tot}}$ corresponds to the contribution of the systematic uncertainty to the overall uncertainty of the determination of the μ. The sources of systematic uncertainties are sorted with the size of $|\Delta\mu|$, from the largest to the smallest. The results for $X \rightarrow aa \rightarrow 6\pi^0$ are qualitatively similar.

Table 13 summarizes the impact $\Delta\mu/\sigma_{\text{total}}$. Additionally, the contribution of the statistical uncertainty divided by σ_{total} is presented. The contribution of the statistical uncertainty is evaluated by repeating an unconditional fit with all the nuisance parameters fixed to their best-fit values, and obtaining the fit error of μ. It is found that the analysis uncertainty is basically dominated by statistical uncertainty. The exception is for low values of m_X, e.g. $m_X = 200$ GeV, for which the impact of the background modelling uncertainty (i.e. Spurious Signal) is similar to that of the statistical uncertainty.

Figure 70 shows the impact of systematic uncertainties on the 95% CL expected upper limits on $\sigma_X \times \mathcal{B}(X \rightarrow aa) \times \mathcal{B}(a \rightarrow \gamma\gamma)^2$. The expected limits evaluated with the nuisance parameters fixed to their nominal values are compared with those for the nominal result. Both results are in agreement, except for the low mass region $m_X \sim 200$ GeV. The impact of the systematic uncertainties on the expected limit decreases with the resonance mass m_X from 51% at most for $m_X = 200$ GeV to 5% at most for $m_X > 800$ GeV. This is because the parametrization of the size of spurious signals slightly overestimates the values at the lower end of the m_X range, as described in Section 5.5.3.

Table 13: The impact of the sources of systematic uncertainties for the case of an unconditional fit. The sum in quadrature of the individual components differs from 100% due to small correlations between the components. The values here are for $X \rightarrow aa \rightarrow 4\gamma$. The mass points $(m_X, m_a) = (200 \text{ GeV}, 0.3 \text{ GeV}), (600 \text{ GeV}, 0.9 \text{ GeV})$ correspond to those values for which the systematic uncertainty of the category fraction f is the highest.

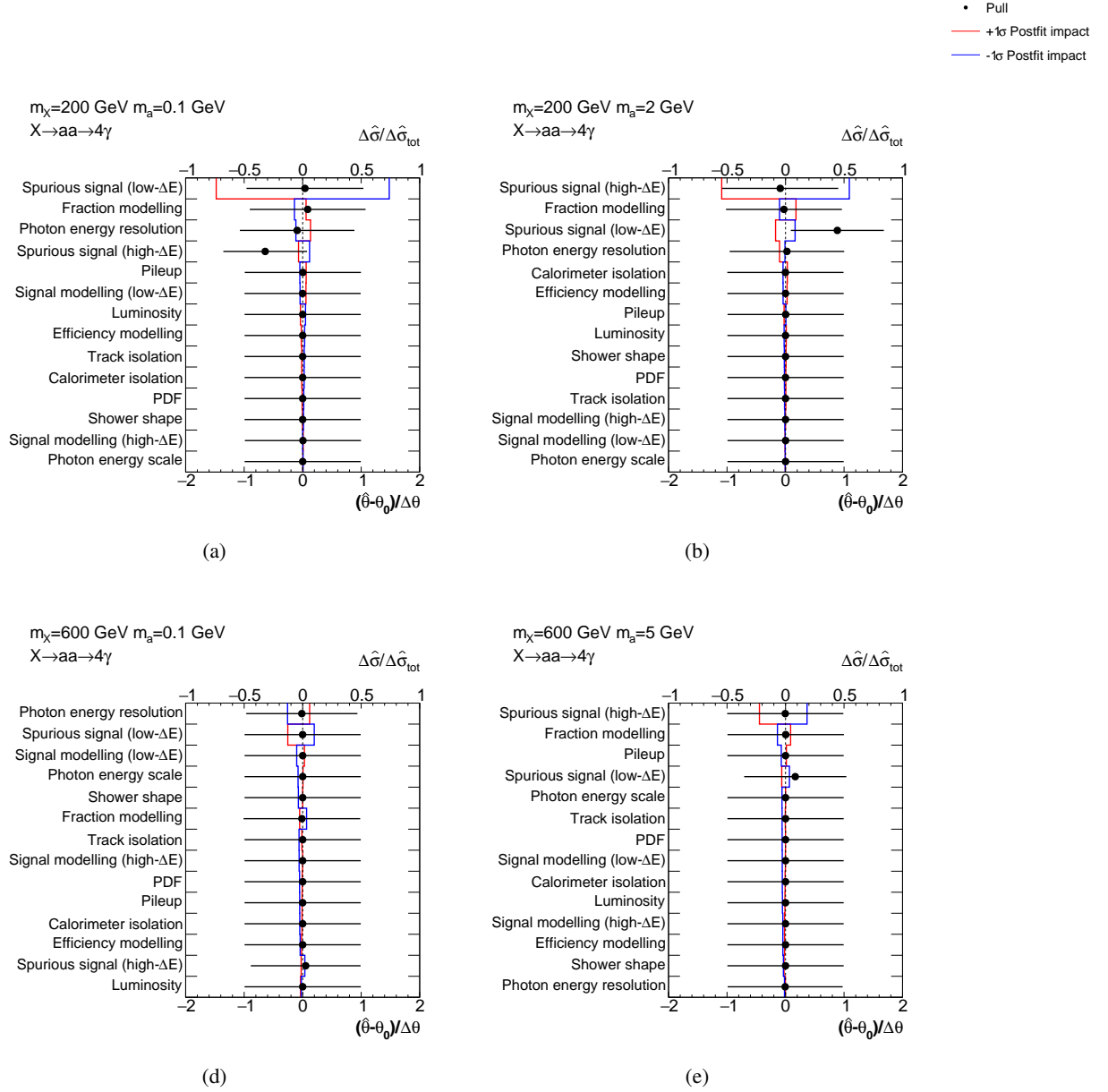| m_X [GeV], m_a [GeV]	(200, 0.1)	(200, 0.3)	(200, 2)	(600, 0.1)	(600, 0.9)	(600, 5)
	$|\Delta\mu|/\sigma_{\text{total}}$					
Statistical	66%	72%	86%	99%	94%	98%
Spurious signal (low-ΔE)	74%	37%	9%	13%	5%	3%
Spurious signal (high-ΔE)	6%	67%	55%	2%	24%	22%
Category fraction f	7%	19%	9%	3%	25%	7%
Signal mass resolution	7%	2%	5%	13%	12%	1%
Signal mass shape (low-ΔE)	3%	1%	–	5%	4%	3%
Signal mass shape (high-ΔE)	–	–	1%	3%	3%	2%

Figure 69: The impact of the sources of systematic uncertainties for the case of an unconditional fit. The markers represent the pull. The bar charts represent the ratio of the impact $\Delta\mu$ and the total uncertainty σ_{tot}. They are presented for $X \to aa \to 4\gamma$, for (a) $(m_X, m_a) = (200\,\text{GeV}, 0.1\,\text{GeV})$, (b) $(m_X, m_a) = (200\,\text{GeV}, 2\,\text{GeV})$, (c) $(m_X, m_a) = (600\,\text{GeV}, 0.1\,\text{GeV})$, and (d) $(m_X, m_a) = (600\,\text{GeV}, 5\,\text{GeV})$.
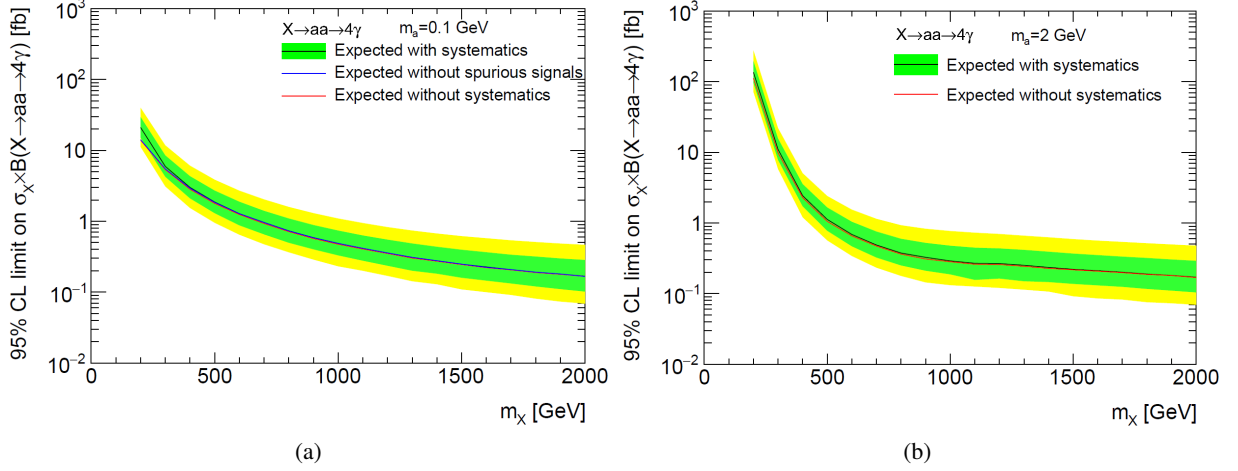
Figure 70: Comparison of the expected 95% CL upper limits on the cross-section times the branching ratio for $X \to aa \to 4\gamma$ without the consideration of systematic uncertainties, and those for the nominal analysis result. (a) $m_a = 0.1$ GeV and (b) $m_a = 2$ GeV.

5.8.5 Upper limits on signal visible cross-sections

The visible cross-section is defined as the product of the signal production cross-section, branching ratios, and the signal selection efficiency, i.e. $\sigma_X \times \mathcal{B}(X \to aa) \times \mathcal{B}(a \to \gamma\gamma)^2 \times \varepsilon$ for $X \to aa \to 4\gamma$, as defined already in Section 5.7.1. The 95% CL observed limit on the visible cross-section for $X \to aa \to 4\gamma$ is presented in Figure 71, as a function of m_X and f. The limits are calculated using the likelihood function defined in Eq. (74). The limits are first calculated as a function of (m_X, m_a), and are translated to a function of (m_X, f) based on the relationship of m_a/m_X and f for $X \to aa \to 4\gamma$ (shown in Figure 49(a) of Section 5.4.3). Here, the values of m_a/m_X are limited to $m_a/m_X < 0.005$, so that the relationship of m_a/m_X and f becomes a one-to-one correspondence.

The limits on visible cross-sections are considered to be model independent, and that they can be used to estimate the upper limit on signal cross-section times branching ratios for a given signal hypothesis if ε and f can be evaluated. One thing to note is that the evaluation of the limits on signal visible cross-sections are performed with an assumption that the size of m_a is small (approximately $m_a \lesssim m_X \times 0.01$). The limit on the visible cross-section will differ depending on the signal mass shape, especially the width σ_{CB}. From a comparison of the limits on visible cross-sections for $m_a/m_X = 0.002$ and those for $m_a/m_X = 0.01$ (which correspond to same values of f as seen in Figure 49(a)), these two limits differ by 20%, with the one for $m_a/m_X = 0.002$ giving stronger (i.e. smaller) limit. This is because of the increase in the size of σ_{CB} with respect to m_a/m_X, as described in Section 5.4.1.

The upper limits on the signal visible cross-sections are utilized for the reinterpretation of the results for the case of long-lived a particles, as described in the next section.
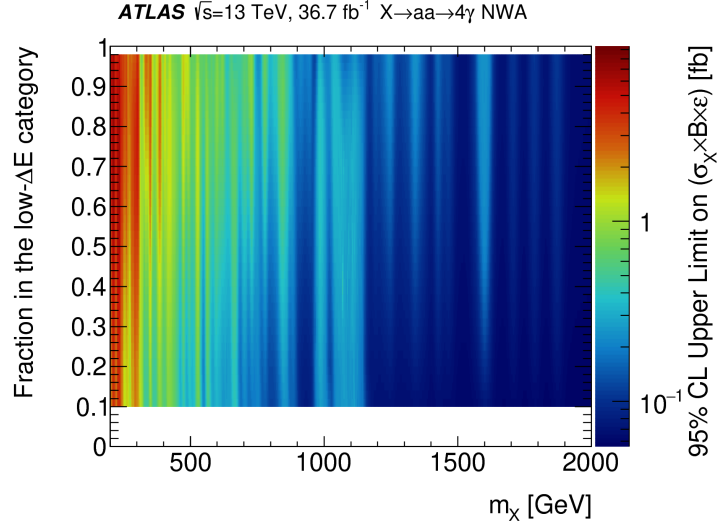
(a)

Figure 71: The observed upper limit on the visible cross-section for the benchmark signal scenario involving a scalar particle X with narrow width decaying via $X \to aa \to 4\gamma$, $\sigma_X \times \mathcal{B}(X \to aa) \times \mathcal{B}(a \to \gamma\gamma)^2 \times \varepsilon$. [72]

5.9 Reinterpretation of the results for the case of long-lived a

For the benchmark signal scenario $X \to aa \to 4\gamma$, the case of a long-lived a is considered, as described in the beginning of Section 5. This is because a long-lived a arises in BSM models, for instance in NMSSM when the decay width of a, Γ_a, is small (e.g. $\Gamma_a \sim O(1 \text{ meV})$), as discussed in Section 2.3.1.

5.9.1 Signal selection efficiency and category fraction parametrization

The decay radius r of the particle a is defined as the distance of the position of its decay and the interaction point in the x–y plane (i.e. $r = \sqrt{x^2 + y^2}$). Its value is approximately $r = \gamma_a \beta_a ct \sin\theta$, where γ_a is the Lorentz factor of a and t is the decay time of the a at its rest frame. β_a is the velocity of the particle a divided by c, and it is approximately $\beta_a = 1$ when $\gamma_a = O(100)$. Hereafter, the factor $\beta_a c$ is omitted for simplicity. The expected value of r can be approximated by the equation $\frac{m_X}{2m_a} \frac{1}{\Gamma_a}$, because $\gamma_a \sim \frac{m_X}{2m_a}$. The decay radius of up to a few meters is considered, corresponding to a small decay width satisfying the condition $\frac{m_X}{2m_a} \frac{1}{\Gamma_a} \lesssim O(1 \text{ m})$.

Considering that the inner radius of the EM calorimeter is $R_{EM} = 1.5$ m, the important case is when r is larger than $r \sim 10$ cm. Two features arise compared to the case of the prompt decay of the particle a: Firstly, the separation of photons entering the EM calorimeter decreases linearly with respect to r, as depicted in Figure 72. Secondly, the selection efficiency is low for particle a not decaying before entering the surface of the EM calorimeter, i.e. $r > R_{EM}$ or $\frac{r}{|\tan\theta|} > Z_{EM}$. Here, $Z_{EM} = 3.7$ m is the distance between the end-cap section of the EM calorimeter and the interaction point. It is low because of the Loose$'$ photon selection requirement: It requires a considerable portion of the EM shower to be deposited in the first layer of the EM calorimeter (namely $f_1 > 0.005$ for the shower shape variable f_1 defined in Table 5), and so events with particle a not decaying before entering the EM calorimeter are rejected from
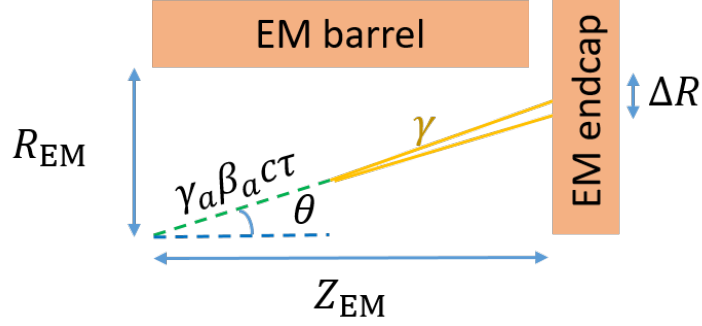
92

Figure 72: Schematic diagram of the separation of the photons originating from $a \to \gamma\gamma$ at the inner surface of the EM calorimeter, ΔR.

the event selection requirements. In this analysis, such events are considered to be completely excluded from the signal region as a conservative approach.

The signal selection efficiency ε for the benchmark signal scenario $X \to aa \to 4\gamma$ for the values (m_X, m_a, Γ_a) can be evaluated by the following equation:

$$\varepsilon(m_X, m_a, \Gamma_a) = \int p(E_{T,1}, \eta_1, t_1, E_{T,2}, \eta_2, t_2 | m_X, m_a, \Gamma_a) \alpha(E_{T,1}, \eta_1, E_{T,2}, \eta_2) \prod_{i=1}^{2} \varepsilon_{\gamma R}(E_{T,i}, \eta_i, t_i) \, dE_{T,i} d\eta_i dt_i \tag{75}$$

Here, $E_{T,i}, \eta_i, t_i$ for $i = 1$ ($i = 2$) are the E_T, η, t of the particle a with the higher (lower) E_T. The function $p(E_{T,1}, \eta_1, t_1, E_{T,2}, \eta_2, t_2 | m_X, m_a, \Gamma_a)$ is the probability density function of the variables. The variable $\varepsilon_{\gamma R}(E_T, \eta, t)$ is defined as the selection efficiency of a reconstructed photon originating from the photon-jet $a \to \gamma\gamma$ with the values of (E_T, η, t).

The function $\alpha(E_{T,1}, \eta_1, E_{T,2}, \eta_2)$ takes the value of either 1 or 0; $\alpha = 1$ when the two a particles are both within the kinematic acceptance of the analysis, and $\alpha = 0$ when they are not. Namely, $\alpha = 1$ when the following requirements are satisfied:

- $E_{T,1} > 0.4 \times m_X$

- $E_{T,2} > 0.3 \times m_X$

- $|\eta_i| < 1.37$ OR $1.52 < |\eta_i| < 2.37$ ($i = 1, 2$)

The parametrization of $\varepsilon_{\gamma R}(E_T, \eta, t)$ is performed using simulated signal samples in a binned region of (E_T, η). The parameter space of (E_T, η) is binned in $4 \times 4 = 16$ regions; $|\eta| < 0.6, 0.6 < |\eta| < 1.37, 1.52 < |\eta| < 1.81$, and $1.82 < |\eta| < 2.37$ in η, and $50 < E_T < 70$ GeV, $70 < E_T < 100$ GeV, $100 < E_T < 200$ GeV, and 200 GeV $< E_T$ in E_T. The binning of η is defined considering the difference in the detector configuration in each region of η. The binning of E_T is defined considering the dependence of the EM shower development, hence the Loose$'$ selection efficiency, on E_T.

The variable $\varepsilon_{\gamma R}$ in a given (E_T, η) bin is parametrized with the following function:

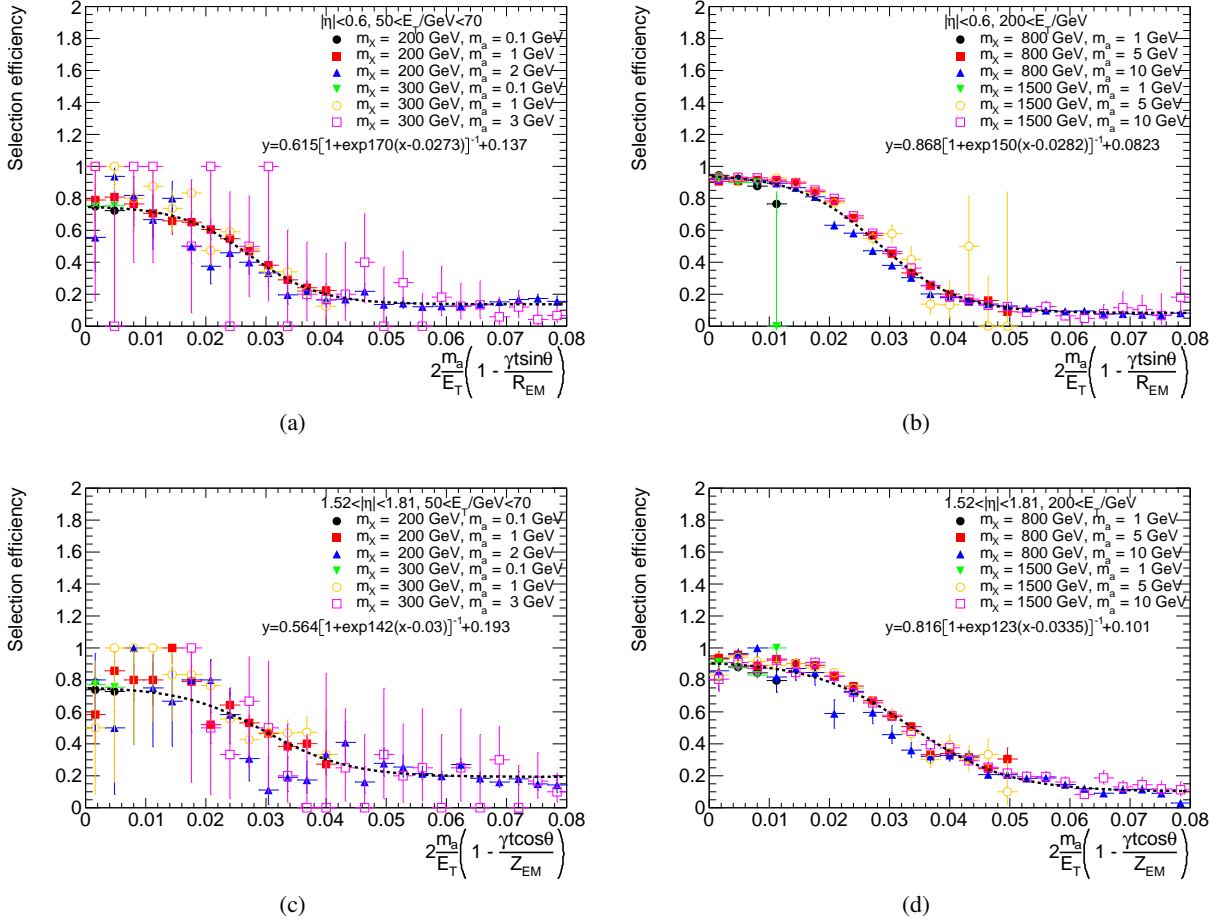$$\varepsilon_{\gamma R}(E_T, \eta, t) = \frac{A}{1 + \exp B(v + C)} + D \tag{76}$$

Figure 73: The result of the parametrization of $\varepsilon_{\gamma_R}(E_T, \eta, t)$. The value of ε_{γ_R} is shown as a function of v. Examples in four (E_T, η) regions are given: (a) $|\eta| < 0.6, 50 < E_T < 70$ GeV, (b) $|\eta| < 0.6, 200$ GeV $< E_T$, (c) $1.52 < |\eta| < 1.81, 50 < E_T < 70$ GeV, and (d) $1.52 < |\eta| < 1.81, 200$ GeV $< E_T$. The results of other (E_T, η) regions are given in Figure 86 in Appendix A.

where the variable v is defined as

$$
v = \begin{cases} \dfrac{2m_a}{E_T}\left(1 - \dfrac{\gamma_a t \sin\theta}{R_{EM}}\right) & (|\eta| < 1.37) \\[4mm] \dfrac{2m_a}{E_T}\left(1 - \dfrac{\gamma_a t \cos\theta}{Z_{EM}}\right) & (1.52 < |\eta| < 2.37) \end{cases} \tag{77}
$$

This variable v is roughly proportional to the separation of the photons originating from $a \to \gamma\gamma$ at the inner surface of the EM calorimeter, as depicted in Figure 72. The result of the parametrization of ε_{γ_R} is shown in Figure 73.

As described above, the value of $\varepsilon_{\gamma_R}(E_T, \eta, t)$ is sufficiently small when the particle a decays after passing the inner surface of the EM calorimeter (i.e. $\gamma_a t \sin\theta > R_{EM}$ for $|\eta| < 1.37$ and $\gamma_a t \cos\theta > Z_{EM}$ for $1.52 < |\eta| < 2.37$). As a conservative approach, the value of $\varepsilon_{\gamma_R}(E_T, \eta, t)$ is treated as 0 in such cases, i.e. $v < 0$.

Similarly, the category fraction f for $X \to aa \to 4\gamma$ for the values (m_X, m_a, Γ_a) can be evaluated by the following equation:

$$f(m_X, m_a, \Gamma_a) = \frac{1}{\varepsilon(m_X, m_a, \Gamma_a)} \int p(E_{T,1}, \eta_1, t_1, E_{T,2}, \eta_2, t_2) \alpha(E_{T,1}, \eta_1, E_{T,2}, \eta_2) \tag{78}$$
$$\times \prod_i \varepsilon_{\gamma_R}(E_{T,i}, \eta_i, t_i) f_{\gamma_R}(E_{T,i}, \eta_i, t_i) \, dE_{T,i} d\eta_i dt_i$$

The variable $f_{\gamma_R}(E_T, \eta, t)$ is defined as the fraction of reconstructed photons with the value of ΔE smaller than the threshold, for reconstructed photons originating from the photon-jet $a \to \gamma\gamma$ and satisfying the event selection requirements. The variable f_{γ_R} in a given (E_T, η) bin is parametrized with the following function:

$$f_{\gamma_R}(E_T, \eta, t) = \frac{A}{1 + \exp B(v + C)} + \frac{D}{1 + \exp E(v + F)} \tag{79}$$

The result of the parametrization is shown in Figure 74.

Using Eq. (75), the signal selection efficiency $\varepsilon(m_X, m_a, \Gamma_a)$ can be estimated using the simulated signal sample of the decay $X \to aa \to 4\gamma$ for the case of the prompt decay of a and the same values of m_X and m_a:

$$\varepsilon(m_X, m_a, \Gamma_a) = \frac{1}{\sum_j w^j} \sum_j w^j \alpha(E_{T,1}^j, \eta_1^j, E_{T,2}^j, \eta_2^j) \tag{80}$$
$$\times \int \prod_i \varepsilon_{\gamma_R}(E_{T,i}^j, \eta_i^j, t_i) \Gamma_a e^{-\Gamma_a t_i} \, dt_i$$

Here, j denotes the j-th event of the simulated signal sample, $\sum_j$ is the summation for all events in the simulated signal sample, w^j is the weight associated to the simulated event, and $E_{T,i}^j, \eta_i^j$ are the values of $E_{T,i}$ and η_i of the simulated event. Similarly, from Eq. (78), the value of $f(m_X, m_a, \Gamma_a)$ can be estimated with the following equation:

$$f(m_X, m_a, \Gamma_a) = \frac{1}{\varepsilon(m_X, m_a, \Gamma_a)} \sum_j w^j \alpha(E_{T,1}^j, \eta_1^j, E_{T,2}^j, \eta_2^j) \tag{81}$$
$$\times \int \prod_i \varepsilon_{\gamma_R}(E_{T,i}^j, \eta_i^j, t_i) f_{\gamma_R}(E_{T,i}^j, \eta_i^j, t_i) \Gamma_a e^{-\Gamma_a t_i} \, dt_i$$

The result of the estimation of the values of ε and f is shown in Figure 75, for some of the values of (m_X, m_a). Also in the figure, the values of ε and f calculated using the simulated signal samples of $X \to aa \to 4\gamma$ are shown. A deviation of the value of ε obtained from the estimation and that obtained from the simulated signal sample is shown in Figure 76(a). For $0.1 < \varepsilon$, this deviation is at the level of 8%, and for $0.03 < \varepsilon < 0.1$, this is at the level of 20%. For $\varepsilon < 0.03$, this deviation is considerably large and so the estimation method described in this section is considered to be unreliable; thus, the reinterpretation of the results is not performed for a signal hypothesis resulting in $\varepsilon < 0.03$. A comparison of the value of f obtained from the estimation, $f_{estimation}$, and that obtained from the simulated signal sample, f_{MC}, is shown in Figure 76(b). The relationship between the two values is evaluated with a function defined as

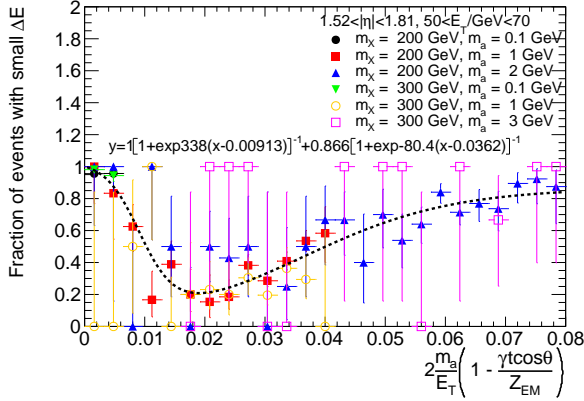$$f_{MC} = \max [0, \min(A, B + C \cdot f_{estimation})] \tag{82}$$

From the fit, the parameters are determined as $A = 0.98, B = -0.056$, and $C = 1.3$. These deviations of the estimated values of ε and f are taken into account in the analysis, as described in Sec. 5.9.2.
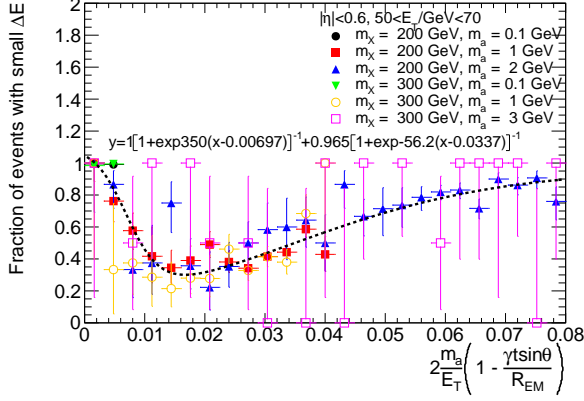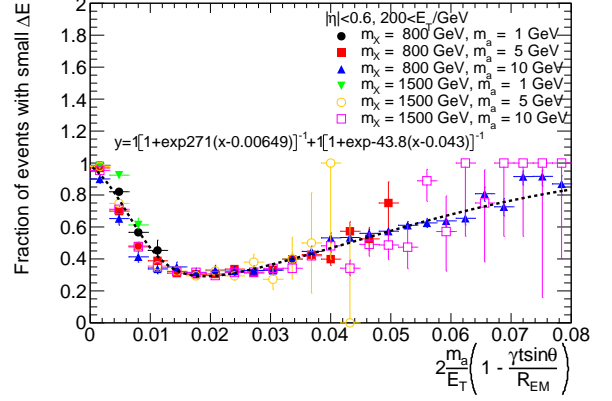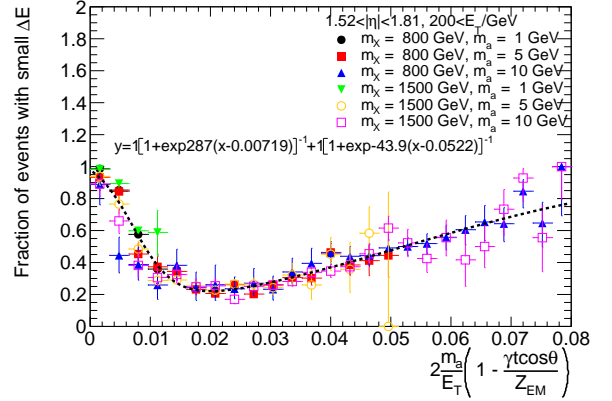
Figure 74: The result of the parametrization of $f_{\gamma_R}(E_T, \eta, t)$. The value of f_{γ_R} is shown as a function of v. Examples in four (E_T, η) regions are given: (a) $|\eta| < 0.6, 50 < E_T < 70$ GeV, (b) $|\eta| < 0.6, 200$ GeV $< E_T$, (c) $1.52 < |\eta| < 1.81, 50 < E_T < 70$ GeV, and (d) $1.52 < |\eta| < 1.81, 200$ GeV $< E_T$. The results of other (E_T, η) regions are given in Figure 87 in Appendix A.
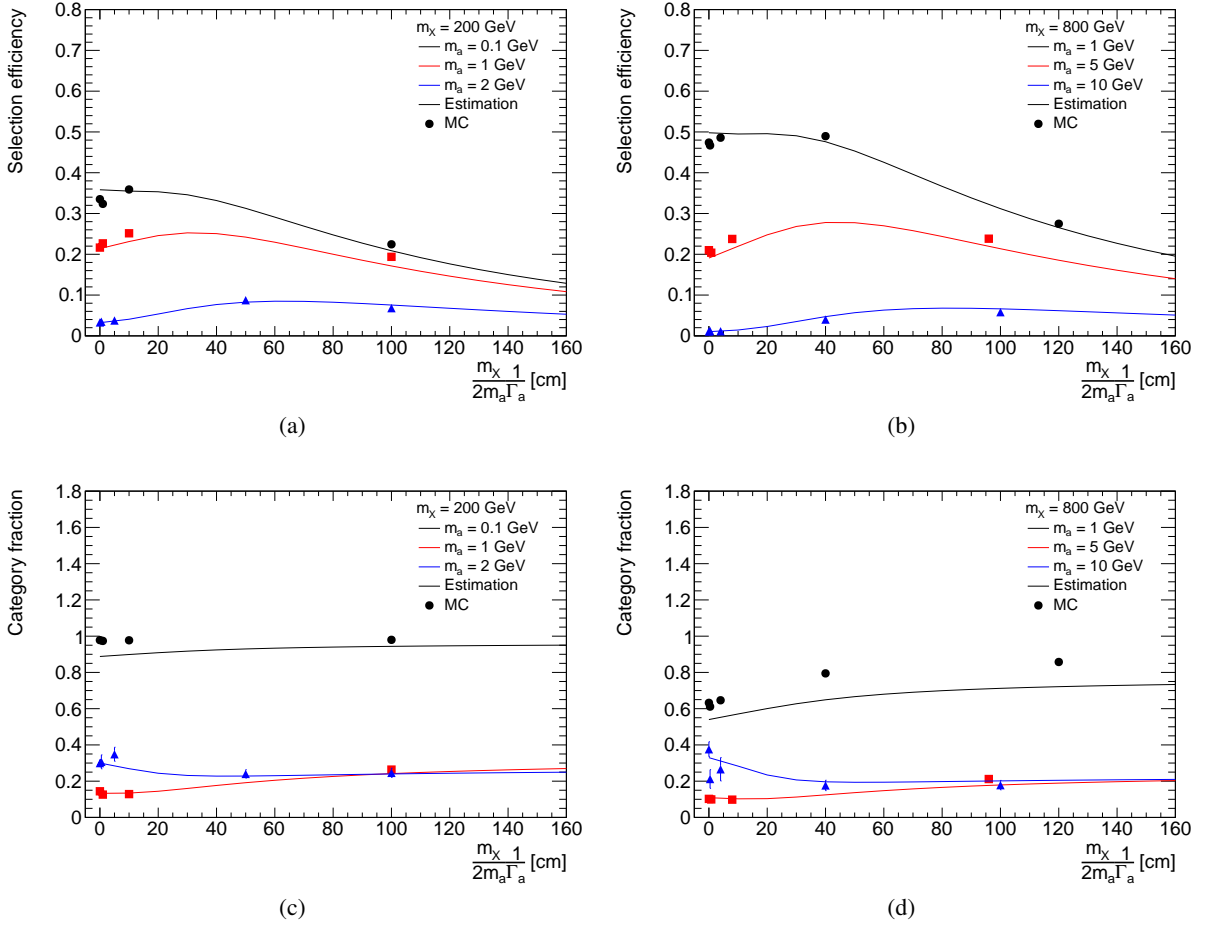
(a)

(b)

(c)

(d)

Figure 75: The values of ε and f for $X \rightarrow aa \rightarrow 4\gamma$. They are shown as functions of the expression $\frac{m_X}{2m_a} \frac{1}{\Gamma_a}$. The lines represent the values evaluated using Eq. (80) and (81). The markers represent the values evaluated using the simulated signal samples for the values (m_X, m_a, Γ_a). (a) and (b) show the results of ε for the case of $m_X = 200$ GeV and $m_X = 800$ GeV, respectively. (c) and (d) show the results of f for the same.

(a)

(b)
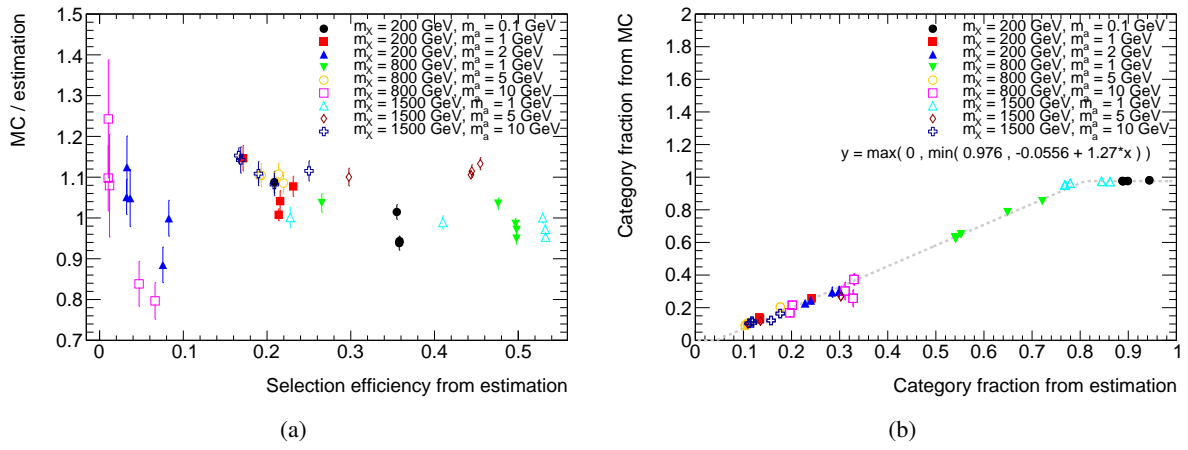
Figure 76: Comparison of the values of ε and f estimated from Eqs. (80) and (81), and those obtained from the simulated signal samples. (a) The ratio of the values of ε obtained from simulated signal samples and from the estimation, shown as a function of the estimated value. (b) The value of f obtained from simulated signal samples shown as a function of the estimated value. The dotted line represents the function used to evaluate the relationship between the two values.

5.9.2 Reinterpretation procedure

The upper limit on the visible cross-section as a function of (m_X, f), shown in Figure 71, is considered to be model-independent, i.e. applicable to signal models with photon-jets in the final state in general. This is because the effect of the difference in the signal mass shape for different signal models on the limit on visible cross-section is small.

For the benchmark signal scenario $X \to aa \to 4\gamma$ for the case of the long-lived a, the values of ε and f can be estimated using Eqs. (80) and (81), respectively. Using these values, the upper limit on the visible cross-section can be approximated by taking the corresponding value in Figure 71 as a function of (m_X, f). Finally, the upper limit on the signal cross-section times branching ratios can be obtained by dividing the upper limit on the visible cross-section by the value of ε.

As discussed in Section 5.9.1 and shown in Figure 76(a), there exists a deviation of the value of ε obtained from the estimation and that obtained from the simulated signal sample. For $0.1 < \varepsilon$, this deviation is at the level of 8%, and for $0.03 < \varepsilon < 0.1$, this is at the level of 20%. For $\varepsilon < 0.03$, this deviation is considerably large. To take this into account, the following procedure is taken as a conservative measure. When the value of ε obtained from Eq. (80), $\varepsilon_{\text{estimation}}$, is smaller than 0.03, the signal hypothesis is ignored from the analysis and the upper limit on the signal cross-section times branching ratios is not evaluated. When $0.03 < \varepsilon_{\text{estimation}} < 0.1$, the value of ε is reduced by a factor 0.8 (i.e. $\varepsilon = \varepsilon_{\text{estimation}} \times 0.8$). When $0.1 < \varepsilon_{\text{estimation}}$, the value of ε is reduced by a factor 0.92 (i.e. $\varepsilon = \varepsilon_{\text{estimation}} \times 0.92$).

The systematic uncertainty of ε arising from sources of experimental uncertainties (i.e. photon energy scale, isolation selection efficiency, shower shape modelling, pileup) are negligibly small compared to the uncertainty of the estimation procedure described above.

To take into account the ambiguity of the estimation of the value of f as shown in Figure 76(b), the following procedure is taken as a conservative measure. The upper limit on the visible cross-section for $f_{\text{estimation}}$ and that for f_{MC} obtained from Eq. (82) are compared, and the limit with larger value is taken as the resulting value.

As discussed in Section 5.8.5, the limit on the visible cross-section slightly depends on the signal mass shape, especially the width σ_{CB}, and the limit may increase (i.e. become weaker) by approximately 20% for larger m_a/m_X. To take this into account, the resulting upper limit on the signal cross-section times branching ratios is increased by a factor 1.2 when $f < 0.5$ as a conservative approach.

These procedures will result in the overestimate of the resulting upper limit on the signal cross-section times branching ratios, as a conservative measure. As a validation of this procedure, the comparison of the upper limit for the case of the prompt decay of the particle a obtained from the estimation procedure, and that obtained from the direct computation in Sec. 5.8.2, is performed. The result is shown in Figure 77. This figure presents the level of agreement of the two methods. It is found that the upper limits obtained from the estimation method are overestimated for some values of (m_X, m_a), because of the conservative approach as described above.

5.9.3 Results

The 95% CL observed upper limit on the product of the production cross-section and the branching ratios for $X \to aa \to 4\gamma$ for the case of the long-lived a is shown in Figure 78. It shows the upper limit on
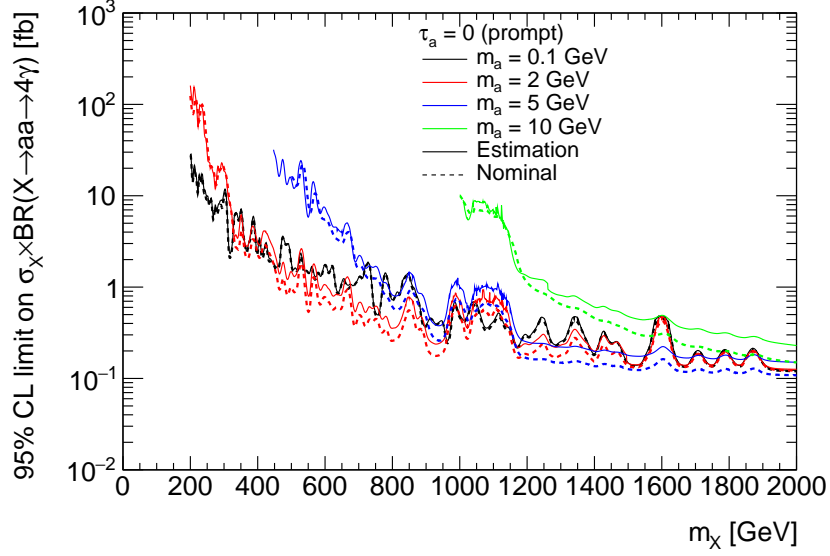
Figure 77: The comparison of the observed upper limits on the production cross-section times the product of branching ratios for $X \to aa \to 4\gamma$ evaluated using two different methods. The solid lines represent the result obtained from the reinterpretation procedure described in Sec. 5.9.2. The dotted lines represent the result obtained from the direct computation described in Sec. 5.8.2.

$\sigma_X \times \mathcal{B}(X \to aa) \times \mathcal{B}(a \to \gamma\gamma)^2$. The limit is calculated based on the result shown in Figure 71, with the reinterpretation procedure described in Section 5.9.2.

A relatively stronger limit is placed for long-lived a around $\frac{m_X}{2m_a}\frac{1}{\Gamma_a} \sim 40$ cm, compared to that for prompt decays. This is because of a mild increase (up to a factor 2) in the signal selection efficiency compared to that for prompt decays, as seen in Figure 75. For larger life time $\frac{m_X}{2m_a}\frac{1}{\Gamma_a} > 50$ cm, the limit becomes weaker due to the decrease in the signal selection efficiency.
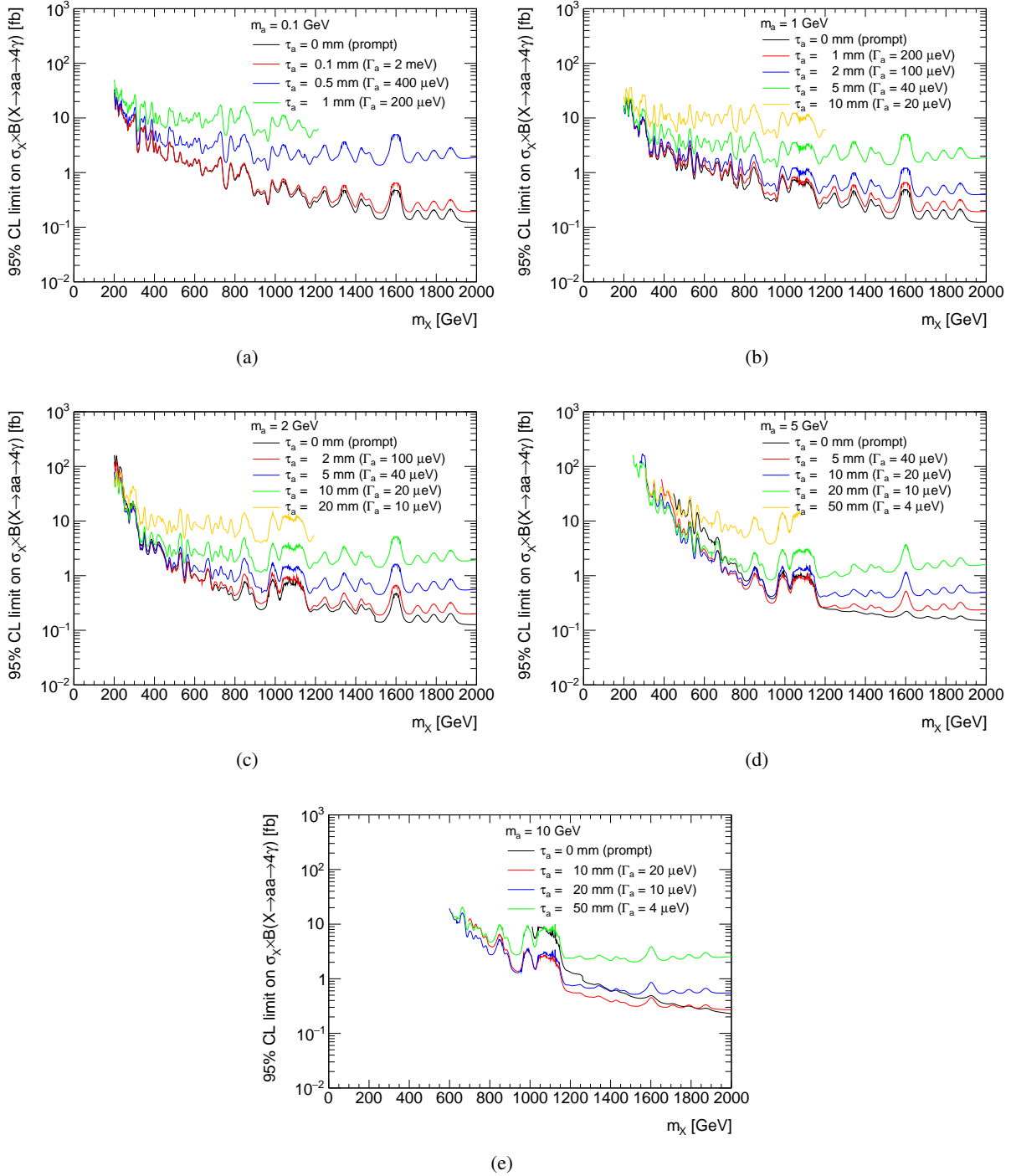
Figure 78: The observed upper limits on the production cross-section times the product of branching ratios for the benchmark signal scenario involving a scalar particle X with a narrow width decaying via $X \rightarrow aa \rightarrow 4\gamma$, $\sigma_X \times \mathcal{B}(X \rightarrow aa) \times \mathcal{B}(a \rightarrow \gamma\gamma)^2$. (a) $m_a = 0.1$ GeV, (b) $m_a = 1$ GeV, (c) $m_a = 2$ GeV, (d) $m_a = 5$ GeV, and (e) $m_a = 10$ GeV.

6 Interpretation of the results in the context of NMSSM

In the NMSSM, the process $H \to aa \to 4\gamma$ can result in a pair of photon-jets, as described in Section 2.3. Here, H is a scalar Higgs boson with a mass larger than 125 GeV, and a is a pseudoscalar Higgs boson with a mass of $O(1)$ GeV. H is assumed to be produced by the gluon–gluon fusion process.

The interpretation of the search result (described in Section 5.8) is performed for the process $H \to aa \to 4\gamma$[24]. A scan of the NMSSM parameters is performed to determine the parameter space in which the signal hypothesis is excluded by the search result.

6.1 Method

The public computation package `NMSSMTools 5.3.1` [77, 78] is used for the computation of the masses, couplings, and decay widths of all Higgs bosons, as well as the masses and decays of the sparticles. The Higgs spectrum is computed including full one-loop, Yukawa-driven two-loop, and pole corrections [79]. Experimental constraints from LEP, Tevatron, LHC experiments, and constraints from B and K physics are checked. `HiggsBounds 5.3.2` [80–84] is used to check the experimental constraints from LEP, Tevatron and LHC experiments for the Higgs sector. The production cross sections of the Higgs particles at 13 TeV pp collisions are computed using `SusHi 1.6.1` [85, 86], interfaced with `LHAPDF 6.2.1` [87] and using `MMHT2014nnlo68cl` [88] as the PDF.

For the computation results in this section, NMSSM parameters that are not directly related to the Higgs sector are fixed to reasonable values, namely

$$
\begin{aligned}
2M_1 = M_2 = \frac{M_3}{3} &= 4 \text{ TeV} \\
A_t &= -20 \text{ TeV} \\
A_b = A_\tau &= 1.5 \text{ TeV} \\
m_{\tilde{L}} &= 800 \text{ GeV} \\
m_{\tilde{Q}} &= 10 \text{ TeV}
\end{aligned}
\tag{83}
$$

M_1, M_2, M_3 are the gaugino masses, A_t, A_b, A_τ are the trilinear soft couplings, $m_{\tilde{L}}$ is the soft masses of the sleptons chosen to be degenerate (for simplicity), and $m_{\tilde{Q}}$ are the squark soft masses chosen to be degenerate (for simplicity).

As described in Eq. (35) of Section 2.2.3, the NMSSM Higgs sector has six independent parameters, which are chosen to be $\mu, \tan\beta, \lambda, \kappa, A_\lambda, A_\kappa$ in this thesis. In the following computation results in this section, μ and $\tan\beta$ are fixed to chosen values for simplicity. As discussed already in Section 2.3, the values of $\tan\beta$ are constrained to $1 \lesssim \tan\beta \lesssim 10$–80, considering that the top quark Yukawa coupling should not become too large at the GUT scale, and the exclusion limit in the $(M_A, \tan\beta)$ plane for the hMSSM model (shown in Figure 6). From the LEP limit for the higgsino mass (shown in Figure 7), an approximate limit of $\mu \gtrsim 100$ GeV is obtained. Also, a value of μ close to the electroweak scale is considered to be "natural"

---

[24]The process $H \to aa \to 6\pi^0 \to 12\gamma$ is not considered. This is because this process arise in the NMSSM only when m_a is within some value, as described in Section 2.3.1 as Case 2. Such case is out of scope of this thesis, and is not considered.

(derived from the value of m_Z^2 in Eq. (28)). Thus, taking these constraints into consideration, the values of μ and $\tan\beta$ are chosen to be the following:

$$\mu = 110 \text{ GeV}$$
$$\tan\beta = 5 \tag{84}$$

Note that with the parameter sets in Eqs. (83) and (84), the value of $\Delta m(\tilde{\chi}_1^\pm, \tilde{\chi}_1^0) = m_{\tilde{\chi}_1^\pm} - m_{\tilde{\chi}_1^0}$, i.e. the mass difference between the lightest chargino and the lightest neutralino, is typically $\Delta m(\tilde{\chi}_1^\pm, \tilde{\chi}_1^0) = 1.2$ GeV. Thus, the parameter sets that are tested (Eqs. (83) and (84)) are not excluded by past searches shown in Figure 7.

6.2 Scan region

A parameter scan is performed in the scan region defined as the following:

$$0.028 < \lambda < 0.043$$
$$3.2\lambda < \kappa < 4.4\lambda$$
$$\frac{2\kappa}{\lambda}\mu \times 1.08 < A_\lambda < \frac{2\kappa}{\lambda}\mu \times 1.14 \tag{85}$$
$$0.1 \text{ GeV} < A_\kappa < 0.7 \text{ GeV}$$

The scan step of λ is 0.001. The scan steps of κ and A_λ are defined as 1/20 of their scan regions. The scan step of A_κ is 0.005 GeV.

The rationale for the choice of this scan region is described below.

Scan region of A_λ

For the pseudoscalar a to have a sizeable $\mathcal{B}(a \to \gamma\gamma)$ (e.g. more than 30%), a has to be a nearly pure singlet state (i.e. the decoupling limit), as described in Section 2.3. In such a case, the branching ratio of a into a pair of SM fermions or gluons is considerably small; a can dominantly decay into $\gamma\gamma$ via a loop of charged higgsinos.

The mass matrix of pseudoscalar Higgs bosons, in the basis ($A_D = \cos\beta H_{uI} + \sin\beta H_{dI}$, $A_S = S_I$) after rotating away the Goldstone mode, is given in Eq. (40). This is rewritten below for convenience:

$$M_P^2 = \begin{pmatrix} M_A^2 & \lambda\left(A_\lambda - \frac{2\kappa}{\lambda}\mu\right)v \\ \lambda\left(A_\lambda - \frac{2\kappa}{\lambda}\mu\right)v & M_{A_S}^2 \end{pmatrix} \tag{86}$$

$$M_A^2 = \frac{2\mu\left(A_\lambda + \frac{\kappa}{\lambda}\mu\right)}{\sin 2\beta} \tag{87}$$

$$M_{A_S}^2 = \lambda^2\left(A_\lambda + \frac{4\kappa}{\lambda}\mu\right)\frac{v^2 \sin 2\beta}{2\mu} - \frac{3\kappa}{\lambda}A_\kappa\mu \tag{88}$$

At tree level, the decoupling limit of the pseudoscalar Higgs bosons is given in Eq. (50) as:

$$\tan 2\theta_A = \frac{2\lambda\left(A_\lambda - \frac{2\kappa}{\lambda}\mu\right)v}{M_A^2 - M_{A_S}^2} \ll 1 \tag{89}$$
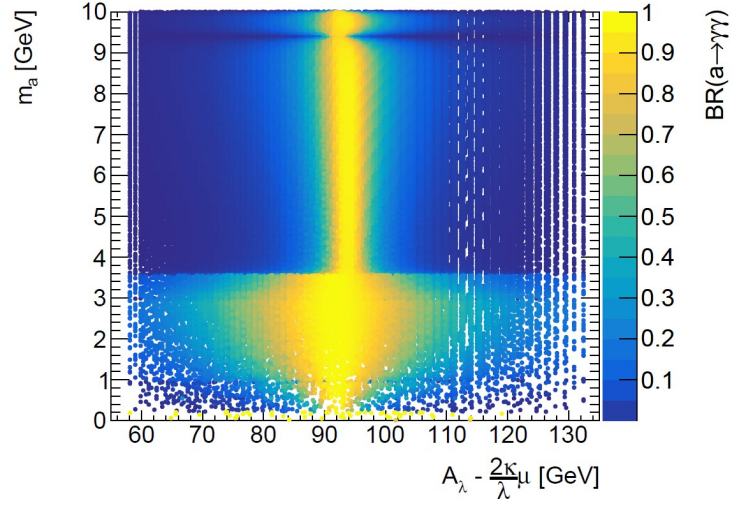
Figure 79: The computational results of $\mathcal{B}(a \to \gamma\gamma)$ with respect to A_λ and m_a, computed in the region defined with Eq. (85).

Thus, the following condition is considered:

$$A_\lambda - \frac{2\kappa}{\lambda}\mu \sim 0 \tag{90}$$

Note that in this case, $M_A^2 \sim \frac{6\kappa}{\lambda \sin 2\beta}\mu^2$.

The values of $\mathcal{B}(a \to \gamma\gamma)$ as a function of $A_\lambda - \frac{2\kappa}{\lambda}\mu$ is shown in Figure 79. The value of $\mathcal{B}(a \to \gamma\gamma)$ increases to 1 when $A_\lambda - \frac{2\kappa}{\lambda}\mu \sim 0$; however, the actual decoupling limit is achieved when $A_\lambda - \frac{2\kappa}{\lambda}\mu \sim$ 90 GeV, as seen in Figure 79, because of the loop corrections to the mass matrix. Thus, to take this shift into account, the scan region of A_λ is defined as $A_\lambda = \frac{2\kappa}{\lambda}\mu \times$ (1.08–1.14).

A notable feature of Figure 79 is the change in the distribution of $\mathcal{B}(a \to \gamma\gamma)$ with respect to m_a. For $m_a > 2m_\tau$, the decay $a \to \tau\tau$ opens up, and thus the region of A_λ in which $\mathcal{B}(a \to \gamma\gamma)$ is near 1 becomes smaller compared to $m_a < 2m_\tau$. For $m_a = 9.4$ GeV or 10 GeV, $\mathcal{B}(a \to \gamma\gamma)$ decreases due to the mixing of a with a pseudoscalar bottomium.

Scan region of A_κ

In the decoupling limit, $m_a \sim M_{A_S}$. As discussed in Section 5.8, the photon-jet search result is sensitive roughly to the region $m_a < 0.01 \times m_X$. For simplicity, the value of m_a is limited to the region $m_a < 10$ GeV in the following discussions in this section. Thus, applying the limit $0 < M_{A_S}^2 < (10 \text{ GeV})^2$ in Eq. (88), the value of A_κ is limited to $O(0.1 \text{ GeV})$. This relationship is shown in Figure 80.
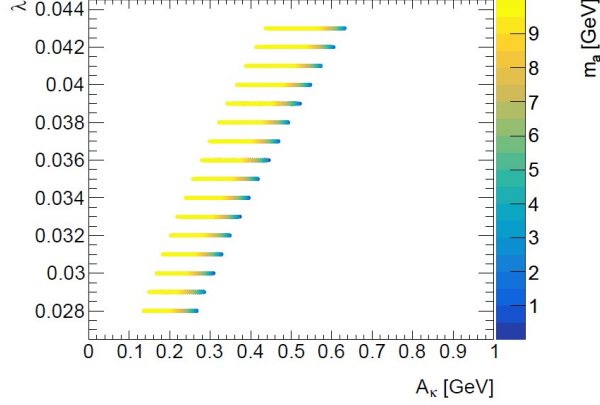
Figure 80: The computational results of m_a projected in the (A_κ, λ) plane, computed in the region defined with Eq. (85). The plotted points are limited to the region $0 < m_a < 10$ GeV.

Scan region of λ and κ

$\sigma(ggF \to H \to aa)$ is the product of the production cross section of the heavy Higgs via gluon–gluon fusion process and the branching ratio into aa pair. For the value of $\sigma(ggF \to H \to aa)$ to be sizeable (e.g. around the order of $O(1$ fb)), it is necessary for the heavy Higgs to have both a large ggH coupling (e.g. $\sim 10\%$ of the SM Higgs-like boson with the same mass) and a large $\mathcal{B}(H \to aa)$ (e.g. more than 0.1). Thus, the BSM scalar Higgs in question has to be a mixed state of the doublet and singlet components, as described in Section 2.3.

The mass matrix of electrically neutral scalar Higgs bosons in the basis ($H_{\mathrm{SM}} = \cos\beta H_{dR} + \sin\beta H_{uR}$, $H_D = -\sin\beta H_{dR} + \cos\beta H_{uR}$, $H_S = S_R$) is given in Eq. (36). This is rewritten below for convenience:

$$M_S^2 = \begin{pmatrix} M_Z^2\cos^2\beta + \lambda^2 v^2 \sin^2 2\beta & (\lambda^2 v^2 - m_Z^2)\sin 2\beta \cos 2\beta & 2\lambda\mu v\left[1 - \left(\frac{M_A \sin 2\beta}{2\mu}\right)^2\right] \\ (\lambda^2 v^2 - m_Z^2)\sin 2\beta \cos 2\beta & M_{H_D}^2 & -\frac{\lambda v}{2\mu}M_A^2 \sin 2\beta \cos 2\beta \\ 2\lambda\mu v\left[1 - \left(\frac{M_A \sin 2\beta}{2\mu}\right)^2\right] & -\frac{\lambda v}{2\mu}M_A^2 \sin 2\beta \cos 2\beta & M_{H_S}^2 \end{pmatrix} \tag{91}$$

$$M_{H_D}^2 = M_A^2 + (m_Z^2 - \lambda^2 v^2)\sin^2 2\beta \tag{92}$$

$$M_{H_S}^2 = \left(\frac{2\kappa}{\lambda}\mu\right)^2\left(1 + \frac{\lambda A_\kappa}{4\kappa\mu}\right) - \frac{\kappa\lambda}{2}v^2 \sin 2\beta\left(1 - \frac{\lambda M_A^2}{\kappa\mu^2}\right) \tag{93}$$

When $M_A \gg v$, $M_{H_D} \sim M_A$. When $1 \gg \frac{\lambda A_\kappa}{4\kappa\mu}$, $M_{H_S} \sim \frac{2\kappa}{\lambda}\mu$. For the heavy scalar Higgs to be a mixed state of the doublet and singlet components, $M_{H_D} \sim M_{H_S}$. Under these assumptions, the following relationship is obtained:

$$A_\lambda + \frac{\kappa}{\lambda}\mu \sim \frac{2\kappa^2 \sin 2\beta}{\lambda^2}\mu \tag{94}$$

Considering the decoupling limit of the pseudoscalar Higgs bosons, Eq. (90),

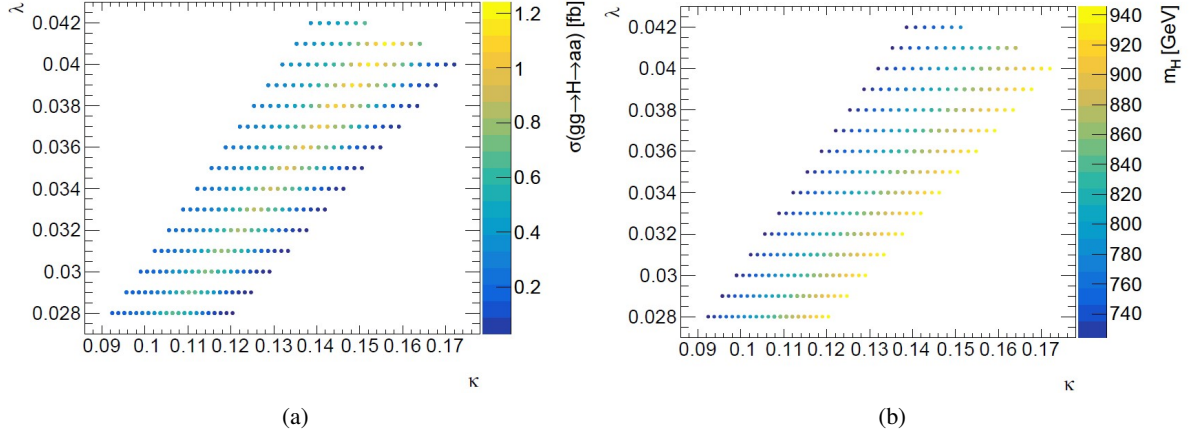$$\frac{\kappa}{\lambda} \sim \frac{3}{2\sin 2\beta} \tag{95}$$

105

Figure 81: The computational result of (a) $\sigma(ggF \to H \to aa)$ and (b) m_H projected in the (λ, κ) plane, computed in the region defined with Eq. (85). For details, see text.

For $\tan \beta = 5$, this relationship leads to $\kappa \sim 3.9\lambda$.

Figure 81(a) shows the values of $\sigma(ggF \to H \to aa)$ projected in the (λ, κ) plane. The maximum of the two values, $\sigma(gg \to H_2 \to aa)$ and $\sigma(gg \to H_3 \to aa)$, is plotted. It is found that, for a fixed value of λ, $\sigma(ggF \to H \to aa)$ is maximum at $\kappa \sim 3.9\lambda$. Additionally, the maximum value of $\sigma(ggF \to H \to aa)$ decreases for smaller λ. This is because $\mathcal{B}(H \to aa)$ decreases, which is because the coupling constant of H and a is proportional to κ.

Figure 81(b) shows the values of m_H projected in the (λ, κ) plane. The value of m_H is chosen to be m_{H_2} if $\sigma(gg \to H_2 \to aa) > \sigma(gg \to H_3 \to aa)$, or m_{H_3} otherwise. It is found that m_H is roughly proportional to $\frac{\kappa}{\lambda}$.

Note that from Eqs. (93) and (95), the following relationship is derived:

$$M_{H_S} \sim \frac{3}{\sin 2\beta} \mu \tag{96}$$

Thus, when considering a large $\sigma(gg \to X \to aa \to 4\gamma)$ (e.g. around the order of $O(1 \text{ fb})$), the value of M_{H_S} is roughly determined by two variables, μ and $\tan \beta$.

6.3 Result

The result of the computational scan is shown in Figure 82. The scan region is that defined in Eq. (85). The selections applied to the plotted points are the following:

- The derived parameters are not excluded by measurements from past experiments at 95% CL[25]. This is checked with the use of NMSSMTools and HiggsBounds, as described in Section 6.1.

- $0 < m_a < 10$ GeV

---

[25]This excludes the measurement result of muon $g - 2$. A dark matter relic density smaller than the observed value is allowed. The SM Higgs mass is allowed to be in the range 122–128 GeV, considering the uncertainty of the calculation of its mass.
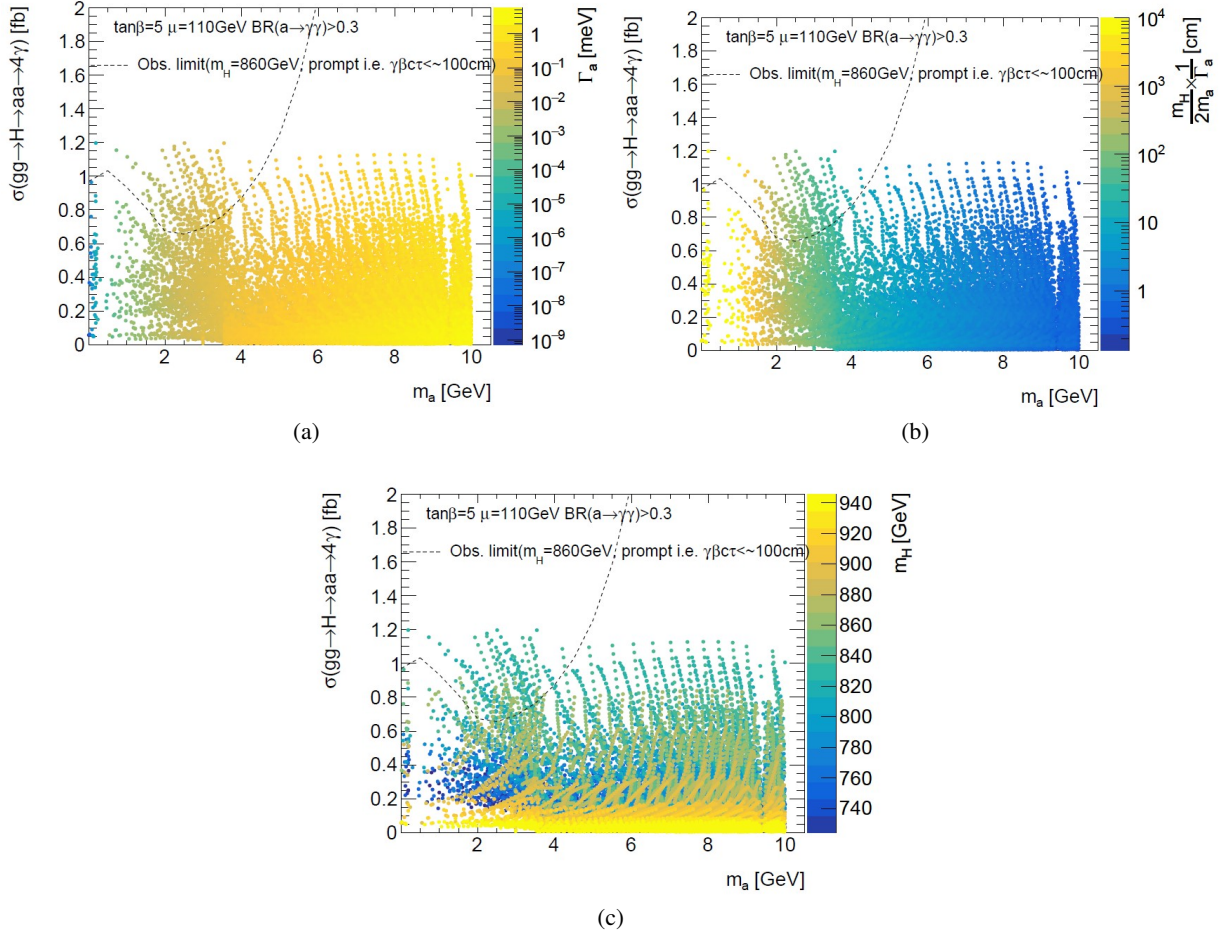
Figure 82: The computational result of $\sigma(gg \to H \to aa \to 4\gamma)$ with respect to m_a. Only the parameter sets with $\mathcal{B}(a \to \gamma\gamma) > 0.3$ are plotted. The dotted line shows the observed upper limit on $\sigma(gg \to H \to aa \to 4\gamma)$ at 95% CL for the case of a prompt decay of the particle a. The z axis shows the values of (a) Γ_a, (b) $\frac{m_H}{2m_a}\frac{1}{\Gamma_a}$, and (c) m_H. For (b), the value of z-axis is plotted as 10^4 cm if it is larger than 10^4 cm. For detail, see text.

- $\mathcal{B}(a \to \gamma\gamma) > 0.3$

For the figure, the maximum of the two values, $\sigma(gg \to H_2 \to aa \to 4\gamma)$ and $\sigma(gg \to H_3 \to aa \to 4\gamma)$, is plotted. The value of m_H is chosen to be m_{H_2} if $\sigma(gg \to H_2 \to aa) > \sigma(gg \to H_3 \to aa)$, or m_{H_3} otherwise.

For the z axis of Figure 82(b), the variable $\frac{m_H}{2m_a}\frac{1}{\Gamma_a}$ is plotted; this is approximately equal to the average of the $\gamma_a\beta_a c\tau_a$ of the a at the lab frame. In these figures, the observed limit for the case of $m_H = 860$ GeV and the prompt decay of a (i.e. $\frac{1}{\Gamma_a} = 0$) is plotted with a dotted line. As described in Section 5.8, the observed limit for the prompt decay case of a is applicable (within a few tens of %) to the cases of $\frac{m_H}{2m_a}\frac{1}{\Gamma_a} \lesssim 1$ m. Thus, from these figures, it is found that the photon-jet search result is sensitive to some parameter sets in the region 2 GeV $\lesssim m_a \lesssim 5$ GeV.

Figure 83 shows the parameter region rejected by the photon-jet search at 95% CL. In this figure, the 4-dimensional parameter space $(\lambda, \kappa, A_\lambda, A_\kappa)$ is projected in the 3-dimensional space $(\lambda, \kappa, A_\kappa)$ (i.e. projected
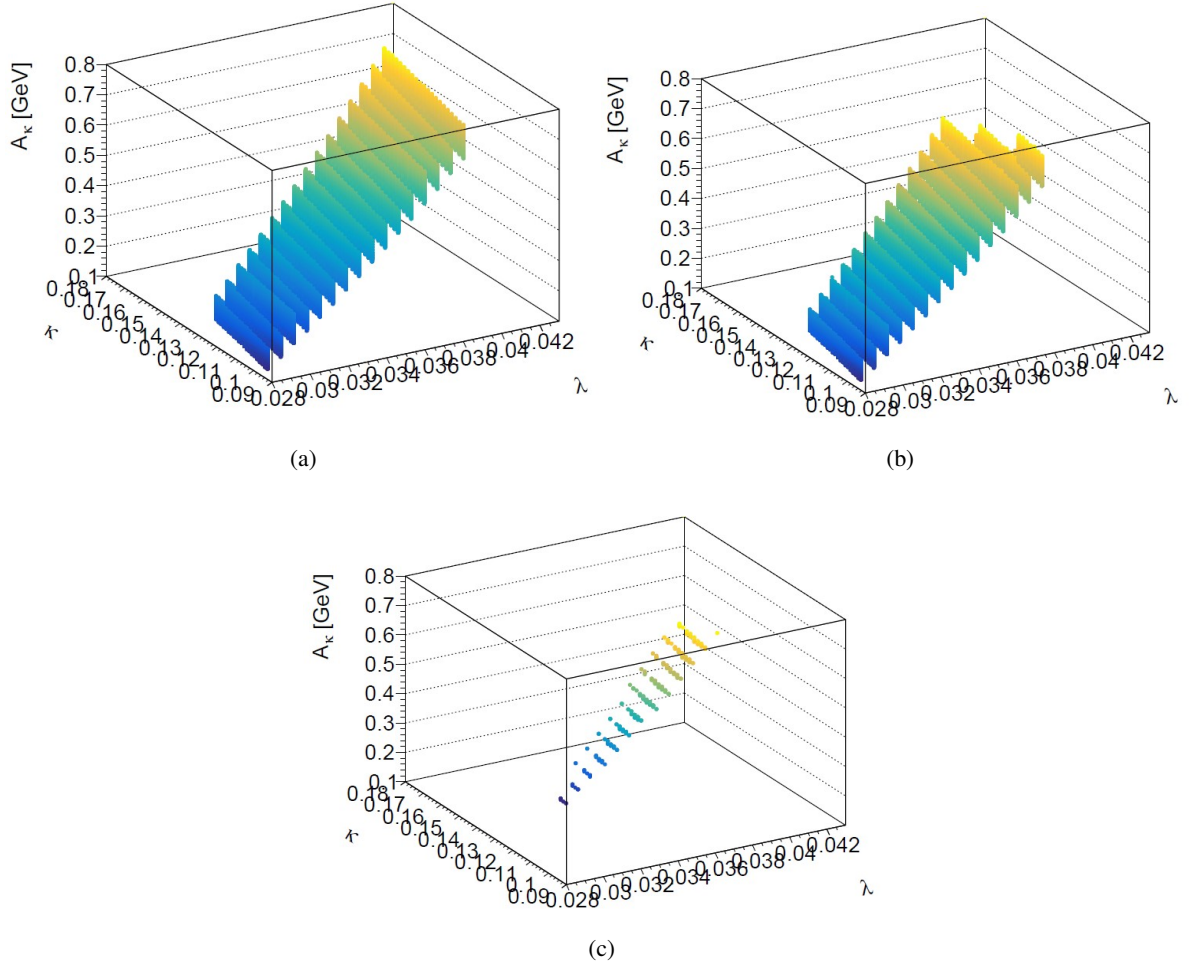
Figure 83: The 4-dimensional parameter space $(\lambda, \kappa, A_\lambda, A_\kappa)$ projected in the 3-dimensional space $(\lambda, \kappa, A_\kappa)$ (i.e. projected in the A_λ direction). The colours of the markers show the value of the z axis, i.e. A_κ, to help the readability of the plots. (a) The parameter region with $0 < m_a < 10$ GeV. (b) The subset of (a) which is not excluded by measurements from past experiments at 95% CL. (c) The subset of (b) which is excluded by the photon-jet search at 95% CL.

in the A_λ direction). Figure 83(a) shows the parameter sets with $0 < m_a < 10$ GeV. Figure 83(b) shows the subset of Figure 83(a) which is not excluded by measurements from past experiments at 95% CL[25]. Figure 83(c) shows the subset of Figure 83(b) which is excluded by the photon-jet search at 95% CL. Figure 84 shows the results shown in Figure 83(c) projected in the (λ, κ) plane or the (λ, A_κ) plane.

From the result presented in Figure 83(c), it is summarized that the photon-jet search result excludes a subset of the $(\lambda, \kappa, A_\lambda, A_\kappa)$ parameter space for the case $\mu = 110$ GeV and $\tan\beta = 5$, namely:

- $0.030 < \lambda < 0.040$

- $\kappa \sim 3.9\lambda$ [26]

---

[26]One thing to note from Figure 84(a) is that the parameter space rejected by the photon-jet search result is centred around two values, $\kappa/\lambda \simeq 3.9$ and $\kappa/\lambda \simeq 3.7$. This is explained by the fact that the observed upper limit for the case of $m_X = 800$ GeV is stronger by a factor 2 compared to that of $m_X = 860$ GeV , due to the statistical fluctuation, as seen in Figure 78.
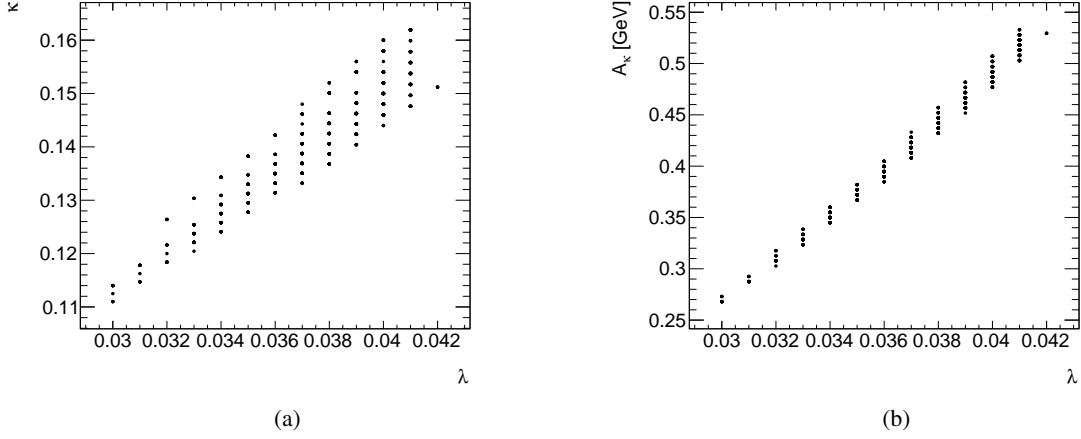
Figure 84: The region of parameter space $(\lambda, \kappa, A_\lambda, A_\kappa)$ excluded by the photon-jet search at 95% CL, projected in the (a) (λ, κ) plane and (b) (λ, A_κ) plane.
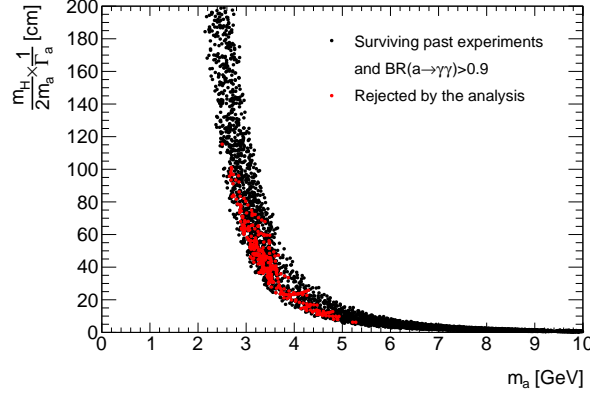

Figure 85: The excluded parameter sets by the photon-jet search at 95% CL in the $\left(m_a, \frac{m_H}{2m_a}\frac{1}{\Gamma_a}\right)$ plane. The black markers are the parameters sets that are not excluded by measurements from past experiments at 95% CL and $\mathcal{B}(a \to \gamma\gamma) > 0.9$. The red markers are the subset of the black markers which are excluded by the photon-jet search.

- $A_\lambda \sim \frac{2\kappa}{\lambda}\mu$ such that $\mathcal{B}(a \to \gamma\gamma) \sim 1$

- $A_\kappa \sim O(0.1\text{ GeV})$ which is corresponding to $2\text{ GeV} \lesssim m_a \lesssim 5\text{ GeV}$

The limit $\lambda < 0.040$ is derived because the region $\lambda > 0.040$ is rejected by the past measurement, namely the SM Higgs cross-section measurement at the LHC experiments. A larger value of λ leads to a larger $\mathcal{B}(h \to aa)$, where h is the SM-like Higgs boson, and thus a smaller cross section of $h \to ZZ$ than the measured value.

Figure 85 shows the parameter sets rejected by the photon-jet search result in the $\left(m_a, \frac{m_H}{2m_a}\frac{1}{\Gamma_a}\right)$ plane. One thing to note is that $\frac{m_H}{2m_a}\frac{1}{\Gamma_a}$ is roughly proportional to the inverse of m_a^2. Another thing to note is that the region which the photon-jet search result is sensitive to is found to be $2\text{ GeV} \lesssim m_a \lesssim 5\text{ GeV}$ and $\frac{m_H}{2m_a}\frac{1}{\Gamma_a} \lesssim 1\text{ m}$.

Finally, it should be mentioned here the dependence of the excluded parameter space on the values of $(\mu, \tan\beta)$. The discussion in this section is limited to the case of $\mu = 110$ GeV and $\tan\beta = 5$, for simplicity. A similar result is inferred for other cases of $(\mu, \tan\beta)$, with the following two points taken into consideration. Firstly, as in Eq. (96), the value of m_H is determined by the values of $(\mu, \tan\beta)$ for the case of a sizeable $\sigma(gg \to H \to aa \to 4\gamma)$. The observed upper limit on $\sigma(gg \to X \to aa \to 4\gamma)$ depends on the value of m_X, and thus the excluded space of the parameters $(\lambda, \kappa, A_\lambda, A_\kappa)$ depends on the values of $(\mu, \tan\beta)$. Secondly, the limit on $(m_A, \tan\beta)$ space for the hMSSM model, as in Figure 6, is naively applicable to the NMSSM, and this needs to be taken into account.

6.4 Future directions

As described in the previous section, the photon-jet search result excludes a subset of the $(\lambda, \kappa, A_\lambda, A_\kappa)$ parameter space, depending on the values of $(\mu, \tan\beta)$.

The excluded region for the parameters λ, κ, and A_λ can be expanded by improving the upper limit on $\sigma(gg \to X \to aa \to 4\gamma)$, e.g. by increasing the statistics of the collision dataset or improving the analysis strategy. This is because the parameters λ, κ, and A_λ are strongly related to the values $\mathcal{B}(H \to aa), \sigma(gg \to H)$, and $\mathcal{B}(a \to \gamma\gamma)$, respectively.

Other regions of A_λ can be checked by performing a search for a scalar resonance decaying into other final states, e.g. $X \to 4\mu, jj, 4\tau$, or $4b$.

The excluded region for the parameter A_κ can be expanded by improving the analysis strategy of the photon-jet search. The parameter A_κ is strongly related to the value of m_a. The upper limit for the parameter A_κ (corresponding to $m_a \lesssim 5$ GeV in the previous section) can be expanded by improving the analysis strategy of the photon-jet search, so that the search is sensitive to less collimated photon-jets, i.e. larger m_a/m_X. The lower limit for the parameter A_κ (corresponding to 2 GeV $\lesssim m_a$ in the previous section) can be expanded by developing an analysis strategy for a long-lived a. The sensitivity of the photon-jet search results is in the region $\frac{m_H}{2m_a}\frac{1}{\Gamma_a} \lesssim 1$ m, because it requires the particle a to decay within the inner radius of the EM calorimeter. To search for a longer-lived a, it is necessary to search for particles that travel long distances (e.g. $> O(10)$ m) before decaying via $a \to \gamma\gamma$. The FASER experiment [89] is a proposal to build a detector far from the ATLAS pp interaction point, that may be able to search for such long-lived particles.

7 Conclusion

A search for a heavy scalar resonance decaying into a pair of photon-jets (i.e. groups of collimated photons that share close trajectories) is performed using pp collisions at $\sqrt{s} = 13$ TeV. The pp collision dataset was collected with the ATLAS detector in 2015 and 2016, corresponding to an integrated luminosity of 36.7 fb^{-1}. The search is performed in a largely model-independent way, so that the search is sensitive to the BSM scenarios leading to a pair of photon-jets in general. Candidate events of a resonance decaying into a pair of photon-jets are selected from events with two high-E_T reconstructed photons, where each reconstructed photon corresponds to a photon-jet in the case of signal events. The event selection and the event categorization are optimized for the signal events, utilizing the EM shower shape observed in the EM calorimeter. To cover a wide range of values of m_X and m_a, several aspects of the search (e.g. $m_{\gamma_R\gamma_R}$ shape of signal events, signal selection efficiency, and category fraction) are parametrized as functions of m_X and m_a. The shape of the background component in the $m_{\gamma_R\gamma_R}$ distributions is evaluated with an analytic function. An excess of events is searched for by performing an unbinned maximum-likelihood fit, with the consideration of the signal and background components, to the $m_{\gamma_R\gamma_R}$ distributions of the two event categories. The observed $m_{\gamma_R\gamma_R}$ distributions are found to be consistent with the SM background expectation, with no significant excess of events being observed.

The results of a null observation are interpreted in the context of BSM scenarios which assume a scalar resonance decaying into a final state with photons. One scenario assumes a scalar resonance X with a mass of $O(100)$ GeV, with a narrow width, and produced by the gluon–gluon fusion process; X decays into a pair of spin-0 particles a with a mass of $O(1)$ GeV that decays into a pair of photons, via $X \to aa \to 4\gamma$. Another scenario assumes the decay of the a particle into three neutral pions, via $X \to aa \to 6\pi^0 \to 12\gamma$. Upper limits on the cross-sections of the two BSM scenarios, $\sigma_X \times \mathcal{B}(X \to aa) \times \mathcal{B}(a \to \gamma\gamma)^2$ and $\sigma_X \times \mathcal{B}(X \to aa) \times \mathcal{B}(a \to 6\pi^0)^2$, are evaluated for the region 200 GeV $< m_X <$ 2 TeV and $m_a < 0.01 \times m_X$, using an asymptotic approximation. They are found to be as low as 0.2 fb for $m_X = 2$ TeV. Some scenarios predict photon-jets produced from a decay of a long-lived boson; the results are interpreted for such a case as well.

The results are interpreted in the context of the NMSSM for the process $H \to aa \to 4\gamma$, where H is a new scalar Higgs boson with a mass larger than 200 GeV, and a is a pseudoscalar Higgs boson with a mass of $O(1)$ GeV. It is possible for the cross section of the process to be sizeable (e.g. around the order of $O(1$ fb)); this possibility arise when the physical state H is a mixed state of the doublet and singlet field components, and the physical state a is a decoupled state with dominant singlet field component. It is found that the photon-jet search result excludes a subset of the parameter space of the NMSSM; for the case of $\tan\beta = 5$ and $\mu = 110$ GeV, a subset of the parameter space with 2 GeV $< m_a <$ 5 GeV and an expected decay radius of a of less than 1 m (i.e. $\frac{m_a}{2m_H}\frac{1}{\Gamma_a} < 1$ m) is excluded.

This is the first result of a search for a heavy ($>$ 200 GeV) resonance decaying into photon-jets, performed to search for new physics at the energy-frontier pp collision experiment at the LHC. This research is a new frontier of direct searches using a novel final state. This result places constraints on the subset of the parameter space of the NMSSM that have not been looked into before.

Acknowledgements

Appendix

A Results of selection efficiency and category fraction parametrizations for the case of long-lived *a*

The signal selection efficiency and category fraction parametrizations for the case of long-lived *a* are described in Section 5.9.1. A few examples are shown in Figures 73 and 74, and all the results in all (E_{T}, η) regions are shown in Figures 86 and 87. These results can be utilized for reinterpretation of the photon-jet search results to a BSM signal scenario leading to photon-jet final states in general.
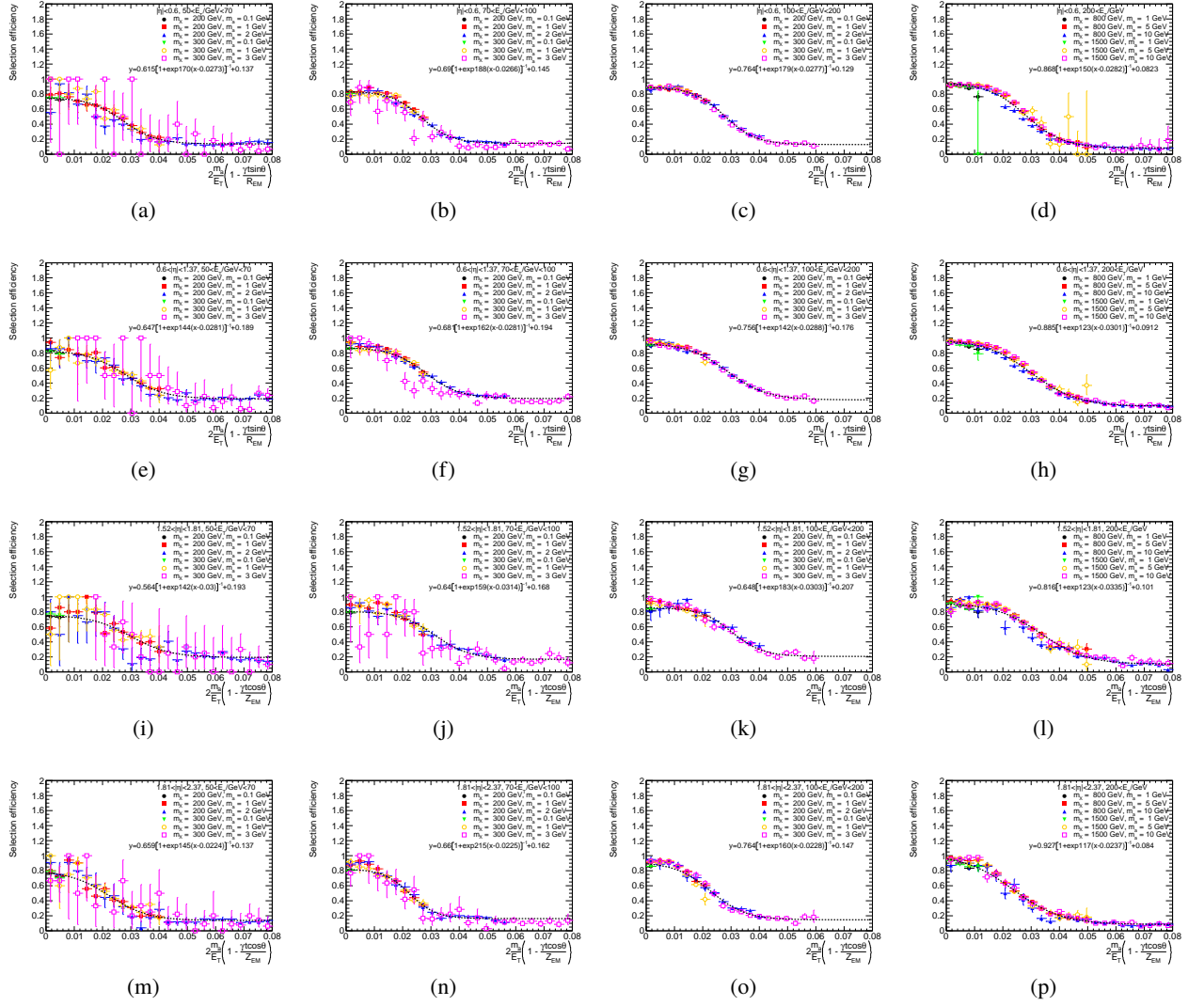
Figure 86: The result of the parametrization of $\varepsilon_{\gamma_R}(E_T, \eta, t)$. The value of ε_{γ_R} is presented as a function of v. The result of the parametrization is presented for each of the 16 bins of the (E_T, η) parameter space of the particle a: $|\eta| < 0.6$ and (a) $50 < E_T < 70$ GeV, (b) $70 < E_T < 100$ GeV, (c) $100 < E_T < 200$ GeV, (d) 200 GeV $< E_T$, $0.6 < |\eta| < 1.37$ and (e) $50 < E_T < 70$ GeV, (f) $70 < E_T < 100$ GeV, (g) $100 < E_T < 200$ GeV, (h) 200 GeV $< E_T$, $1.52 < |\eta| < 1.81$ and (i) $50 < E_T < 70$ GeV, (j) $70 < E_T < 100$ GeV, (k) $100 < E_T < 200$ GeV, (l) 200 GeV $< E_T$, $1.81 < |\eta| < 2.37$ and (m) $50 < E_T < 70$ GeV, (n) $70 < E_T < 100$ GeV, (o) $100 < E_T < 200$ GeV, (p) 200 GeV $< E_T$.
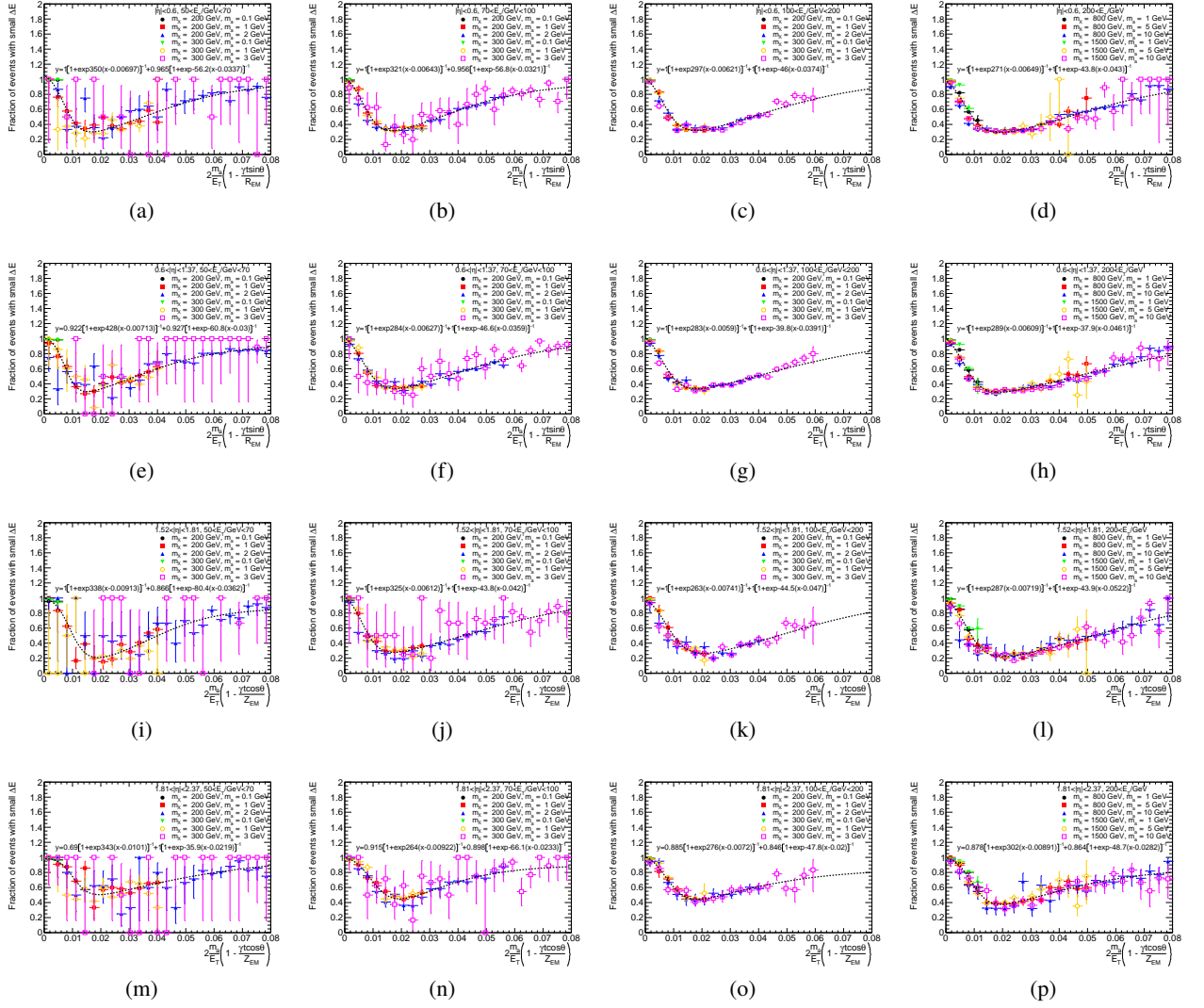
Figure 87: The result of the parametrization of $f_{\gamma_R}(E_{\mathrm{T}}, \eta, t)$. The value of f_{γ_R} is presented as a function of v. The result of the parametrization is presented for each of the 16 bins of the (E_{T}, η) parameter space of the particle a: $|\eta| < 0.6$ and (a) $50 < E_{\mathrm{T}} < 70$ GeV, (b) $70 < E_{\mathrm{T}} < 100$ GeV, (c) $100 < E_{\mathrm{T}} < 200$ GeV, (d) 200 GeV $< E_{\mathrm{T}}$, $0.6 < |\eta| < 1.37$ and (e) $50 < E_{\mathrm{T}} < 70$ GeV, (f) $70 < E_{\mathrm{T}} < 100$ GeV, (g) $100 < E_{\mathrm{T}} < 200$ GeV, (h) 200 GeV $< E_{\mathrm{T}}$, $1.52 < |\eta| < 1.81$ and (i) $50 < E_{\mathrm{T}} < 70$ GeV, (j) $70 < E_{\mathrm{T}} < 100$ GeV, (k) $100 < E_{\mathrm{T}} < 200$ GeV, (l) 200 GeV $< E_{\mathrm{T}}$, $1.81 < |\eta| < 2.37$ and (m) $50 < E_{\mathrm{T}} < 70$ GeV, (n) $70 < E_{\mathrm{T}} < 100$ GeV, (o) $100 < E_{\mathrm{T}} < 200$ GeV, (p) 200 GeV $< E_{\mathrm{T}}$.

B Distributions of shower shape variables

The definitions of the shower shape variables are given in Table 5 of Section 4.2. The distributions of the shower shape variables are shown in Figures 88 and 89. They are shown for simulated events of photons and hadronic jets, with no selections applied.
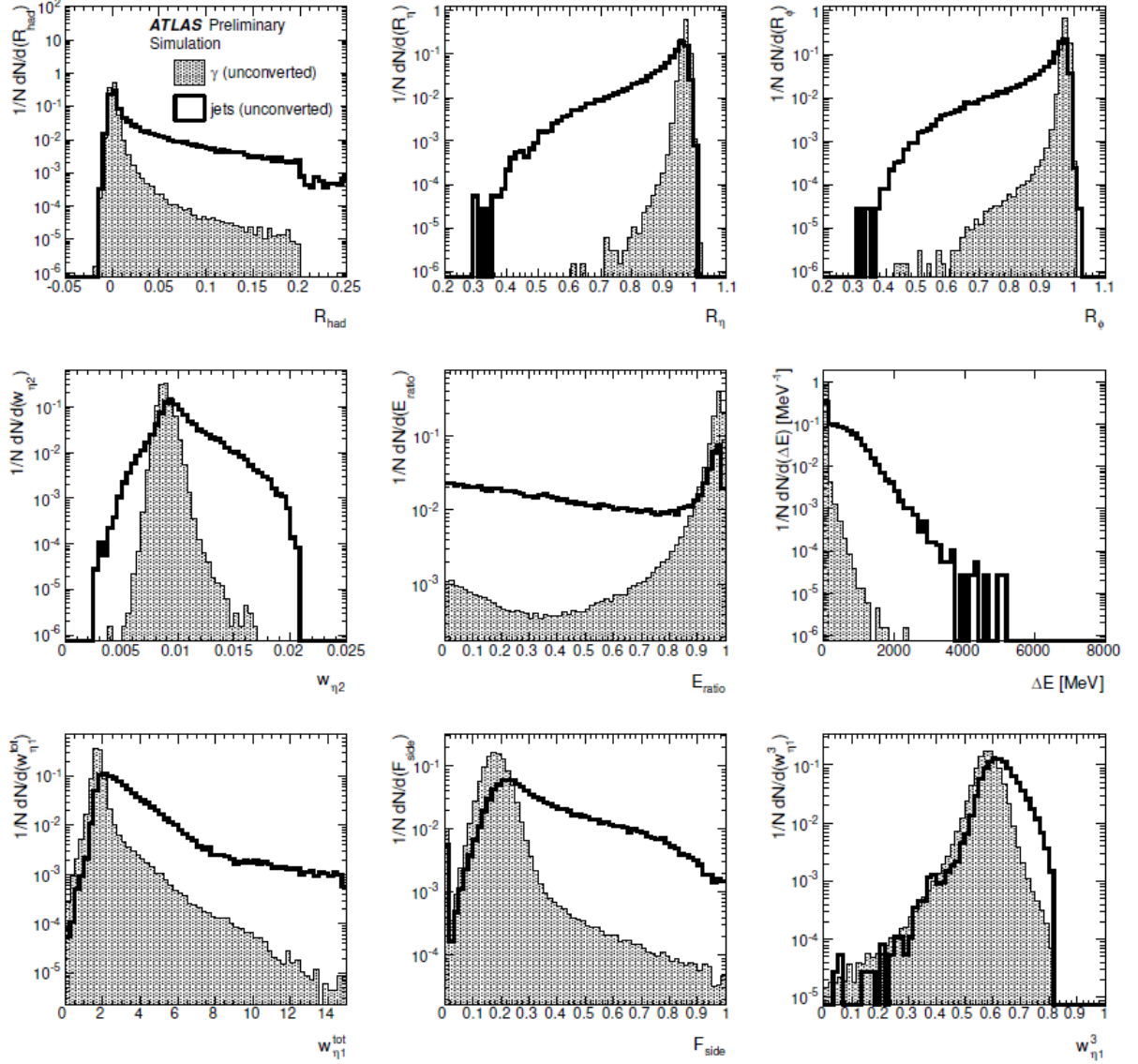

Figure 88: The distributions of the shower shape variables for unconverted photons in the region $|\eta| < 0.6$ and $E_T > 20$ GeV [90]. Those for reconstructed photons originating from prompt photons (shaded histogram) and backgrounds (i.e. hadronic jets, and photons originating from hadronic decays) (unshaded histogram) are shown. These distributions are calculated using simulated events at $\sqrt{s} = 7$ TeV. Here, w_{s3} is denoted by $w_{\eta1}^3$, w_{stot} is denoted by $w_{\eta1}^{tot}$, and f_{side} is denoted by F_{side}.
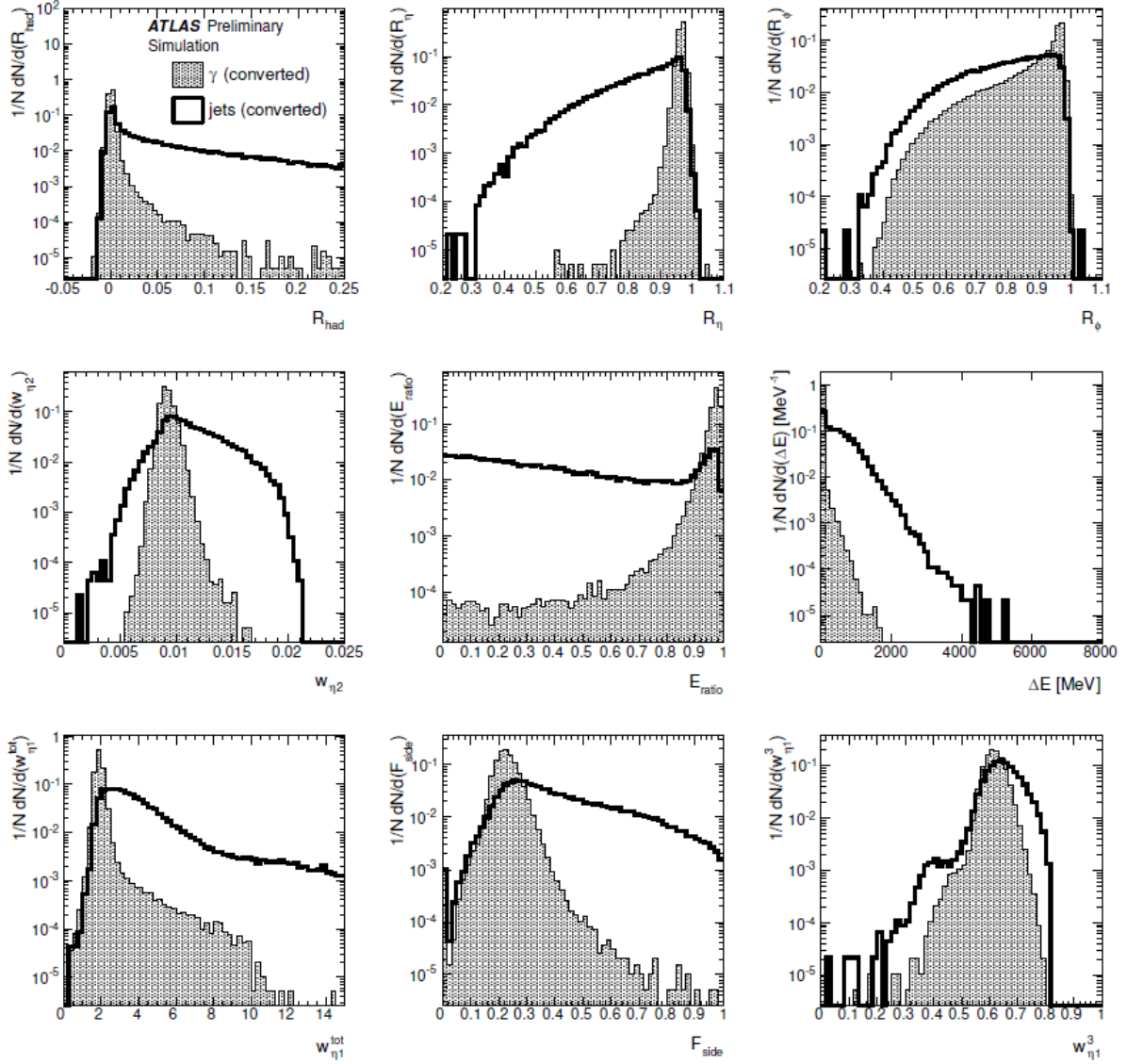
Figure 89: The distributions of the shower shape variables for converted photons in the region $|\eta| < 0.6$ and $E_T > 20$ GeV [90]. Those for reconstructed photons originating from prompt photons (shaded histogram) and backgrounds (i.e. hadronic jets, and photons originating from hadronic decays) (unshaded histogram) are shown. These distributions are calculated using simulated events at $\sqrt{s} = 7$ TeV. Here, w_{s3} is denoted by $w_{\eta1}^3$, w_{stot} is denoted by $w_{\eta1}^{tot}$, and f_{side} is denoted by F_{side}.
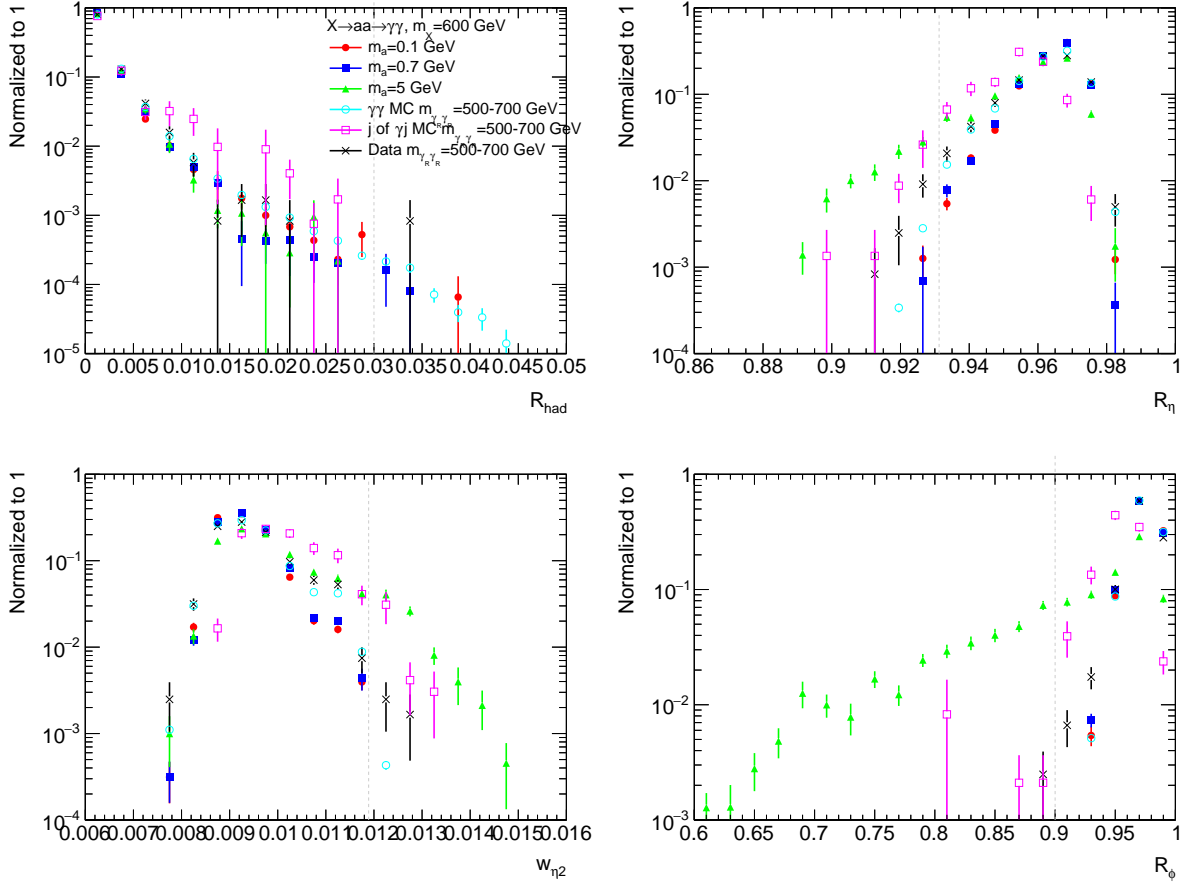
Figure 90: The distributions of the shower shape variables defined using the information of the EM calorimeter second layer. The histograms are plotted as the sum of leading and subleading reconstructed photons. The events which satisfy the preselection, isolation, and the E_T selection requirements are plotted. The filled markers represent the distributions obtained from simulated signal samples of $X \rightarrow aa \rightarrow 4\gamma$ for $m_X = 600$ GeV. The empty markers represent the distributions obtained from simulated samples of SM processes $\gamma\gamma$ and γj in the region 500 GeV $< m_{\gamma_R\gamma_R} <$ 700 GeV. For the square markers, reconstructed photons originating from hadronic jets are exclusively chosen. The "X" markers represent the distributions obtained from collision dataset in the region 500 GeV $< m_{\gamma_R\gamma_R} <$ 700 GeV. The vertical dotted line represents the threshold used for the Tight photon ID selection for unconverted photons in the region $|\eta| < 0.6$. The first bins include the underflows, and the last bins include the overflows.

Figures 90 and 91 show the distributions of the shower shape variables for the process $X \rightarrow aa \rightarrow 4\gamma$ as well as photons and hadronic jets. They are shown for events in a region similar to the signal region (defined in Section 5.3.1), with the Loose photon ID selection applied instead of the Loose$'$5 photon ID selection.
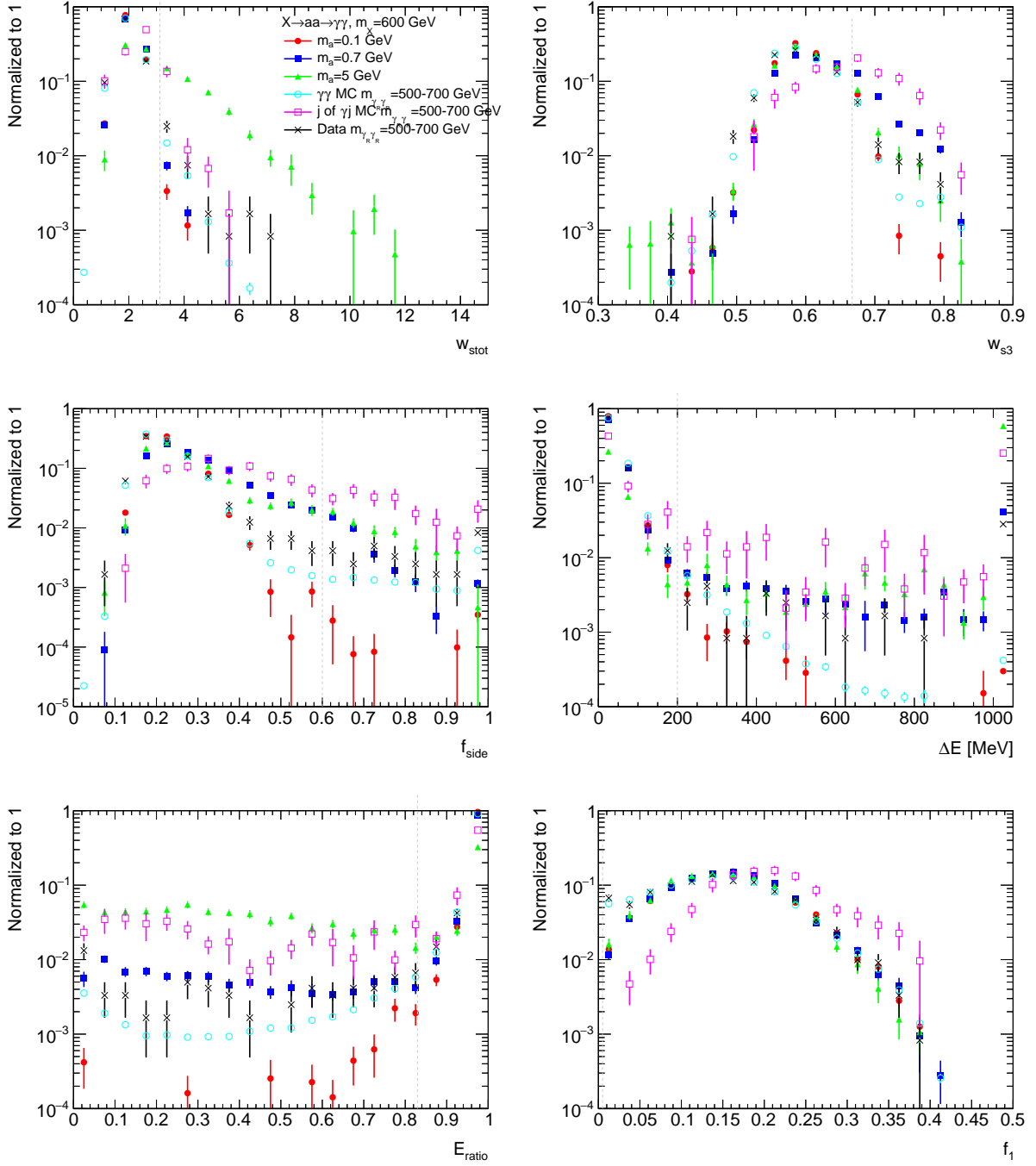
Figure 91: The distributions of the shower shape variables defined using the information of the EM calorimeter first layer. The histograms are plotted as the sum of leading and subleading reconstructed photons. The events which satisfy the preselection, isolation, and the E_{T} selection requirements are plotted. The filled markers represent the distributions obtained from simulated signal samples of $X \rightarrow aa \rightarrow 4\gamma$ for $m_X = 600$ GeV. The empty markers represent the distributions obtained from simulated samples of SM processes $\gamma\gamma$ and γj in the region 500 GeV $< m_{\gamma_R\gamma_R} <$ 700 GeV. For the square markers, reconstructed photons originating from hadronic jets are exclusively chosen. The "X" markers represent the distributions obtained from collision dataset in the region 500 GeV $< m_{\gamma_R\gamma_R} <$ 700 GeV. The vertical dotted line represents the threshold used for the Tight photon ID selection for unconverted photons in the region $|\eta| < 0.6$. The first bins include the underflows, and the last bins include the overflows.

C Sensitivity estimation using simulated events for optimization of the event selection

As described in Section 5.3.1, the Loose$'$5 photon ID selection is used for the definition of the signal region. Also, an event categorization based on the values of the shower shape variable ΔE is introduced, as described in Section 5.3.2. These choices are made based on estimations of the "sensitivity" of the analysis strategy to $X \rightarrow aa \rightarrow 4\gamma$ signal events. The estimations are performed using simulated event samples.

Here, the "sensitivity" is quantified by evaluating the expected value of the signal production cross section times branching ratios, $\sigma_X \times \mathcal{B}(X \rightarrow aa) \times \mathcal{B}(a \rightarrow \gamma\gamma)^2$, that correspond to an expected discovery significance of 3σ. The expected significance, in units of Gaussian σ, is estimated with an asymptotic approximation [75]:

$$Z = \sqrt{2\left[(s+b)\log\left(1 + \frac{s}{b}\right) - s\right]} \tag{97}$$

Here, s is the yield of signal events, and b is the yield of background events. Note that for $s \ll b$, this expression leads to $Z \simeq s/\sqrt{b}$, which is a commonly used expression for the estimation of the discovery significance. Using this expression, the value of $\sigma_X \times \mathcal{B}(X \rightarrow aa) \times \mathcal{B}(a \rightarrow \gamma\gamma)^2$ which corresponds to $Z = 3$ is evaluated.

The sensitivity estimation follows the following procedure, which is schematically illustrated in Figure 92:

1. The integrated luminosity assumed for this evaluation is 35 fb^{-1}[27].

2. The value of s is estimated using simulated signal samples. For a given $\sigma_X \times \mathcal{B}(X \rightarrow aa) \times \mathcal{B}(a \rightarrow \gamma\gamma)^2$, the $m_{\gamma_R\gamma_R}$ distribution of signal events that satisfy event selection requirements is calculated using simulated signal samples. The value of s is defined as the number of events within the region $m_{\text{average}} - 2m_{\text{std. dev.}} < m_{\gamma_R\gamma_R} < m_{\text{average}} + 2m_{\text{std. dev.}}$, where m_{average} and $m_{\text{std. dev.}}$ are the average and standard deviation of the signal $m_{\gamma_R\gamma_R}$ distribution.

3. The value of b is estimated using simulated samples of SM $\gamma\gamma$ events. The $m_{\gamma_R\gamma_R}$ distribution of background events that satisfy event selection requirements is calculated using the simulated samples. The normalization of the $m_{\gamma_R\gamma_R}$ distribution is defined so that the event yield in the region $m_{\gamma_R\gamma_R} > 175$ GeV is equal to that observed in the collision dataset[28]. The value of b is defined as the number of events within the region $m_{\text{average}} - 2m_{\text{std. dev.}} < m_{\gamma_R\gamma_R} < m_{\text{average}} + 2m_{\text{std. dev.}}$.

Comparison of estimated sensitivity for different photon ID selections

The comparison of estimated sensitivities for signal regions defined using different photon ID selections is shown in Figure 93. As seen in the figure, a photon ID selection which is less stringent results in better sensitivity (i.e. lower $\sigma_X \times \mathcal{B}(X \rightarrow aa) \times \mathcal{B}(a \rightarrow \gamma\gamma)^2$ that corresponds to $Z = 3$); using Loose photon selection or Loose$'$5 selection results in better sensitivity compared to using Tight selection or

---

[27]As the integrated luminosity, 35 fb^{-1} is used in this evaluation instead of 36.7 fb^{-1}, which corresponds to the collision dataset used in this thesis. This is simply because this evaluation was performed before the data taking in 2016 was completed. Nevertheless, the impact of this difference in the result of this evaluation is negligible.

[28]With this method, the event yield of the sum of all background components, i.e. $\gamma\gamma$, γj, and jj, is estimated. This method relies on the fact that the overall shape of the $m_{\gamma_R\gamma_R}$ distribution is approximately the same for each background component, $\gamma\gamma$, γj, and jj, as seen in Figure 53.
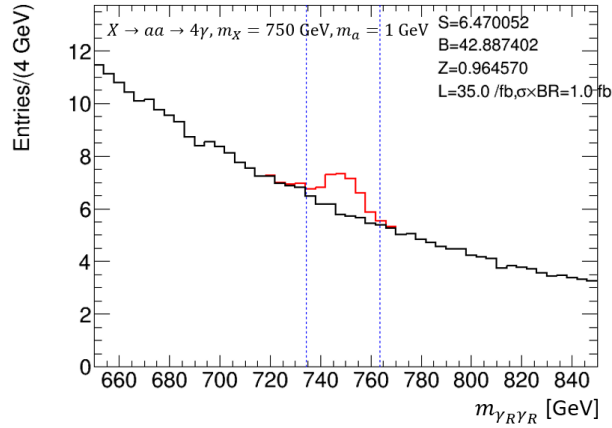
Figure 92: A schematic representation of the procedure for the sensitivity estimation. This figure shows an example for $X \to aa \to 4\gamma$, $m_X = 750$ GeV, $m_a = 1$ GeV, and $\sigma_X \times \mathcal{B}(X \to aa) \times \mathcal{B}(a \to \gamma\gamma)^2 = 1$ fb. The histograms are stacked, with the red histogram representing the signal component and the black histogram representing the background component. The blue vertical dotted lines show the region $m_{\text{average}} - 2m_{\text{std. dev.}} < m_{\gamma_R\gamma_R} < m_{\text{average}} + 2m_{\text{std. dev.}}$. For details, see text.

Loose$'$4 selection. Thus, the Loose$'$5 selection is used for the definition of the signal region, as described in Section 5.3.1[29].

Comparison of estimated sensitivity for different categorization definitions

The comparison of estimated sensitivities for event categorization defined using different shower shape variables is shown in Figure 94. Here, the categorization is defined similarly to that described in Section 5.3.2. The discovery significance resulting from the combination of two event categories is estimated by $Z = \sqrt{Z_1^2 + Z_2^2}$, where Z_1 and Z_2 are the discovery significances estimated for the first and the second event category, respectively. As seen in the figure, the event categorization using ΔE results in the largest sensitivity (i.e. lowest $\sigma_X \times \mathcal{B}(X \to aa) \times \mathcal{B}(a \to \gamma\gamma)^2$ corresponding to $Z = 3$). Thus, the shower shape variable ΔE is used for the definition of the event categorization, as described in Section 5.3.2.

Figure 95 shows the "gain" in sensitivity by introducing the event categorization using ΔE. Here, the "gain" is quantified by evaluating the ratio of the values of $\sigma_X \times \mathcal{B}(X \to aa) \times \mathcal{B}(a \to \gamma\gamma)^2$ corresponding to $Z = 3$ before and after introducing the event categorization (i.e. the ratio of the results in Figure 93(c) and Figure 94(a)). The introduction of event categorization based on ΔE results in a sensitivity gain of approximately as much as a factor 2.

---

[29]As seen in Figure 93, using the Loose$'$5 selection for the signal region definition results in a slightly worse sensitivity compared to that defined using the Loose selection, for large values of m_a/m_X (e.g. worse by approximately a factor 2 for $m_a/m_X = 0.01$). However, as described in Section 5.3.1, an important point is that a control region (i.e. a region similar and orthogonal to the signal region) can be defined with the use of the Loose$'$5 selection. This is because the Loose$'$5 selection is a tighter selection compared to the Loose photon ID selection. As described in Section 5.1.1, the collision dataset is collected with the diphoton trigger, which requires two EM clusters to satisfy the trigger-level Loose photon ID selection. Reconstructed photons in the dataset that do not satisfy the Loose$'$5 selection is used for the estimation of the rate of hadronic jets satisfying the calorimeter isolation requirement, as described in Section 5.5.1
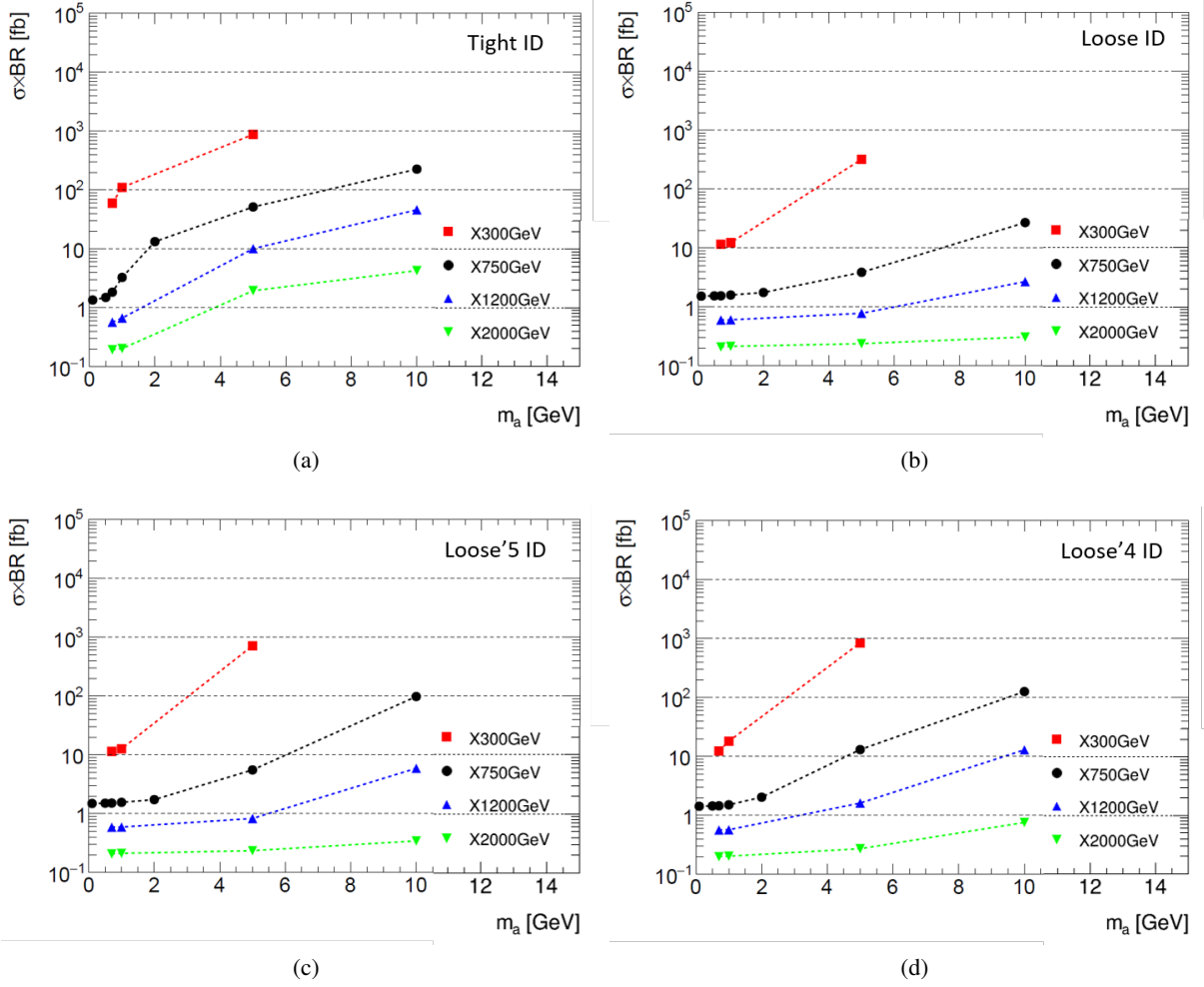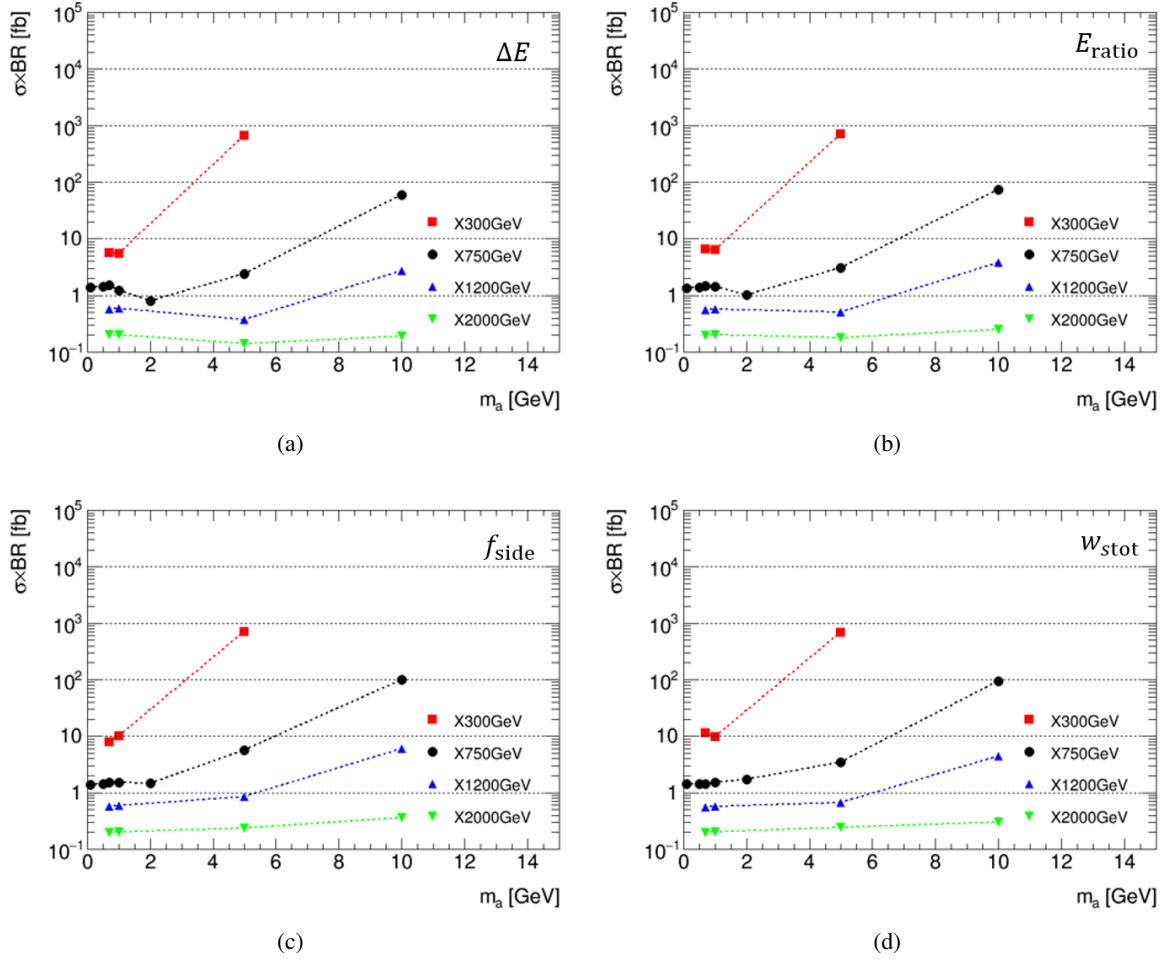
Figure 93: The estimation of the values of $\sigma_X \times \mathcal{B}(X \rightarrow aa) \times \mathcal{B}(a \rightarrow \gamma\gamma)^2$ corresponding to $Z = 3$. The signal region is defined similarly to that described in Section 5.3.1, with different photon ID selections used; (a) Tight selection, (b) Loose selection, (c) Loose′5 selection, and (d) Loose′4 selection.

122

Figure 94: The estimation of the values of $\sigma_X \times \mathcal{B}(X \to aa) \times \mathcal{B}(a \to \gamma\gamma)^2$ corresponding to $Z = 3$. The event categorization is defined similarly to that described in Section 5.3.2, with different shower shape variables used for the definition of the categories; (a) ΔE, (b) E_{ratio}, (c) f_{side}, and $w_{s\text{tot}}$. The result using w_{s3} is similar to that using $w_{s\text{tot}}$, and so is not shown here.
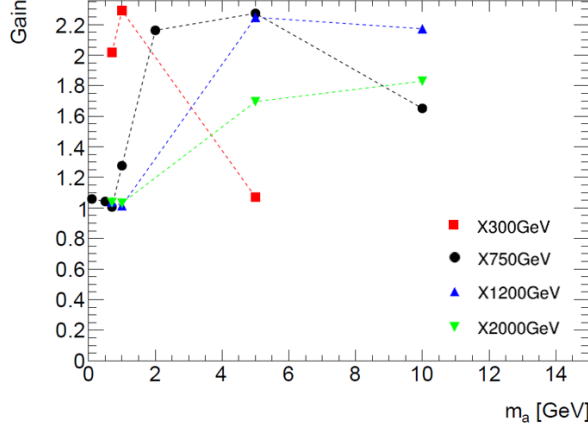
Figure 95: The gain in sensitivity by introducing the event categorization using the ΔE variable. The gain is quantified by evaluating the ratio of the values of $\sigma_X \times \mathcal{B}(X \to aa) \times \mathcal{B}(a \to \gamma\gamma)^2$ corresponding to $Z = 3$ before and after introducing the event categorization (i.e. the ratio of the results in Figure 93(c) and Figure 94(a)).

D Additional details to the hypothesis testing method

The definition of the likelihood is described in Section 5.7.1, and the hypothesis testing method is described in Section 5.7.2. The definitions of the test statistics, the details of the asymptotic approximations, and the definition of the CL_s method are described below.

Define the profile likelihood ratio as

$$\lambda(\mu) = \frac{L(\mu, \hat{\hat{\theta}})}{L(\hat{\mu}, \hat{\theta})} \tag{98}$$

Here, $L(\mu, \theta)$ is the overall likelihood defined in Eq. (73) for a given signal hypothesis with mass values of (m_X, m_a). The parameter of interest $\mu = \sigma \times BR$ is the product of the signal production cross section and the branching ratios. θ collectively designates all free parameters excluding μ (i.e. $N_{B,1}, N_{B,2}, \boldsymbol{k}_1, \boldsymbol{k}_2$, and $\boldsymbol{\theta}$ in Eq. (73)). $\hat{\hat{\theta}}$ denotes the conditional maximum-likelihood estimators, i.e. values of θ that maximizes L for a given μ. Thus, $\hat{\hat{\theta}}$ is a function of μ. $\hat{\mu}$ and $\hat{\theta}$ are the unconditional maximum-likelihood estimators.

The calculation of p-values for the background-only hypothesis (p_0)

The test statistic q_0 is defined as [75]

$$q_0 = \begin{cases} -2\log \lambda(0) = -2\log \dfrac{L(0, \hat{\hat{\theta}})}{L(\hat{\mu}, \hat{\theta})} & \hat{\mu} \geq 0 \\ 0 & \hat{\mu} < 0 \end{cases} \tag{99}$$

Let μ' be the expected value of μ. The value of p_0 is calculated as

$$p_0 = \int_{q_{0,\text{obs}}}^{\infty} f(q_0 | \mu' = 0) \, dq_0 \tag{100}$$

124

$q_{0,\text{obs}}$ is the observed value of q_0. $f(q_0|\mu')$ is the probability density function of q_0 under the assumption of μ'. The discovery significance is defined as

$$Z = \Phi^{-1}(1 - p_0) \tag{101}$$

Here, Φ is the cumulative distribution of a standard Gaussian distribution.

Under the asymptotic approximation $\hat{\mu} \sim N(\mu', \sigma)$, the p_0 value is approximated by [75]

$$p_0 = 1 - \Phi(\sqrt{q_{0,\text{obs}}}) \tag{102}$$

Thus, the discovery significance is approximated by

$$Z = \sqrt{q_{0,\text{obs}}} \tag{103}$$

The calculation of CL$_s$ limits

The test statistic $\tilde{q}_\mu$ is defined as [75]

$$\tilde{q}_\mu = \begin{cases} -2\log\dfrac{L(\mu, \hat{\hat{\theta}})}{L(0, \hat{\hat{\theta}})} & \hat{\mu} \leq 0 \\[3mm] -2\log\dfrac{L(\mu, \hat{\hat{\theta}})}{L(\hat{\mu}, \hat{\theta})} & 0 \leq \hat{\mu} < \mu \\[3mm] 0 & \mu < \hat{\mu} \end{cases} \tag{104}$$

CL_s, the modified frequentist method, is defined as [76]

$$CL_s(\mu) = \frac{\int_{\tilde{q}_{\mu,\text{obs}}}^{\infty} f(\tilde{q}_\mu|\mu' = \mu)\, d\tilde{q}_\mu}{\int_{\tilde{q}_{\mu,\text{obs}}}^{\infty} f(\tilde{q}_\mu|\mu' = 0)\, d\tilde{q}_\mu} \tag{105}$$

The 95% CL upper limit on μ is evaluated by taking the value of μ when $CL_s = 0.05$.

Under the asymptotic approximation $\hat{\mu} \sim N(\mu', \sigma)$, the cumulative distribution function of $\tilde{q}_\mu$ is approximated as [75]

$$\int_{-\infty}^{\tilde{q}_{\mu,\text{obs}}} f(\tilde{q}_\mu|\mu')\, d\tilde{q}_\mu = \begin{cases} \Phi\left(\sqrt{\tilde{q}_{\mu,\text{obs}}} - \dfrac{\mu - \mu'}{\sigma}\right) & 0 < \tilde{q}_{\mu,\text{obs}} \leq \dfrac{\mu^2}{\sigma^2} \\[4mm] \Phi\left(\dfrac{\tilde{q}_{\mu,\text{obs}} - \frac{\mu^2 - 2\mu\mu'}{\sigma^2}}{\frac{2\mu}{\sigma}}\right) & \dfrac{\mu^2}{\sigma^2} < \tilde{q}_{\mu,\text{obs}} \end{cases} \tag{106}$$

The value of $\frac{\mu}{\sigma}$ is approximated by the Asimov method [75], and it is approximated as

$$\frac{\mu}{\sigma} \simeq \sqrt{\tilde{q}_{\mu,A}} \tag{107}$$

The value of $\tilde{q}_{\mu,A}$ is evaluated by calculating the value of $\tilde{q}_\mu$ for an "Asimov dataset". The Asimov dataset is a dataset that when one uses it to obtain the maximum-likelihood estimators $\hat{\mu}$ and $\hat{\theta}$, one obtains the true parameter values. In this research, the Asimov dataset is defined as a weighted dataset that is obtained from a background-only fit to the $m_{\gamma_R \gamma_R}$ distributions of the collision data, i.e. the blue lines shown in Figure 61.

The expected (i.e. median) upper limit is evaluated by substituting $\tilde{q}_{\mu,\text{obs}}$ with $\tilde{q}_{\mu,A}$, thus resulting in

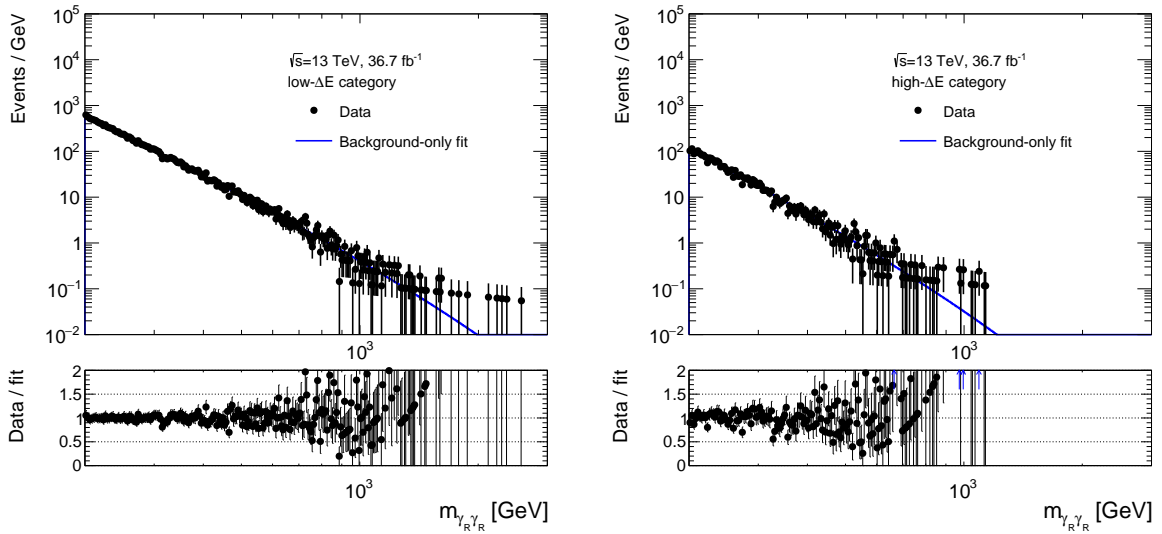$$CL_s^{\text{expected}}(\mu) = 2\left(1 - \Phi(\sqrt{\tilde{q}_{\mu,A}})\right) \tag{108}$$

Figure 96: The observed $m_{\gamma_R\gamma_R}$ distributions in the two event categories of the signal region. The result of a background-only fit assuming $\mu = 0$ is superimposed. In the lower panels, the ratios of the observed event yield and the expectation from the fit result are presented. The blue arrows represent the bins with this ratio larger than two, i.e. out of the range of the plot.

E Distributions of $m_{\gamma_R\gamma_R}$ in the signal region, with the bin widths set to the detector resolution

Figure 96 shows the $m_{\gamma_R\gamma_R}$ distributions in the signal region obtained from collision data (i.e. the same result as those shown in Figure 61). In this figure, the bin widths are set to be equal to the energy resolution of the detector. Here, the detector resolution is estimated as $0.991 \times (1 + 0.680 \times \frac{m_X}{100\ \text{GeV}})$ GeV, i.e. the parametrized result of σ_{CB} shown in Table 9 in the limit $m_a \rightarrow 0$.

References

[1] K. G. Wilson, *Renormalization Group and Strong Interactions*, Phys. Rev. D **3** (8 1971) 1818,
URL: https://link.aps.org/doi/10.1103/PhysRevD.3.1818.

[2] G. 't Hooft, *Naturalness, chiral symmetry, and spontaneous chiral symmetry breaking*,
NATO Sci. Ser. B **59** (1980) 135.

[3] R. D. Peccei and H. R. Quinn, CP *Conservation in the Presence of Pseudoparticles*,
Phys. Rev. Lett. **38** (25 1977) 1440,
URL: https://link.aps.org/doi/10.1103/PhysRevLett.38.1440.

[4] R. D. Peccei and H. R. Quinn,
Constraints imposed by CP *conservation in the presence of pseudoparticles*,
Phys. Rev. D **16** (6 1977) 1791,
URL: https://link.aps.org/doi/10.1103/PhysRevD.16.1791.

[5] S. D. Ellis, T. S. Roy and J. Scholtz, *Phenomenology of photon-jets*,
Phys. Rev. D **87** (2013) 014015, arXiv: 1210.3657 [hep-ph].

[6] S. D. Ellis, T. S. Roy and J. Scholtz, *Jets and Photons*, Phys. Rev. Lett. **110** (2013) 122003,
arXiv: 1210.1855 [hep-ph].

[7] B. C. Allanach, D. Bhatia and A. M. Iyer,
Dissecting Multi-Photon Resonances at the Large Hadron Collider, Eur. Phys. J. **C77** (2017) 595,
arXiv: 1706.09039 [hep-ph].

[8] ATLAS Collaboration, *Observation of a new particle in the search for the Standard Model Higgs boson with the ATLAS detector at the LHC*, Phys. Lett. B **716** (2012) 1,
arXiv: 1207.7214 [hep-ex].

[9] CMS Collaboration,
Observation of a new boson at a mass of 125 GeV with the CMS experiment at the LHC,
Phys. Lett. B **716** (2012) 30, arXiv: 1207.7235 [hep-ex].

[10] F. Domingo, S. Heinemeyer, J. S. Kim and K. Rolbiecki,
The NMSSM lives: with the 750 GeV diphoton excess, Eur. Phys. J. C **76** (2016) 249,
arXiv: 1602.07691 [hep-ph].

[11] U. Ellwanger and C. Hugonie,
A 750 GeV Diphoton Signal from a Very Light Pseudoscalar in the NMSSM, JHEP **05** (2016) 114,
arXiv: 1602.03344 [hep-ph].

[12] C.-W. Chiang, H. Fukuda, M. Ibe and T. T. Yanagida,
750 GeV diphoton resonance in a visible heavy QCD axion model,
Phys. Rev. D **93** (2016) 095016, arXiv: 1602.07909 [hep-ph].

[13] L. Aparicio, A. Azatov, E. Hardy and A. Romanino, *Diphotons from diaxions*,
JHEP **05** (2016) 077, arXiv: 1602.00949 [hep-ph].

[14] N. Toro and I. Yavin, *Multiphotons and photon jets from new heavy vector bosons*,
Phys. Rev. D **86** (2012) 055005, arXiv: 1202.6377 [hep-ph].

[15] M. Chala, M. Duerr, F. Kahlhoefer and K. Schmidt-Hoberg,
Tricking Landau–Yang: How to obtain the diphoton excess from a vector resonance,
Phys. Lett. **B755** (2016) 145, arXiv: 1512.06833 [hep-ph].

[16] B. M. Dillon, C. Han, H. M. Lee and M. Park,
KK graviton resonance and cascade decays in warped gravity,
Int. J. Mod. Phys. **A32** (2017) 1745006, arXiv: 1606.07171 [hep-ph].

[17] S. P. Martin, 'A Supersymmetry Primer', *Perspectives on Supersymmetry II*, 2010 1,
arXiv: hep-ph/9709356 [hep-ph],
URL: https://www.worldscientific.com/doi/abs/10.1142/9789814307505_0001.

[18] U. Ellwanger, C. Hugonie and A. M. Teixeira,
The Next-to-Minimal Supersymmetric Standard Model, Phys. Rept. **496** (2010) 1,
arXiv: 0910.1785 [hep-ph].

[19] P. Langacker, *The Physics of Heavy Z′ Gauge Bosons*, Rev. Mod. Phys. **81** (2009) 1199,
arXiv: 0801.1345 [hep-ph].

[20] L. Randall and R. Sundrum, *A Large mass hierarchy from a small extra dimension*,
Phys. Rev. Lett. **83** (1999) 3370, arXiv: hep-ph/9905221 [hep-ph].

[21] J. Chang, K. Cheung and C.-T. Lu,
Interpreting the 750 GeV diphoton resonance using photon jets in hidden-valley-like models,
Phys. Rev. D **93** (2016) 075013, arXiv: 1512.06671 [hep-ph].

[22] M. Bauer, M. Neubert and A. Thamm, *Collider Probes of Axion-Like Particles*,
JHEP **12** (2017) 044, arXiv: 1708.00443 [hep-ph].

[23] ATLAS Collaboration, *Search for new phenomena in events with at least three photons collected in pp collisions at $\sqrt{s}$ = 8 TeV with the ATLAS detector*, Eur. Phys. J. C **76** (2016) 210,
arXiv: 1509.05051 [hep-ex].

[24] ATLAS Collaboration, *Search for a Higgs boson decaying to four photons through light CP-odd scalar coupling using 4.9 fb^{-1} of 7 TeV pp collision data taken with ATLAS detector at the LHC*,
ATLAS-CONF-2012-079, URL: http://cds.cern.ch/record/1460391.

[25] ATLAS Collaboration,
Search for resonances in diphoton events at $\sqrt{s}$=13 TeV with the ATLAS detector,
JHEP **09** (2016) 001, arXiv: 1606.03833 [hep-ex].

[26] N. Aghanim et al., *Planck 2018 results. VI. Cosmological parameters*, (2018),
arXiv: 1807.06209 [astro-ph.CO].

[27] N. Arkani-Hamed, A. Delgado and G. F. Giudice, *The Well-tempered neutralino*,
Nucl. Phys. **B741** (2006) 108, arXiv: hep-ph/0601041 [hep-ph].

[28] G. Aad et al., *Summary of the ATLAS experiment's sensitivity to supersymmetry after LHC Run 1 — interpreted in the phenomenological MSSM*, JHEP **10** (2015) 134,
arXiv: 1508.06608 [hep-ex].

[29] A. Djouadi et al., *The post-Higgs MSSM scenario: Habemus MSSM?*,
Eur. Phys. J. **C73** (2013) 2650, arXiv: 1307.5205 [hep-ph].

[30] ATLAS Collaboration, *Summary plots from the ATLAS Higgs physics group*, URL:
https://atlas.web.cern.ch/Atlas/GROUPS/PHYSICS/CombinedSummaryPlots/HIGGS/.

[31] ATLAS Collaboration, *Summary plots from the ATLAS Supersymmetry physics group*, URL:
https://atlas.web.cern.ch/Atlas/GROUPS/PHYSICS/CombinedSummaryPlots/SUSY/.

[32] B. A. Dobrescu and K. T. Matchev,
Light axion within the next-to-minimal supersymmetric standard model, JHEP **09** (2000) 031,
arXiv: hep-ph/0008192 [hep-ph].

[33] L. O'Raifeartaigh, *Spontaneous Symmetry Breaking for Chiral Scalar Superfields*,
Nucl. Phys. **B96** (1975) 331.

[34] A. Arhrib, K. Cheung, T.-J. Hou and K.-W. Song,
Associated production of a light pseudoscalar Higgs boson with a chargino pair in the NMSSM,
JHEP **03** (2007) 073, arXiv: hep-ph/0606114 [hep-ph].

[35] M. Guchait and J. Kumar, *Diphoton Signal of light pseudoscalar in NMSSM at the LHC*,
Phys. Rev. **D95** (2017) 035036, arXiv: 1608.05693 [hep-ph].

[36] G. Belanger, B. Dumont, U. Ellwanger, J. F. Gunion and S. Kraml,
Status of invisible Higgs decays, Phys. Lett. **B723** (2013) 340, arXiv: 1302.5694 [hep-ph].

[37] F. Domingo and G. Weiglein, *NMSSM interpretations of the observed Higgs signal*,
JHEP **04** (2016) 095, arXiv: 1509.07283 [hep-ph].

[38] F. Domingo, *Decays of a NMSSM CP-odd Higgs in the low-mass region*, JHEP **03** (2017) 052,
arXiv: 1612.06538 [hep-ph].

[39] L. Evans and P. Bryant, *LHC Machine*, JINST **3** (2008) S08001.

[40] ATLAS Collaboration, *The ATLAS Experiment at the CERN Large Hadron Collider*,
JINST **3** (2008) S08003.

[41] CMS Collaboration, *The CMS Experiment at the CERN LHC*, JINST **3** (2008) S08004.

[42] CERN, *The CERN accelerator complex - August 2018*, 2018,
URL: https://cds.cern.ch/record/2636343.

[43] ATLAS Collaboration, *ATLAS Insertable B-Layer Technical Design Report*, ATLAS-TDR-19,
2010, URL: https://cds.cern.ch/record/1291633,
ATLAS Insertable B-Layer Technical Design Report Addendum, ATLAS-TDR-19-ADD-1, 2012,
URL: https://cds.cern.ch/record/1451888.

[44] M. Aaboud et al., *Measurement of the photon identification efficiencies with the ATLAS detector
using LHC Run 2 data collected in 2015 and 2016*, Submitted to: Eur. Phys. J. (2018),
arXiv: 1810.05087 [hep-ex].

[45] ATLAS Collaboration, *Event display photon / pi0*,
URL: https://atlas.web.cern.ch/Atlas/GROUPS/PHYSICS/EGAMMA/PublicPlots/
20100721/display-photons/index.html.

[46] G. Avoni et al., *The new LUCID-2 detector for luminosity measurement and monitoring in ATLAS*,
Journal of Instrumentation **13** (2018) P07017,
URL: http://stacks.iop.org/1748-0221/13/i=07/a=P07017.

[47] ATLAS Collaboration,
Luminosity determination in pp collisions at $\sqrt{s}$ = 8 TeV using the ATLAS detector at the LHC,
Eur. Phys. J. C **76** (2016) 653, arXiv: 1608.03953 [hep-ex].

[48] ATLAS Collaboration, *Performance of the ATLAS trigger system in 2015*,
Eur. Phys. J. C **77** (2017) 317, arXiv: 1611.09661 [hep-ex].

[49] ATLAS Collaboration, *LuminosityPublicResultsRun2*, URL: https:
//twiki.cern.ch/twiki/bin/view/AtlasPublic/LuminosityPublicResultsRun2.

[50] M. Aaboud et al., *Electron reconstruction and identification in the ATLAS experiment using the 2015 and 2016 LHC proton-proton collision data at $\sqrt{s}$ = 13 TeV*, Submitted to: Eur. Phys. J. (2019), arXiv: 1902.04655 [physics.ins-det].

[51] W. Lampl et al., *Calorimeter clustering algorithms: Description and performance*, (2008).

[52] *The Optimization of ATLAS Track Reconstruction in Dense Environments*, tech. rep. ATL-PHYS-PUB-2015-006, CERN, 2015, URL: https://cds.cern.ch/record/2002609.

[53] M. Aaboud et al., *Performance of the ATLAS Track Reconstruction Algorithms in Dense Environments in LHC Run 2*, Eur. Phys. J. **C77** (2017) 673, arXiv: 1704.07983 [hep-ex].

[54] R. Frühwirth, *Application of Kalman filtering to track and vertex fitting*, Nuclear Instruments and Methods in Physics Research Section A: Accelerators, Spectrometers, Detectors and Associated Equipment **262** (1987) 444, ISSN: 0168-9002, URL: http://www.sciencedirect.com/science/article/pii/0168900287908874.

[55] T. G. Cornelissen et al., *The global χ2track fitter in ATLAS*, Journal of Physics: Conference Series **119** (2008) 032013, URL: https://doi.org/10.1088%2F1742-6596%2F119%2F3%2F032013.

[56] *Improved electron reconstruction in ATLAS using the Gaussian Sum Filter-based model for bremsstrahlung*, tech. rep. ATLAS-CONF-2012-047, CERN, 2012, URL: https://cds.cern.ch/record/1449796.

[57] M. Aaboud et al., *Electron and photon energy calibration with the ATLAS detector using 2015-2016 LHC proton-proton collision data*, Submitted to: JINST (2018), arXiv: 1812.03848 [hep-ex].

[58] J. Saxon, 'Discovery of the Higgs Boson, Measurements of its Production, and a Search for Higgs Boson Pair Production', PhD thesis, 2014, URL: https://cds.cern.ch/record/1746004.

[59] ATLAS Collaboration, *Electron and photon energy calibration with the ATLAS detector using LHC Run 1 data*, Eur. Phys. J. C **74** (2014) 3071, arXiv: 1407.5063 [hep-ex].

[60] J. Alwall et al., *The automated computation of tree-level and next-to-leading order differential cross sections, and their matching to parton shower simulations*, JHEP **07** (2014) 079, arXiv: 1405.0301 [hep-ph].

[61] R. D. Ball et al., *Parton distributions for the LHC Run II*, JHEP **04** (2015) 040, arXiv: 1410.8849 [hep-ph].

[62] T. Sjöstrand, S. Mrenna and P. Z. Skands, *A brief introduction to PYTHIA 8.1*, Comput. Phys. Commun. **178** (2008) 852, arXiv: 0710.3820 [hep-ph].

[63] ATLAS Collaboration, *ATLAS Pythia 8 tunes to 7 TeV data*, ATL-PHYS-PUB-2014-021, 2014, URL: https://cds.cern.ch/record/1966419.

[64] T. Gleisberg et al., *Event generation with SHERPA 1.1*, JHEP **02** (2009) 007, arXiv: 0811.4622 [hep-ph].

[65] S. Schumann and F. Krauss, *A Parton shower algorithm based on Catani-Seymour dipole factorisation*, JHEP **03** (2008) 038, arXiv: 0709.1027 [hep-ph].

[66] S. Hoeche, F. Krauss, S. Schumann and F. Siegert, *QCD matrix elements and truncated showers*, JHEP **05** (2009) 053, arXiv: `0903.1219 [hep-ph]`.

[67] H.-L. Lai et al., *New parton distributions for collider physics*, Phys. Rev. D **82** (2010) 074024, arXiv: `1007.2241 [hep-ph]`.

[68] ATLAS Collaboration, *Summary of ATLAS Pythia 8 tunes*, ATL-PHYS-PUB-2012-003, 2012, URL: `https://cds.cern.ch/record/1474107`.

[69] A. Martin, W. Stirling, R. Thorne and G. Watt, *Parton distributions for the LHC*, Eur. Phys. J. C **63** (2009) 189, arXiv: `0901.0002 [hep-ph]`.

[70] ATLAS Collaboration, *The ATLAS Simulation Infrastructure*, Eur. Phys. J. C **70** (2010) 823, arXiv: `1005.4568 [physics.ins-det]`.

[71] S. Agostinelli et al., *Geant4: A Simulation toolkit*, Nucl. Instrum. Meth. A **506** (2003) 250.

[72] ATLAS Collaboration, *Search for pairs of highly collimated photon-jets in pp collisions at $\sqrt{s} = 13$ TeV with the ATLAS detector*, Phys. Rev. D **99** (2019) 012008, arXiv: `1808.10515 [hep-ex]`.

[73] CDF Collaboration, *Search for new particles decaying into dijets in proton-antiproton collisions at $\sqrt{s} = 1.96$ TeV*, Phys. Rev. D **79** (2009) 112002, arXiv: `0812.4036 [hep-ex]`.

[74] ATLAS Collaboration, *Measurement of the isolated di-photon cross-section in pp collisions at $\sqrt{s} = 7$ TeV with the ATLAS detector*, Phys. Rev. D **85** (2012) 012003, arXiv: `1107.0581 [hep-ex]`.

[75] G. Cowan, K. Cranmer, E. Gross and O. Vitells, *Asymptotic formulae for likelihood-based tests of new physics*, Eur. Phys. J. C **71** (2011) 1554, arXiv: `1007.1727 [physics.data-an]`, Erratum: Eur. Phys. J. C **73** (2013) 2501.

[76] A. L. Read, *Presentation of search results: the CL_s technique*, Journal of Physics G: Nuclear and Particle Physics **28** (2002) 2693.

[77] U. Ellwanger, J. F. Gunion and C. Hugonie, *NMHDECAY: A Fortran code for the Higgs masses, couplings and decay widths in the NMSSM*, JHEP **02** (2005) 066, arXiv: `hep-ph/0406215 [hep-ph]`.

[78] U. Ellwanger and C. Hugonie, *NMHDECAY 2.0: An Updated program for sparticle masses, Higgs masses, couplings and decay widths in the NMSSM*, Comput. Phys. Commun. **175** (2006) 290, arXiv: `hep-ph/0508022 [hep-ph]`, URL: `http://www.th.u-psud.fr/NMHDECAY/nmssmtools.html`.

[79] G. Degrassi and P. Slavich, *On the radiative corrections to the neutral Higgs boson masses in the NMSSM*, Nucl. Phys. **B825** (2010) 119, arXiv: `0907.4682 [hep-ph]`.

[80] P. Bechtle, O. Brein, S. Heinemeyer, G. Weiglein and K. E. Williams, *HiggsBounds: Confronting Arbitrary Higgs Sectors with Exclusion Bounds from LEP and the Tevatron*, Comput. Phys. Commun. **181** (2010) 138, arXiv: `0811.4169 [hep-ph]`.

[81] P. Bechtle, O. Brein, S. Heinemeyer, G. Weiglein and K. E. Williams, *HiggsBounds 2.0.0: Confronting Neutral and Charged Higgs Sector Predictions with Exclusion Bounds from LEP and the Tevatron*, Comput. Phys. Commun. **182** (2011) 2605, arXiv: `1102.1898 [hep-ph]`.

[82] P. Bechtle et al., *Recent Developments in HiggsBounds and a Preview of HiggsSignals*, PoS **CHARGED2012** (2012) 024, arXiv: `1301.2345 [hep-ph]`.

[83] P. Bechtle et al., HiggsBounds − 4*: Improved Tests of Extended Higgs Sectors against Exclusion Bounds from LEP, the Tevatron and the LHC*, Eur. Phys. J. **C74** (2014) 2693, arXiv: `1311.0055 [hep-ph]`.

[84] P. Bechtle, S. Heinemeyer, O. Stal, T. Stefaniak and G. Weiglein, *Applying Exclusion Likelihoods from LHC Searches to Extended Higgs Sectors*, Eur. Phys. J. **C75** (2015) 421, arXiv: `1507.06706 [hep-ph]`.

[85] R. V. Harlander, S. Liebler and H. Mantler, *SusHi: A program for the calculation of Higgs production in gluon fusion and bottom-quark annihilation in the Standard Model and the MSSM*, Comput. Phys. Commun. **184** (2013) 1605, arXiv: `1212.3249 [hep-ph]`.

[86] R. V. Harlander, S. Liebler and H. Mantler, *SusHi Bento: Beyond NNLO and the heavy-top limit*, Comput. Phys. Commun. **212** (2017) 239, arXiv: `1605.03190 [hep-ph]`.

[87] A. Buckley et al., *LHAPDF6: parton density access in the LHC precision era*, Eur. Phys. J. **C75** (2015) 132, arXiv: `1412.7420 [hep-ph]`.

[88] L. A. Harland-Lang, A. D. Martin, P. Motylinski and R. S. Thorne, *Parton distributions in the LHC era: MMHT 2014 PDFs*, Eur. Phys. J. **C75** (2015) 204, arXiv: `1412.3989 [hep-ph]`.

[89] A. Ariga et al., *Letter of Intent for FASER: ForwArd Search ExpeRiment at the LHC*, (2018), arXiv: `1811.10243 [physics.ins-det]`.

[90] ATLAS Collaboration, *Expected photon performance in the ATLAS experiment*, ATL-PHYS-PUB-2011-007, 2011, URL: `https://cds.cern.ch/record/1345329`.